BIOACTIVE POLYSACCHARIDES AND SMALL MOLECULES FROM THE NATIVE NORTH AMERICAN FUNGUS *ECHINODONTIUM TINCTORIUM*

by

Mehreen Zeb

(MPhil Biochemistry/Molecular Biology), Quaid-e-Azam University, Islamabad, Pakistan, 2013
(Doctor of Pharmacy, PharmD), Riphah International University, Islamabad, Pakistan, 2009

DISSERTATION SUBMITTED IN PARTIAL FULFILLMENT OF
THE REQUIREMENTS FOR THE DEGREE OF
DOCTOR OF PHILOSOPHY
IN
HEALTH SCIENCE

UNIVERSITY OF NORTHERN BRITISH COLUMBIA

December, 2021

ABSTRACT

Mushrooms, the fruiting bodies of fungi, are known to be powerful sources of nutraceuticals and pharmaceuticals but there are limited studies focusing on exploring the medicinal value of mushrooms native to North America. Here, I describe the isolation of two novel bioactive polysaccharides from the aqueous extracts of the fungus *Echinodontium tinctorium*: an immuno-stimulatory complex polysaccharide (EtISPFa) of 1354 kDa, and a growth-inhibitory *β*-glucan of 275 kDa. In addition, six small molecules including a phenol derivative, a new diphenylmethane derivative and three lanostane-type triterpenes were isolated from the organic extracts of *E. tinctorium*. The molar mass of these isolated small molecules (labelled **1-6)** was determined to be 124, 260, 506, 498, 496, and 440 g/mol respectively.

Phase separation, Sephadex LH-20 size exclusion, Sephadex DEAE ion exchange chromatography, Sephacryl S-500 HR size exclusion, silica column chromatography, and HPLC were used for bioactivity-guided purification. Chemical structures and linkages of EtISPFa and EtGIPL1a polysaccharides were determined by gas chromatography mass spectrometry (GC-MS) and nuclear magnetic resonance (NMR). Final structures of small molecules were determined by Fourier transform infrared spectroscopy (FTIR), electrospray ionization mass spectrometry (ESI-MS), NMR, and X-ray crystallography.

Immuno-stimulatory activity of EtISPFa was assessed by immunoassay in Raw 264.7 murine macrophage cells and growth-inhibitory activity of EtGIPL1a and small molecules were assessed by MTT growth-inhibitory assay in cancer cell lines. The mechanism of growth inhibition was assessed via apoptosis and cell cycle assays. EtISPFa stimulated the immune response by inducing TNF-α and other inflammatory cytokines in murine macrophage cells. In contrast, EtGIPL1a showed promising anti-proliferative activity against U251 glioblastoma cells and on

ten other cancer cell lines. EtGIPL1a induced apoptosis in U251 cells with an increased cleaved caspase-3 apoptotic marker and significant DNA fragmentation in cell cycle analysis. Amongst the small molecules, compounds **(2)**, **(4)** and **(5)** caused growth-inhibition in U251 cells; compound **(4)** also showed promising effects on multiple other cancer cell lines; all its bioactivities are reported here for the first time. The crystal structures of compounds **(2)**, **(4)** and **(5)** have also been reported for the first time. Molecular targets of **(1)**, **(2)**, **(4)** and **(5)** by MolTarPred were predicted and warrants further experimental investigation.

PREFACE

This current PhD dissertation has yielded two manuscripts where Chapter 1 and Chapter 2 have been published as:

Paper 1/ Chapter 1: Zeb, M., & Lee, C. H. (2021). Medicinal properties and bioactive compounds from wild mushrooms native to North America. *Molecules*, *26*(2), 1-24.

Paper 2/ Chapter 2: Zeb, M., Tackaberry, L. E., Massicotte, H. B., Egger, K. N., Reimer, K., Lu, G., Heiss, C., Azadi, P., & Lee, C. H. (2021). Structural elucidation and immuno-stimulatory activity of a novel polysaccharide containing glucuronic acid from the fungus *Echinodontium tinctorium*. *Carbohydrate Polymers*, *258*, 1-9.

TABLE OF CONTENTS

LIST OF TABLES

Chapter 1

Chapter 2

Chapter 3

Chapter 4

Chapter 5

Supplementary

LIST OF FIGURES

Chapter 1

Chapter 2

Chapter 3

Chapter 4

Chapter 5

Supplementary

LIST OF ABBREVIATIONS

COSY	Correlation Spectroscopy
CD_3CN	Acetonitrile-d
DAD	Diode Array Detector
DEAE	Diethylaminoethyl
DEPT	Distortionless Enhancement by Polarization Transfer
DMEM	Dulbecco's Modified Eagle Medium
DPBS	Dulbecco's Phosphate Buffered Saline
EA	Ethyl acetate
ELISA	Enzyme-linked Immunosorbent Assay
EMEM	Eagle Minimum Essential Medium
ESI-MS	Electro Spray Ionization-Mass Spectrometry
FBS	Fetal Bovine Serum
FIA	Flow Injection Analysis
FTIR	Fourier Transform InfraRed Spectroscopy
GB	Glioblastoma
HPLC	High Performance Liquid Chromatography
HMBC	Heteronuclear Multiple Bond Correlation
HRESI-MS	High Resolution Electro Spray Ionization-Mass Spectrometry
HSQC	Heteronuclear Single Quantum Coherence
MTT	3-(4,5-Dimethylthiazol-2-YI)-2,5-Diphenyltetrazolium Bromide
Mp	Peak maxima molecular weight
Mn	Number average molecular weight
Mw	Weight average molecular weight
NOESY	Nuclear Overhauser Effect Spectroscopy
TNF- α	Tumor Necrosis Factor-alpha
SEC	Size Exclusion Chromatography
VWD	Variable Wavelength Detector
^{1}H NMR	Proton Nuclear Magnetic Resonance
^{13}C NMR	Carbon Nuclear Magnetic Resonance

ACKNOWLEDGEMENT

I would like to express my gratitude to my supervisor Dr. Chow Lee for giving me the opportunity to pursue PhD research. I am extremely thankful for his guidance, mentorship, and continuous support. His thoughtful recommendations and timelines helped me achieve my research goals in a timely fashion. I am also extremely grateful to all my committee members, Dr. Kerry Reimer, Dr. Hugues Massicotte, and Dr. Keith Egger, for providing insightful comments and suggestions that helped me shape my dissertation. I greatly acknowledge the assistance of Dr. Reimer in guiding me on structure elucidation and other chemistry related aspects. I very much appreciate the critical discussions with Dr. Wai Ming Li on experiments that helped me grow and think in multiple dimensions. It was a pleasure working and learning chemistry techniques from Dr. Kaila Fadock. I also want to thank the NALS members (Charles Bradshaw and Dr. Hossein Kazemian) for providing all the critical support that was much needed to perform important analysis for my dissertation. I also had the great pleasure of working with former and current Lee lab members including Sumreen Javed, Almas Yaqoob, Victor Liu, Hooi Xian, Noburu Kato, and others. Much thanks to my best PhD cohort, Daman Kandola, Lisa Kyle, and Steinunn Jonathan who have always provided unparalleled support.

The endless moral support from my spouse Muhammad Ali Khan and my children Meerab Ali Khan and FariahAli Khan has always been behind all my accomplishments. A very special thanks to my parents Aurangzeb Khan and Tabassum Fayyaz for always believing in me and motivating me to achieve more. My appreciation also goes to my brother Jahanzeb Khan and sisters Aqsa Khan and Romaisa Khan for their encouragement.

Chapter 1: Introduction and Literature Review

1.1 Medicinal mushrooms

Natural products have been used as medicines for centuries; however, it is only in the last century that researchers have begun to diligently characterize their biological and chemical properties. Mushrooms are natural reservoirs of potent pharmaceuticals and continue to be an interface for drug discovery. Mushrooms belong mostly to phyla Ascomycota or Basidiomycota, and together they constitute the sub-kingdom Dikarya within the Kingdom Fungi. Mushrooms are defined as "*epigeous and hypogeous fruiting bodies of macroscopic fungi*" (Chang, 2013). Fungi are defined as "*achlorophyllous, heterotrophic (saprophytic, parasitic, or symbiotic), eukaryotic and spore-bearing organisms surrounded by a well-defined cell wall made up of chitin, with or without fungal cellulose along with many other complex organic molecules*" (Sharma, 1989). According to recent estimates, fungi constitute 2.2 – 3.8 million species worldwide (Hawksworth & Lucking, 2017). These fungal estimates include all the different types of fungi including mushrooms. Earlier estimates indicated the total number of mushrooms to be 140,000-160,000 species, where only 10% have been explored (Hawksworth, 2001; Wasser, 2014).

Mushrooms have a long history of medicinal use in various cultures across the globe. They have earned medicinal status long ago in China and other parts of Asia including Japan and Korea. The scope of medicinal mushrooms has expanded to other countries such as the USA and eastern European countries such as Russia (Chang, 1999; Reshetnikov & Tan, 2001; Van Griensven, 2009; Wasser & Weis, 1999; Wasser, 2010). Initially, mushrooms became popular as a folklore remedy. For example, in the sixteenth century in Russia and Europe, *Inonotus obliquus* (chaga) became famous as a folklore medicine for cancer treatment (Zheng *et al*., 2010). Later

on, scientists became interested in finding the evidence behind the diverse bioactive potential that is contained in mushrooms. This has led to the exploration of untapped mushroom resources for their medicinal benefit and the bioactive compounds that impart these properties. Unlike in Asia and parts of Eastern Europe, there are relatively few studies on the exploration of mushrooms native to North America for medicinal properties.

The purpose of this review is to provide up-to-date information on the bioprospecting efforts on mushrooms native to North America. With literature searches and the information gained, the aim is to answer the following questions: (i) Do similar species found in North America compared to the ones found in Asia or Europe exhibit similar bioactivities and bioactive compounds? (ii) Do similar species found in North America and Asia or Europe exhibit distinct bioactivity and produce distinct compounds? (iii) Do new species found in North America produce new compound(s)? and (iv) Based on the answers to (i) to (iii) above, the efforts to explore mushrooms native to North America for medicinal properties warrants new medicinal compounds?

1.2 Mushrooms native to North America

North America, encompassing the northern subcontinent of the Americas that includes Canada, the United States, Mexico, and Greenland, has one of the world's largest and most diverse ecological systems. It is also home to diverse mushrooms that are relatively unexplored for their therapeutic benefit. Although new species continue to be discovered in North America, about 22-55% of the mushroom species remain unexplored (Hawksworth, 2001). Like elsewhere, mushrooms were recognized as an important source for medicine by people who lived in North America centuries ago. The indigenous people of North America had used *Calvatia* mushrooms (more commonly known as puffballs) to heal wounds (Burk, 1983). The therapeutic value of

Fomitopsis officinalis was also discovered by First Nations peoples of North America, including those in British Columbia (BC) where *F. officinalis* sporophores were carved as shaman grave guardians (Blanchette *et al*., 1992).

In recent years, there has been increasing reports on mushrooms native to North America possessing medicinal properties. Whether it be *Hericium* sp., found growing on hardwood and coniferous trees that contains a number of small molecules with antibacterial properties (Song *et al*., 2020) or *Echinodontium tinctorium*, native to British Columbia and commonly found as a woody conk on hemlocks, with immuno-stimulatory and anti-inflammatory compounds in its fruiting bodies (Javed *et al*., 2019; Zeb *et al*., 2021). Others include *Cortinarius armillatus* which grows in moist coniferous forests and contains orellanine, a potential toxin against renal carcinoma (Shao *et al*., 2016; Buvall *et al*., 2017). Table 1.1 summarizes all the mushrooms found in North America that have been reported to possess medicinal properties and their origin of collection and/or discovery.

1.3 Medicinal properties of mushrooms native to North America

Mushrooms are known to possess medicinal properties that provide benefits against a large number of diseases. Some of the important medicinal benefits reported include antimicrobial, antioxidant, anticancer, immune system enhancer, antiviral, anti-hyperlipidemia, radical scavenger, anti-parasitic and anti-inflammatory activity (Wasser, 2017). Amongst these, the most common medicinal properties reported from mushrooms native to North America are anticancer, immuno-stimulatory, anti-inflammatory, antimicrobial and antioxidant as shown in Table 1.1 (Song *et al*., 2020; Javed *et al*., 2019; Zeb *et al*., 2021; Shao *et al*., 2016, Buvall *et al*., 2017; Wasser, 2017; Shideler *et al*., 2017; Stanikunaite *et al*., 2009; Yaqoob *et al*., 2020; Liu *et al*., 2010; Smith *et al*., 2017; Barad *et al*., 2018; Pacheco-Sanchez *et al*., 2006 & 2007).

1.3.1 Anti-bacterial and anti-viral activities

Antimicrobial resistance is a major healthcare problem worldwide. A recent landmark report indicated that bacterial infections resistant to treatment are likely to grow from 26% in 2018 to 40% by 2050, and such increases are expected to cost thousands of lives, billions of dollars in hospital expenses and gross domestic product, and have a negative social impact on people worldwide (Council of Canadian Academies, 2019). Therefore, it is recommended that efforts to discover new antimicrobial drugs to combat specific antibiotic-resistant pathogens should be strengthened and should include innovative strategies (Council of Canadian Academies, 2019; Strachan & Davie, 2017; Gould *et al*., 2019). To this end, researchers have focused on unexplored and unique environments and resources, including mushrooms, as avenues to discover novel antimicrobial metabolites. Grifolin, neogrifolin and confluentin isolated from *Albatrellus flettii* collected in California were found to have potent activity against gram-positive bacteria *Bacillus cereus* and *Enterococcus faecalis* (Liu *et al.*, 2010). Another lanostane-type tripterpene isolated from *Jahnoporus hirtus* also inhibited the growth of *Bacillus cereus* and *Enterococcus faecalis* (Liu *et al.*, 2010). Supernatants from culture of *Lenzites betulina* and *Haploporus odorus* (Shideler *et al*., 2017) as well as extracts from *Pleurotus ostreatus* and *P. levis* (Adebayo *et al*. 2018), also have antimicrobial activity. However, the responsible antimicrobial compounds have not been isolated from these mushrooms. In another study using extracts from 75 mushrooms collected in Oxford, Ohio, USA, it was found that a total of 25 species had antibacterial activity against at least one of the bacterial strains assessed (Hassan *et al*., 2019). From this study, extracts from *Ganoderma lucidum* and *Laetiporus sulphureus* were found to have the strongest antibacterial activity (Hassan *et al*., 2019).

Table 1.1. Mushrooms native to North America studied for bioactivities

Mushroom	Origin	Bioactivity	Bioactive component[1]
Albatrellus flettii	Smithers, BC	Anti-proliferative (Yaqoob *et al.*, 2020), antimicrobial (Liu *et al.*, 2010)	Small molecules
Amanita augusta	Haida Gwaii, BC	Anti-proliferative, immuno-stimulatory, anti-inflammatory (Deo *et al.*, 2019)	Extracts
Amanita muscaria	Prince George, BC	Anti-proliferative, immuno-stimulatory (Smith *et al.*, 2017)	Extracts
Astraeus pteridis	Linn County, Oregon	Antituberculosis (Stanikunaite *et al.*, 2007)	Extracts
Barssia oregonensis	Clackamas, Oregon	Antituberculosis (Stanikunaite *et al.*, 2007)	Extracts
Boletus curtisii	Chapel Hill, NC	ND	ND
Cantharellus cibarius	Haida Gwaii, BC	Anti-proliferative, immuno-stimulatory, anti-inflammatory (Deo *et al.*, 2019)	Extracts
Chroogomphus tomentosus	Haida Gwaii, BC	Anti-proliferative, immuno-stimulatory, anti-inflammatory (Deo *et al.*, 2019)	Extracts
Clavulina cinerea	Haida Gwaii, BC	Anti-proliferative (Deo *et al.*, 2019)	Extracts
Collybia dryophila	Quebec	Anti-inflammatory (Pacheco-Sanchez *et al.*, 2006 & 2007)	Polysaccharide
Coprinellus sp.	Seattle, WA, USA	Anti-proliferative (Wang *et al.*, 2007)	Extracts
Coprinus comatus	Seattle, WA, USA	Anti-proliferative (Wang *et al.*, 2007)	Extracts (Gu *et al.*, 2006) Protein (Zhang *et al.*, 2017)
Cortinarius armillatus	Massachusetts	Anti-proliferative, anticancer (Buvall *et al.*, 2017; Shao *et al.*, 2016)	Small molecule
Echinodontium tinctorium	Smithers and Terrace, BC	Anti-inflammatory Javed *et al.*, 2019), immuno-stimulatory (Zeb *et al.*, 2021)	Polysaccharides
Elaphomyces granulatus	Oregon and Bonner County, Idaho	Anti-inflammatory (Stanikunaite *et al.*, 2009 & 2007), antioxidant (Stanikunaite *et al.*, 2007)	Small molecules and extracts
Elaphomyces muricatus	Benton County, Oregon	Anti-inflammatory, antioxidant, antituberculosis (Stanikunaite *et al.*, 2007)	Extracts
Flammulina velutipes	Seattle, WA, USA	Anti-proliferative (Gu *et al.*, 2006)	Extracts
Fomes fomentarius	Prince George, BC	Anti-proliferative, immuno-stimulatory, anti-inflammatory (Smith *et al.*, 2017)	Extracts

Ganoderma applanatum	Terrace, BC and Oxford, Ohio	Anti-proliferative, immuno-stimulatory, anti-inflammatory (Smith *et al.*, 2017), antimicrobial (Hassan *et al.*, 2019)	Extracts
Ganoderma lucidum	Oxford, Ohio	Antimicrobial (Hassan *et al.*, 2019)	Extracts
Ganoderma tsugae	Haida Gwaii, BC	Anti-proliferative, immuno-stimulatory, anti-inflammatory (Deo *et al.*, 2019)	Extracts
Gautieria monticola	Benton County, Oregon	Antioxidant (Stanikunaite *et al.*, 2007)	Extracts
Geopora clausa	Inyo Country, California	Antioxidant, anti-proliferative (Stanikunaite *et al.*, 2007)	Extracts
Guepina helvelloides	Haida Gwaii, BC	Anti-proliferative, immuno-stimulatory, anti-inflammatory (Deo *et al.*, 2019)	Extracts
Gyromitra esculenta	Prince George, BC	Anti-proliferative, immuno-stimulatory (Smith *et al.*, 2017)	Extracts
Haploporus odorus	Calgary, Canada	Antimicrobial (Shideler *et al.*, 2017)	Extracts
Hericium corralloides	Prince George, BC	Immuno-stimulatory, anti-inflammatory (Smith *et al.*, 2017)	Extracts
Hericium sp.	Minnesota	Antimicrobial (Song *et al.*, 2020)	Small molecule
Hydnellum sp.	Prince George, BC	Anti-proliferative, immuno-stimulatory (Smith *et al.*, 2017)	Extracts
Hydnum repandum	Haida Gwaii, BC	Anti-proliferative, anti-inflammatory (Deo *et al.*, 2019)	Extracts
Hygrophoropsis aurantiaca	Haida Gwaii, BC	Anti-proliferative, anti-inflammatory (Deo *et al.*, 2019)	Extracts
Hymenogaster subalpinus	Benton County, Oregon	Anti-inflammatory, antituberculosis (Stanikunaite *et al.*, 2007)	Extracts
Hymenopellis furfuracea	Oxford, Ohio	Antimicrobial (Hassan *et al.*, 2019)	Extracts
Hypholoma fasciculare	Haida Gwaii, BC	Anti-proliferative, anti-inflammatory (Deo *et al.*, 2019)	Extracts
Inocybe sp.	Haida Gwaii, BC	Anti-proliferative, immuno-stimulatory, anti-inflammatory (Deo *et al.*, 2019)	Extracts
Inonotus obliquus	Manitoba & Prince George, BC	Anti-inflammatory (Javed *et al.*, 2019; Van *et al.*, 2009)	Extracts
Jahnoporus hirtus	USA	Antimicrobial (Liu *et al.*, 2010)	Small molecule
Laetiporus conifericola	Haida Gwaii, BC	Anti-proliferative, immuno-stimulatory, anti-inflammatory (Deo *et al.*, 2019)	Extracts
Laetiporus sulphureus	Oxford, Ohio	Antimicrobial (Hassan *et al.*, 2019)	Extracts

Lentinellus subaustralis	Oxford, Ohio	Antimicrobial (Hassan *et al.*, 2019)	Extracts
Lentinus edodes	Quebec	Anti-inflammatory (Pacheco-Sanchez *et al.*, 2006)	Polysaccharide
Leucogaster rubescens	Pend Oreille County, Oregon	Antioxidant (Stanikunaite *et al.*, 2007)	Extracts
Leucocybe connata	Prince George, BC	Anti-proliferative, immuno-stimulatory, anti-inflammatory (Smith *et al.*, 2017)	Extracts
Marasmius oreades	Quebec	Anti-inflammatory (Pacheco-Sanchez *et al.*, 2006)	Polysaccharide
Melanogaster tuberiformis	Lane County, Oregon	Antituberculosis, anti-inflammatory, antioxidant (Stanikunaite *et al.*, 2007)	Extracts
Paxillus involutus	Prince George, BC	Anti-proliferative (Barad *et al.*, 2018)	Polysaccharide
Phellinopsis conchata	Oxford, Ohio	Antimicrobial (Hassan *et al.*, 2019)	Extracts
Phellinus conchatus	Oxford, Ohio	Antimicrobial (Hassan *et al.*, 2019)	Extracts
Phellinus conchatus	Terrace, BC	Anti-proliferative, anti-inflammatory (Smith *et al.*, 2017)	Extracts
Phellinus nigricans	Terrace, BC	Anti-proliferative, immuno-stimulatory, anti-inflammatory (Smith *et al.*, 2017)	Extracts
Phellodon atratus	Haida Gwaii, BC	Anti-proliferative, immuno-stimulatory, anti-inflammatory (Deo *et al.*, 2019)	Extracts
Pholiota terrestris	Oxford, Ohio	Antimicrobial (Hassan *et al.*, 2019)	Extracts
Piptoporus betulinus	Prince George, BC	Anti-proliferative, immuno-stimulatory, anti-inflammatory (Smith *et al.*, 2017)	Extracts
Pleurotus djamor	Mexico	Anthelmintic activity (Pineda-Alegria *et al.*, 2017)	Small molecules
Pleurotus levis	Mexico	Antimicrobial, antioxidant (Adebayo *et al.*, 2018)	Extracts
Pleurotus ostreatus	USA & Haida Gwaii, BC	Anti-proliferative, immuno-stimulatory, anti-inflammatory (Deo *et al.*, 2019), antioxidant, antimicrobial (Adebayo *et al.*, 2018)	Extracts
Pleurotus tuber-regium	Olympia, WA	Anti-proliferative (Zhang *et al.*, 2011), antimicrobial (Adebayo *et al.*, 2018)	Polysaccharide and extracts
Polyporus badius	Oxford, Ohio	Antimicrobial (Hassan *et al.*, 2019)	Extracts
Polyporus squamosus	Oxford, Ohio	Antimicrobial (Hassan *et al.*, 2019)	Extracts
Pyrofomes demidoffi	Oxford, Ohio	Antimicrobial (Hassan *et al.*, 2019)	Extracts

Ramaria cystidiophora	Haida Gwaii, BC	Anti-proliferative, anti-inflammatory (Deo *et al.*, 2019), antimicrobial (Centko *et al.*, 2012)	Small molecules and extracts
Rhizopogon couchii	Lebanon State Forest, New Jersey	Anti-inflammatory, antioxidant, antituberculosis (Stanikunaite *et al.*, 2007)	Extracts
Rhizopogon nigrescens	Lebanon State Forest, New Jersey	Anti-inflammatory, antioxidant (Stanikunaite *et al.*, 2007)	Extracts
Rhizopogon pedicellus	Pend Oreille County, Oregon	Antioxidant, antituberculosis (Stanikunaite *et al.*, 2007)	Extracts
Rhizopogon subareolatus	Lewis County, Washington	Antimalarial (Stanikunaite *et al.*, 2007)	Extracts
Rhizopogon subaustralis	Lebanon State Forest, New Jersey	Anti-inflammatory, antioxidant (Stanikunaite *et al.*, 2007)	Extracts
Rhizopogon subgelatinosus	Jackson County, Oregon	Anti-inflammatory, anti-proliferative (Stanikunaite *et al.*, 2007)	Extracts
Royoporus badius	Prince George, BC	Immuno-stimulatory (Lee, 2020)	Polysaccharide-protein
Russula paludosa	Haida Gwaii, BC	Anti-proliferative, anti-inflammatory (Deo *et al.*, 2019)	Extracts
Scleroderma laeve	Lebanon State Forest, New Jersey	Anti-inflammatory, antioxidant, antituberculosis (Stanikunaite *et al.*, 2007)	Extracts
Stereum hirsutum	Oxford, Ohio	Antimicrobial (Hassan *et al.*, 2019)	Extracts
Trametes versicolor	Oxford, Ohio	Antimicrobial (Hassan *et al.*, 2019)	Extracts
Trichaptum abietinum	Prince George, BC	Anti-proliferative, immuno-stimulatory, anti-inflammatory (Smith *et al.*, 2017)	Extracts
Tricholomopsis rutilans	Haida Gwaii, BC	Anti-proliferative, anti-inflammatory (Deo *et al.*, 2019)	Extracts
Tyromyces chioneus	Haida Gwaii, BC	Anti-proliferative, immuno-stimulatory, anti-inflammatory (Deo *et al.*, 2019)	Extracts

[1]Refer to Table 1.2 for more information of bioactive small molecules and polysaccharides.

Extracts of polypore mushrooms native to North America have been shown to have antiviral activities against viruses that attack honey bees (Stamets *et al*., 2018). Mycelium extracts from *Fomes fomentarius* collected in Ithaca, New York and *Ganoderma resinaceum* culture from

Ontario, Canada were found to reduce the levels of honey bee deformed wing virus and Lake Sinai virus *in vivo* in both laboratory and field studies (Stamets *et al*., 2018).

1.3.2 Anti-proliferative activity

Mushrooms native to North America have been explored for anti-proliferative activity against cancer cell lines. For instance, out of 29 species of mushrooms examined from north-central British Columbia (BC) (Smith *et al*., 2017) and Haida Gwaii, BC (Deo *et al*., 2019), 27 species exhibited anti-proliferative activity; 16 out of the 27 species (59%) had their anti-proliferative activity reported for the first time (Deo *et al*., 2019; Smith *et al*., 2017). These species include *Amanita augusta, Cantharellus cibarius, Chroogomphus tomentosus, Guepinia helvelloides, Gyromitra esculenta, Hydnellum* sp*., Inocybe* sp*., Laetiporus conifericola, Leucocybe connata, Phellodon atratus, Pleurotus ostreatus, Ramaria cystidiophora, Russula paludosa, Trichaptum abietinum, Tricholomopsis rutilans*, and *Tyromyces chioneus*. Inspired by such findings, we have further explored BC wild mushrooms for bioactivities. Out of 49 species collected from northern interior BC, we found that 21 species (43%) exhibited potent anti-proliferative activity that has not been previously reported (Lee, 2020, pers. comm.). Another study was conducted on 38 species of mushrooms collected from greater Seattle area, Washington State, USA, and out of these, aqueous extracts from 3 species were identified as anti-proliferative in human estrogen receptor negative (MDA-MB-231, BT-20) and estrogen receptor positive (MCF-7) breast cancer cells. These included *Coprinus comatus*, *Coprinellus* sp., and *Flammulina velutipes* (Gu & Leonard, 2006). Elsewhere, the ethanol and water extracts of *Pleurotus tuber-regium* from Washington State displayed anti-proliferative effects in HCT-116 colon and HeLa cervical cancer cell lines (Maness *et al*., 2011). Although in most cases the identity of anti-proliferative compounds from the mushroom species described above remains unknown, there are detailed

structural elucidation and mechanistic studies of both bioactive small molecules and polysaccharides isolated from selected species. For example, a growth-inhibitory polysaccharide GIPinv that caused growth inhibition in several cancer cell lines and induced apoptosis in HeLa cancer cells was isolated from *Paxillus involutus* (Barad *et al*., 2018). Small molecules grifolin, neogrifolin and confluentin were found to be the major growth-inhibitory compounds in the ethanol extracts of *Albatrellus flettii* (Yaqoob *et al*., 2020). It was also discovered that confluentin can inhibit the RNA-binding function of the oncogenic protein insulin-like growth factor 2 mRNA-binding protein 1 (IMP1) (Yaqoob *et al*., 2020). Elsewhere, an exopolysaccharide isolated from *P. tuber-regium* inhibited the growth of chronic myelogenous leukemia K562 cells (Zhang & Cheung, 2011). Orellanine, a small molecule originally isolated from a European mushroom species *Cortinarius orellanus,* has recently been isolated from a North American mushroom species *C. armillatus,* with cytotoxic potential against renal carcinoma in a dose-dependent manner (Buvall *et al*., 2017).

1.3.3 Anti-inflammatory activity

Mushrooms native to North America have also been explored for anti-inflammatory activity. Out of 29 species examined from north-central BC (Smith *et al*., 2017) and Haida Gwaii (Deo *et al*., 2019), 26 (69%) had their anti-inflammatory activity reported for the first time (Deo *et al*., 2019; Smith *et al*., 2017). These species include *Amanita augusta, Chroogomphus tomentosus, Clavulina cinerea, Guepinia helvelloides, Gyromitra esculenta, Hydnum repandum, Hygrophoropsis aurantiaca, Hypholoma fasciculare, Inocybe sp., Laetiporus conifericola, Leucocybe connata, Phellinus nigricans, Phellodon atratus, Pleurotus ostreatus, Ramaria cystidiophora, Russula paludosa, Trichaptum abietinum, Tricholomopsis rutilans,* and *Tyromyces chioneus.* We have further explored BC wild mushrooms for anti-inflammatory

activity. Out of 49 species collected from northern interior BC, we found 34 species (69%) that exhibited potent anti-inflammatory activity not been previously reported (Lee, 2020, pers. comm.). Extracts from *Inonotus obliquus collected* in BC, like those found in other parts of the world, showed strong anti-inflammatory activity *in vitro* (Javed *et al*., 2019; Smith *et al*., 2017). In addition, Javed *et al*. (2019) demonstrated for the first time the ability of methanol extracts of *I. obliquus* to attenuate histamine-induced inflammation in the arterioles of gluteus muscle of mice. A limited number of anti-inflammatory compounds have been isolated from mushrooms native to North America. A polysaccharide called CDP from *Collybia dryophila,* and CDP-like polysaccharides from *Lentinula edodes* and *Marasmius oreades,* can inhibit nitric oxide production in Raw264.7 macrophage cells (Pacheco-Sanchez *et al*., 2007). Javed *et al*. (2019) demonstrated that a 5 kDa polysaccharide (AIPetinc) isolated from the NaOH extract of *E. tinctorium* showed anti-inflammatory activity *in vitro* as well as in the histamine-induced inflammatory mouse microcirculation model. Elsewhere, the ethanolic extract as well as two small molecules, syringaldehyde and syringic acid, isolated from *Elaphomyces granulatus* inhibited COX-2 enzyme in Raw264.7 cells; the extract caused 68% inhibition of COX-2 at 50 µg/mL, whereas syringaldehyde and syringic acid were effective with IC_{50} of 3.5 µg/mL and 0.4 µg/mL respectively (Shao *et al*., 2016).

1.3.4 Immuno-stimulatory activity

Mushroom species are known to have immunotherapeutic properties and over 270 species had been recognized (Ooi & Liu, 2000). Mushrooms are natural immune-modulators that can enhance the host immune system by activating dendritic cells, T cells, NK cells, macrophages, and cytokines. A desired immune status requires an equilibrium in T helper type 1 (Th1) cellular immune response and T helper type 2 (Th2) humoral immune response. Th1 cells are

components of cell-mediated immune responses and they produce cytokines interferon-γ (IFN-γ), Tumor necrosis factor (TNF)-α, interleukin-12 (IL-12) and interleukin-2 (IL-2) whereas Th2 cells are involved in humoral immune responses and express IL-5, 6, 9, 10, 13, GM-CSF and macrophage-derived chemokines (Mosmann & Sad, 1996; Romagnani, 2000). Th1 immune response is required for cancer treatment. Th2 immune response is usually not associated with cancer. In the context of such immune response patterns, mushrooms which have the ability to stimulate Th1 responses by increasing IFN-γ and IL-2 production are known to possess immunomodulatory activity.

Mushroom native to North America have also been explored for immuno-stimulatory activity. Out of 29 species of mushrooms examined from north-central British Columbia (BC) (Smith *et al*., 2017) and Haida Gwaii, BC (Deo *et al*., 2019), 20 exhibited immuno-stimulatory activity. Fifteen out of the 20 species (75%) had their immuno-stimulatory activity reported for the first time (Deo *et al*., 2019; Smith *et al*., 2017). These species include *Amanita augusta, Chroogomphus tomentosus, Clavulina cinerea, Fomes fomentarius, Guepinia helvelloides, Gyromitra esculenta, Hericium coralloides, Hydnum repandum, Hydnellum* sp*., Hygrophoropsis aurantica, Hypholoma fasciculare, Inocybe* sp*., Laetiporus conifericola, Leucocybe connata, Phellinus nigricans, Phellodon atratus,* and *Piptoporus betulinus*. Furthermore, out of 49 additional species collected from northern interior BC, 25 (51%) exhibited potent immuno-stimulatory activity that has not been previously reported (Lee, 2020, pers. comm.). Table 1.2 lists several bioactive compounds characterized from diverse mushrooms from elsewhere with immuno-stimulatory potential.

Table 1. 2. Immuno-stimulatory compounds from mushrooms

Mushroom name	Common name	Bioactive compounds	Reference
Agaricus blazei, Agaricus subrufescens	Almond mushroom Cogumelo do Sol (Brazil), Himematsutake (Japan)	Polysaccharide (β-D-glucan)	(Guggenheim *et al*., 2014; Kim *et al*., 2009; Wilbers *et al*., 2016)
Agaricus bisporus	White button mushroom	Polysaccharide	(Zhang *et al*., 2014)
Antrodia camphorata	Stout camphor fungus	Protein ACA	(Sheu *et al.,* 2009)
Cordyceps sinensis	Caterpillar fungus	Nucleotide (Adenosine, Cordycepin)	(Guggenheim *et al*., 2014; Hsieh *et al*., 2013)
Trametes versicolor (Coriolus versicolor)	Turkey tail fungus	Polysaccharide-protein complexes (PSPC), Polysaccharide-peptide (PSP), Polysaccharide-K (PSK)	(Guggenheim *et al*., 2014; Luo et al., 2014; Tzianabos, 2000)
Ganoderma lucidum	Reishi, Lingzhi "King of herbs" "soul/spirit mushroom"	Protein (Ganoderic acid, Danoderiol, Danderenic acid, Lucidenic acid). Polysaccharide (GLPS- *G. lucidum* polysaccharide)	(Guggenheim *et al*., 2014; Lin *et al*., 2009; Zhou *et al.,* 2015)
Ganoderma microsporum	-	Protein	(Lin *et al*., 2010)
Inonotus obliquus	Chaga	Polysaccharide	(Baek *et al.,* 2012)
Grifola frondosa	Hen of the woods, Maitake	Grifolan Polysaccharide (β-D-glucan, D-fraction, MD-fraction), Protein low molecular wt.	(Guggenheim *et al*., 2014; Kodama *et al*., 2010; Park *et al.,* 2015)
Dictyophora indusiata	Veiled Lady Mushroom	β-D-glucan	(Fu *et al.,* 2015)
Sparassis crispa	-	β-(1,3)-glucan	(Harada & Ohno, 2008)
Lentinus edodes	Shiitake mushroom	Lentinan (β-(1,3), β-(1-6) D-glucan)	(Abel *et al.,* 1989; Chihara *et al.,* 1987; Wasser & Weis, 1999)
Schizophyllum commune	-	Schizophyllan (β-(1-3), β-(1-6) D-glucan)	(Miyazaki *et al.,* 1995)
Tricholoma mongolicum	-	TML-1 and TML-2	(Wang *et al*., 1996)

Pleurotus eryngii	King oyster mushroom	Polysaccharide	(Liu *et al*., 2015)

To date, most of the immuno-stimulatory compounds from mushrooms are polysaccharides or polysaccharide-protein complexes (Giavasis, 2014; Enshasy & Hatti-Kaul, 2014). Immunopotentiator polysaccharides isolated from mushrooms are chemically categorized as β-D-glucans or β-D-glucans conjugated with proteins. Researchers believe that immuno-stimulation mechanism involves the binding of β-D-glucans to membrane receptors on the surface of cells, as they cannot enter the cells due to their large size. β-D-glucans have affinity to bind with different receptors which include β-D-glucan inhibitable receptor (Czop and Austen, 1985), Dectin-1 receptor (Adachi *et al*. 2004; Brown *et al*. 2003), Lactosylceramide (LacCer), Toll-like receptor (TLR) 2, and Complement receptor type 3 (CR3) (Ross *et al.* 1999; Xia *et al*. 1999). CR3 is also recognized as Mac-1, CD11b/CD18 or αMβ2-integrin. Based on this evidence, CR3 is the major β-glucan receptor potentiating the immunomodulatory responses of polysaccharides; it acts as an adhesion molecule and a receptor for factor I-cleaved C3b (iC3b) on macrophages. When CR3 binds to iC3b, CD11b I-domain binding site recognizes iC3b whereas the lectin site of CR3 recognizes glucans. This interaction results in phagocytosis and cytotoxic degranulation (Chen & Seviour, 2007; Guggenheim *et al.,* 2014).

Due to problems such as: (i) high variability of polysaccharides, that is further exacerbated during extraction and purification, (ii) impurities and contaminants, and (iii) difficulty in defining the structure and chemical fingerprint to understand structure-function relationships (Persin *et al*., 2011), there has been little interest amongst scientists in North America to study and isolate immuno-stimulatory polysaccharides from mushrooms native to North America. Despite such obstacles, we have isolated two immuno-stimulatory compounds from mushrooms

native to northern BC. A complex glucuronic acid-rich polysaccharide called EtISPFa was isolated from *Echinodontium tinctorium* (Zeb *et al*., 2021), and a polysaccharide-protein complex rich in galactose and mannose called ISPP-Rb was isolated from *Royoporus badius* (Lee, 2020, pers. comm.). Both EtISPFa and ISPP-Rb are capable of inducing the production of TNF-α and other pro-inflammatory cytokines and chemokines (Lee, 2020; Zeb *et al*., 2021).

1.3.5 Anti-oxidant activity

There have been relatively less studies on anti-oxidant activity of mushrooms native to North America. One study reported ethanolic extracts from 11 species of mushrooms collected from Idaho, Oregon, and New Jersey, to have moderate to weak anti-oxidant activity (Stanikunaite *et al*., 2007). The ethanolic extract, as well as syringic acid isolated from the fruiting bodies of *Elaphomyces granulatus,* showed potent antioxidant effect on myelomonocytic HL-60 cells with an IC_{50} of 41 µg/mL for the extract and 0.7 µg/mL for syringic acid (Stanikunaite *et al*., 2009). Two edible mushrooms, *Pleurotus ostreatus* from USA and *P. levis* from Mexico, also showed antioxidant activity (Adebayo *et al*., 2018).

1.3.6 Anti-fungal activity

Many mushrooms are known to possess antifungal activity (Alves *et al*., 2013). However, there has been only one study on anti-fungal activity of mushroom native to North America; it shows that a chlorinated orcinol derivative, 2-chloro-1,3-dimethoxy-5-methyl benzene isolated from *Hericium* sp. collected in Minnesota, USA, has inhibitory effect on *Candida albicans* and *Candida neoformans*, suggesting its role as an antifungal agent (Song *et al*., 2020).

1.3.7 Other bioactivities

In addition to the bioactivities described above, mushrooms from North America have also been investigated for antiparasitic, antimalarial and antituberculosis activities. A study conducted

in Mexico showed antiparasitic effects of hydroalcoholic extracts from *Pleurotus djamor* against *Haemonchus contortus* eggs (Pineda-Alegria *et al*., 2017), suggesting its metabolites can act as anthelmintics. In the same study, a few small molecules with antiparasitic activity, pentadecanoic, hexadecanoic, octadecadienoic, octadecanoic acid, *β*-sitosterol, were also isolated (Pineda-Alegria *et al*., 2017). Stanikunaite and co-workers assessed 22 species of mushrooms native to North America and found *Rhizopogon subareolatus* to have antimalarial activity (Stanikunaite *et al*., 2007). They also found the following species to have antituberculosis activity: *Astraeus pteridis, Barssia oregonensis, Elaphomyces granulatus, E. muricatus, Hymenogaster subalpinus, Melanogaster tuberiformis, Rhizopogon couchii, R. pedicellus, R. subareolatus,* and *Scleroderma laeve* (Stanikunaite *et al*., 2007).

1.4 Bioactive compounds from mushrooms native to North America

Since there is a relatively limited number of studies on mushrooms native to North America, it is not surprising to find relatively limited number of bioactive compounds isolated from the mushrooms. Here, we summarize all the bioactive compounds that have been isolated from mushrooms native to North America into two general groups; large molecules and small molecules (Table 1.3) (Fig. 1.1).

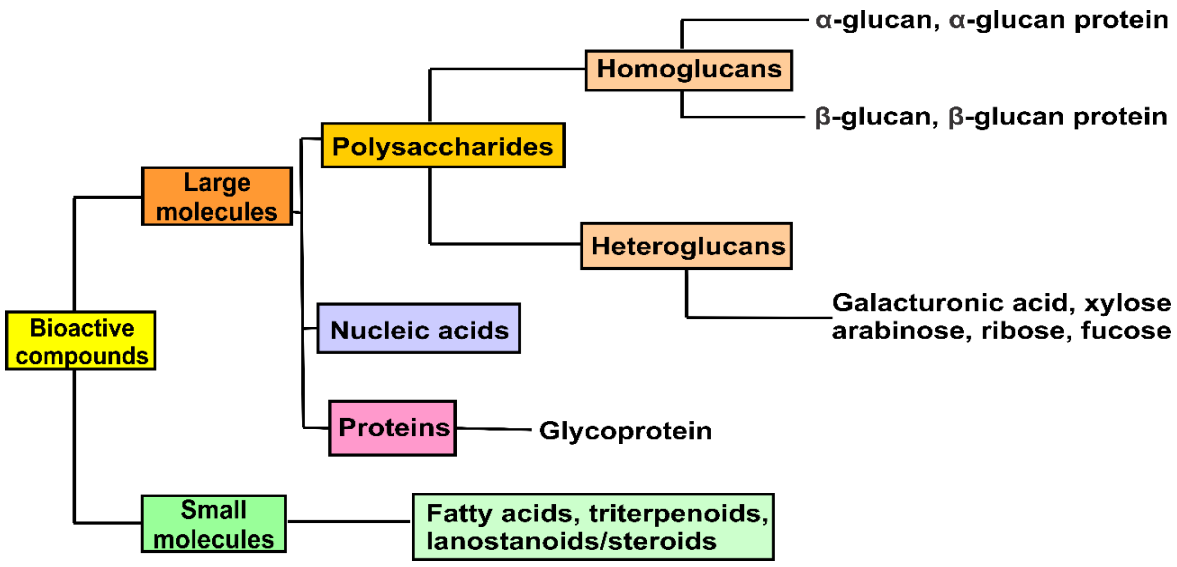

Fig. 1. 1. Classification of bioactive compounds isolated from mushrooms.

1.4.1 Large molecular weight compounds

Large molecular weight compounds isolated from mushrooms are typically homo- and heteroglycans, proteins, polysaccharide-protein complexes and nucleic acids-protein complexes (Fig.1.1) (Ferreira *et al*., 2010). Table 1.3 summarizes the bioactive large molecules that have been isolated from North American wild mushrooms. A 229 kDa growth-inhibitory heteroglycan GIPinv was isolated from the 5% NaOH extract of *Paxillus involutus* (Barad *et al*., 2018). GIPinv is made up predominantly of glucose (65.9%), galactose (20.8%) and mannose (7.8%) with traces of fucose (3.2%) and xylose (2.3%) (Barad *et al*., 2018). It has mixed linkages in the backbone containing (1→6)-Gal, (1→4)-Glc, (1→6)-Glc, (1→3)-Glc, and (1→2)-Xyl, with branching points at (1→2,6)-Man and (1→3,6)-Man. Another growth-inhibitory polysaccharide, an exopolysaccharide called EPS, was isolated from *P. tuber-regium* (Maness *et al*., 2011). EPS is 3,180 kDa and consisted mainly of mannose (57.5%) and glucose (42.5%). Another study showed anti-proliferative effect of a 12 kDa 130-amino acid containing glycan-binding protein

(Y3). Y3 is a tertiary protein isolated from *Coprinus comatus* and exhibited selective anti-proliferative effects in human T cell leukemia Jurkat cells (Zhang *et al*., 2017).

A 1,234 kDa anti-inflammatory β-glucan polysaccharide CDP consisting of (1→3) and (1→4) glucosidic linkages was isolated from aqueous extract of the fruiting bodies of *Collybia dryophila* (Pacheco-Sanchez *et al*., 2006, 2007). Some other CDP-like polysaccharides with anti-inflammatory potential, 610 kDa and 1,316 kDa in size, were isolated from the aqueous extracts of *Lentinula edodes* and *Marasmius oreades* respectively (Pacheco-Sanchez *et al*., 2006). In the same study, water-soluble CDP-like polysaccharides were also isolated from multiple mushrooms obtained from Quebec, Canada. These include *Agaricus arvensis*, *Amanita muscaria*, *A. rubescens*, *Coprinus atramentarius*, *C. comatus*, *Hydnum imbricatum*, *Lycoperdon pyriforme*, *Lactarius deliciosus*, *Leccinum aurantiacum*, *L. subglabripes*, *Lepiota americana*, *Panellus serotinus*, *Piptoporus betulinus*, *Polyporus squamosus*, *Russula variata*, *Suillus americanus*, *Tricholoma flavovirens*, *T. vaccinum* (Pacheco-Sanchez *et al*., 2006). Another relatively small 5 kDa β-glucan called AlPetinc with anti-inflammatory activity was isolated from the 5% NaOH extract of *E. tinctorium* (Javed *et al*., 2019); AlPetinc is a heteroglucan composed mainly of glucose (88.6%) with a small amount of mannose (4.4%), galactose (4.0%), xylose (2.3%), and fucose (0.7%).

Two immuno-stimulatory polysaccharides have been isolated from mushrooms native to North America. EtISPFa with an estimated size of 1,294 kDa was isolated from the water extract of *E. tinctorium* (Zeb *et al*., 2021). It is composed of glucose (66.2%), glucuronic acid (10.1%), mannose (6.7%), galactose (6.4%), xylose (5.6%), rhamnose (3.1%), fucose (1.8%), and arabinose (0.2%). 2-D NMR analysis showed that EtISPFa has a backbone containing mostly of 3-substituted β-glucopyranose with some 4-substituted glucopyranosyl uronic acid (Zeb *et al*.,

2021). ISPP-Rb has an estimated size of 1,053 kDa is a polysaccharide-protein complex isolated from *Royoporus badius* (Lim, 2018). Its polysaccharide component consisted of glucose (49.2%), galactose (11.3%), mannose (10.8%), rhamnose (9.6%), galacturonic acid (8.2%), xylose (5.2%), fucose (2.8%), N-acetyl glucosamine (1.8%), and arabinose (1.2%). The protein component of ISPP-Rb, which is indispensable for its immuno-stimulatory activity, is currently unknown (Lim, 2018).

As mentioned briefly in earlier sections, there has been a lack of interest amongst scientists in the West, especially in North America, in studying bioactive polysaccharides for use as medicinal compounds (Persin *et al*., 2011). However, with recent advances in identifying biosynthetic gene clusters and transcriptomic studies including those in fungi, it is now possible to produce compounds including large polysaccharides using heterologous expression systems by genetic engineering (Almeida *et al*., 2019; Skinnider *et al*., 2015; Skellam, 2019; Zhang *et al*., 2017). Such efforts are expected to enable large scale production of pure bioactive polysaccharides, thereby overcoming some if not all of the problems previously encountered (Persin *et al*., 2011).

Table 1. 3. Bioactive molecules from mushrooms native to North America

Types	**Bioactive compound**	**Mushrooms**	**References**
Small molecule	Syringaldehyde (1)	*E. granulatus*	(Stanikunaite *et al.*, 2009)
	Syringic acid (2)	*E. granulatus*	(Stanikunaite *et al.*, 2009)
	Grifolin (3)	*A. flettii*	(Liu *et al.*, 2010; Yaqoob *et al.*, 2020)
	Neogrifolin (4)	*A. flettii*	(Liu *et al.*, 2010; Yaqoob *et al.*, 2020)
	Confluentin (5)	*A. flettii*	(Liu *et al.*, 2010; Yaqoob *et al.*, 2020)
	3,11-Dioxolanosta-8,24(*Z*)-diene-26-oic acid[1] (6)	*J. hirtus*	(Liu *et al.*, 2010)
	Erinacerin V[1] (7)	*Hericium* sp.	(Song *et al.*, 2020)

	4-Hydroxy-2,2-dimethyl chromane-6-carbaldehyde[1] (8)	*Hericium* sp.	(Song *et al.*, 2020)
	4-Chloro-3,5-dimethoxybenzaldehyde (9)	*Hericium* sp.	(Song *et al.*, 2020)
	2-Chloro-1,3-dimethoxy-5-methyl benzene (10)	*Hericium* sp.	(Song *et al.*, 2020)
	4-Chloro-3,5-dimethoxyphenylmethanol (11)	*Hericium* sp.	(Song *et al.*, 2020)
	3,6-Bis(hydroxyl methyl)-2-methyl-4*H*-pyran-4-one (12)	*Hericium* sp.	(Song *et al.*, 2020)
	4-Chloro-3,5-dimethoxybenzoic acid (13)	*Hericium* sp.	(Song *et al.*, 2020)
	5-Hydroxy-6-(1-hydroxyethyl) isobenzofuran-1(3*H*)-one (14)	*Hericium* sp.	(Song *et al.*, 2020)
	Erinacine (15)	*Hericium* sp.	(Song *et al.*, 2020)
	Pentadecanoic acid (16), Hexadecanoic acid (17), Octadecadienoic acid (18), Octadecanoic acid (19), *β*-sitosterol (20)	*P. djamor*	(Pineda-Alegria *et al.*, 2017)
	Orellanine (3,3′,4,4′-tetrahydroxy-2,2′-bipyridine-1,1′-dioxide) (21)	*C. armillatus*	(Shao *et al.*, 2016)
	Ramariolide A[1] (22)	*R. cystidiophora*	(Centko *et al.*, 2012)
	Ramariolide B[1] (23)	*R. cystidiophora*	(Centko *et al.*, 2012)
	Ramariolide C[1] (24)	*R. cystidiophora*	(Centko *et al.*, 2012)
	Ramariolide D[1] (25)	*R. cystidiophora*	(Centko *et al.*, 2012)
Large molecule	GIPinv[1]	*P. involutus*	(Barad *et al.*, 2018)
	CDP[1]	*C. dryophila*	(Pacheco-Sanchez *et al.*, 2006 & 2007)
	AlPetinc[1]	*E. tinctorium*	(Javed *et al.*, 2019)
	EtISPFa[1]	*E. tinctorium*	(Zeb *et al.*, 2021)
	CDP-like polysaccharide[1]	*L. edodes*	(Pacheco-Sanchez *et al.*, 2006)
	CDP-like polysaccharide[1]	*M. oreades*	(Pacheco-Sanchez *et al.*, 2006)
	EPS[1]	*P. tuber-regium*	(Maness *et al.*, 2011)
	ISPP-Rb[1]	*R. badius*	(Lim, 2018)
	Y3[1]	*C. comatus*	(Zhang *et al.*, 2017)

[1]New compounds.

1.4.2 Small molecules

Small molecules isolated from mushrooms are usually chemically characterized as quinones, isoflavones, cerebrosides, amines, catechols, sesquiterpenes, triacylglycerols, steroids, organic germanium, and selenium (Fig. 1.1) (Ferreira *et al*., 2010). Amongst the handful of small molecules isolated from North American mushrooms, most are terpene derivatives as shown in Table 1.3.

Two small molecules, syringaldehyde and syringic acid, with molar mass of 183 and 199 respectively, were isolated from 95% ethanol extract of the fruiting bodies of *E. granulatus* (Stanikunaite *et al*., 2009). Grifolin (m/z = 329), neogrifolin (m/z = 329) and confluentin (m/z = 327), known to exhibit growth-inhibitory and antibacterial activities, were isolated from the ethanol extract of the fruiting bodies of *A. flettii* (Liu *et al*., 2010; Yaqoob *et al*., 2020). A lanostane-type triterpene named 3, 11-dioxdanosta-8,24(Z)-diene-26-oic acid with molar mass of 469 was isolated from *J. hirtus*; this triterpene effectively inhibited the growth of two gram-positive bacteria: *Bacillus cereus* and *Enterococcus faecalis* (Liu *et al*., 2020). The compound canthin-6-one and its thiomethylated derivative 5-methyl-thiocanthin-6-one, were isolated from *Boletus curtisii,* but to date there has been no activity reported for these small molecules (Pacheco-Sanchez *et al*., 2007).

Many small molecules were isolated from *Hericium* sp. which included two new compounds, an erinacerin V alkaloid with molar mass of 258 and an aldehyde derivative of 4-hydroxy chroman, 4-chloro-3,5-dimethoxybenzaldehyde with molar mass of 207 (Song *et al*., 2020). Seven known compounds were also isolated from *Hericium* sp., including 2-chloro-1,3-dimethoxy-5-methyl benzene, (4-chloro-3,5-dimethoxyphenyl) methanol, 3,6-bis (hydroxyl

methyl)-2-methyl-4*H*-pyran-4-one, 4-chloro-3,5-dimethoxybenzoic acid, 5-hydroxy-6-(1-hydroxyethyl) isobenzofuran-1(3*H*)-one, and erinacine (Song *et al*., 2020).

Some other small molecules that have been isolated from North American mushrooms include pentadecanoic acid, hexadecanoic acid, octadecadienoic acid, octadecanoic acid and *β*-sitosterol from *Pleurotus djamor* (Pineda-Alegria *et al*., 2017), and orellanine from *Cortinarius armillatus* (Shao *et al*., 2016). Four new compounds belonging to the butenolide groups called ramariolides A-D were isolated from the coral mushroom *Ramaria cystidiophora* collected in southwestern British Columbia (Centko *et al*., 2012). Ramariolides A was found to have antimicrobial activity against *Mycobacterium smegmatis* and *Mycobacterium tuberculosis* (Centko *et al*., 2012).

1.5 Overview of strategies used for natural products discovery

Bioactive compounds can be categorized based on their molecular size and pharmaceutical importance as large molecular weight (LMW) compounds and small molecules. LMW compounds do not have a definite molecular weight as they are a population of molecules (polymeric) that display a distribution of molecular weights (Zhu *et al*., 1998) compared to the small molecules which are discrete and have a definite structure with exact molecular weight. LMW compounds usually have molecular weight more than 600-700 Da and include polysaccharides, proteins, polysaccharide conjugated with proteins and nucleic acids whereas small molecules have a molecular size less than 600 Da and comprise of steroids, lanostanoids, terpenes and others as described later in this section. LMW compounds are important from a biopharmaceutical perspective while small molecules are a more attractive target for formulating pharmaceutical drugs. The purpose of defining these two categories is to set a basis for conducting my current research with a focus on designing methodologies that will specifically isolate either of these compounds. Fig. 1.2 shows a comparative methodology for

characterization of small and large molecular weight compounds. Table 1.4 and 1.5 illustrate specific methodologies used by researchers to characterize small and large molecules from mushrooms.

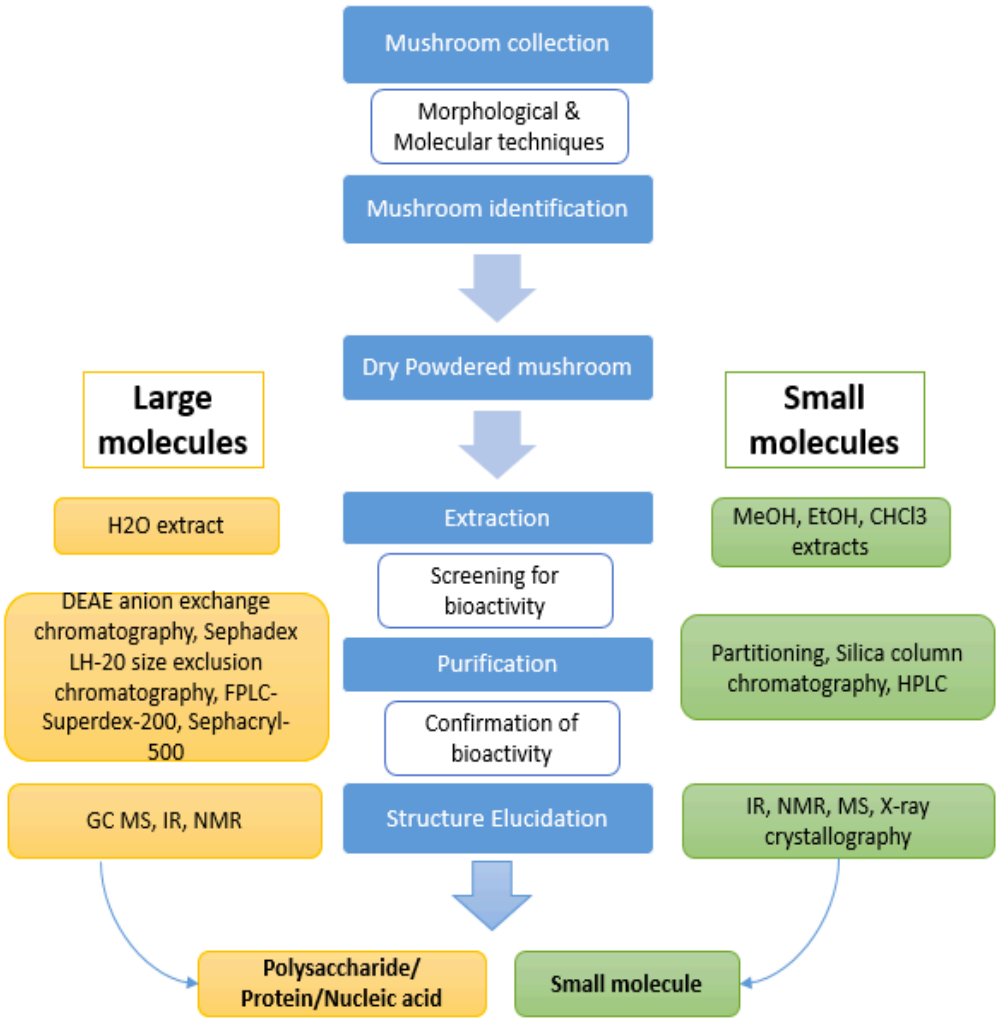

Fig. 1. 2. Research methodology towards the discovery of bioactive compound(s) from natural products.

Table 1. 4. Methodologies for purification and characterization of large molecules

Mushroom (Compound)	**Extraction**	**Purification**	**Chemical characterization**	**Reference**
Lentinus edodes	Aqueous extraction	Alcohol precipitation, HPGPC	Phenol-sulfuric acid method, FTIR, GC-MS, Congo Red test	Wang *et al.,* 2013
G. lucidum (Polysaccharide)	Alkaline extraction (0.1N NaOH)	Anion exchange chromatography (Diaion–WA30 column), Gel filtration chromatography (Sephacryl S-500 and TSK HW-75 column)	Phenol-sulfuric acid method	Chen *et al.,* 2004
G. lucidum (Polysaccharide)	Aqueous extraction	Trichloroacetic acid treatment, DEAE–cellulose column, Sephacryl S-300 HR and Sephadex G-10 SEC	RI detection, NMR, GC-MS, ESI-MS	Bao *et al.,* 2002
G. lucidum (Polysaccharide)	Aqueous extraction	Deproteination (trichloroacetic acid), DEAE–cellulose column, Sephacryl S-200 HR and Sephadex G-10 SEC	Phenol-sulfuric acid method, NMR, TLC, GLC, HPSEC (Ultrahydrogel 1000 column), Congo Red	Bao *et al.,* 2001
Tricholoma matsutake (Polysaccharide TMP-A)	Aqueous extraction	Sevag method, Ion exchange chromatography (DEAE-cellulose column), Sephadex (G-100 column) SEC	Phenol sulfuric acid method, FTIR, GC–MS, NMR	Ding *et al.,* 2010
G. tsugae (Glycans)	85% ethanol, hot water, ammonium oxalate, 5% NaOH.	Ion-exchange chromatography (DEAE-cellulose column), gel filtration (Toyopearl HW-65F column), Affinity chromatography (Con A-AF-Formyl Toyopearl 6S0M column)	Phenol-sulfuric acid method, Total protein by Lowry method, Mol wt by gel filtration (Toyo pearl HW-65F column), GC, FTIR, Amino acid analysis, NMR	Wang *et al.,* 1993
G. tsugae (Polysaccharide-protein complexes)	Phosphate buffer, water and NaOH	Defatted with acetone and ethyl ester, treated with ethanol, Sevag method, Size exclusion chromatography	Protein content assay, FTIR, Monosaccharide analysis (HPLC with RI detector	Peng *et al.,* 2003

			and Shodex Sugar C1011 column), GC, NMR	

*FTIR (Fourier Transform Infrared); GC (Gas chromatography); NMR (Nuclear magnetic resonance); High performance gel permeation chromatography (HPGPC); MS (Mass spectrometry); TLC (Thin layer chromatography); RI (Refractive Index).

Table 1. 5. Methodologies for purification and characterization of small molecules

Mushroom (Compound)	**Extraction**	**Purification**	**Structure elucidation**	**Reference**
G. tsugae (steroids)	Extract with CHCl3	Silica gel column chromatography	FTIR, NMR, EIMS	Lin *et al.,* 1997b
G. tsugae (Ganodone)	Extracted with ethanol	Partitioning, Dry column vacuum chromatography (DCVC) and flash chromatography, HPLC	FTIR, LC-MS, X-ray crystallography, NMR	La Clair *et al.,* 2011
G. tsugae (Lanostanoids-tsugaric acids)	Extracted with methanol	Silica gel flash column chromatography	FTIR, NMR, EIMS	Su *et al.,* 2000
Piptoporus betulinus (Hydroquinone)	Extracted with ethanol	Partitioning with CHCl3 and EtOAc, Silica gel flash column chromatography, RP-HPLC	FTIR, EIMS, NMR	Kawagishi *et al.,* 2002
G. pfeifferi (farnesylhydroquinone, ganomycin K)	DCM extract	Sephadex LH-20 column, TLC, silica gel flash column chromatography, HPLC	LCMS, NMR	Niedermeyer *et al.,* 2013
G. lucidum (Ganodermenonol, ganodermadiol, and ganodermatriol	MeOH extract	Partitioning with different solvents, silica gel column chromatography (EtOAc/hexane)	FTIR, NMR, MS	Arisawa *et al.,* 1986
G. lucidum (Ganoderic acid ∑)	Extracted with H2O, EtOH and ionic liquids	Partitioning with hexanes, RP-HPLC	NMR, ESI-HRMS	Murata *et al.,* 2016
G. lucidum (Triterpenoids)	Ethanol extract	Flash chromatography, HPLC	ESI-MS, NMR	Ruan *et al.,* 2014
G. lucidum (Triterpenoids)	Refluxed with ethanol	Flash chromatography, HPLC	ESI-MS, NMR	Ruan *et al.,* 2015

* RP-HPLC (Reversed-phase high-performance liquid chromatography); NMR (Nuclear magnetic resonance); LC-IT-TOFMS (Liquid chromatography ion trap-time of flight mass spectrometry); ESI-MS (Electrospray ionization-mass spectrometry)

1.6 Mushrooms from North America as a source for drug discovery

As shown in Table 1.1, to date 75 species of mushrooms native to North America have been investigated and exhibited medicinal properties. Out of these, 47 species (63%) have bioactivities that have not been previously reported (Table 1.6). These include *A. augusta* with strong anti-proliferative activity, *C. dryophila* with anti-inflammatory activity, *G. esculenta* and *H. coralloides* with strong immuno-stimulatory activities (Deo *et al*., 2019; Smith *et al*., 2017). This also includes *C. tomentosus, G. helvelloides, L. conifericola, L. connata, T. abietinum* with potent activity in anti-proliferation, immuno-stimulation and anti-inflammation (Deo *et al*., 2019; Smith *et al*., 2017). There were two specimens that could only be identified to the genus level, *Inocybe* sp. and *Hydnellum* sp., suggesting that they are poorly known or undescribed species. *Inocybe* sp. showed strong anti-proliferative, immuno-stimulatory and anti-inflammatory activities (Deo *et al*., 2019), while *Hydnellum* sp. exhibited strong anti-proliferative activity (Smith *et al*., 2017). There were 13 species that had been studied elsewhere, but their new bioactivities were discovered in the species collected in North America (Table 1.6). This includes *Haploporus odorus* with antimicrobial activity; *Clavulina cinerea, Hydnum repandum, Hygrophoropsis aurantiaca, Hypholoma fasciculare, Phellinus nigricans,* and *Pleurotus ostreatus* with anti-inflammatory activity; *Ramaria cystidiophora, Russula paludosa, Tricholomopsis rutilans,* and *Tyromyces chioneus* with anti-proliferative and anti-inflammatory activities.

In addition to the reported studies described above, we have recently collected additional mushroom specimens in the northern interior of BC. Out of the 49 species collected, we found 21 species (43%) and 34 species (69%) that exhibited potent anti-proliferative and anti-inflammatory activities respectively, and these have not been previously reported (Lee, 2020,

pers. comm.). We also found 25 species (51%) exhibiting potent immuno-stimulatory activity that has not been previously reported (Lee, 2020, pers. comm.).

As shown in Table 1.3, there has been very limited number of studies exploring bioactive compounds from North American mushrooms. Despite the limited number of studies, 7 new small molecules, 8 new polysaccharides and a new protein with bioactivity have been discovered (Table 1.6). Such observations and the fact that a large number of mushrooms native to North America having bioactivities that have never been previously described, strongly suggests that North American mushrooms are indeed an excellent source for drug discovery.

Table 1. 6. Medicinal properties of North American mushrooms

Species[1]	**New bioactivity described for the species**	**Known activity**[2]
Amanita augusta	Anti-proliferative, immuno-stimulatory, anti-inflammatory	None
Astraeus pteridis	Antituberculosis	None
Barrsia oregonensis	Antituberculosis	None
Chroogomphus tomentosus	Anti-proliferative, immuno-stimulatory, anti-inflammatory	None
Clavulina cinerea	Anti-inflammatory	Anti-proliferative (Njue *et al*., 2017)
Collybia dryophila	Anti-inflammatory	None
Coprinellus sp.	Anti-proliferative	None
Coprinus comatus	Anti-proliferative	Antioxidant (Li *et al*., 2010), Hypoglycemic (Han *et al*., 2006)
Elaphomyces muricatus	Anti-inflammatory, antioxidant, antituberculosis	None
Gautieria monticola	Antioxidant	None
Geopora clausa	Antioxidant, anti-proliferative	None
Guepinia helvelloides	Anti-proliferative, immuno-stimulatory, anti-inflammatory	None
Gyromitra esculenta	Anti-proliferative, immuno-stimulatory	None
Haploporus odorus	Antimicrobial	Anticancer (Zmitrovich *et al*., 2019)
Hericium corraloides	Immuno-stimulatory, anti-inflammatory	None

Hydnellum sp.	Anti-proliferative, immuno-stimulatory	None
Hydnum repandum	Anti-inflammatory	Anti-proliferative (Takahashi *et al*., 1992; Vasdekis *et al*., 2018), antioxidant, antimicrobial (Ozen *et al*., 2011)
Hygrophoropsis aurantiaca	Anti-inflammatory	Anti-proliferative (Nowak *et al*., 2016)
Hymenogaster subalpinus	Anti-inflammatory, antituberculosis	None
Hymenopellis furfuracea	Antimicrobial	None
Hypholoma fasciculare	Anti-inflammatory	Anti-proliferative (Beattie *et al*., 2011), antioxidant (Barros *et al*., 2008), antimicrobial (Millar *et al*., 2019; Pereira *et al*., 2013)
Inocybe sp.	Anti-proliferative, immuno-stimulatory, anti-inflammatory	None
Laetiporus conifericola	Anti-proliferative, immuno-stimulatory, anti-inflammatory	None
Lentinellus subaustralis	Antimicrobial	None
Leucocybe connata	Anti-proliferative, immuno-stimulatory, anti-inflammatory	None
Leucogaster rubescens	Antioxidant	None
Melanogaster tuberiformis	Antituberculosis, anti-inflammatory, antioxidant	None
Phellinopsis conchata	Antimicrobial	None
Phellinus conchatus	Antimicrobial	Anti-proliferative (Ren *et al*., 2006)
Phellodon atratus	Anti-proliferative, immuno-stimulatory, anti-inflammatory	None
Phellinus nigricans	Anti-inflammatory	Anticancer (Li *et al*., 2008), antioxidant (Wang *et al*., 2014), immuno-stimulatory (Li *et al*., 2008; Wang *et al*., 2014)
Pholiota terrestris	Antimicrobial	None
Pleurotus ostreatus	Anti-inflammatory	Immuno-stimulatory (Ooi & Liu, 2000), anti-proliferative, antioxidant (Wong *et al*., 2020)
Polyporus badius	Antimicrobial	None
Pyrofomes demidoffi	Antimicrobial	None
Ramaria cystidiophora	Anti-proliferative, anti-inflammatory	Antimicrobial (Centko *et al*., 2012)

Rhizopogon couchii	Anti-inflammatory, antioxidant, antituberculosis	None
Rhizopogon nigrescens	Anti-inflammatory, antioxidant	None
Rhizopogon pedicellus	Antioxidant, antituberculosis	None
Rhizopogon subareolatus	Antimalarial	None
Rhizopogon subaustralis	Anti-inflammatory, antioxidant	None
Rhizopogon subgelatinosus	Anti-inflammatory, anti-proliferative	None
Russula paludosa	Anti-proliferative, anti-inflammatory	Anti-HIV (Wang *et al*., 2007)
Scleroderma laeve	Anti-inflammatory, antioxidant, antituberculosis	None
Trichaptum abietinum	Anti-proliferative, immuno-stimulatory, anti-inflammatory	None
Tricholomopsis rutilans	Anti-proliferative, anti-inflammatory	Antioxidant (Ribeiro *et al*., 2006)
Tyromyces chioneus	Anti-proliferative, anti-inflammatory	Anti-HIV (Liu *et al*., 2007)

[1]Species from Table 1.1 that has novel bioactivity compared to elsewhere but has remained unstudied. [2]Bioactivities reported for mushrooms found elsewhere.

North American mushrooms offer a wide variety of medicinal benefits and some have been appreciated for their exquisite flavors. While some are unique and edible, others are toxic for human consumption. North American medicinal mushrooms that are considered toxic or non-edible for general human consumption can be tailored as drugs after sufficient toxicity testing and targeted dosage from development. Some of the features that make mushrooms inedible are the presence of toxic metabolites in the whole mushroom, its taste and toughness. *E. tinctorium* is a hard inedible conk. *P. atratus* and *J. hirtus* are also tough mushrooms and apparently *J. hirtus* has a bitter taste. *P. involutus* is considered poisonous for human use. *E. granulatus* is also non-edible. *C. armillatus* is considered toxic at higher doses due to the presence of orellanine, a potent nephrotoxin (Shao *et al*., 2016).

1.7 Conclusions

Having extensively reviewed the literature on the bioactivities and compounds isolated from mushrooms native to North America, the questions posed at the beginning of this review are answered. (i) Do species found in North America similar to those in Asia or Europe exhibit similar bioactivities and produce similar group of bioactive compounds? Based on subjective approach of bioactivity-guided investigations on selective species, similar species found in North America and Asia or Europe indeed produce similar bioactivities. For example, this is true for the commonly studied *I. obliquus* and *P. ostreatus*. Furthermore, compounds such as grifolin, neogrifolin and confluentin produced in North American *A. flettii*, are also made by other *Albatrellus* species found elsewhere (Liu *et al.,* 2010; Yaqoob *et al.,* 2020). However, a more definitive answer can only be obtained by using more advanced and objective methods such as Quadrupole Time-of-Flight Mass Spectrometry to globally examine the metabolites produced and using multiple biological screening assays to simultaneously monitor different bioactivities. (ii) Do similar species found in North America and elsewhere exhibit distinct bioactivity and produce distinct compounds? Again, the answer to this question will come from more advanced approaches described above. (iii) Do new species found in North America produce new compound(s)? Due to the limited number of studies on mushrooms native to North America, it is currently unknown whether new species found in North America produce new compound(s). However, based on very limited study (Centko *et al.,* 2012), it is highly likely new medicinal compounds are produced by new species found in North America. (iv) Based on the answers to (i) to (iii) above, is it worth the efforts to explore mushrooms native to North America for medicinal properties and for new compounds? The answer to this question is a definite yes. This is based on the fact that there are many species, including new species, in North America whose

bioactivities have never been previously reported (Table 1.6) (Lee, 2020). Furthermore, novel compounds have been isolated from North American mushrooms despite the very limited number of studies.

In summary, to date only 75 mushroom species in North America have been studied and reported to possess medicinal properties. Of these, 47 species (63%) exhibited bioactivities that have never been previously reported. To date, only 15 mushroom species in North America have been subjected to bioactivity-guided compound isolation studies. Out of this limited number of studies, already 7 new small molecules, 8 new polysaccharides and a new protein with medicinal properties have been discovered. In conclusion, mushrooms native to North America are indeed an excellent source for drug discovery. Further exploration of new species as well as known species that are found elsewhere are therefore warranted. Since most of the studies conducted to determine the medicinal effects have so far involved *in-vitro* cell lines, it would be of interest to see if the *in-vitro* cell studies can be translated to *in-vivo* studies performed using relevant animal models.

1.8 *Echinodontium tinctorium*

Echinodontium tinctorium, known as Indian body paint fungus, is a tree-dwelling conk with a distinct orange to red color. Due to its distinct color, it was commonly used by Native American tribes as a war paint (Ye *et al.,* 1996). *E. tinctorium* is an Agaricomycete fungus that belongs to genus *Echinodontium* of the Echinodontiaceae family. Based on morphological similarities, Gross (1964) classified six species of Echinodontiaceae which included *E. tinctorium, E. tsugicola, E. japonicum, E. ballouii, E. taxodii and E. sulcatum.* However, Liu *et al.* (2017) revised the taxa based on molecular techniques where *E. tinctorium, E. tsugicola* and a new specie *E. ryvardenii* were included in *Echinodontium*. In addition to this, *E. japonicum* was

placed in a new genus *Echinodontiellum* due to its different hardwood host (Quercus). The remaining species; *Lauriliella taxodii* and *Laurilia sulcata*, classified by Gross (1964) in *Echinodontium* were placed in different genera of family Bondarzewiaceae. *E. ballouii* being a rare specie was not included in the analysis. Phylogenetic studies have also been conducted (Tabata *et al.*, 2000) to indicate the placement of *E. tinctorium* with other related species in the same group. Studies regarding the bioactivity of this mushroom remain limited and the literature available deals mostly with its taxonomy, phylogeny and symbiotic relationships (Aho *et al.,* 1987; Larsen *et al.,* 1987, Liu *et al.,* 2017). Bond *et al.* (1966) have characterized a triterpene echinodol from *E. tinctorium* (Bond *et al.,* 1966). Ye *et al*. (1996) have also isolated, purified and characterized a small molecule echinotinctone from *E. tinctorium*. Echinotinctone was isolated from a methanolic extract of *E. tinctorium* and was referred to as a first natural orange pigment that structurally resembles xanthene dyes fluorescein and eosin. One of the studies cross-referenced by Ye *et al*. (1996), based on a private communication by Dr. D. H. French (Reed College, Portland, Oregon), stated that Oregon natives used this mushroom for antibacterial activity and also that the extracts possess antitumor properties (Ye *et al.,* 1996).

1.9 Research Hypothesis

At the outset of this literature review, I hypothesized that immuno-stimulatory and growth-inhibitory large and small molecules are present in BC wild mushrooms. Besides the description of only a few small molecules with unknown bioactivity (Ye *et al*., 1996) and anti-inflammatory polysaccharide (Javed *et al*., 2019) from *E. tinctorium*, this species has not been fully explored for its therapeutic potential. Therefore, the goal of my PhD project is to uncover the therapeutic potential of *E. tinctorium*. I will isolate, purify and characterize the responsible bioactive compounds which are currently unexplored.

1.10 Research Objectives

To test my hypothesis, this project was divided into 3 experimental chapters. The following objectives were set for each of the experimental chapter:

1. Isolation, purification, characterization of immuno-stimulatory large molecules from *E. tinctorium,* (Chapter 2)
2. Isolation, purification and characterization of growth-inhibitory large molecules from *E. tinctorium,* (Chapter 3)
3. Isolation, purification and characterization of growth-inhibitory small molecules from *E. tinctorium,* (Chapter 4)

1.11 References

Abel, G., Sz ll si, J., Chihara, G., & Fachet, J. (1989). Effect of lentinan and mannan on phagocytosis of fluorescent latex microbeads by mouse peritoneal macrophages: a flow cytometric study. *International journal of immunopharmacology*, 11(6), 615-621.

Adachi, Y., Ishii, T., Ikeda, Y., Hoshino, A., Tamura, H., Aketagawa, J., Tanaka S & Ohno, N. (2004). Characterization of β-glucan recognition site on C-type lectin, dectin 1. *Infection and immunity*, 72(7), 4159-4171.

Adebayo, E. A., Martínez-Carrera, D., Morales, P., Sobal, M., Escudero, H., Meneses, M. E., Avila-Nava, A.; Castillo, I & Bonilla, M. (2018). Comparative study of antioxidant and antibacterial properties of the edible mushrooms *Pleurotus levis, P. ostreatus, P. pulmonarius* and *P. tuber-regium*. *International journal of food science & technology*, *53*(5), 1316-1330.

Aho, PE., Filip, GM., Lombard, FF. (1987) Decay Fungi and Wounding in Advance Grand and White Fir Regeneration. *Forest service by the society of American foresters*, 33(2), 347-355.

Almeida, H.; Tsang, A.; Diallo, A.B. (2019) Towards accurate identification of biosynthetic gene clusters in fungi. F1000 Research. Presented at ISMB/ECCB.

Jose Alves, M., CFR Ferreira, I., Dias, J., Teixeira, V., Martins, A., & Pintado, M. (2013). A review on antifungal activity of mushroom (basidiomycetes) extracts and isolated compounds. *Current topics in medicinal chemistry*, *13*(21), 2648-2659.

Arisawa, M., Fujita, A., Saga, M., Fukumura, H., Hayashi, T., Shimizu, M., & Morita, N. (1986). Three new lanostanoids from *Ganoderma lucidum*. *Journal of natural products*, *49*(4), 621-625.

Baek, G. H., Jeong, H. S., Kim, H., Yoon, T. J., Suh, H.J., & Yu, K. W. (2012). Pharmacological activity of Chaga mushroom on extraction conditions and immuno-stimulating polysaccharide. *Journal of the Korean society of food science and nutrition*, 41(10), 1378-1387.

Bao, X., Duan, J., Fang, X., & Fang, J. (2001). Chemical modifications of the (1→ 3)-α-D-glucan from spores of *Ganoderma lucidum* and investigation of their physicochemical properties and immunological activity. *Carbohydrate research*, *336*(2), 127-140.

Bao, X. F., Wang, X. S., Dong, Q., Fang, J. N., & Li, X. Y. (2002). Structural features of immunologically active polysaccharides from *Ganoderma lucidum*. *Phytochemistry*, *59*(2), 175-181.

Barad, A., Mackedenski, S., Li, W. M., Li, X. J., Lim, B. C. C., Rashid, F., Tackaberry, L.E.; Massicotte, H.B.; Egger, K.N.; Reimer, K.; Cheung, P.C.K. & Lee, C. H. (2018). Anti-proliferative activity of a purified polysaccharide isolated from the basidiomycete fungus *Paxillus involutus*. *Carbohydrate polymers*, *181*, 923-930.

Barros, L., Venturini, B. A., Baptista, P., Estevinho, L. M., & Ferreira, I. C. (2008). Chemical composition and biological properties of Portuguese wild mushrooms: a comprehensive study. *Journal of agricultural and food chemistry*, *56*(10), 3856-3862.

Beattie, K. D., Ulrich, R., Grice, I. D., Uddin, S. J., Blake, T. B., Wood, K. A., Steele, J.; Iu, F.; May, T.W. & Tiralongo, E. (2011). Ethanolic and aqueous extracts derived from Australian fungi inhibit cancer cell growth in vitro. *Mycologia*, *103*(3), 458-465.

Blanchette, R. A., Compton, B. D., Turner, N. J., & Gilbertson, R. L. (1992). Nineteenth century shaman grave guardians are carved *Fomitopsis officinalis* sporophores. *Mycologia*, *84*(1), 119-124.

Bond, F. T., Fullerton, D. S., Sciuchetti, L. A., & Catalfomo, P. (1966). The Isolation and Structure of Echinodol, a Triterpene Acetate. *Journal of the American chemical society*, 88(16), 3882-3883.

Brown, G. D., Herre, J., Williams, D. L., Willment, J. A., Marshall, A. S., & Gordon, S. (2003). Dectin-1 mediates the biological effects of β-glucans. *Journal of experimental medicine*, 197(9), 1119-1124.

Burk, W. R. (1983). Puffball usages among North American indians. *Journal of ethnobiology, 3*(1), 56-62.

Buvall, L., Hedman, H., Khramova, A., Najar, D., Bergwall, L., Ebefors, K., Sihlbom, C., Lundstam, S., Herrmann, A., Wallentin, H., Roos, C., & Nyström, J. (2017). Orellanine specifically targets renal clear cell carcinoma. *Oncotarget*, *8*(53), 91085.

Centko, R. M., Ramon-Garcia, S., Taylor, T., Patrick, B. O., Thompson, C. J., Miao, V. P., & Andersen, R. J. (2012). Ramariolides A–D, antimycobacterial butenolides isolated from the mushroom *Ramaria cystidiophora*. *Journal of natural products*, *75*(12), 2178-2182.

Chang, S.T.; Hayes, W.A. (Eds.) (2013). *The biology and cultivation of edible mushrooms*, Academic Press Inc., New York*;* pp. xix.

Chang, S. T. (1999). Global impact of edible and medicinal mushrooms on human welfare in the 21st century: nongreen revolution. *International journal of medicinal mushrooms*, 1(1).

Chen, J., & Seviour, R. (2007). Medicinal importance of fungal β-(1→ 3), (1→ 6) glucans. *Mycological research*, 111(6), 635-652.

Chen, H. S., Tsai, Y. F., Lin, S., Lin, C. C., Khoo, K. H., Lin, C. H., & Wong, C. H. (2004). Studies on the immuno-modulating and anti-tumor activities of *Ganoderma lucidum* (Reishi) polysaccharides. *Bioorganic & medicinal chemistry*, 12(21), 5595-5601.

Chihara, G., Hamuro, J., Maeda, Y. Y., Shiio, T., Suga, T., Takasuka, N., & Sasaki, T. (1987). Antitumor and metastasis-inhibitory activities of lentinan as an immunomodulator: an overview. Cancer detection and prevention. Supplement: official publication of the *International society for preventive oncology*, Inc, 1, 423-443.

Council of Canadian academies. (2019) When antibiotics fail. Ottawa (ON): The expert panel on the potential socio-economic impacts of antimicrobial resistance in Canada, council of Canadian academies.

Czop, J. K., & Austen, K. F. (1985). Properties of glycans that activate the human alternative complement pathway and interact with the human monocyte beta-glucan receptor. *The Journal of immunology*, 135(5), 3388-3393.

Deo, G. S., Khatra, J., Buttar, S., Li, W. M., Tackaberry, L. E., Massicotte, H. B., Egger, K.N.; Reimer, K. & Lee, C. H. (2019). Antiproliferative, immunostimulatory, and anti-inflammatory activities of extracts derived from mushrooms collected in Haida Gwaii, British Columbia (Canada). *International journal of medicinal mushrooms*, *21*(7), 629-643.

Ding, X., Tang, J., Cao, M., Guo, C. X., Zhang, X., Zhong, J., Zhang, J., Sun, Q., Feng, S., Tang, Z. R., & Zhao, J. (2010). Structure elucidation and antioxidant activity of a novel polysaccharide isolated from *Tricholoma matsutake*. *International journal of biological macromolecules*, *47*(2), 271-275.

El Enshasy, H. A., & Hatti-Kaul, R. (2013). Mushroom immunomodulators: unique molecules with unlimited applications. *Trends in biotechnology*, *31*(12), 668-677.

Ferreira, I.C.F.R., A Vaz, J., Vasconcelos, M. H., & Martins, A. (2010). Compounds from wild mushrooms with antitumor potential. *Anti-cancer agents in medicinal chemistry (formerly current medicinal chemistry-anti-cancer agents)*, *10*(5), 424-436.

Fu, H., Deng, C., Teng, L., Yu, L., Su, T., Xu, X., & Yang, C. (2015). Immunomodulatory Activities on RAW 264.7 Macrophages of a Polysaccharide from Veiled Lady Mushroom, *Dictyophora indusiata* (Higher Basidiomycetes). *International journal of medicinal mushrooms*,17(2).

Giavasis, I. (2014). Bioactive fungal polysaccharides as potential functional ingredients in food and nutraceuticals. *Current opinion in biotechnology*, *26*, 162-173.

Gould, I. M., Gunasekera, C., & Khan, A. (2019). Antibacterials in the pipeline and perspectives for the near future. *Current opinion in pharmacology*, *48*, 69-75.

Gross, H. L. (1964). The Echinodontiaceae. *Mycopathologia et mycologia applicata*, *24*(1), 1-26.

Gu, Y. H., & Leonard, J. (2006). In vitro effects on proliferation, apoptosis and colony inhibition in ER-dependent and ER-independent human breast cancer cells by selected mushroom species. *Oncology reports*, *15*(2), 417-423.

Guggenheim, A. G., Wright, K. M., & Zwickey, H. L. (2014). Immune modulation from five major mushrooms: Application to integrative oncology. *Integrative medicine: a clinician's journal*, 13(1), 32.

Han, C., Yuan, J., Wang, Y., & Li, L. (2006). Hypoglycemic activity of fermented mushroom of *Coprinus comatus* rich in vanadium. *Journal of trace elements in medicine and biology*, *20*(3), 191-196.

Harada, T., & Ohno, N. (2008). Contribution of dectin-1 and granulocyte macrophage–colony stimulating factor (GM-CSF) to immunomodulating actions of β-glucan. *International immunopharmacology*, 8(4), 556-566.

Hassan, F., Ni, S., Becker, T. L., Kinstedt, C. M., Abdul-Samad, J. L., Actis, L. A., & Kennedy, M. A. (2019). Evaluation of the antibacterial activity of 75 mushrooms collected in the vicinity of Oxford, Ohio (USA). *International journal of medicinal mushrooms*, *21*(2), 131-141.

Hawksworth, D. L., & Lücking, R. (2017). Chapter 4: Fungal Diversity Revisited: 2.2 to 3.8 Million Species. J. Heitman, BJ Howlett, Pedro. W. Crous, EH Stukenbrock, TY James, NAR Gow eds. *The fungal kingdom*. Pp. 79-95.

Hawksworth, D. L. (2001). Mushrooms: the extent of the unexplored potential. *International journal of medicinal mushrooms*, *3*(4).

Javed, S., Li, W. M., Zeb, M., Yaqoob, A., Tackaberry, L. E., Massicotte, H. B., Egger, K.N.; Cheung, P.C.K.; Payne, G.W. & Lee, C. H. (2019). Anti-inflammatory activity of the wild mushroom, *Echinodontium tinctorium*, in RAW264. 7 macrophage cells and mouse microcirculation. *Molecules*, *24*(19), 3509.

Javed, S., Mitchell, K., Sidsworth, D., Sellers, S. L., Reutens-Hernandez, J., Massicotte, H. B., Egger, K.N.; Payne, G.W. & Lee, C.H. (2019). *Inonotus obliquus* attenuates histamine-induced microvascular inflammation. *PLoS one*, *14*(8), e0220776.

Kawagishi, H., Hamajima, K., & Inoue, Y. (2002). Novel hydroquinone as a matrix metallo-proteinase inhibitor from the mushroom, *Piptoporus betulinus*. *Bioscience, biotechnology, and biochemistry*, *66*(12), 2748-2750.

Kim, C. F., Jiang, J. J., Leung, K. N., Fung, K. P., & Bik-San Lau, C. (2009). Inhibitory effects of *Agaricus blazei* extracts on human myeloid leukemia cells. *Journal of ethnopharmacology*, 122(2), 320-326.

Kodama, N., Mizuno, S., Nanba, H., & Saito, N. (2010). Potential antitumor activity of a low molecular-weight protein fraction from *Grifola frondosa* through enhancement of cytokine production. *Journal of medicinal food*, 13(1), 20-30.

La Clair, J. J., Rheingold, A. L., & Burkart, M. D. (2011). Ganodone, a bioactive benzofuran from the fruiting bodies of *G. tsugae*. *Journal of natural products*, *74*(10), 2045-2051.

Larsen, MJ., Jurgensen, MF., Harvey, AE. (1987) N2 Fixation Associated with Wood Decayed by some Common Fungi in Western Montana. *Forest service by the society of american foresters*. 33(2), 347-355.

Lee, C.H. (2020), (University of Northern British Columbia, Prince George, BC, Canada). Personal communication.

Li, B., Lu, F., Suo, X., Nan, H., & Li, B. (2010). Antioxidant properties of cap and stipe from *Coprinus comatus*. *Molecules*, *15*(3), 1473-1486.

Li, X., Jiao, L. L., Zhang, X., Tian, W. M., Chen, S., & Zhang, L. P. (2008). Anti-tumor and immunomodulating activities of proteoglycans from mycelium of *Phellinus nigricans* and culture medium. *International immunopharmacology*, *8*(6), 909-915.

Lim, B. (2018). Purification and Characterization of an Immuno-stimulatory Compound from the Water Extract of *Royoporus badius* (Pers.) AB De (Master's thesis, University of Northern British Columbia).

Lin, C. N., Fann, Y. F., & Chung, M. I. (1997). Steroids of formosan *Ganoderma tsugae*. *Phytochemistry*, *46*(6), 1143-1146.

Lin, Y. L., Liang, Y. C., Tseng, Y. S., Huang, H. Y., Chou, S. Y., Hseu, R. S., Huang, C. T., & Chiang, B. L. (2009). An immunomodulatory protein, Ling Zhi-8, induced activation and maturation of human monocyte-derived dendritic cells by the NF-κB and MAPK pathways. *Journal of leukocyte biology*, 86(4), 877-889.

Lin, C. H., Sheu, G. T., Lin, Y. W., Yeh, C. S., Huang, Y. H., Lai, Y. C., Chang, J. G., & Ko, J. L. (2010). A new immunomodulatory protein from *Ganoderma microsporum* inhibits epidermal growth factor mediated migration and invasion in A549 lung cancer cells. *Process biochemistry*, 45(9), 1537-1542.

Liu, D. Z., Wang, F., Yang, L. M., Zheng, Y. T., & Liu, J. K. (2007). A new cadinane sesquiterpene with significant anti-HIV-1 activity from the cultures of the basidiomycete *Tyromyces chioneus*. *The journal of antibiotics*, *60*(5), 332-334.

Liu, X., Wang, L., Zhang, C., Wang, H., Zhang, X., & Li, Y. (2015). Structure characterization and antitumor activity of a polysaccharide from the alkaline extract of king oyster mushroom. *Carbohydrate polymers*, 118, 101-106.

Liu, X. T., Winkler, A. L., Schwan, W. R., Volk, T. J., Rott, M. A., & Monte, A. (2010). Antibacterial compounds from mushrooms I: a lanostane-type triterpene and prenylphenol derivatives from *Jahnoporus hirtus* and *Albatrellus flettii* and their activities against *Bacillus cereus* and *Enterococcus faecalis*. *Planta medica*, *76*(02), 182-185.

Liu, S. L., Zhao, Y., Dai, Y. C., Nakasone, K. K., & He, S. H. (2017). Phylogeny and taxonomy of *Echinodontium* and related genera. *Mycologia*, *109*(4), 568-577.

Lo, H. C., Hsieh, C., Lin, F. Y., & Hsu, T. H. (2013). A systematic review of the mysterious caterpillar fungus *Ophiocordyceps sinensis* in DongChongXiaCao and related bioactive ingredients. *Journal of traditional and complementary medicine*, *3*(1), 16-32.

Luo, K. W., Yue, G. G. L., Ko, C. H., Lee, J. K. M., Gao, S., Li, L. F., ... & Bik-San Lau, C. (2014). In vivo and in vitro anti-tumor and anti-metastasis effects of *Coriolus versicolor* aqueous extract on mouse mammary 4T1 carcinoma. *Phytomedicine*, 21(8), 1078-1087.

Maness, L., Sneed, N., Hardy, B., Yu, J., Ahmedna, M., & Goktepe, I. (2011). Anti-proliferative effect of *Pleurotus tuberregium* against colon and cervical cancer cells. *Journal of medicinal plants research*, *5*(30), 6650-6655.

Millar, B. C., Nelson, D. W., Moore, R. E., Rao, J. R., & Moore, J. E. (2019). Antimicrobial properties of basidiomycota macrofungi to *Mycobacterium abscessus* isolated from patients with cystic fibrosis. *International journal of mycobacteriology*, 8*,* 93-97.

Miyazaki, K., Mizutani, H., Katabuchi, H., Fukuma, K., Fujisaka, S., & Okamura, H. (1995). Activated (HLA-DR+) T-lymphocyte subsets in cervical carcinoma and effects of radiotherapy and immunotherapy with sizofiran on cell-mediated immunity and survival. *Gynecologic oncology*, *56*(3), 412-420.

Mosmann, T. R., & Sad, S. (1996). The expanding universe of T-cell subsets: Th1, Th2 and more. *Immunology today*, 17(3), 138-146.

Murata, C., Tran, Q. T., Onda, S., & Usuki, T. (2016). Extraction and isolation of ganoderic acid Σ from *Ganoderma lucidum*. *Tetrahedron letters*, *57*(48), 5368-5371.

Niedermeyer, T. H., Jira, T., Lalk, M., & Lindequist, U. (2013). Isolation of farnesyl hydroquinones from the basidiomycete *Ganoderma pfeifferi*. *Natural products and bioprospecting*, *3*(4), 137-140.

Njue, A. W., Omolo, J. O., Cheplogoi, P. K., & Waweru, A. W. (2017). Cytotoxic triterpenoids from the mushroom *Clavulina cinerea* (Bull) J. Schröt (cantharellaceae). *International Journal of biological and chemical sciences*, *11*(2), 865-873.

Nowak, R., Drozd, M., Mendyk, E., Lemieszek, M., Krakowiak, O., Kisiel, W., Rzeski, W. & Szewczyk, K. (2016). A new method for the isolation of ergosterol and peroxyergosterol as active compounds of *Hygrophoropsis aurantiaca* and *in vitro* antiproliferative activity of isolated ergosterol peroxide. *Molecules*, *21*(7), 946.

Ooi, V. E., & Liu, F. (2000). Immunomodulation and anti-cancer activity of polysaccharide-protein complexes. *Current medicinal chemistry*, *7*(7), 715-729.

Ozen, T., Darcan, C., Aktop, O., & Turkekul, I. (2011). Screening of antioxidant, antimicrobial activities and chemical contents of edible mushrooms wildly grown in the Black Sea region of Turkey. *Combinatorial chemistry & high throughput screening*, *14*(2), 72-84.

Pacheco-Sanchez, M., Boutin, Y., Angers, P., Gosselin, A., & Tweddell, R. J. (2006). A bioactive (1→ 3)-, (1→ 4)-β-d-glucan from *Collybia dryophila* and other mushrooms. *Mycologia*, *98*(2), 180-185.

Pacheco-Sánchez, M., Boutin, Y., Angers, P., Gosselin, A., & Tweddell, R. J. (2007). Inhibitory effect of CDP, a polysaccharide extracted from the mushroom *Collybia dryophila*, on nitric oxide synthase expression and nitric oxide production in macrophages. *European journal of pharmacology*, *555*(1), 61-66.

Park, H. S., Hwang, Y. H., Kim, M. K., Hong, G. E., Lee, H. J., Nagappan, A., Yumnam, S., Kim, E. H., Heo, J. D., Lee, S. J., & Won, C. K. (2015). Functional polysaccharides from *Grifola frondosa* aqueous extract inhibit atopic dermatitis-like skin lesions in NC/Nga mice. *Bioscience, biotechnology, and biochemistry*, 79(1), 147-154.

Peng, Y., & Zhang, L. (2003). Characterization of a polysaccharide–protein complex from *Ganoderma tsugae* mycelium by size-exclusion chromatography combined with laser light scattering. *Journal of biochemical and biophysical methods*, *56*(1), 243-252.

Persin, Z., Stana-Kleinschek, K., Foster, T. J., Van Dam, J. E., Boeriu, C. G., & Navard, P. (2011). Challenges and opportunities in polysaccharides research and technology: The EPNOE views for the next decade in the areas of materials, food and health care. *Carbohydrate polymers*, *84*(1), 22-32.

Pereira, E., Santos, A., Reis, F., Tavares, R. M., Baptista, P., Lino-Neto, T., & Almeida-Aguiar, C. (2013). A new effective assay to detect antimicrobial activity of filamentous fungi. *Microbiological research*, *168*(1), 1-5.

Pineda-Alegría, J. A., Sánchez-Vázquez, J. E., Gonzalez-Cortazar, M., Zamilpa, A., López-Arellano, M. E., Cuevas-Padilla, E. J., Mendoza-de-Gives, P. & Aguilar-Marcelino, L. (2017). The edible mushroom *Pleurotus djamor* produces metabolites with lethal activity against the parasitic nematode *Haemonchus contortus*. *Journal of medicinal food*, *20*(12), 1184-1192.

Ren, G., Liu, X. Y., Zhu, H. K., Yang, S. Z., & Fu, C. X. (2006). Evaluation of cytotoxic activities of some medicinal polypore fungi from China. *Fitoterapia*, *77*(5), 408-410.

Reshetnikov, S. V., & Tan, K. K. (2001). Higher Basidiomycota as a source of antitumor and immuno-stimulating polysaccharides. *International journal of medicinal mushrooms*, *3*(4), 1-34.

Ribeiro, B., Rangel, J., Valentao, P., Baptista, P., Seabra, R. M., & Andrade, P. B. (2006). Contents of carboxylic acids and two phenolics and antioxidant activity of dried Portuguese wild edible mushrooms. *Journal of agricultural and food chemistry*, *54*(22), 8530-8537.

Romagnani, S. (2000). T-cell subsets (Th1 versus Th2). *Annals of allergy, asthma & immunology*, 85(1), 921-18.

Ross, G. D., Větvička, V., Yan, J., Xia, Y., & Větvičkov, J. (1999). Therapeutic intervention with complement and β-glucan in cancer. *Immunopharmacology*, 42(1), 61-74.

Ruan, W., Lim, A. H. H., Huang, L. G., & Popovich, D. G. (2014). Extraction optimization and isolation of triterpenoids from *Ganoderma lucidum* and their effect on human carcinoma cell growth. *Natural product research*, *28*(24), 2264-2272.

Ruan, W., Wei, Y., & Popovich, D. G. (2015). Distinct responses of cytotoxic *Ganoderma lucidum* triterpenoids in human carcinoma cells. *Phytotherapy research*, *29*(11), 1744-1752.

Shao, D., Tang, S., Healy, R. A., Imerman, P. M., Schrunk, D. E., & Rumbeiha, W. K. (2016). A novel orellanine containing mushroom *Cortinarius armillatus*. *Toxicon*, *114*, 65-74.

Sharma, O. P. (1989). Textbook of fungi. Tata McGraw-Hill Education, Pg.1.

Sheu, F., Chien, P. J., Hsieh, K. Y., Chin, K. L., Huang, W. T., Tsao, C. Y., Chen, Y. F., Cheng, H. C., & Chang, H. H. (2009). Purification, cloning, and functional characterization of a novel immunomodulatory protein from *Antrodia camphorata* (bitter mushroom) that exhibits TLR2-dependent NF-κB activation and M1 polarization within murine macrophages. *Journal of agricultural and food chemistry*, 57(10), 4130-4141.

Shideler, S.; Reckseidler-Zenteno, S.; Treu, R.; Lewenza, S. (2017). Membrane damage-responsive biosensors for the discovery of antimicrobials from *Lenzites betulina* and *Haploporus odorus*. *URSCA proceedings*, *3*.

Skinnider, M. A., Dejong, C. A., Rees, P. N., Johnston, C. W., Li, H., Webster, A. L., Wyatt, M.A. & Magarvey, N. A. (2015). Genomes to natural products prediction informatics for secondary metabolomes (PRISM). *Nucleic acids research*, *43*(20), 9645-9662.

Skellam, E. (2019). Strategies for engineering natural product biosynthesis in fungi. *Trends in biotechnology*, *37*(4), 416-427.

Smith, A., Javed, S., Barad, A., Myhre, V., Li, W. M., Reimer, K., Massicotte, H.B., Tackaberry, L.E., Payne, G.W., Egger, K.N. & Lee, C. H. (2017). Growth-inhibitory and immuno modulatory activities of wild mushrooms from North-Central British Columbia (Canada). *International journal of medicinal mushrooms*, *19*(6), 485-497.

Song, X., Gaascht, F., Schmidt-Dannert, C., & Salomon, C. E. (2020). Discovery of antifungal and biofilm preventative compounds from mycelial cultures of a unique North American *Hericium sp*. fungus. *Molecules*, *25*(4), 963.

Stamets, P. E., Naeger, N. L., Evans, J. D., Han, J. O., Hopkins, B. K., Lopez, D., Moershel, H.M., Naily, R., Sumerlin, D., Taylor, A.W., Carris, L.M. & Sheppard, W. S. (2018). Extracts of polypore mushroom mycelia reduce viruses in honey bees. *Scientific reports*, *8*(1), 1-6.

Stanikunaite, R., Khan, S. I., Trappe, J. M., & Ross, S. A. (2009). Cyclooxygenase-2 inhibitory and antioxidant compounds from the truffle *Elaphomyces granulatus*. *Phytotherapy research: an international journal devoted to pharmacological and toxicological evaluation of natural product derivatives*, *23*(4), 575-578.

Stanikunaite, R., Trappe, J. M., Khan, S. I., & Ross, S. A. (2007). Evaluation of therapeutic activity of hypogeous ascomycetes and basidiomycetes from North America. *International journal of medicinal mushrooms*, *9*(1), 7-14.

Strachan, C. R., & Davies, J. (2017). The whys and wherefores of antibiotic resistance. *Cold spring harb perspect med* 7: a025171.

Su, H. J., Fann, Y. F., Chung, M. I., Won, S. J., & Lin, C. N. (2000). New Lanostanoids of *G. tsugae*. *Journal of natural products*, *63*(4), 514-516.

Tabata, M., Harrington, T. C., Chen, W., & Abe, Y. (2000). Molecular phylogeny of species in the genera *Amylostereum* and *Echinodontium*. *Mycoscience*, 41(6), 585-593.

Takahashi, A., Endo, T., & Nozoe, S. (1992). Repandiol, a new cytotoxic diepoxide from the mushrooms *Hydnum repandum* and *H. repandum* var. album. *Chemical and pharmaceutical bulletin*, *40*(12), 3181-3184.

Tzianabos, A. O. (2000). Polysaccharide immunomodulators as therapeutic agents: structural aspects and biologic function. *Clinical microbiology reviews*, 13(4), 523-533.

Van Griensven, L. J. (2009). Culinary-medicinal mushrooms: Must action be taken? *International journal of medicinal mushrooms*, *11*(3), 281-286.

Van, Q., Nayak, B. N., Reimer, M., Jones, P. J. H., Fulcher, R. G., & Rempel, C. B. (2009). Anti-inflammatory effect of *Inonotus obliquus*, *Polygala senega L.*, and *Viburnum trilobum* in a cell screening assay. *Journal of ethnopharmacology*, *125*(3), 487-493.

Vasdekis, E. P., Karkabounas, A., Giannakopoulos, I., Savvas, D., & Lekka, M. E. (2018). Screening of mushrooms bioactivity: piceatannol was identified as a bioactive ingredient in the order Cantharellales. *European food research and technology*, *244*(5), 861-871.

Wang, H. X., Liu, W. K., Ng, T. B., Ooi, V. E. C., & Chang, S. T. (1996). The immunomodulatory and antitumor activities of lectins from the mushroom *Tricholoma mongolicum*. *Immunopharmacology*, 31(2-3), 205-211.

Wang, J., Wang, H. X., & Ng, T. B. (2007). A peptide with HIV-1 reverse transcriptase inhibitory activity from the medicinal mushroom *Russula paludosa*. *Peptides*, *28*(3), 560-565.

Wang, K. P., Zhang, Q. L., Liu, Y., Wang, J., Cheng, Y., & Zhang, Y. (2013). Structure and inducing tumor cell apoptosis activity of polysaccharides isolated from *Lentinus edodes. Journal of agricultural and food chemistry*, *61*(41), 9849-9858.

Wang, G., Zhang, J., Mizuno, T., Zhuang, C., Ito, H., Mayuzumi, H., & Li, J. (1993). Antitumor active polysaccharides from the Chinese mushroom Songshan lingzhi, the fruiting body of *G. tsugae*. *Bioscience, biotechnology, and biochemistry*, *57*(6), 894-900.

Wang, Z., Zhou, F., & Quan, Y. (2014). Antioxidant and immunological activity in vitro of polysaccharides from *Phellinus nigricans* mycelia. *International journal of biological macromolecules*, *64*, 139-143.

Wasser, S. (2014). Medicinal mushroom science: Current perspectives, advances, evidences, and challenges. *Biomedical journal*, *37*(6), 345-356.

Wasser, S. P., & Weis, A. L. (1999). Medicinal properties of substances occurring in higher basidiomycetes mushrooms: current perspectives. *International journal of medicinal mushrooms*, *1*(1), 31-62.

Wasser, S. P. (2010). Medicinal mushroom science: history, current status, future trends, and unsolved problems. *International journal of medicinal mushrooms*, *12*(1), 1-16.

Wasser, S. P. (2017). Medicinal mushrooms in human clinical studies. Part I. Anticancer, onco-immunological, and immunomodulatory activities: a review. *International journal of medicinal mushrooms*, *19*(4).

Wasser, S. P., & Weis, A. L. (1999). Therapeutic effects of substances occurring in higher Basidiomycetes mushrooms: a modern perspective. *Critical reviews™ in Immunology*, 19(1).

Wilbers, R. H., Westerhof, L. B., van de Velde, J., Smant, G., van Raaij, D. R., Sonnenberg, A. S., Bakker, J., & Schots, A. (2016). Physical interaction of T cells with Dendritic cells is not required for the immunomodulatory effects of the edible Mushroom *Agaricus subrufescens*. *Frontiers in immunology*, 7.

Wong, J. H., Ng, T. B., Chan, H. H. L., Liu, Q., Man, G. C. W., Zhang, C. Z., Guan, S., Ng, C.C.W., Fang, E.F., Wang, H., Liu, F., Ye, X., Rolka, K., Naude, R., Zhao, S., Sha, O., Li, C. & Xia, L. (2020). Mushroom extracts and compounds with suppressive action on breast cancer: Evidence from studies using cultured cancer cells, tumor-bearing animals, and clinical trials. *Applied microbiology and biotechnology*, *104*(11), 4675-4703.

Xia, Y., Větvička, V., Yan, J., Hanikýřov, M., Mayadas, T., & Ross, G. D. (1999). The β-glucan-binding lectin site of mouse CR3 (CD11b/CD18) and its function in generating a primed state of the receptor that mediates cytotoxic activation in response to iC3b-opsonized target cells. *The journal of immunology*, 162(4), 2281-2290.

Yaqoob, A., Li, W. M., Liu, V., Wang, C., Mackedenski, S., Tackaberry, L. E., Massicotte, H.B.; Egger, K.N.; Reimer, K. & Lee, C. H. (2020). Grifolin, neogrifolin and confluentin from the terricolous polypore *Albatrellus flettii* suppress KRAS expression in human colon cancer cells. *PloS one*, *15*(5), e0231948.

Ye, Y., Josten, I., Arnold, N., Steffan, B., and Steglich, W. (1996) Isolation of a fluorone pigment from the Indian paint fungus *Echinodontium tinctorium* and *Pyrofomes albomarginatus*. *Tetrahedron*, 52, 5793-5798.

Zheng, W., Miao, K., Liu, Y., Zhao, Y., Zhang, M., Pan, S., & Dai, Y. (2010). Chemical diversity of biologically active metabolites in the sclerotia of *Inonotus obliquus* and submerged culture strategies for up-regulating their production. *Applied microbiology and biotechnology*, *87*(4), 1237-1254.

Zeb, M., Tackaberry, L. E., Massicotte, H. B., Egger, K. N., Reimer, K., Lu, G., Heiss, C.; Azadi, P. & Lee, C. H. (2021). Structural elucidation and immuno-stimulatory activity of a novel polysaccharide containing glucuronic acid from the fungus *Echinodontium tinctorium*. *Carbohydrate polymers*, *258*, 117700.

Zhang, B. B., & Cheung, P. C. (2011). Use of stimulatory agents to enhance the production of bioactive exopolysaccharide from *Pleurotus tuber-regium* by submerged fermentation. *Journal of agricultural and food chemistry*, *59*(4), 1210-1216.

Zhang, P., Li, K., Yang, G., Xia, C., Polston, J. E., Li, G., Li, G., Li, S., Lin, Z., Yang, L.J., Bruner, S.D. & Ding, Y. (2017). Cytotoxic protein from the mushroom *Coprinus comatus*

possesses a unique mode for glycan binding and specificity. *Proceedings of the national academy of sciences*, *114*(34), 8980-8985.

Zhang, Y., Ma, G., Fang, L., Wang, L., & Xie, J. (2014). The Immuno-stimulatory and Antitumor Activities of Polysaccharide from *Agaricus bisporus* (brown). *Journal of food and nutrition research*, 2(3), 122-126.

Zhang, M. M., Qiao, Y., Ang, E. L., & Zhao, H. (2017). Using natural products for drug discovery: the impact of the genomics era. *Expert opinion on drug discovery*, *12*(5), 475-487.

Zhou, L. W., Cao, Y., Wu, S. H., Vlas k, J., Li, D. W., Li, M. J., & Dai, Y. C. (2015). Global diversity of the *Ganoderma lucidum* complex (Ganodermataceae, Polyporales) inferred from morphology and multilocus phylogeny. *Phytochemistry*, 114, 7-15.

Zhu, H., Yalcin, T., & Li, L. (1998). Analysis of the accuracy of determining average molecular weights of narrow polydispersity polymers by matrix-assisted laser desorption ionization time of flight mass spectrometry. *Journal of the american society for mass spectrometry, 9(4), 275-281.*

Zmitrovich, I. V., Arefyev, S. P., Bondartseva, M. A., Belova, N. V., Khimich, Y. R., Isaeva, L. G., Kapitonov, V.I., Vlasenko, V.A., Volobuev, S.V., Ezhov, O.N. & Wasser, S. P. (2019). Profiles of little-known medicinal polypores: *Haploporus odorus* (Agaricomycetes). *International journal of medicinal mushrooms*, *21*(8), 783-791.

Chapter 2: Structural elucidation and immuno-stimulatory activity of a novel polysaccharide containing glucuronic acid from the fungus *Echinodontium tinctorium*

ABSTRACT

An immuno-stimulatory polysaccharide (EtISPFa) was purified from water extract of the fungus *Echinodontium tinctorium*. EtISPFa has an estimated weight average molecular weight (Mw) of 1354 kDa and is composed of glucose (66.2 %), glucuronic acid (10.1 %), mannose (6.7 %), galactose (6.4 %), xylose (5.6 %), rhamnose (3.1 %), fucose (1.8 %), and arabinose (0.2 %). It has multiple glycosidic linkages, with 3-Glc*p* (19.8 %), 4-Glc*p*A (10.8 %), 6-Glc*p* (10.7 %), and 3,6-Glc*p* (8.7 %) being the most prominent. NMR analysis showed that EtISPFa has a backbone containing mostly 3-substituted *β*-glucopyranose with 4-substituted glucopyranosyl uronic acid. Short side chains consisting of an average of two *β*-glycopyranose residues, connected through 1→6 linkages, are attached to the 6-position of about every 4th or 5th backbone glucose residue. EtISPFa is a novel glucuronic acid-containing *β*-glucan capable of significantly inducing the production of cytokines IL-17, IL-16, MIP-2, G-CSF, GM-CSF, LIF, MIP-1α, MIP-1β, and RANTES *in vitro*. EtISPFa should be further explored for its immuno-stimulatory activity *in vivo*.

2.1. Introduction

Recent success in immunotherapy and immune checkpoint blockade has led to a renewed interest in finding compounds with immuno-modulatory effects (Havel, Chowell, & Chan, 2019). Many immuno-modulatory compounds isolated from mushrooms are polysaccharides (El Enshasy & Hatti-Kaul, 2013; Lull, Wichers, & Savelkoul, 2005; Rowan *et al*., 2003). Given the limited information on the therapeutic potential of *E. tinctorium*, crude extracts of the fungus were screened for three major bioactivities related to cancer treatment, including immuno-

stimulatory activity. At the outset of this research, I hypothesized that *E. tinctorium* would yield immuno-stimulatory polysaccharide(s) and it was documented that its water extract possessed strong immuno-stimulatory activity (Javed *et al*., 2019). To assess for immuno-stimulatory activity, activation of Raw 264.7 murine macrophage cells was monitored to produce the pro-inflammatory cytokine tumor necrosis factor (TNF)-α. Activation of macrophages to produce TNF-α is one of the critical innate immune responses and has proven to be a gold standard in monitoring for immuno-stimulation (El Enshasy & Hatti-Kaul, 2013; Lull *et al*., 2005).

The aim of the present study was to purify and characterize an immuno-stimulatory polysaccharide from *E. tinctorium*. The water extract from *E. tinctorium* was subjected to multiple chromatographic steps (Sephadex LH-20, DEAE-Sephadex, Sephacryl S-500 HR, and HPLC BioSEC-5 chromatography) for purification of the immuno-stimulatory compound. Following this, structural analyses were performed. This included gas chromatography-mass spectrometry (GC–MS) to determine monosaccharide content and glycosidic linkages, Fourier transform infrared (FTIR) spectroscopy for identification of functional groups, and finally, 2-D NMR analyses for determination of the constitution and monosaccharide sequence of the EtISPFa polysaccharide.

2.2. Materials and methods

2.2.1. Materials and reagents

All the reagents used were of analytical grade. Dulbecco's Modified Eagle Medium (DMEM) from LONZA (Walkersville, Maryland, USA), and fetal bovine serum (FBS) from Life Technologies Inc. (Waltham, Massachusetts, USA) were used. SephadexTM LH-20, DEAE-Sephadex, and HiPrep 26/60 SephacrylTM S-500 HR pre-packed columns were obtained from GE Healthcare (Chicago, IL, USA). Dextran standards (T1, T5, T12, T25, T50, T80, T150,

T270, T410) were purchased from Sigma- Aldrich (Oakville, ON, Canada), and HPLC BioSEC-5 column and guard column were purchased from Agilent (Santa Clara, CA, USA).

2.2.2. Collection and extraction of the mushroom

E. tinctorium conks were collected from hemlock trees in Terrace (CL103) and Smithers (CL37), BC, Canada, in August 2014 and 2015, respectively. Voucher specimens for these collections were deposited at the University of Northern British Columbia, Canada. The specimens, previously confirmed using morphological and molecular techniques (Javed *et al*., 2019), were dried in a hot air oven (55 °C, 24− 48 h), cut into smaller pieces using a saw machine, and ground to fine powder using a hammer mill. Powdered mushrooms (300 g) were sequentially extracted with 80 % ethanol (1.5 L, 65 °C, 3 h). The extract was vacuum filtered through Whatman filter paper No. 3 and the filtrate was designated 1A. The residue was further extracted with 50 % methanol (1.5 L, 65 °C, 3 h). The methanol extract was filtered and the filtrate was designated 1B. The residue was further extracted with water (1.5 L, 65 °C, 6 h) and the filtrate was named 1C. Crude extract 1C was concentrated, lyophilized, and filter sterilized before assessment for immuno-stimulatory activity.

2.2.3. Immuno-stimulatory assay

Raw 264.7 murine macrophage cell line was used to conduct immuno-stimulatory assays essentially as described previously (Smith *et al*., 2017). After 16−18 h of plating at a density of 1 × 10^5 cells/well in 96-well plates in 200 µL of serum-free DMEM, cells were treated with 1C at doses ranging from 0.1−1 mg/mL and incubated for 6 h. Water was used as a negative control, whereas lipopolysaccharide (LPS) at 500 ng/uL was used as a positive control in most experiments. After 6 h incubation, 100 µL of cell supernatants were collected to determine the levels of TNF-α as well as other cytokines produced upon stimulation by test agents. TNF-α

stimulation was determined by sandwich ELISA as previously described (Smith et al., 2017). Samples were analyzed at 450 nm and 550 nm using Synergy-2 multiplate reader (BioTek®, VT, USA). Other cytokines and chemokines were measured by Eve Technologies (Calgary, AB, Canada) using a mouse cytokine array/chemokine array 32-plex.

2.2.4. Purification of immuno-stimulatory compound(s) from *E. tinctorium*

The crude water extract 1C was subjected to purification on a 400 mL Sephadex LH-20 designated column-2 (C26/100 by GE Healthcare), previously equilibrated with 2–3 column volumes (C.V.) of degassed water. 1C was reconstituted in water to a concentration of 30 mg/mL, spun at 1000 × g for 5 min, before loading onto the column. Sample injection volume was 2% of the total bed volume. Degassed water was allowed to run through the column at a flow rate of 1 mL/min and 10 mL fractions were collected over 2 C.V. The eluted fractions were assessed for carbohydrate content using phenol sulfuric acid method (DuBois, Gilles, Hamilton, Rebers, & Smith, 1956) and protein content using PIERCE BCA protein assay (Waltham, MA, USA).

The pooled fractions from column-2 were concentrated to yield bioactive fraction 2A (100 mg) and subjected to anion exchange chromatography using DEAE-Sephadex A50 resin (designated column-3). Multiple buffers were assessed on small scale (10 mL) DEAE gravity drip column as shown in Fig. S1 to get the optimized conditions (L-Histidine buffer, pH 6.2, 1 mL/min). A XK-50 size column-3 (50 mm x 100 cm, GE Healthcare) was used. Flow-through and eluent (using 1 M NaCl) were concentrated, dialyzed (MWCO 3500 Da), lyophilized, re-suspended (1 mg/mL), and assessed for immuno-stimulatory activity. Bioactive elution 3A was then purified using a Sephacryl S-500 HR (column-4) (150 mM NaCl, 1.3 mL/min, 1.5 C.V., 10 mL fractions) connected to an AKTA Pure system. Sample (2 mL at 50 mg/mL) was loaded onto

the column using a 2 mL sample loop. Eluted fractions were analyzed for TNF-α stimulation by immuno-stimulatory assay as described in Section 2.2.3.

2.2.5. Molecular size distribution and ultrapurification using HPLC

HPLC SEC was used to further purify the bioactive compound, and for estimation of purity as well as molecular size distribution. HPLC SEC was performed on Agilent HPLC 1200 series using an Agilent BioSEC-5 column-5 (5 μm, 500 A, 4.6 × 300 mm), equipped with a guard column (5 μm, 500 A, 4.6 × 50 mm). Refractive index detector (Agilent 1200 Infinity II series, G7162A RID) with standard optical unit was used for detection purposes. The temperature was kept at 28 ± 0.2 °C. The peak maxima molecular weight (M_p) of EtISPFa was estimated by calibrating with T-series Dextran standards (25–2000 kDa). The column was equilibrated with mobile phase to get a stable baseline. Active fraction 4A (10 μL at 10 mg/mL) was injected through an autosampler (Agilent 1200 series G1329A) and water was used as a mobile phase (flow rate = 0.4 mL/min). Once the HPLC profile was obtained, the respective peaks were purified by fraction collection. Fraction collected peaks were re-injected to confirm sample purity. The peaks were assessed for immuno-stimulatory activity as described in Section 2.2.3. Fractions containing the bioactive peak were lyophilized and subjected to structural elucidation methods as described below.

2.2.6. Enzyme digestion and heat denaturation of polysaccharides from *E. tinctorium*

To further delineate the role of polysaccharides from *E. tinctorium* in contributing to the immuno-stimulatory activity, both EtISPFa and EtISPFb were digested with several enzymes capable of cleaving glycosidic bonds. Two mg/mL of EtISPFa and EtISPFb were treated with cellulase (10 and 30 units) for 2 h at 37 ºC followed by heat deactivation at 80 ºC for 20 min. In the case for the treatment with fucosidase (0.01 unit) and galactosidase (0.1 unit), both

polysaccharides were incubated at 37 ºC for 24 h and heat deactivated as described above. The reaction mixtures were kept at -20 ºC until further analysis for immuno-stimulatory activity as described above.

2.2.7. Monosaccharide composition analysis

Monosaccharide content of HPLC-purified sample was determined by GC–MS. EtISPFa (360 μg) and internal standard inositol (20 μg) were subjected to acid methanolysis by heating with 1 M methanolic HCl in a sealed screw capped glass tube (18 h, 80 ˚C). The samples were dissolved under nitrogen stream and treated with methanol, pyridine, and acetic anhydride for 30 min. Excess solvent was removed and samples were subjected to derivatization with Tri-Sil HTP (80 ˚C, 30 min). The resulting per-O-trimethylsilyl (TMS) derivatives of the monosaccharide methyl glycosides were analyzed by GC–MS (Agilent 7890A GC, 5975C MSD) on a Supelco Equity-1 fused silica column (30 m × 0.25 mm ID).

2.2.8. Methylation and linkage analysis

Glycosyl linkage analysis was conducted by methylating 1 mg of EtISPFa with dimsyl potassium (15 min) and methyl iodide (15 min) in a screw-capped glass tube. After extracting with dichloromethane and reducing with $LiAlD_4$ (lithium aluminum deuteride) in THF for 4 h at 100 ˚C, the sample was permethylated with NaOH (15 min) and methyl iodide (45 min), depolymerized with 400 μL of 2 M TFA (trifluoro acetic acid) in a sealed tube (2 h, 121 ˚C), reduced with $NaBD_4$ (sodium borodeuteride), and acetylated with a mixture of acetic anhydride and TFA (25 min, 50 ˚ C), resulting in partially methylated alditol acetates (PMAAs). The undermethylated polysaccharides after permethylation using NaOH and methyl iodide were permethylated again. This fraction was then depolymerized, reduced, acetylated, and combined with the fraction permethylated in the first run. The combined collection was subjected to GC–

MS analysis using a 30 m Supelco SP-2331 fused silica column on a GC–MS instrument (Agilent 7890A GC, Agilent 5975C MSD with electron impact ionization source).

2.2.9. Structural elucidation by spectral analysis

The presence of proteins and nucleic acids was determined through UV nanodrop scan on a UV spectrophotometer with a detection range of 200-400 nm. Sample was analyzed at a wavelength of 280 nm for proteins and 260 nm for nucleic acids. FTIR spectroscopy was conducted to analyze functional groups of EtISPFa using Bruker ATR-FTIR spectrophotometer (Billerica, MA, USA), with a detection frequency from 4000-400 cm^{-1}. For FTIR, a small amount of EtISPFa was placed on a diamond window and analyzed by OPUS software. Twenty two scans were performed to obtain a representative FTIR spectrum.

For further detailed structural characterization, NMR analysis was conducted. EtISPFa (5.4 mg) was dissolved in 99.8 % of deuterium oxide (D_2O, Sigma), lyophilized and redissolved in 320 µL of 99.96 % D_2O (Cambridge Isotope Laboratories). D2O exchanged EtISPFa was then subjected to 1D proton NMR (^{1}H-NMR) and 2D NMR including ^{1}H-^{1}H- correlation spectroscopy (COSY), total correlation spectroscopy (TOCSY), nuclear Overhauser effect spectroscopy (NOESY), ^{1}H-^{13}C NMR heteronuclear single quantum correlation spectroscopy (HSQC), HSQC-TOCSY, and heteronuclear multiple bond correlation (HMBC) on an Agilent Inova 600 MHz NMR, equipped with a cryoprobe, using standard pulse sequences. Acetone was used as an internal standard (δ_H = 2.218 ppm, δ_C = 33.0 ppm). NMR analysis was carried out at 65°C.

2.2.10. Estimation of glucan content in EtISPFa

The α- and β-glucan contents were determined using a Megazyme kit (Wicklow, Ireland), based on manufacturer guidelines. Using this kit, EtISPFa was subjected to multiple steps of acid

hydrolysis and enzyme cleavage to yield D-glucose molecules which were then detected by measuring absorbance at 510 nm using Synergy 2 multiplate reader. Yeast β-glucan was used as a standard.

2.3. Results and discussion

2.3.1. Extraction and assessment of E3 water extract for immuno-stimulatory activity

We have previously shown that the water extract from *E. tinctorium* possesses strong immuno-stimulatory activity (Javed *et al.*, 2019). Here, we took the initiative to purify, identify and characterize the immuno-stimulatory compound(s) from *E. tinctorium.* The powdered mushroom was sequentially extracted, as illustrated in Fig. 2.1A. The sequential extractions with ethanol and methanol were expected to remove any small molecules, thereby retaining large molecules (polysaccharides, proteins or complexes of both) in the water extract. Extraction of powdered *E. tinctorium* (300 g) generated water extract 1C which was concentrated by freeze drying to yield a dried extract (4 g). Crude extract 1C was reconstituted in water to give a concentration of 20 mg/mL and filter sterilized. A dose-dependent immuno-stimulatory assay was then performed. As shown in Fig. 2.1B, E3 was found to induce TNF-α in Raw 264.7 cells at concentrations ranging from 0.1-1 mg/mL.

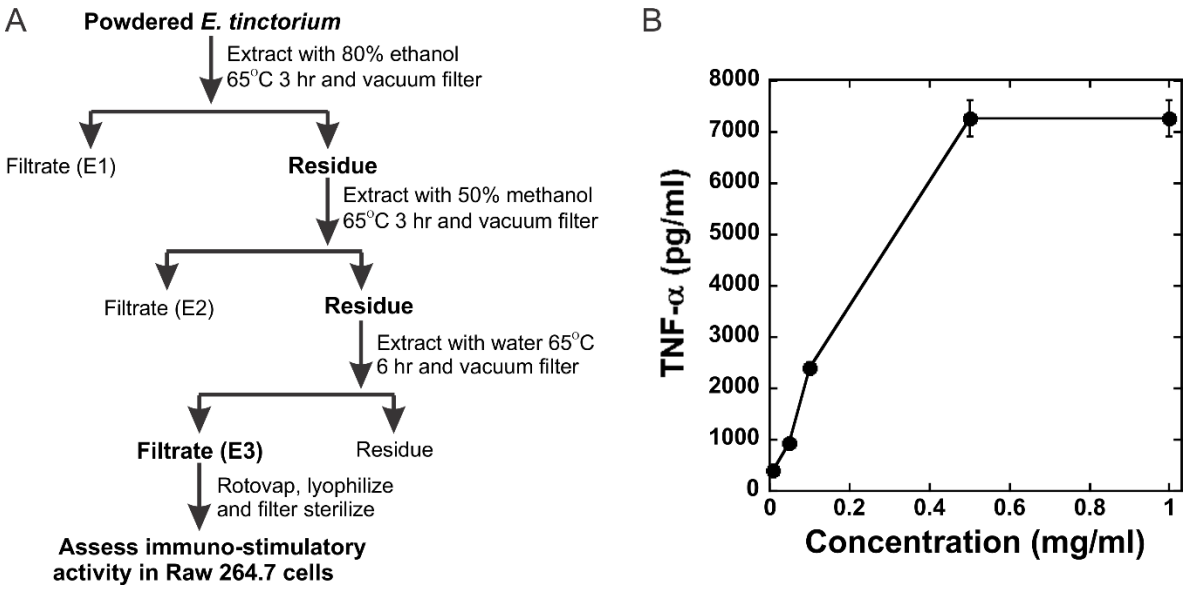

Fig. 2. 1. Chemical extraction of *E. tinctorium* and assessment of the water extract E3 for immuno-stimulatory activity on macrophage cells (A) Chemical extraction scheme to obtain water extract E3 from *E. tinctorium*. (B) Dose-dependent immuno-stimulatory assay shows induction of TNF-α production in Raw 264.7 macrophage cells by E3 extract from 0.1-1 mg/mL. Error bars represent S.D. Results shown are representative from three biological replicates.

2.3.2. Purification of immuno-stimulatory polysaccharide from *E. tinctorium*

The overall scheme adopted for the purification of the immuno-stimulatory polysaccharide from *E. tinctorium* (EtISPFa) is shown in Fig. 2.2A and the amounts obtained at each step are given in Table S2. The 1C extract was first subjected to Sephadex LH-20 size-exclusion chromatography column-2. As shown in Fig. 2.3A, the major immuno-stimulatory activity was found at elution volume 30-48 mL (0.5-0.7 C.V.) (fractions 27-39), suggesting that the immuno-stimulatory compound has a relatively large molecular weight. The fractions collected from column-2 were also assessed for carbohydrate (CHO) and protein content. Results in Fig. 2.2B show that the major immuno-stimulatory activity correlated strongly with carbohydrate content. The activity also correlated with the first protein content peak (Fig. 2.2C). This result suggests

that the major immuno-stimulatory activity eluted at volume 30-48 mL contains both carbohydrate and protein components.

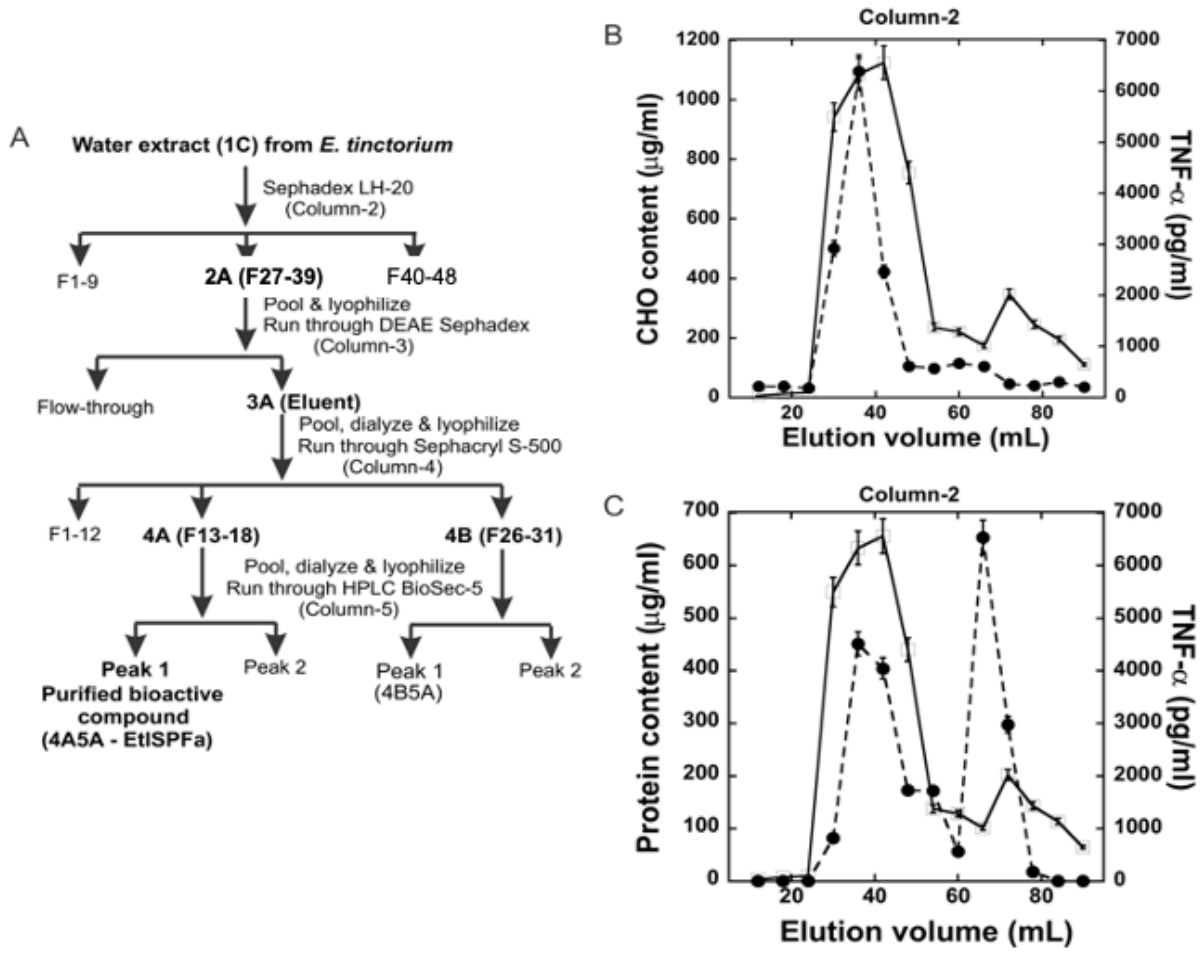

Fig. 2. 2. Purification of the immuno-stimulatory polysaccharide (EtISPFa) from *E. tinctorium.* (A) Summary of the purification scheme used. 1C extract from *E. tinctorium* was purified using Sephadex LH-20 size-exclusion chromatography (column-2). Fractions collected from column-2 were assessed for immuno-stimulatory activity (solid line in B and C), carbohydrate content (dotted line in B) and protein content (dotted line in C). Error bars represent S.D. Results shown are representative from three biological replicates.

The immuno-stimulatory fractions 10-16 from column-2 (Fig. 2.3A) were then pooled, concentrated, lyophilized, and resuspended in water. It was then subjected to column-3, DEAE-

Sephadex anion exchange chromatography using L-Histidine (pH 6.2) as the buffer of choice. The flow-through and eluent from column-3 were concentrated, dialyzed, lyophilized, filter sterilized, and assessed for immuno-stimulatory activity. As shown in Fig. 2.3B, the eluent referred to as 3A (but not the flow-through from DEAE-Sephadex) contains the immuno-stimulatory activity (Fig. 2.3B). This result suggested the presence of acidic groups on the immuno-stimulatory polysaccharide that were effectively associated with positively charged DEAE-Sephadex resin and were eluted upon addition of salt to the mobile phase.

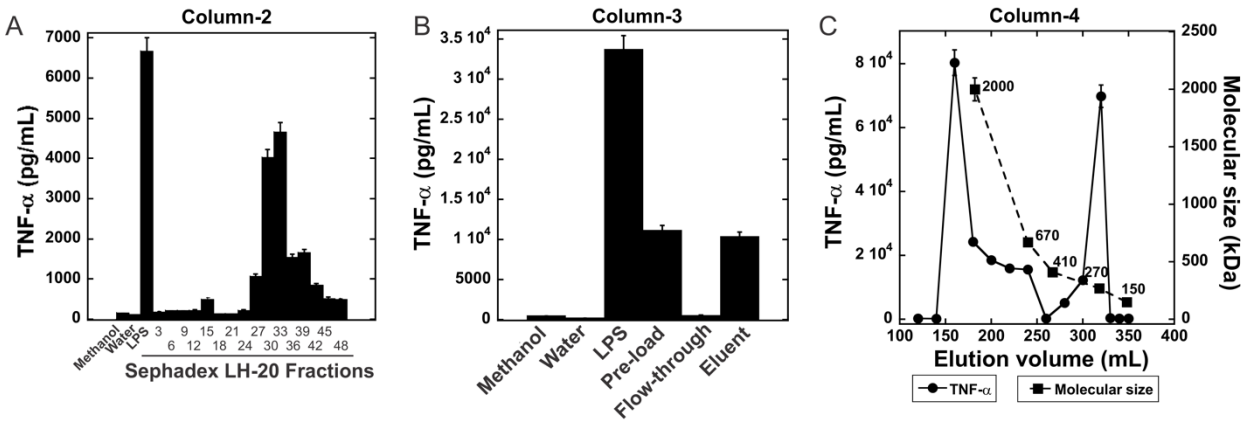

Fig. 2. 3. Purification of the immuno-stimulatory polysaccharide from *E. tinctorium* (EtISPFa) (A) Purification using Sephadex LH-20 size exclusion chromatography (column-2). Fractions collected were assessed for immuno-stimulatory activity. (B) Purification using DEAE-Sephadex anion exchange chromatography (column-3). Pre-load, flow-through and eluent were assessed for immuno-stimulatory activity. Medium and water were used as negative controls. LPS was used as a positive control. (C) Sephacryl S-500 HR SEC (column-4) elution profile correlating TNF-α stimulation with relative size of bioactive fractions. Raw 264.7 macrophage cells were

used to assess TNF-α production as an indicator of immuno-stimulatory activity. Error bars represent S.D.

Bioactive elution collected from column-3 (Fig. 2.3B) was concentrated, lyophilized, filter sterilized, and subjected to column-4, Sephacryl S-500 high resolution size-exclusion chromatography. As shown in Figs. 2.3C & S2, 4A (fractions 14-18) and 4B (fractions 30-32) recovered from the elution of column-4 at retention volumes 150-190 mL and 300-320 mL retained bioactivity. T-series Dextran standards were used to estimate the relative molecular size of bioactive compounds on column-4. As shown in Fig. 2.3C, 4A had a predicted molecular size of 670-2000 kDa or greater, whereas 4B was 200-300 kDa in size. The two sets of bioactive fractions were pooled separately, concentrated, dialyzed, and lyophilized.

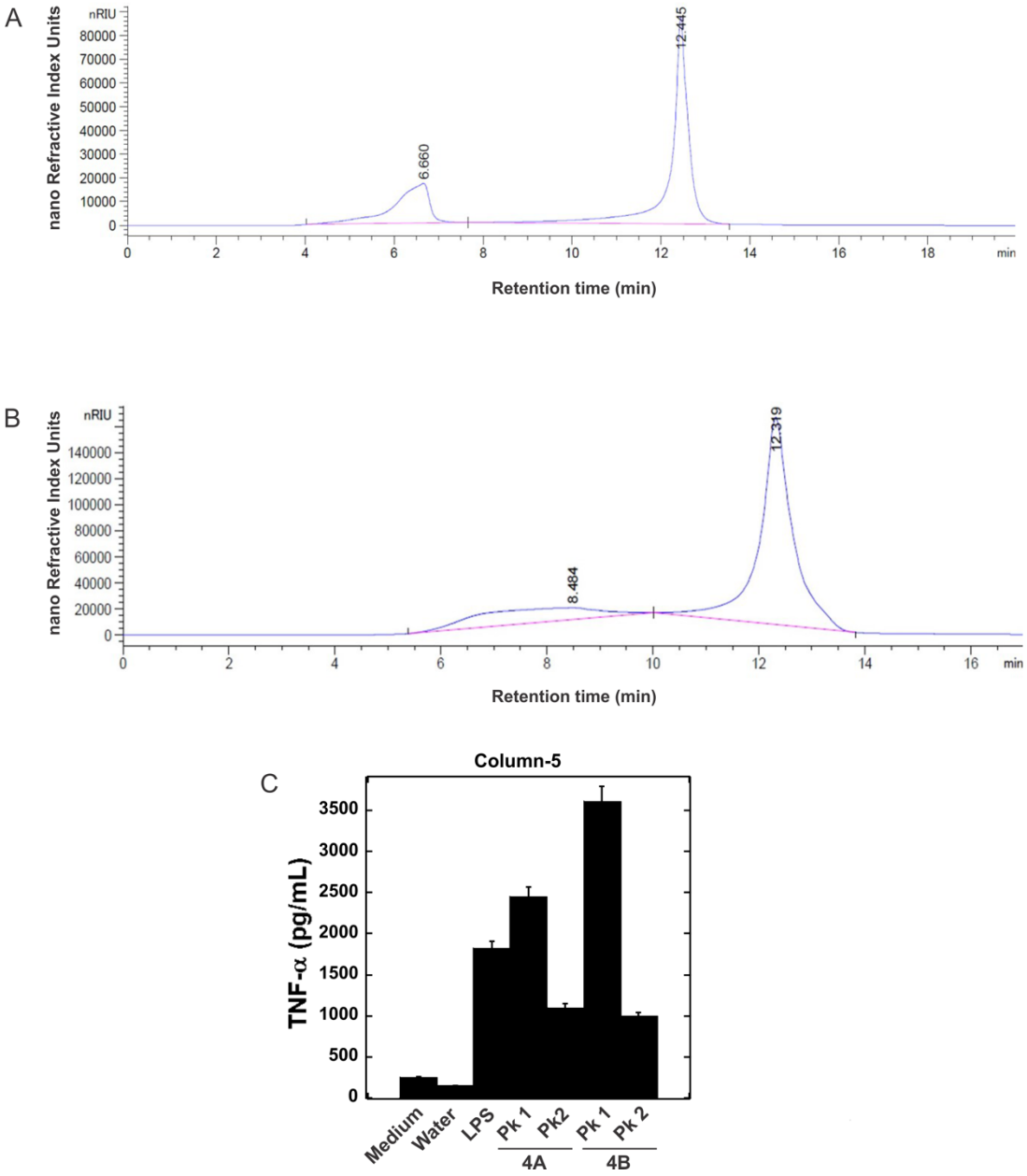

Fig. 2. 4. HPLC BioSEC-5 full elution profile of (A) 4A and (B) 4B. The collected two peaks in (A) and (B) were assessed for immuno-stimulatory activity shown in (C).

Bioactive fractions 4A and 4B were further purified by HPLC using Agilent Bio SEC-5 column-5. The HPLC profiles of 4A and 4B (Fig. 2.4) show the presence of two significant peaks eluting at retention times 6.66 min and 12.44 min for 4A (Fig. 2.4A), and 8.48 min and 12.31 min for 4B (Fig. 2.4B), respectively. The respective peaks were fraction collected and

assessed for immuno-stimulatory activity. Peak 1 in both 4A and 4B at retention times 6.66 min and 8.48 min showed maximum TNF-α stimulation, compared to their respective peak 2 (Fig. 2.4C). The fractions collected containing the bioactive peaks were re-assessed for purity using column-5 (Fig. 2.5). The bioactive peak 1 (4A5A; EtISPFa) from 4A was retained at 5.72 min while bioactive peak 1 (4B5A) from 4B was eluting at retention time of 5.70 min. Since these retention times are quite similar, both 4A5A (referred to as EtISPFa) and 4B5A are most likely similar compounds or they share common chemical characteristics.

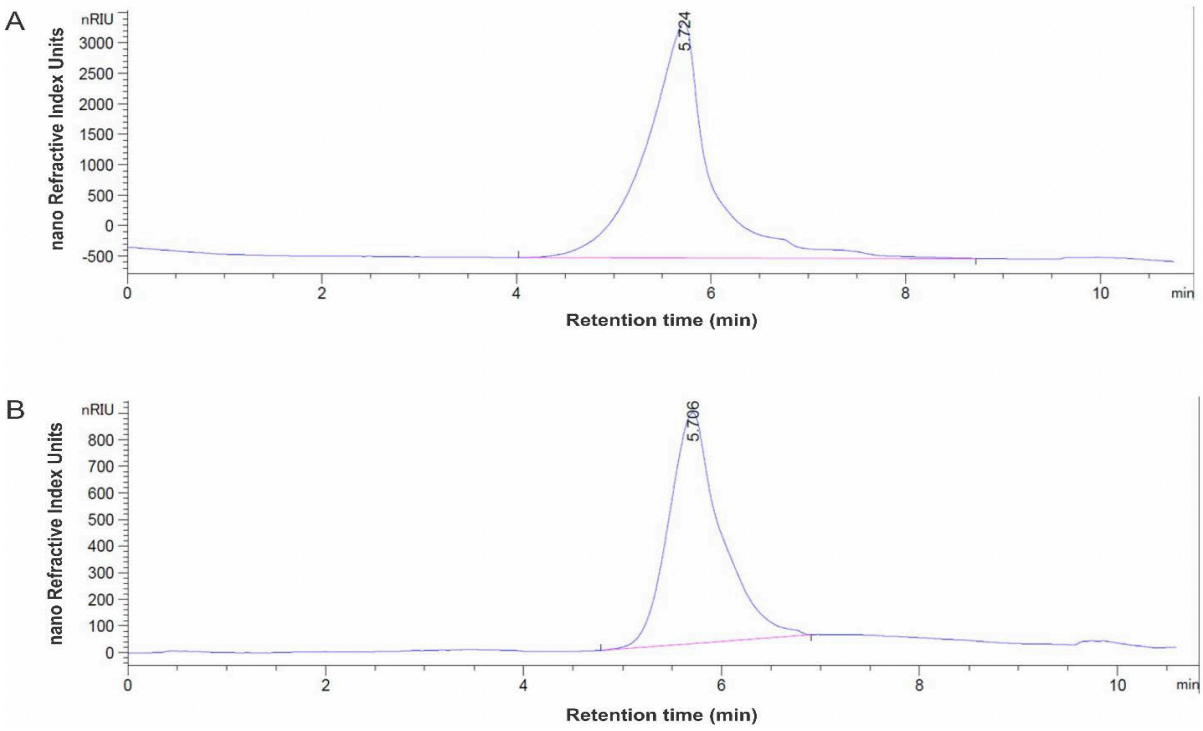

Fig. 2. 5. (A) HPLC BioSEC-5 profile of purified Peak 1 EtISPFa. (B) HPLC BioSEC-5 purified Peak 1 EtISPFb.

Based on the assumption that both are similar compounds, EtISPFa was chosen for further structural elucidation studies as described below. To more accurately estimate the size of EtISPFa, T-series dextrans with molecular weight ranging 25-2000 kDa were used on BioSEC-5 (Fig. S3). Based on the results, the peak maxima molecular weight (M_p) of EtISPFa was

estimated to be 1302 kDa. We further performed calculations to determine the number (M_n) and weight average molecular weight (M_W) of EtISPFa. As shown in Table S1, the M_n and M_W of EtISPFa was calculated to be 1302 kDa and 1354 kDa respectively. The polydispersity index was calculated to be 1.04.

2.3.3. Cytokine and chemokine secretion in Raw264.7 cells induced by 4A

Besides TNF-α, secretion of cytokines such as colony stimulating factor (CSF), interleukins (ILs), chemokines, and interferons (IFNs) by macrophages is also important in regulating the immune system. A mouse cytokine/chemokine array 32 plex was used to determine the cytokine and chemokine secretion profile of Raw 264.7 cells induced by a 6 h treatment with bioactive fraction 4A. The array covers both pro-inflammatory cytokines (IL-1β, IL-6, TNF-α, GM-CSF) and chemokines (RANTES, MCP-1, MIP-1α, MIP-1β) as well as anti-inflammatory cytokines (IL-4, IL-10, IL-11, G-CSF) that are commonly used to monitor the capacity of mushroom-derived compounds to elicit an immune response (El Enshasy & Hatti-Kaul, 2013; Lull et al., 2005). The results are summarized in Table 2.1. Treatment with 4A markedly enhanced the secretion of cytokines, which ranged from an increase of 2.1-683 times higher than the control. The cytokines that were most significantly induced (> 10-fold increase) included interleukin-17 (IL-17), interleukin-6 (IL-6), macrophage inflammatory protein-2 (MIP-2), granulocyte-colony stimulating factor (G-CSF), granulocyte macrophage-colony stimulating factor (GM-CSF), leukemia inhibitory factor (LIF), macrophage inflammatory protein-1α (MIP-1α), macrophage inflammatory protein-1β (MIP-1β), and RANTES (regulated on activation, normal T cell expressed and secreted). The cytokines that were moderately induced (2 to 10-fold increase) included interleukin-10 (IL-10), interferon gamma-induced protein 10 (IP-10), eotaxin,

interleukin-1α (IL-1α), monocyte chemo attractant protein-1 (MCP-1), and interleukin-12 (IL-12).

Table 2. 1. Cytokines induction by EtincFa in Raw 264.7 murine macrophage cells

Cytokine		**Fold ± S.D[a]**
IFNγ	Interferon gamma	1.22 ± 0.32
TNF-α	Tumor necrosis factor-α	58.04 ± 6.83
IL-2	Interleukin-2	0.87[b]
IL-10	Interleukin-10	4.47 ± 1.42
IL-12 p70	Interleukin-12	1.46[b]
IL-4	Interleukin-4	1.48 ± 0.33
IL-5	Interleukin-5	1.0
IL-9	Interleukin-9	0.97 ± 0.05
IL-17	Interleukin-17	12.95 ± 1.06
IL-6	Interleukin-6	65.05 ± 7.22
IP-10	Interferon gamma-induced protein-10	3.63[b]
MIP-2	Macrophage inflammatory protein-2	24.55[b]
CCL11	Eotaxin	2.11 ± 1.56
G-CSF	Granulocyte-colony stimulating factor	683.93 ± 22.73
GM-CSF	Granulocyte macrophage-colony stimulating factor	208.78 ± 27.56
IL-1α	Interleukin-1α	2.40 ± 1.66
IL-1β	Interleukin-1β	1.50 ± 0.98
LIF	Leukemia inhibitory factor	86.47[b]
MCP-1	Monocyte chemo attractant protein-1	1.58[b]
IL-15	Interleukin-15	1.50 ± 0.27
MIP-1α	Macrophage inflammatory protein-1α	21.7 ± 6.87
MIP-1β	Macrophage inflammatory protein-1β	22.34 ± 7.57
RANTES (CCL5)	Regulated on activation, normal T cell expressed and secreted [Chemokine (C-C motif) ligand 5]	5.19[b]

[a]The fold changes indicated in the table are relative to the control (H_2O). The mean fold change ± standard deviation (S.D) is taken for data set n = 2.

These results confirmed the immuno-stimulatory effect of 4A on murine macrophage cells *in vitro*. It is important to point out that this *in vitro* study cannot distinguish whether our purified polysaccharide exerts immuno-stimulatory effect and/or induce inflammation. Such distinction can only be determined using an animal model.

2.3.4. Glucan content analysis

The *α*-glucan and *β*-glucan contents were estimated in Sephacryl S-500-purified 4A and 4B. Yeast *β*-glucan was used as a positive control. *β*-glucan content in 4A and 4B fractions was estimated to be 89.9 % (10.16 % w/w) and 82.4 % (9.9 % w/w). However, α-glucan in 4A and 4B was estimated to be 10.1 (1.14 % w/w) and 17.6 % (2.11 % w/w), respectively. In summary, both 4A and 4B predominantly contain *β*-glucan and this was further studied using GC–MS and NMR analyses as described below.

2.3.5. Role of polysaccharide component in contributing to the immuno-stimulatory activity

Several enzymes capable of cleaving glycosidic bonds were used to digest the Sephacryl S-500-purified 4A and 4B (Fig. 2.6-2.9). EtISPFa and EtISPFb were subjected to enzymes digestion to assess the role of a particular glycosidic linkage in contributing to the immuno-stimulatory activity. As shown in Fig. 2.6, the immune-stimulatory activity of 4A and 4B was not affected by cellulase digestion. Cellulase are specific in hydrolyzing the *β*-1,4 linkage. Interestingly, from the chemical characterization data (Table 2.4), it was revealed that EtISPFa indeed has a *β*-1,4 linked GlcA. The unexpected negative results suggest that *β*-1,4 linkage may not be easily accessible to cellulase due to the complex structure of EtISPFa. Alternatively, it could be that celuulase hydrolyzes *β*-1,4 linkage between Glc molecules whereas EtISPFa has *β*-1,4 linkage between Glc and GlcA.

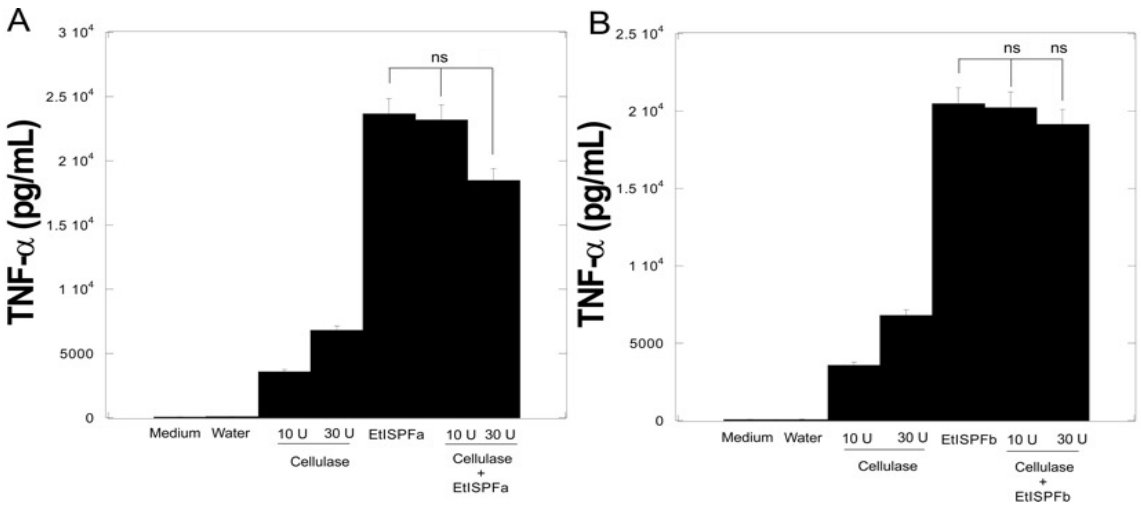

Fig. 2. 6. Effect of cellulase on immuno-stimulatory activity of EtISPFa (A) and EtISPFb (B) from *E. tinctorium*. One-way ANOVA (Tukey's test) was used for statistical analysis. Error bars represent S.D. ns represents non-significant.

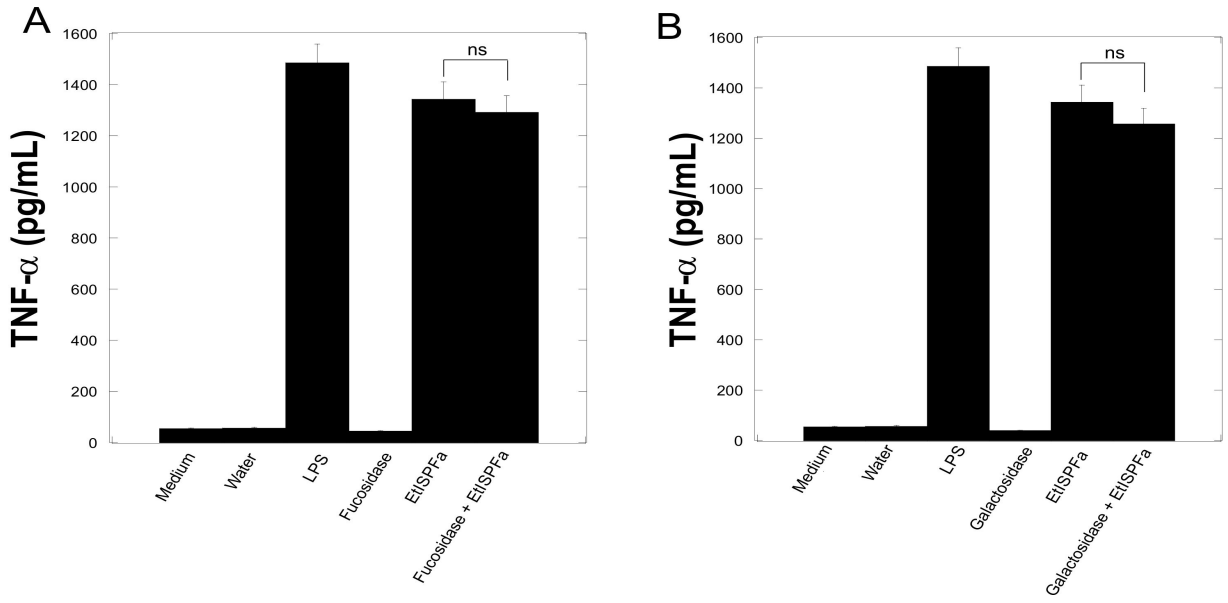

Fig. 2. 7. Effect of fucosidase (A) and galactosidase (B) on immuno-stimulatory activity of EtISPFa from *E. tinctorium*. One-way ANOVA (Tukey's test) was used for statistical analysis. Error bars represent S.D. ns represents non-significant ($p > 0.05$).

In addition to this, α-fucosidase (0.01 units) and α-galactosidase (0.1 units) had no effect on the immuno-stimulatory activity of EtISPFa (Fig. 2.7). EtISPFa does not contain any α-linked fucose or galactose (Table 2.4), which explains the unaffected immuno-stimulatory activity.

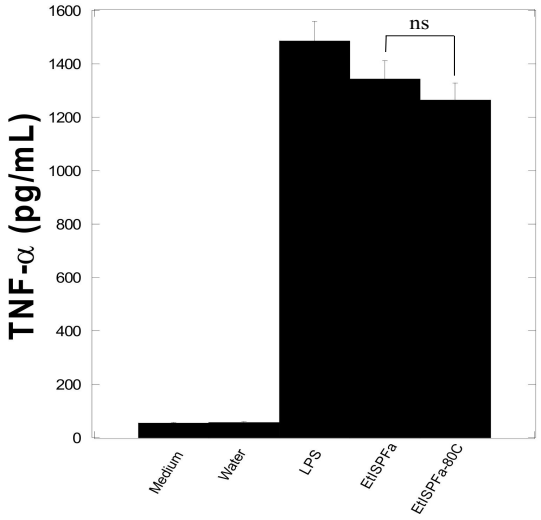

Fig. 2. 8. Effect of heat denaturation on immuno-stimulatory activity of EtISPFa from *E. tinctorium*. One-way ANOVA (Tukey's test) was used for statistical analysis. ns represents non-significant ($p > 0.05$). Error bars represent S.D.

Another important point to draw from these studies is that EtISPFa is a very stable polysaccharide. As shown in Fig. 2.8, that the immuno-stimulatory activity of EtISPFa was not abolished at high temperature.

2.3.6. Monosaccharide composition analysis

The monosaccharide analysis by TMS derivatization using GC–MS revealed that EtISPFa consisted of predominantly glucose (Glc). Relatively large amounts of glucuronic acid (GlcA), mannose (Man), and galactose (Gal) were also found in EtISPFa (Fig. S4 and Table 2.2).

Some other glycosyl residues were also found in small amounts including xylose (Xyl), rhamnose (Rha), fucose (Fuc) and arabinose (Ara). These glycosyl residues accounted for 49.2 %

of the total weight of carbohydrate. It is likely that this somewhat underestimates the actual carbohydrate due to the resistance of GlcA to acid-catalyzed depolymerization.

Table 2. 2. Monosaccharide composition of EtISPFa

Monosaccharide residue	Mass (µg)	Mol %
Glucose (Glc)	118	66.2
Glucuronic acid (GlcA)	19.4	10.1
Mannose (Man)	11.9	6.7
Galactose (Gal)	11.4	6.4
Xylose (Xyl)	8.3	5.6
Rhamnose (Rha)	5.0	3.1
Fucose (Fuc)	2.9	1.8
Arabinose (Ara)	0.4	0.2
Total =	177.2	100

*Analysis performed by Complex Carbohydrate Research Center (CCRC), University of Georgia, US.

2.3.7. Glycosyl linkage analysis by GC–MS

Consistent with the composition analysis, the glycosyl linkage analysis showed a majority of glucose linkages (61.8 %) in EtISPFa (Fig. S5 and Table 2.3). The main glucose linkages were 3-substituted, terminal, 6-substituted and 3,6-disubstituted. The linkage analysis also showed a greater proportion of glucuronic acid residues than what the composition analysis detected. The Glc:GlcA ratio was 6:1 in the composition analysis, but 3:1 in the linkage analysis. This difference is explained by the known resistance of uronic acids to acid hydrolysis or methanolysis (De Ruiter, Schols, Voragen, & Rombouts, 1992), which is required for the composition analysis. This resistance is not a factor in the linkage analysis because before hydrolysis, the glucuronic acids are reduced to glucose, which is readily hydrolyzed. According

to the composition analysis, about 10 % of the total carbohydrate is GlcA, whereas that number is slightly above 20 % in the linkage analysis. We noted the presence of fully-branched glucose (2,3,4,6-Glc*p*) and this is most likely due to undermethylation during the derivation. The proportion of this fully-branched glucose is only 2% and is considered insignificant. The presence of significant amounts of glucuronic acid in EtISPFa distinguishes it from other fungal polysaccharides, which are mostly devoid of or low in GlcA content (Wang, Wang, Xu, & Ding, 2017). Minor glycosidic linkages were from mannose, galactose, fucose, xylose, and rhamnose residues. These results suggested that EtISPFa is similar to a (1→3) (1→6)-*β*-glucan with 3-linked backbone and 6-linked side chains. However, a significant portion of the backbone 3-substituted Glc residues are replaced by 4-substituted GlcA residues. Considering only the abundances of major backbone residues in the linkage analysis, 3-Glc, 3,6-Glc, and 4-GlcA, the ratio of straight-chain to branched residues is about 4:5, indicating the presence of side chains on every 4th or 5th backbone residue. Many studies have reported the presence of *β*-1→3 and β-1→6 in immuno-stimulatory polysaccharides isolated from mushrooms. Some examples include polysaccharides from *Lentinula edodes, Sclerotium rolfsii, Dictyophora indusiata* and *Pleurotus sajor-caju* (Ferreira *et al.*, 2015). These studies relate to the presence of *β*-1→3 and β-1→6 as a structural feature that contributes to the immuno-stimulatory activity of EtISPFa.

Table 2. 3. Glycosyl linkage analysis* of EtISPFa by partially methylated alditol acetates

PMAA	**Linkage**	**Mol%[a]**
1,5-Di-*O*-acetyl-1-deuterio-6-deoxy-2,3,4-tri-*O*-methylgalactitol	t-Fuc*p*	1.1
1,2,5-Tri-*O*-acetyl-1-deuterio-6-deoxy-3,4-di-*O*-methylmannitol	2-Rha*p*	1.4
1,5-Di-*O*-acetyl-1-deuterio-2,3,4,6-tetra-*O*-methylmannitol	t-Man*p*	1.1
1,3,5-Tri-*O*-acetyl-1-deuterio-6-deoxy-2,4-di-*O*-methylmannitol	3-Rha*p*	1.8
1,5-Di-*O*-acetyl-1-deuterio-2,3,4,6-tetra-*O*-methylglucitol	t-Glc*p*	12.8
1,5-Di-*O*-acetyl-1,6,6'-trideuterio-2,3,4,6-tetra-*O*-methylglucitol	t-Glc*p*A	3.5
1,3,5-Tri-*O*-acetyl-1-deuterio-6-deoxy-2,4-di-*O*-methylgalactitol	3-Fuc*p*	1.1
1,5-Di-*O*-acetyl-1-deuterio-2,3,4,6-tetra-*O*-methylgalactitol	t-Gal*p*	1.5

1,3,5-Tri-*O*-acetyl-1-deuterio-2,4,6-tri-*O*-methylglucitol	3-Glc*p*	19.8
1,3,5- Tri-*O*-acetyl-1,6,6'-trideuterio-2,4,6-tri-*O*-methylglucitol	3-Glc*p*A	6.0
1,2,5- Tri-*O*-acetyl-1-deuterio-3,4,6-tri-*O*-methylmannitol and 1,3,5- Tri-*O*-acetyl-1-deuterio-2,4,6-tri-*O*-methylmannitol	2-Man*p* and 3-Man*p*	3.1
1,5,6- Tri-*O*-acetyl-1-deuterio-2,3,4-tri-*O*-methylmannitol	6-Man*p*	1.4
1,5,6- Tri-*O*-acetyl-1-deuterio-2,3,4-tri-*O*-methylglucitol	6-Glc*p*	10.7
1,4,5- Tri-*O*-acetyl-1-deuterio-2,3,6-tri-*O*-methylglucitol	4-Glc*p*	7.6
1,4,5- Tri-*O*-acetyl-1,6,6'-trideuterio-2,3,6-tri-*O*-methylglucitol	4-Glc*p*A	10.8
1,5,6- Tri-*O*-acetyl-1-deuterio-2,3,4-tri-*O*-methylgalactitol	6-Gal*p*	2.6
1,3,5,6- Tetra-*O*-acetyl-1-deuterio-2,4-di-*O*-methylglucitol	3,6-Glc*p*	8.7
1,2,3,4,5-Penta-*O*-acetyl-1-deuterioxylitol	2,3,4-Xyl*p*	2.7
1,2,3,4,5,6- Hexa-*O*-acetyl-1-deuterioglucitol	2,3,4,6-Glc*p*	2.2

*Analysis performed by CCRC, University of Georgia, US.

2.3.8. Structural analysis by FTIR

Functional group analysis was conducted using FTIR within the frequency range of 4000-400 cm^{-1} (Fig. 2.9). The stretches found in EtISPFa are typical for fungal polysaccharides, except for glucuronic acid which was more abundant in EtISPFa. The FTIR spectrum of EtISPFa showed a broad OH stretch at 3285 cm^{-1}, sp^3 C–H stretches at 2892 cm^{-1}, and 1036 cm^{-1} for C-O from pyranose ring. The band at 1608 cm^{-1} indicated a carbonyl C-O that might be due to glucuronic acid identified in high amounts by GC-MS analysis (Tables 2.2 and 2.3) of EtISPFa. There were some weak stretches at 875-890 cm^{-1} indicative of the presence of β-glucan that was confirmed by 2D-NMR.

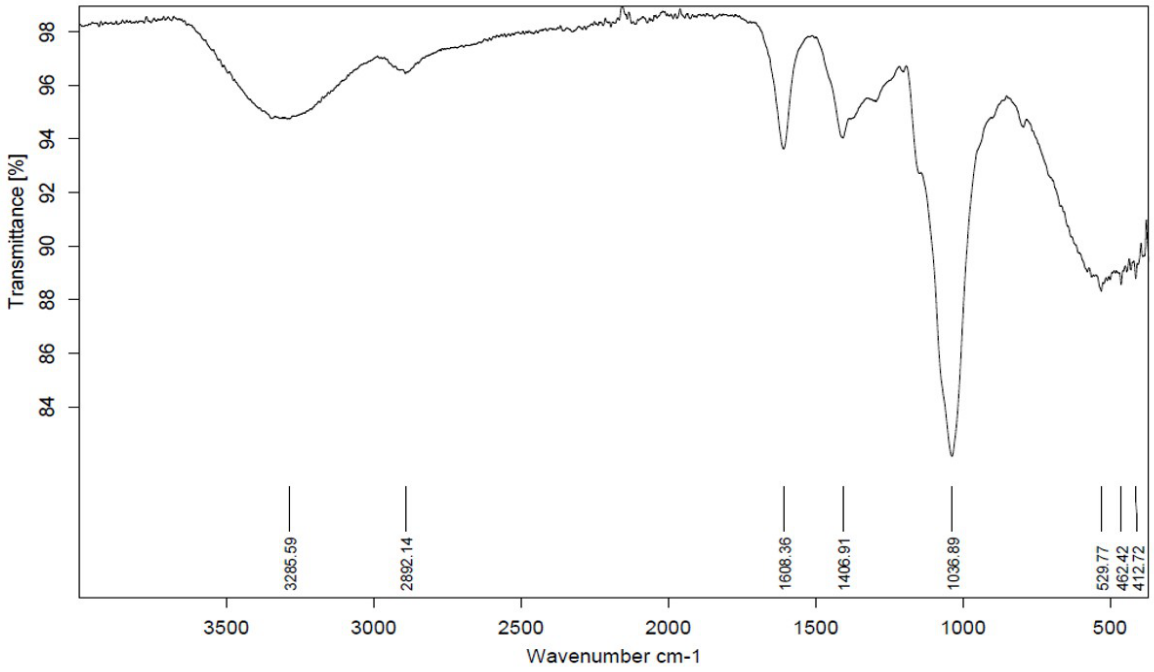

Fig. 2. 9. FTIR spectrum of EtISPFa.

2.3.9. NMR analyses of EtISPFa

For further structural analysis, 1D and 2D NMR was performed. The H-NMR (Fig. 2.10) shows the structural characteristics of a large molecular weight polysaccharide. The negative signal at 4.36 ppm originated from pre-saturation suppression of residual water. The signal at 2.218 ppm corresponded to acetone as internal reference. The peak pattern in the anomeric region between 4.5 and 5.5ppm was complicated and suggested that EtISPFa has a complex and heterogeneous structure. The majority of anomeric signals resonated below 5 ppm, suggesting that most residues were in the β-anomeric configuration. The signal around 1.3 ppm likely originated from Rha and Fuc, small amounts of which were detected in composition and linkage analysis.

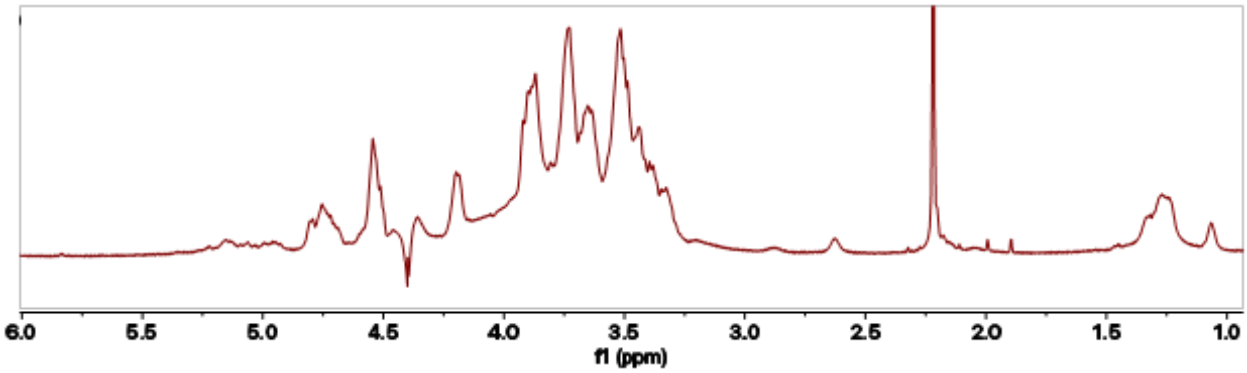

Fig. 2. 10. ^{1}H-NMR spectrum of EtISPFa.

In order to get further details on the complexity of this large polysaccharide, 2D NMR was carried out. The 2D NMR results (Figs. 2.11-2.13) were consistent with a complex, high-molecular weight *β*-glucan polysaccharide containing a significant amount of glucuronic acid. Several different *β*-glucose residues were found, mostly in 3-, 6, and 3,6-linkages and as terminal residues, as well as terminal and 4-linked *β*-glucuronic acid residues (Table 2.4). Although significant signal overlap and broad signals due to high molecular weight precluded definitive sequence determination, we were able to assign several monosaccharide residues and their linkages. The HSQC spectrum (Fig. 2.11) showed two major clusters of overlapping anomeric signals. Both of these were in the *β*-anomeric region and were further resolved in the COSY spectrum (Fig. 2.12) into about 8 residues each. The H-1 and H-2 chemical shifts indicated that all of these spin systems belonged to Glc or GlcA residues (Hu, Jiang, Huang, & Sun, 2016; Skelton, Cherniak, Poppe, & van Halbeek, 1991). Cluster I had H-1 chemical shifts between 4.8 and 4.7 ppm, and Cluster II had H-1 chemical shifts between 4.6 and 4.5 ppm. The HMBC spectrum (Fig. 2.13) clearly showed 3-bond correlations from Cluster I to carbons between 86 and 88 ppm. This downfield carbon chemical shift is characteristic of C-3 of 3-substituted Glc (Barbosa, Steluti, Dekker, Cardoso, & Da Silva, 2003), demonstrating that the residues whose anomeric protons belonged to Cluster I were attached to O-3 of their neighbors. The HMBC

spectrum also showed a strong cross peak correlating the Cluster II protons with carbons resonating between 71 and 72 ppm. The corresponding signals in the multiplicity-edited HSQC spectrum at this carbon chemical shift were from methylene groups, as attested by their negative intensity. This indicated that they originated from the secondary alcohols in the 6-position of 6-substituted Glc (Barbosa *et al.,* 2003), and further demonstrated that most of the residues belonging to Cluster II were attached to O-6 of their neighboring Glc residues. However, there was also a weaker HMBC cross peak around 84 ppm, which is indicative of C-4 of 4-substituted Glc or GlcA (Katzenellenbogen *et al.*, 1994). Hence at least one of the residues in Cluster II was attached to O-4 of its neighbor.

We were able to assign several of the residues in each of the clusters, based on the correlations found in the COSY and TOCSY spectra, along with the carbon chemical shifts read from the HSQC and HMBC spectra (Table 2.4). Thus, in Cluster I, Residue A was identified as 3,6-disubstituted β-Glc by the downfield displacement of its C-3 (87.7 ppm) and C-6 (71.7 ppm) chemical shifts (Barbosa *et al*., 2003). Residue B also had a downfield C-3 chemical shift, but its C-6 resonated at 63.7 ppm, showing that Residue B was 3-monosubstituted *β*-Glc. Residue C was found to have a downfield C-4 (83.9 ppm) and a downfield H-5 (3.90 ppm) that was correlated in HMBC to a C-6 at 177.5 ppm, consistent with 4-substituted *β*-GlcA (Katzenellenbogen *et al*., 1994). Residue D was characterized by a relatively downfield H-5 (3.75 ppm) that was correlated in HMBC to a C-6 at 177.8 ppm, indicating unsubstituted *β*-GlcA (Heiss, Klutts, Wang, Doering, & Azadi, 2009). The final residue we were able to assign in Cluster I was unsubstituted *β*-Glc (Residue E). As mentioned above, all the residues in Cluster I were attached to O-3 of their neighboring residues. Analysis was performed by CCRC.

Table 2. 4. NMR chemical shift assignments* for the residues found in EtISPFa.

No.	Residue	Chemical shift (ppm)						HMBC
		1	2	3	4	5	6	
A	3,6-β-Glc*p*-1→3	4.80	3.53	3.79	3.53	3.65	4.20/3.87	
		105.1	75.6	87.7	71.2	77.7	71.7	A/B-3
B	3-β-Glc*p*-1→3	4.80	3.53	3.74	3.53	3.51	3.91/3.74	
		105.1	75.6	87.7	71.2	78.5	63.7	A/B-3
C	4-β-Glc*p*A-1→3	4.78	3.46	3.68	3.71	3.90	-	
		105.3	75.8	77.5	83.9	78.2	177.5	A/B-3
D	β-Glc*p*A-1→3	4.75	3.44	3.54	3.64	3.75	-	
		105.5	75.9	78.5	73.1	78.7	177.8	A/B-3
E	β-Glc*p*-1→3	4.72	3.36	3.54	3.39	3.49	3.91/3.74	
		105.8	76.0	78.6	72.5	78.7	63.7	A/B-3
F	3-β-Glc*p*-1→4	4.54	3.54	3.80	3.63	3.51	3.91/3.74	
		105.3	75.8	86.4	72.3	78.5	63.7	C-4
G	6-β-Glc*p*-1→6	4.52	3.38	3.63	3.45	3.63	4.20/3.87	
		105.5	76.4	77.4	72.6	77.7	71.7	A-6
H	β-Glc*p*-1→6	4.51	3.34	3.48	3.42	3.45	3.91/3.74	
		105.6	76.0	78.5	72.6	78.7	63.7	G-6

*Analysis performed by CCRC, University of Georgia, US.

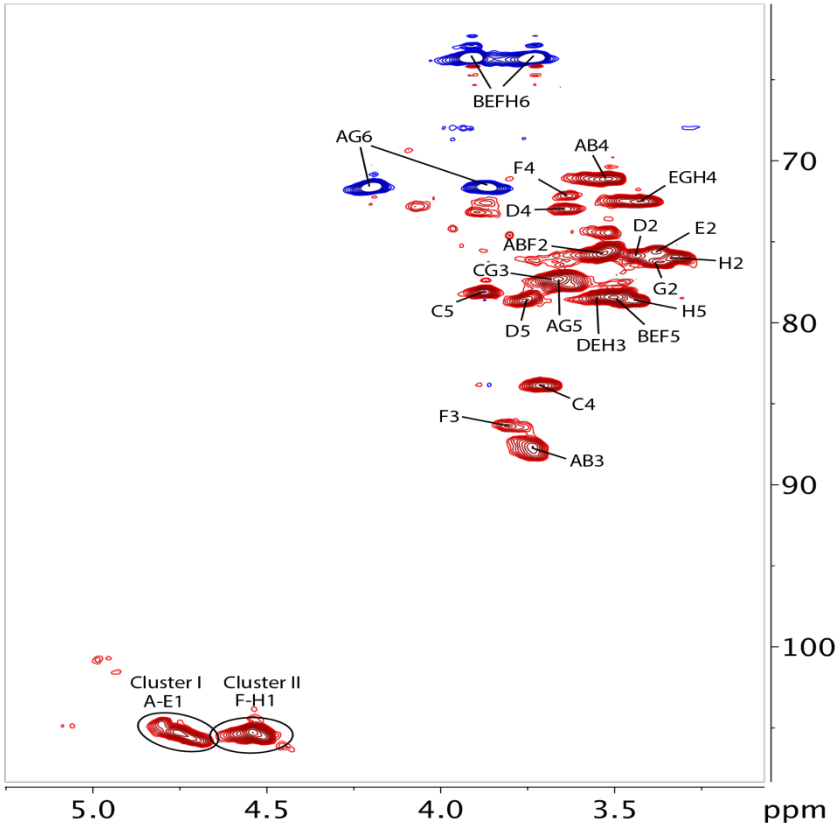

Fig. 2. 11. Partial multiplicity-edited ^{1}H-^{13}C-HSQC NMR spectrum of EtISPFa, showing anomeric Clusters I and II and peak assignment detailed in Table 2.4. Red signals are positive and correspond to CH groups, and blue signals are negative and correspond to CH_2 groups.

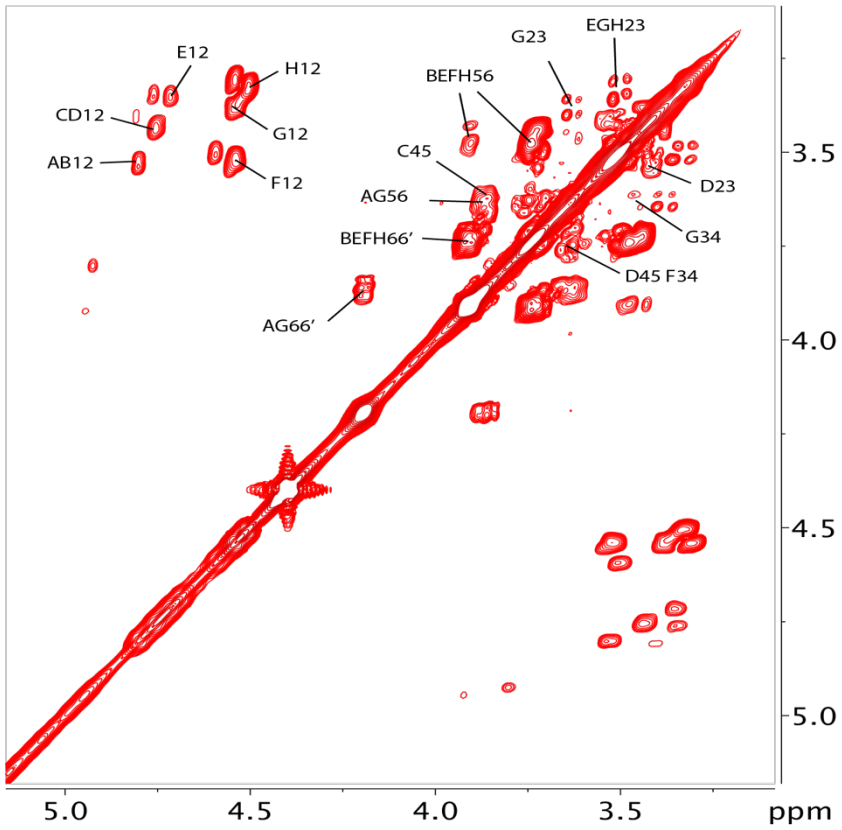

Fig. 2. 12. Partial ^{1}H-^{1}H COSY spectrum of EtISPFa.

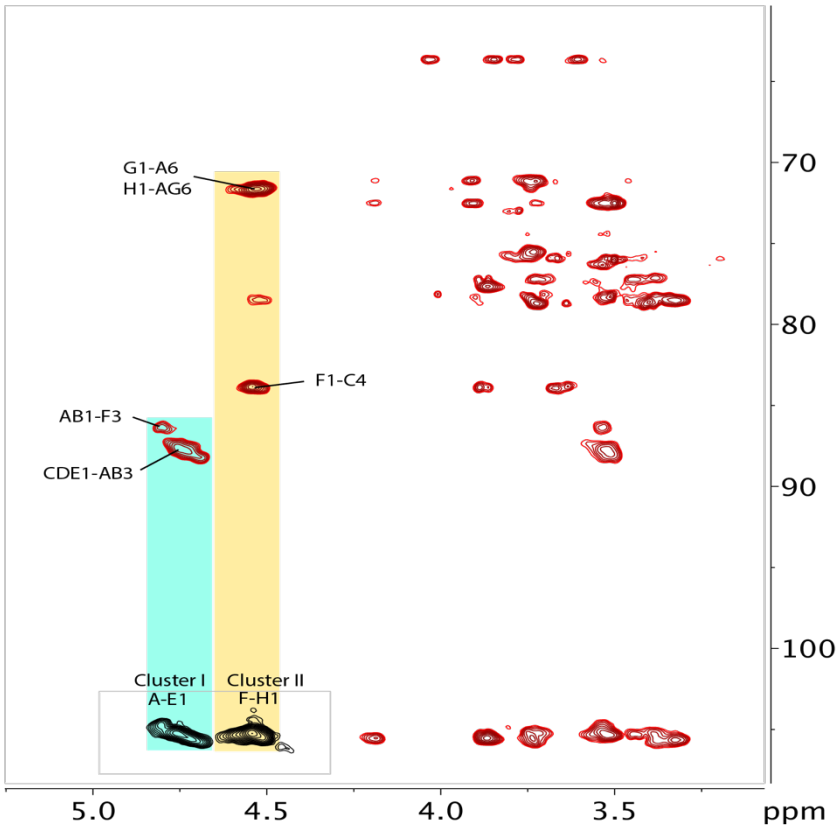

Fig. 2. 13. Partial ^{1}H-^{13}C HMBC spectrum of EtISPFa. The inset represents part of the anomeric region of the HSQC spectrum, showing Clusters I and II.

The residues in Cluster II were identified as follows: Residue F clearly showed downfield displacement of C-3 and an HMBC correlation between its C-4 at 71.2 ppm the pair of methylene protons at 3.91 and 3.74 ppm, which resonated in HSQC at 63.7 ppm, proving that Residue F was 3-substituted *β*-Glc. The HMBC correlation between its H-1 and a signal at 83.9 ppm showed that it was attached to O-4 of Residue D, a 4- substituted GlcA residue. Residue G showed an upfield H-3 chemical shift, indicating that it was not 3-O-substituted. It was not possible to directly ascertain that this residue was 6-O-substituted, but the presence of a cross peak in the HSQC-TOCSY spectrum at 4.54 ppm and 77.7 ppm, which belonged to C-5 next to a glycosylated C-6 (Lundborg & Widmalm, 2011), indicated that at least part of Cluster II

consisted of 6-substituted Glc residues. Residue H on the other hand, had a cross peak in HSQC-TOCSY at 78.7 ppm, belonging to C-5 next to unglycosylated C6, and thus Residue H was identified as terminal *β*-Glc residue substituting O-6 of its neighbor and concluded to be the terminal residue of the side chain.

In addition to the anomeric signals belonging to Clusters I and II, we observed minor anomeric peaks whose chemical shifts were consistent with α-mannose, in agreement with the presence of terminal and 6- substituted Man in the linkage analysis. However, because of their low abundance, they were not assigned further.

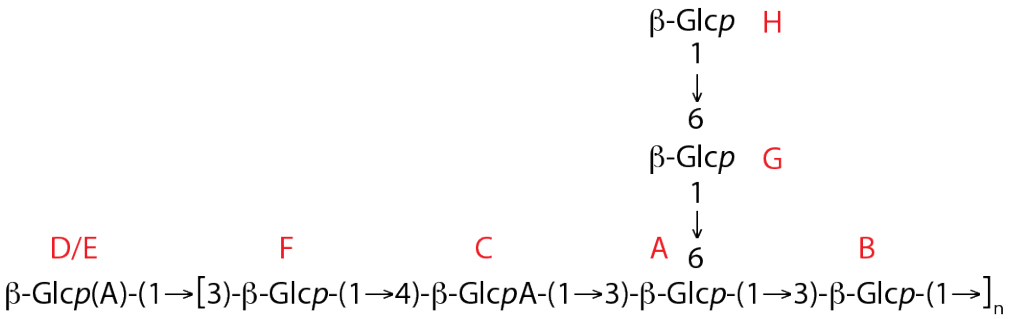

Fig. 2. 14. Proposed representative structure of the immuno-stimulatory polysaccharide EtISPFa. The labels A-G correspond to those in Table 2.4.

Based on the sugar composition, methylation analysis and NMR spectroscopy, a representative structure incorporating the chemical and spectroscopic data of EtISPFa is proposed in Fig. 2.14. This is an average structure, and the exact sequence of Glc and GlcA residues is presently unknown. For example, linkages such as 3-GlcA and 4-Glc are not accounted for in the proposed structure because we believe that it is part of the heterogeneity of the polysaccharide. To confirm the composition and linkages for a more definite structure or other possible structures, in addition to the already available data more vigorous techniques need to be used. Some of these techniques include capillary electrophoresis, matrix assisted laser

desorption ionization-time of flight-mass spectrometry (MALDI-TOF-MS) and HPLC-fluorometric/UV detection. In capillary electrophoresis, derivatized monosaccharides are separated based on their electrophoretic mobility (Guo *et al*., 2013; Volpi *et al*., 2008). For HPLC analysis, polysaccharides are hydrolyzed, derivatized with 1-phenyl-3-methyl-5-pyrazolone (PMP), separated and analyzed with fluorometric or UV detection (Harazono *et al*., 2011). For analysis on MALDI-TOF-MS, complex polysaccharides are converted to smaller oligosaccharide fragments by partial acidic or enzymatic hydrolysis. The fragments obtained after hydrolysis are separated and subjected to analysis (Xing *et al*., 2015). In addition to this, since EtISPFa contains more glucuronic acid, it is recommended that uronic acids be reduced with sodium borodeuteride first into neutral monosaccharide before carrying out methylation during GC-MS analysis.

To the best of our knowledge, the *β*–glucan structure of EtISPFa with a high amount of glucuronic acid (10–20 %) is unique. Mushroom polysaccharides containing such high amounts of glucuronic acid are rare (Ruthes, Smiderle, & Iacomini, 2016; Wang *et al*., 2017). There are two known mushroom polysaccharides that contain high amounts of glucuronic acid are PUP80S1 and PUP60S2, isolated from *Polyporus umbellatus,* a widely used mushroom in traditional Chinese medicine. PUP80S1 is an 8.8 kDa *β*–glucan containing about 8.5 % uronic acid (He, Zhang, Wang *et al.*, 2016; He, Zhang, Zhang, Linhardt, & Sun, 2016), while PUP60S2 is a 14.4 kDa *β*–glucan containing about 22.3 % uronic acid (He, Zhang, Wang *et al*., 2016; He, Zhang, Zhang *et al.*, 2016). Polysaccharides containing uronic acid, rhamnose and mannose are known to display significant anti-oxidant activity (He, Zhang, Wang *et al*., 2016; He, Zhang, Zhang *et al.*, 2016; Wang *et al*., 2017). Therefore, it would be of interest to determine whether EtISPFa possesses such biological activity.

2.4. Conclusion

This is the first description on the isolation of an immuno-stimulatory polysaccharide from *E. tinctorium*. Using Sephadex LH-20, DEAE-Sephadex, Sephacryl S-500 HR, and HPLC BioSEC-5, an immuno-stimulatory polysaccharide (EtISPFa) was successfully isolated with weight average molecular weight (M_W) of 1354 kDa from the water extract of *E. tinctorium*. EtISPFa is a complex and unique *β*-glucan polysaccharide rich in glucuronic acid (10–20 %). Besides glucose and glucuronic acid, the minor sugars present include mannose (6.7 %), galactose (6.4 %), xylose (5.6 %), rhamnose (3.1 %), fucose (1.8 %) and arabinose (0.2 %). The combined results from GC–MS and NMR analyses reveal that EtISPFa is made up mostly of a backbone consisting of *β*-(1→3)-Glc*p* residues and *β*-(1→4)-Glc*p*A residues, with branching points at *β*-(1→3, 6)-Glc*p* to which are attached short *β*-(1→6)-linked glucooligosaccharide side chains. EtISPFa also has terminal xylose, fucose, rhamnose, and arabinofuranose. Besides TNF-α, EtISPFa was found to significantly enhance IL-6, MIP-2, G-CSF, GM-CSF, LIF, MCP-1, MIP-1α, MIP-1β and RANTES in macrophage cells. Further biological characterization of EtISPFa is required to determine its mechanism of action and whether it exerts immuno-stimulatory activity in animals.

Appendix A. Supplementary data

Supplementary material related to this chapter can be found in Appendix A.

2.5. References

Barbosa, A. M., Steluti, R. M., Dekker, R. F., Cardoso, M. S., & Da Silva, M. C. (2003). Structural characterization of Botryosphaeran: a (1→ 3; 1→ 6)-β-d-glucan produced by the ascomycetous fungus, *Botryosphaeria* sp. *Carbohydrate research, 338*(16), 1691–1698.

De Ruiter, G. A., Schols, H. A., Voragen, A. G., & Rombouts, F. M. (1992). Carbohydrate analysis of water-soluble uronic acid-containing polysaccharides with high- performance anion-exchange chromatography using methanolysis combinaed with TFA hydrolysis is superior to four other methods. *Analytical biochemistry, 207*(1), 176–185.

El Enshasy, H. A., & Hatti-Kaul, R. (2013). Mushroom immunomodulators: Unique molecules with unlimited applications. *Trends in biotechnology, 31*(12), 668–677.

Ferreira, S. S., Passos, C. P., Madureira, P., Vilanova, M., & Coimbra, M. A. (2015). Structure–function relationships of immunostimulatory polysaccharides: A review. *Carbohydrate polymers*, *132*, 378-396.

Guo, H. Z., Liu, F. L., Jia, G. Y., Zhang, W. Q., & Wu, F. (2013). Extraction optimization and analysis of monosaccharide composition of fucoidan from *Saccharina japonica* by capillary zone electrophoresis. *Journal of applied psycology, 25*(6), 1903–1908.

Harazono, A., Kobayashi, T., Kawasaki, N., Itoh, S., Tada, M., Hashii, N., Yamaguchi, T. (2011). A comparative study of monosaccharide composition analysis as a carbohydrate test for biopharmaceuticals. *Biologicals, 39*(3), 171–180.

He, P.-F., Zhang, A.-Q., Wang, X.-L., Qu, L., Li, G. L., & Li, Y.-P. (2016). Structure elucidation and antioxidant activity of a novel polysaccharide from *Polyporus umbellatus* sclerotia. *International journal of biological macromolecules, 82*, 411–417.

He, P., Zhang, A., Zhang, F., Linhardt, R. J., & Sun, P. (2016). Structure and bioactivity of a polysaccharide containing uronic acid from *Polyporus umbellatus* sclerotia. *Carbohydrate polymers, 152*, 222–230.

Heiss, C., Klutts, J. S., Wang, Z., Doering, T. L., & Azadi, P. (2009). The structure of *Cryptococcus neoformans* galactoxylomannan contains β-D-glucuronic acid. *Carbohydrate research, 344*(7), 915–920.

Hu, T., Jiang, C., Huang, Q., & Sun, F. (2016). A comb-like branched β-d-glucan produced by a *Cordyceps sinensis* fungus and its protective effect against cyclophosphamide- induced immunosuppression in mice. *Carbohydrate polymers, 142*, 259–267.

Javed, S., Li, W. M., Zeb, M., Yaqoob, A., Tackaberry, L. E., Massicotte, H. B., et al. (2019). Anti-inflammatory activity of the wild mushroom, *Echinodontium tinctorium*, in RAW264. 7 macrophage cells and mouse microcirculation. *Molecules, 24*, 3509.

Katzenellenbogen, E., Romanowska, E., Shashkov, A. S., Kocharova, N. A., Knirel, Y. A., & Kochetkov, N. K. (1994). The structure of the O-specific polysaccharide of *Hafnia alvei* strain 1216. *Carbohydrate research, 259*(1), 67–76.

Lull, C., Wichers, H. J., & Savelkoul, H. F. J. (2005). Antiinflammatory and immunomodulating properties of fungal metabolites. *Mediators of inflammation, 2005*(2), 63–80.

Lundborg, M., & Widmalm, G. (2011). Structural analysis of glycans by NMR chemical shift prediction. *Analytical chemistry, 83*(5), 1514–1517.

Rowan, N. J., Smith, J. E., & Sullivan, R. (2003). Immunomodulatory activities of mushroom glucans and polysaccharide-protein complexes in animals and humans (a review). *International journal of medicinal mushrooms, 5*(2), 1–16.

Ruthes, A. C., Smiderle, F. R., & Iacomini, M. (2016). Mushroom heteropolysaccharides: A review on their sources, structure and biological effects. *Carbohydrate polymers, 136*, 358–375.

Skelton, M. A., Cherniak, R., Poppe, L., & van Halbeek, H. (1991). Structure of the De-O-acetylated glucuronoxylomannan from *Cryptococcus neoformans* serotype D, as determined by 2D NMR spectroscopy. *Magnetic resonance in chemistry, 29*(8), 786–793.

Smith, A., Javed, S., Barad, A., Myhre, V., Li, W. M., Reimer, K., et al. (2017). Growth-inhibitory and immunomodulatory activities of wild mushrooms from north-central British Columbia (Canada). *International journal of medicinal mushrooms, 19*(6), 485–497.

Volpi, N., Maccari, F., & Linhardt, R. J. (2008). Capillary electrophoresis of complex natural polysaccharides. *Electrophoresis, 29*(15), 3095–3106.

Wang, Q., Wang, F., Xu, Z., & Ding, Z. (2017). Bioactive mushroom polysaccharides: A review on monosaccharide composition, biosynthesis and regulation. *Molecules, 22*, 955.

Xing, X., Cui, S. W., Nie, S., Phillips, G. O., Goff, H. D., & Wang, Q. (2015). Study on *Dendrobium officinale O*-acetyl-glucomannan (Dendronan®): Part V. Fractionation and structural heterogeneity of different fractions. *Bioactive carbohydrates and dietary fibre, 5*(2), 106–115

Appendix A. Supplementary data

DEAE-Sephadex Optimization

Multiple buffers including piperazine (pH 5.3 and 9.73), bis-Tris (pH 6.4), propane (pH 6.8), Tris (pH 8.1), and L-Histidine (pH 6.2) were first assessed to determine the optimum buffer for use in the purification. For the optimum buffer, the bioactive compound should retain its activity whether it binds or does not bind to the resin. If it does not bind, it would be present in the flow-through. On the other hand, if it binds to the resin, then it would be eluted (present in elution buffer) by an increasing concentration of salt. For most of the buffers except L-Histidine, the bioactivity was present in both the flow-through and eluent and, for some, the bioactivity was lower than the preload. When using L-Histidine (pH 6.2) as buffer as shown in Fig. 3B, the bioactive compound was bound to DEAE-Sephadex resin and was then eluted by high salt concentration (1 M NaCl). In addition, the bioactivity was fully retained in the eluent. Therefore, L-Histidine (pH 6.2) was selected as the buffer of choice.

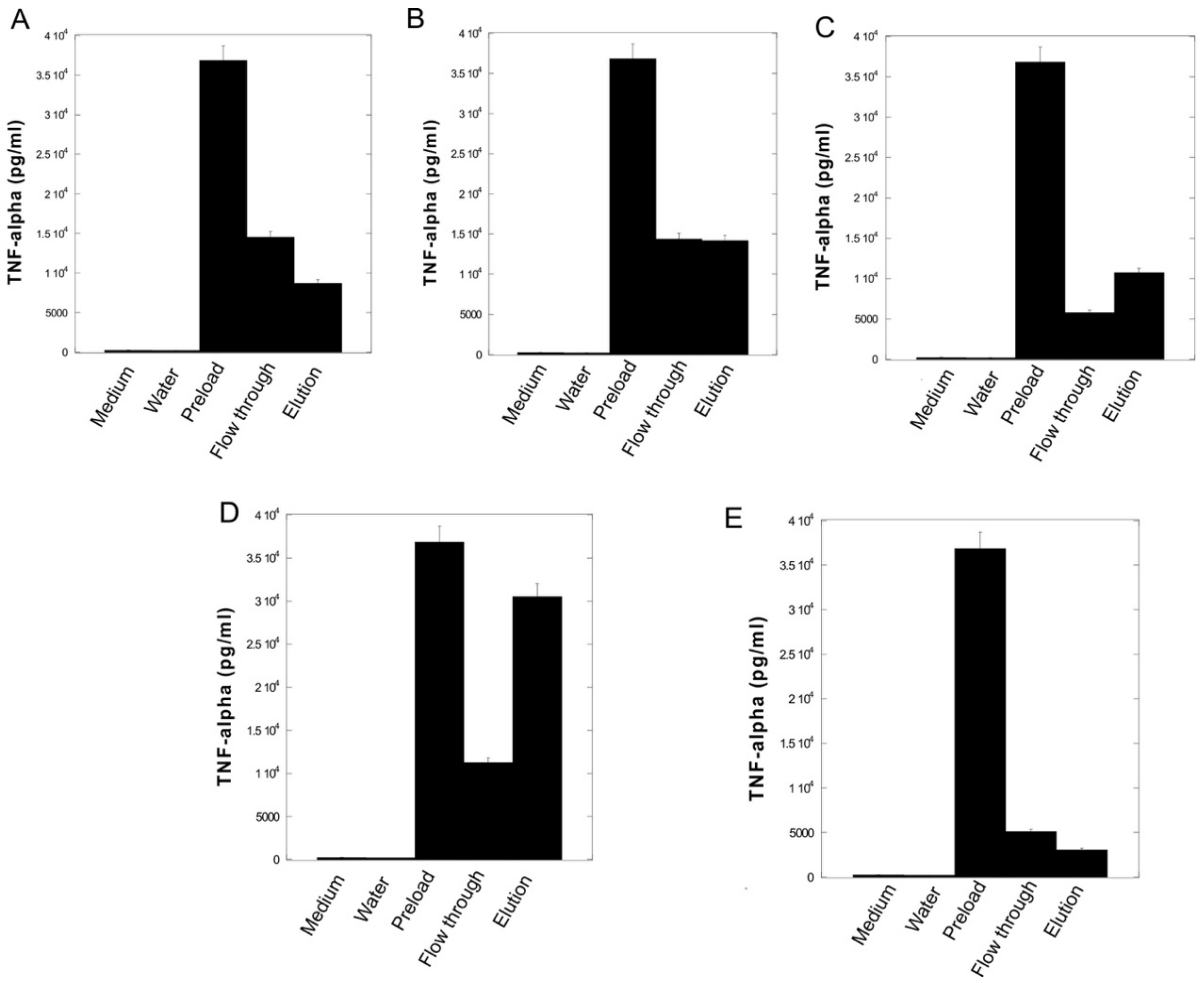

Fig. S 1. Optimization of conditions for anion exchange chromatography using multiple buffers. TNF-α stimulation by 2A using bis-Tris at pH= 6.4 (A), Tris at pH= 8.1 (B), propane 1,2-Di-amino buffer at pH= 6.8 (C), piperazine at pH= 5.33 (D), and piperazine at pH= 9.73 (E). Preload, flow through and elution were assessed for immuno-stimulatory activity. Medium and water were used as negative controls. Error bars represent S.D.

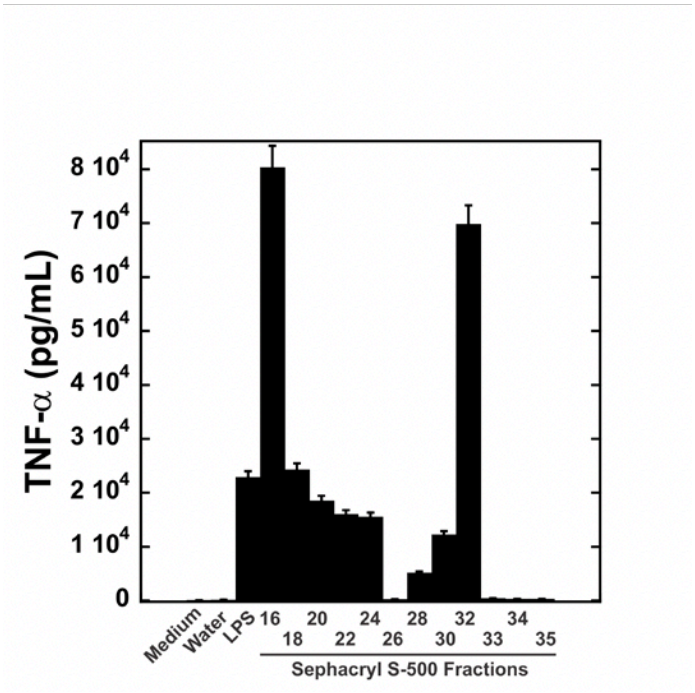

Fig. S 2. Purification of the immuno-stimulatory polysaccharide from *E. tinctorium* (EtISPFa) using Sephacryl S-500 size exclusion chromatography. Fractions collected were assessed for immuno-stimulatory activity. Medium and water were used as negative controls. LPS was used as positive control.

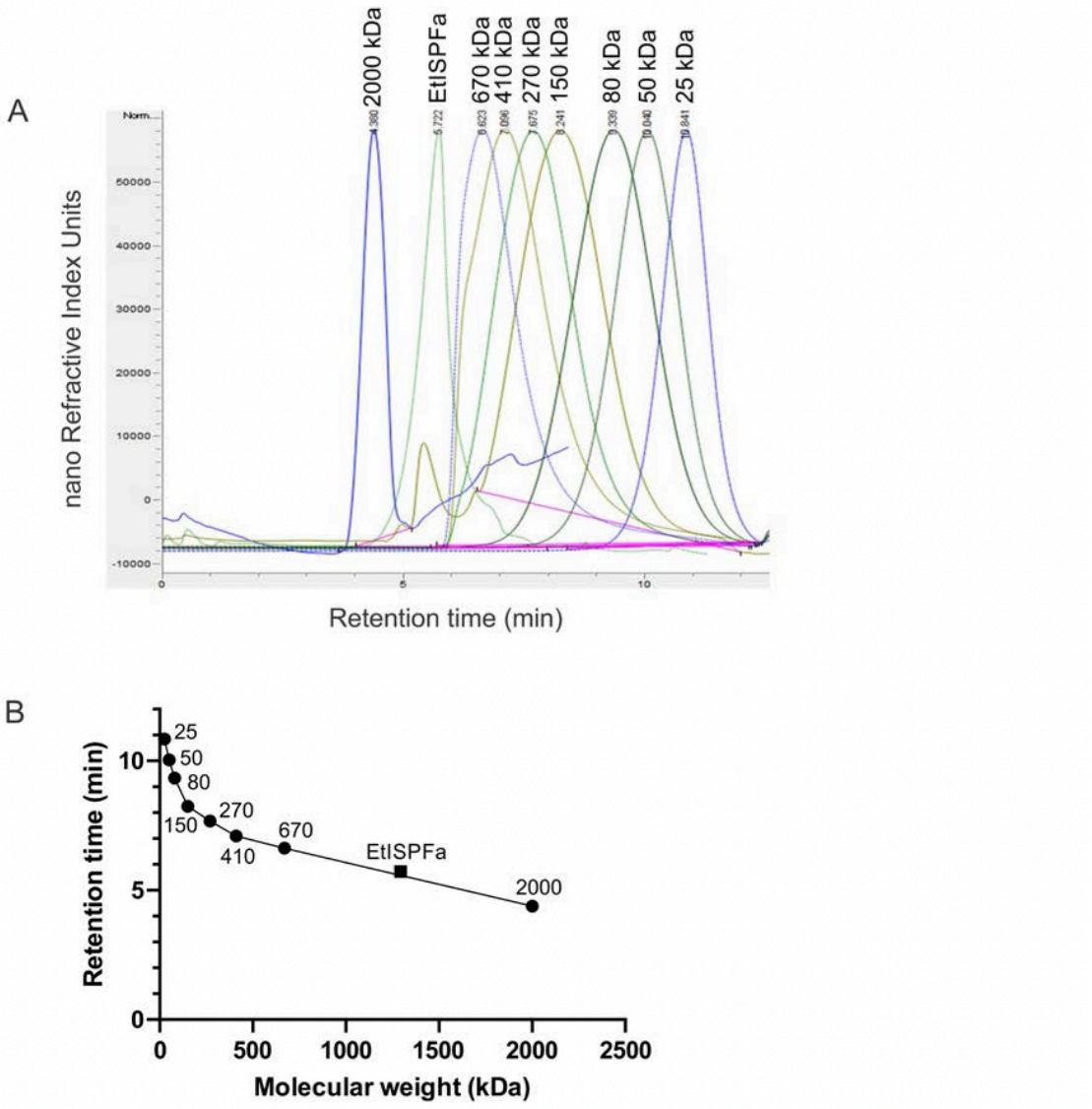

Fig. S 3. Estimating the peak maxima molecular weight (Mp) of EtISPFa using HPLC BioSEC-5. (A) Overlay spectra of dextran standards (25-2000 kDa) with EtISPFa. Samples were run in water at a flowrate of 0.4 mL/min. RID detector was used. (B) Retention times (min) of dextran standards were plotted against their molecular weight (kDa).

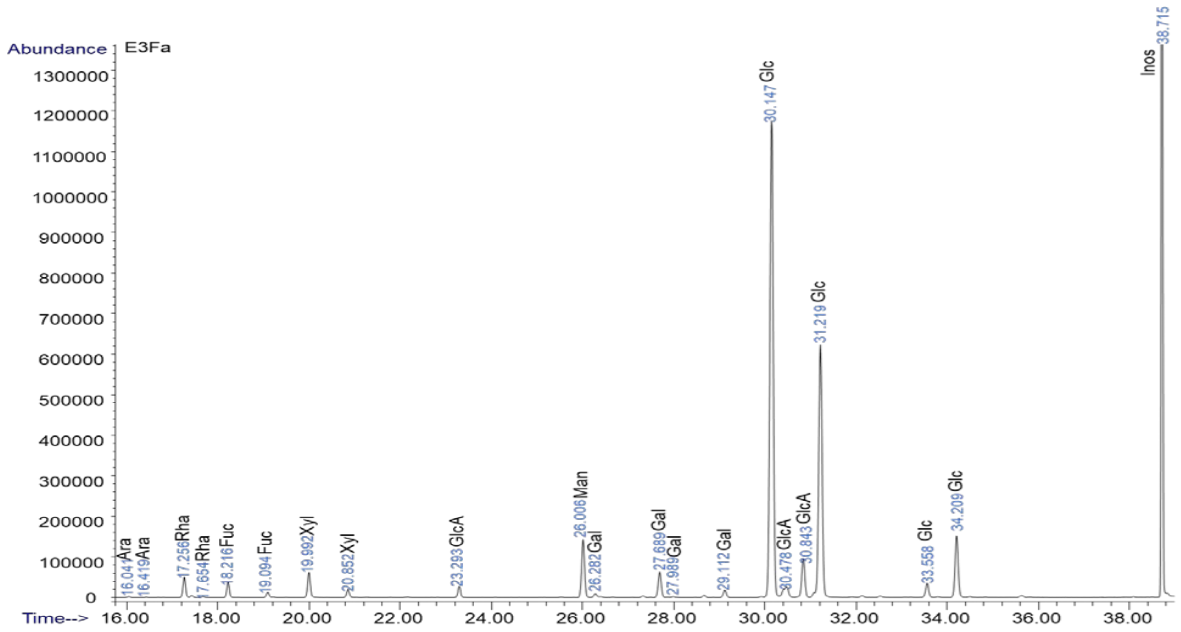

Fig. S 4. The GC-MS chromatograms from glycosyl composition analysis using TMS derivatization.

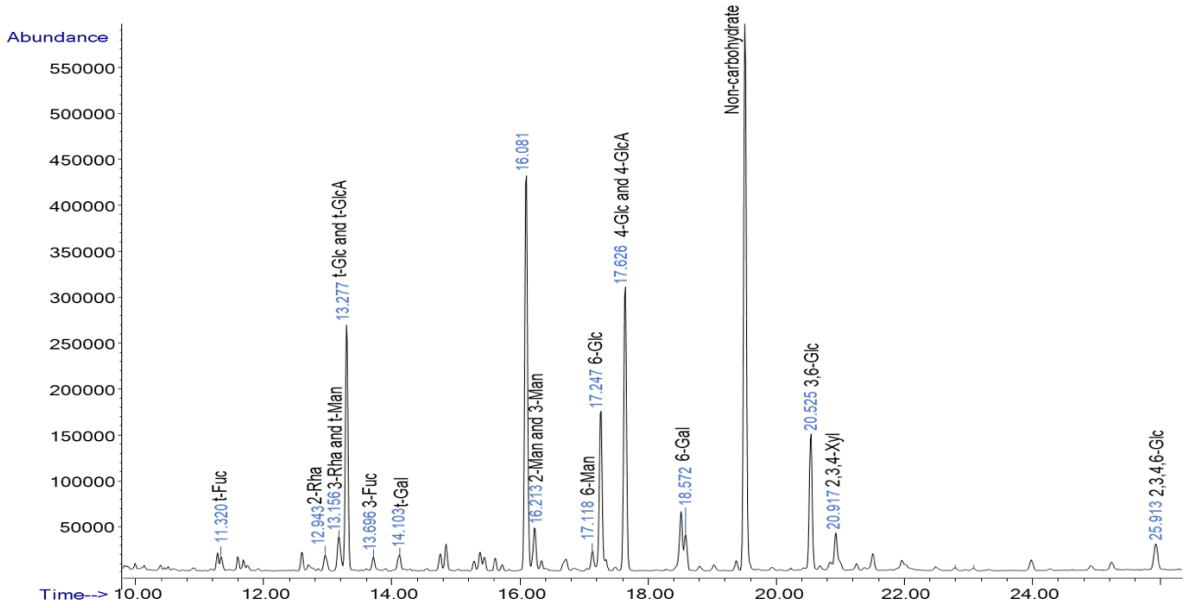

Fig. S 5. GC-MS chromatogram resulting from glycosyl linkage analysis of neutral and uronic acid residues. Glycosyl linkage analysis was performed by partially methylated alditol acetates (PMAAs).

Table S 1. Calculating the number (Mn) and weight average molecular weight (Mw) of EtISPFa

Concentration (g)	Rt (min)	MW (kDa)	MW or Mi (g/mol)	Moles	ni	niMi	wi	wiMi
0.00002	4.5	1737.397	1737397.2	1.1511E-11	6.93221E+12	1.2044E+19	0.090043621	156441.5393
0.00002	4.7	1664.833	1664833.5	1.2013E-11	7.23436E+12	1.2044E+19	0.090043621	149907.6425
0.00002	4.9	1592.269	1592269.8	1.2561E-11	7.56404E+12	1.2044E+19	0.090043621	143373.7457
0.00002	5.1	1519.706	1519706.1	1.316E-11	7.92522E+12	1.2044E+19	0.090043621	136839.849
0.00002	5.3	1447.142	1447142.5	1.382E-11	8.32261E+12	1.2044E+19	0.090043621	130305.9522
0.00002	5.5	1374.578	1374578.8	1.455E-11	8.76196E+12	1.2044E+19	0.090043621	123772.0554
0.00002	5.7	1302.015	1302015.1	1.5361E-11	9.25028E+12	1.2044E+19	0.090043621	117238.1586
0.00002	5.9	1229.451	1229451.4	1.6267E-11	8.76196E+12	1.07724E+19	0.080536859	99016.15954
0.00002	6.1	1156.887	1156887.7	1.7288E-11	8.32261E+12	9.62832E+18	0.071983488	83276.81712
0.00002	6.3	1084.324	1084324.0	1.8445E-11	7.92522E+12	8.5935E+18	0.064246937	69664.50198
0.00002	6.5	1011.760	1011760.4	1.9768E-11	7.56404E+12	7.653E+18	0.057215534	57888.41242
0.00002	6.7	939.196	939196.7	2.1295E-11	7.23436E+12	6.79448E+18	0.050797075	47708.44643
0.00002	6.9	866.633	866633.0	2.3078E-11	6.93221E+12	6.00768E+18	0.044914759	38924.61416
					∑=1.02731E+14	1.33757E+20		1354357.894

Molecular weight peak maxima (M_p) = 1302015 g/mol.

Weight average molecular weight (M_w) = 1354357 g/mol.

Number average molecular weight (M_n) = 1302015 g/mol. ($M_n = \Sigma niMi/\Sigma ni$)

Polydispersity index = 1.04 ($PDI = M_w/M_n$)

Table S 2. Quantitative estimation of material recovered from each purification step

Processing step	**Starting material**	**Amount obtained**	**% Yield**
Aqueous extract (E3)	300 g	3.7 g	1.2 %
Sephadex LH-20 SEC			
25 mL column	8.8 mg	4 mg	45 %
85 mL column	63 mg	12.8 mg	20 %
400-500 mL column	250 mg	50 mg	20 %
Sephadex DEAE AEC			
70 mL column	18 mg	6.8 mg	37 %
100 mL column	27 mg	8 mg	29 %
150 mL column	40 mg	13.7 mg	34 %
400 mL column	100 mg	30 mg	30 %
800-1000 mL column	400 mg	120 mg	30 %
	500 mg	150 mg	30 %
	650 mg	171 mg	26 %
Sephacryl S500 HR SEC (5x)	100 mg	12 mg	12 %
HPLC BioSEC-5 (100-120)	60-70 mg	3 mg	5 %

Chapter 3: Structural elucidation of an anti-proliferative polysaccharide from the fungus *Echinodontium tinctorium*

ABSTRACT

An anti-proliferative polysaccharide (EtGIPL1a) was isolated from methanol extract of the fungus *Echinodontium tinctorium*. EtGIPL1a has an estimated weight average molecular weight of 275 kDa and is composed of glucose (54.3%), galactose (19.6%), mannose (11.1%), fucose (10.3%), glucuronic acid (4%) and rhamnose (0.6%). It has multiple glycosidic linkages, with 3-Glc*p* (28.9 %), 6-Glc*p* (18.3 %), 3,6-Glc*p* (13 %), 4-Glc*p*A (9.2 %), 6-Gal*p* (3.9 %), 2,6-Gal*p* (2.6 %), 3-Fuc*p* (2.5 %), 6-Man*p* (2.4 %) being the most prominent, and unsubstituted glucose (15.3 %), mannose (1.3 %) and fucose (0.9 %) as major terminal sugars. NMR analysis showed that EtGIPL1a has a backbone containing mostly 3-substituted β-glucopyranose with 4-substituted glucopyranosyluronic acid. EtGIPL1a showed anti-proliferative activity against multiple cancer cell lines with IC_{50} ranging from 50.6-1446 nM. EtGIPL1a induced apoptosis in U251 glioblastoma cells and caused $subG_0$ phase arrest with significant DNA fragmentation.

3.1. Introduction

It is believed that structural complexity of polysaccharides contributes to its bioactive potential. Medicinal mushrooms have demonstrated anti-proliferative effects from multiple studies (Barad *et al*., 2018; Blagodatski *et al*., 2018; Shnyreva, Shnyreva, Espinoza, Padrón, & Trigos, 2018; Panda *et al*., 2020; Souilem *et al*., 2017; Yaqoob *et al*., 2020; Zeb & Lee, 2021). Fungal polysaccharides have been shown to possess diverse bioactivities and have been studied extensively, especially from known medicinal and edible mushrooms (Ferreira *et al*., 2015; He *et al*., 2020; Venturella, Ferraro, Cirlincione, & Gargano, 2021). Examples include lentinan from *Lentinula edodes* (Dubey *et al*., 2019), schizophyllan from *Schizophyllum commune* (Zhong *et*

al., 2015), Maitake D-fraction from *Maitake* (Zhuang, & Wasser, 2004), polysaccharide K (PSK or Krestin) from *Coriolus versicolor* (Blagodatski *et al*., 2018), ganoderan from *Ganoderma lucidum* (Wang, Gou, Xue, & Liu, 2019), and pleuran from *Pleurotus* species (Urbancikova *et al*., 2020); all have been shown to possess anti-cancer activity. To this end, extensive investigations have been conducted on the chemistry of fungal polysaccharides in relation to their bioactivities (Wang, Wang, Xu, & Ding, 2017). Studies have shown that fungal polysaccharides are structurally complex molecules due to their monosaccharide distribution, degree of branching, large molecular size and complex linkages. Based on their monosaccharide content, they can be homo- or heteropolysaccharide with respective bioactivities. For example, homopolysaccharide from *Agaricus bisporus* (Pires *et al.,* 2017), *Lentinula edodes* (Ya, 2017), *Pleurotus eryngii* (Ma *et al*. 2014), and *Ganoderma lucidum* (Yang, Yang, Zhuang, Qian, & Shen, 2016) have shown anti-proliferative effects. Heteropolysaccharide from *Lentinula edodes* (Wang *et al*., 2017), *Pleurotus eryngii* (Ren, Wang, Guo, Yuan, & Yang, 2016), and *Flammulina velutipes* (Chen *et al*., 2018) have also shown anti-proliferative potential. An anti-inflammatory and immuno-stimulatory polysaccharide from *E. tinctorium* has already been isolated (Javed *et al*., 2019; Zeb *et al*., 2021), but its potential anti-proliferative role against cancer cells has yet to be explored.

The aim of the present study was to purify and characterize an anti-proliferative polysaccharide from *E. tinctorium*. As in previous studies, *E. tinctorium* was sequentially extracted using 80% ethanol followed by 50% methanol. The methanol extract was phase separated and assessed for anti-proliferative activity using the cytotoxic MTT assay. Our results indeed showed that the methanol extract of *E. tinctorium* has anti-proliferative activity against HeLa human cervical cancer cells. The methanol extract from *E. tinctorium* was subjected to

multiple chromatographic steps (Sephadex LH-20, DEAE-Sephadex, Sephacryl S-500 HR, and HPLC BioSEC-3 chromatography) for purification of the anti-proliferative compound. Structural analyses were performed which included gas chromatography-flame ionization detector (GC-FID) to determine monosaccharides content, gas chromatography-mass spectrometry (GC-MS) to determine the glycosidic linkages, Fourier transform infrared (FTIR) spectroscopy for identification of functional groups, and finally, NMR analyses to determine the constitution and monosaccharide sequence of the EtGIPL1a polysaccharide. Growth-inhibitory effect of EtGIPL1a was assessed on multiple cancer cell lines and details on mechanism of induction of apoptosis in U251 glioblastoma cells was explored.

3.2. Materials and methods

3.2.1. Materials, reagents and cell lines

All the reagents were of analytical grade. Eagle's Minimal Essential Medium was from LONZA (Walkersville, Maryland, USA). 3-(4,5-dimethylthiazol-2-yl)-2-5 diphenyltetrazolium bromide (MTT), dimethylsulfoxide (DMSO) and the dextran standards (T1, T5, T12, T25, T50, T80, T150, T270, T410) were obtained from Sigma-Aldrich (St. Louis, MO, USA). Fetal bovine serum (FBS) was from Life Technologies Inc. (Waltham, Massachusetts, USA). Sephadex™ LH-20 resin, DEAE-Sephadex, and HiPrep 26/60 Sephacryl™ S-500 HR pre-packed columns were purchased from GE Healthcare (Chicago, IL, USA). HPLC BioSEC-3 column and guard column were purchased from Agilent (Santa Clara, CA, USA). All cell lines were obtained from American Type Culture Collection. All cells were maintained in Eagle's Minimal Essential Medium except Panc-1 which was maintained in Dulbecco's Modified Eagle Medium (LONZA).

3.2.2. Collection and extraction of the mushroom

E. tinctorium conks were collected from hemlock trees (*Tsuga heterophylla*) in Terrace (CL103) and Smithers (CL37), BC, Canada, in August 2014 and 2015, respectively. Voucher specimens for these collections were deposited at the University of Northern British Columbia, Canada. The specimens, previously confirmed using morphological and molecular techniques (Javed *et al.,* 2019), were dried in a hot air oven (55 ºC, 24-48 h), cut into smaller pieces using a saw machine, and ground to fine powder using a hammer mill. Powdered mushrooms (300 g) were sequentially extracted with 80% ethanol (1.5 L, 65 ºC, 3 h). The extract was vacuum filtered through Whatman filter paper No. 3 and the filtrate was designated 1A. The residue was further extracted with 50% methanol (1.5 L, 65 ºC, 3 h). The methanol extract was filtered and the filtrate was designated 1B. Crude extract 1B was concentrated, lyophilized, and filter sterilized before assessment for anti-proliferative activity.

3.2.3. Anti-proliferative assay

Anti-proliferative activity of 1B was assessed by % cell viability using the cytotoxic MTT assay. HeLa cells were plated (96 well, 1.5 x 10^4 cells/well), and after 22-24 h, cells were treated with crude methanol extract (1B) and phase separated aqueous layer (L1) for 48 h at concentrations ranging from 0.1-1 mg/mL. Cells were observed for morphological changes under a microscope and incubated with 50 µL of MTT solution (3 h, 37°C). Medium was then removed from the wells and 150 µl DMSO was added and incubated for another 5 min. Different purple color intensities of formazan were observed, indicative of dose-dependent anti-proliferative response. Formazan purple color was quantified by determining the absorbance of samples at 570 nm using Bio-Tek's Synergy-2 multi-plate reader. The purified polysaccharide EtGIPL1a was assessed against multiple cancer cell lines including HeLa, SW-480, U87, U251, DU145,

HCT116, Panc-1, MD-MB-231, MCF-7, and SKOV-3. Cell viability was assessed using MTT assay as described above.

3.2.4. Purification of anti-proliferative polysaccharide from *E. tinctorium*

Phase separation was performed by dissolving 500 mg of 1B in water and partitioning with chloroform, that resulted in two distinct layers: aqueous (L1) and organic (L2). L1 was then subjected to a 100 mL Sephadex LH-20 designated column-1 (80 mg L1,1 mL/min, 3 mL fraction size, 2 CV). Collected fractions containing anti-proliferative activity were pooled, lyophilized and subjected to DEAE-Sephadex (designated column-2) using L-Histidine as the running buffer (pH = 5.7-6.4). The column was first equilibrated (L-Histidine buffer, 2 CV, 1 mL/min), followed by sample application (500 mg). Initially, L-Histidine buffer (2 CV) was allowed to run through the column to obtain flow-through (FT). Elution buffer (1 M NaCl in L-Histidine buffer, 2.5 CV) was added and eluent was collected. The FT and eluent were concentrated, dialyzed (MWCO 3500 kDa), lyophilized, filter sterilized and tested for anti-proliferative activity. The bioactive eluent 2A from DEAE-Sephadex was then subjected to Sephacryl S-500 HR SEC designated as column-3. Column-3 was equilibrated (4 CV, 150 mM NaCl, 1.3 mL/min) and injected with 100 mg 2A (2 mL sample loop). Fractions collected (10 ml fraction size, 2.5 CV) were assessed for anti-proliferative activity, carbohydrate (phenol-sulfuric acid method) and protein contents (BCA protein assay, Waltham, MA, USA). The bioactive fractions from column-3 were pooled, dialyzed, lyophilized and designated as L1a.

3.2.5. Molecular size distribution and ultrapurification using HPLC

L1a was subjected to HPLC size-exclusion chromatography for purification and molecular size estimation. The molecular size was estimated by running standard T-series Dextrans. Initially, the HPLC BioSEC-3 column (designated column-4) (Agilent BioSEC-3, 3 μm, 100 A,

7.8 × 300 mm, Guard column Agilent BioSEC-3, 3 µm, 100 A, 7.8 × 50 mm) was equilibrated and then L1a was injected (5-10 uL, 1.2 mL/min, Water) through an autosampler. A Refractive Index Detector (RID) was used for analysis. The HPLC profile for L1a showed two peaks retained at 5.835 and 7.941 mins. These peaks were fraction collected (300-400 runs), lyophilized, and assessed for anti-proliferative activity. The bioactive Peak 1 was subsequently named EtGIPL1a.

3.2.6. Monosaccharide composition analysis

Monosaccharide content of EtGIPL1a was determined by GC-MS. EtGIPFa (330 µg) and internal standard inositol (20 µg) were hydrolyzed, acetylated and derivatized using the same approach as previously described (Zeb *et al*., 2021). The TMS methyl glycoside derivatives were analyzed by GC-MS (Agilent 7890A GC, 5975C MSD) using a Supelco Equity-1 fused silica capillary column (30 m × 0.25 mm ID).

3.2.7. Methylation and linkage analysis

Glycosyl linkage analysis was conducted as previously described (Zeb *et al*., 2021). One mg of EtGIPL1a was suspended in 200 µL of DMSO, stirred, permethylated, hydrolyzed, reduced and acetylated to yield partially methylated alditol acetates (PMAAs). The PMAAs were then analyzed on an Agilent 7890A GC connected to a 5975C MSD (EI ionization source) using a 30 m Supelco SP-2331 bonded phase fused silica capillary column.

3.2.8. Structural elucidation by spectral analysis

EtGIPL1a was subjected to functional group analysis by FTIR (Bruker ATR-FTIR spectrophotometer, Billerica, MA, USA) with a detection wave range of 4000-400 cm^{-1}. Twenty two scans were obtained and an IR spectrum was generated using OPUS software.

For further structural analysis, NMR was conducted as previously described (Zeb *et al*., 2021). 1D proton NMR (H^1-NMR) and 2D NMR including ^1H-^1H-correlation spectroscopy (COSY), total correlation spectroscopy (TOCSY), nuclear Overhauser effect spectroscopy (NOESY), ^1H-^{13}C-NMR heteronuclear single quantum correlation spectroscopy (HSQC), HSQC-TOCSY, and heteronuclear multiple bond correlation (HMBC) were carried out on an Agilent Inova 600 MHz NMR.

3.2.9. Growth-inhibition in U251 glioblastoma cells

EtGIPL1a was tested for growth inhibition in U251 cells through MTT assay as mentioned in section 2.3. Morphological changes induced by EtGIPL1a were observed at different doses and time intervals under a microscope. In order to further confirm whether the changes were due to differentiation, western blot was carried out and the expression levels of glial fibrillary acidic protein (GFAP) differentiation marker as well as vimentin were determined. For first two biological replicates, cells were plated at a density of 30 x 10^4 cells/well and 50 x 10^4 cells/well for biological replicate 3, incubated overnight and treated at 12.5 µg/mL and 6.25 µg/mL of EtGIPL1a for 48 h. Cell lysates were collected and protein content was estimated. For immunoblot analysis, 15 ug of protein (21 ug for biological replicate 3) was loaded and resolved on 13.3 % of SDS-PAGE gel (200 V, 15 min) and transferred to a nitrocellulose membrane (100 V, 1 h, 4ºC). The protein was blocked with skim milk (5% w/v, 1 h, RT), incubated overnight with primary antibody (1:1000), washed, and incubated with secondary antibody (1:2000, 1 h, RT); it was then imaged with Pico ECL solution and visualized with the FluorChem Q system (ProteinSimple, CA, USA) alongwith AlphaView Q software (ProteinSimple). The primary antibodies that were used include vimentin (1:1000), GFAP (1:1000), LC3B (1:1000), and cleave

caspase 3 (1:1000) whereas the secondary antibodes included thioredoxin (1:2000) and GAPDH (1:2000).

3.2.10. Flow cytometry analysis

Flow cytometry analysis was conducted on SW480 and U251 cells. SW480 cells were plated at a density of 5 x 10^5 cells/well in a 6-well plate; after 24 h, cells were treated with 0.4 mg/mL of filter-sterilized EtGIPL1a for 48 h. In contrast, U251 cells were plated at a density of 20 x 10^4 cells/well and treated with 27nM of EtGIPL1a. Water was used as a negative control. After 48 h of treatment, cells were observed for any changes in morphology. Each well treated with sample and control was trypsinized, centrifuged, and washed with PBS twice. Live cells were then double stained with PE Annexin-V and 7-AAD supplied with the Apoptosis detection kit I (BD Pharmingen), kept in dark and filtered into a sieve cap glass test tube. Stained cells were then analyzed by BD FACSMelody cell sorter flow cytometer (BD Biosciences) using BD FACSChorus software (V 1.0).

For apoptosis, a total of 10,000 events were recorded for each sample. The percentage of viable and apoptotic cells was calculated from FACS Chorus version 1.0 (Becton Dickinson & Company, USA). For cell cycle analysis, a total of 40,000 events were recorded for each sample. The percentage of cells residing in each G1, S and G2/M phase of cell cycle were calculated from Flowjo software version 10.7.2 (Becton Dickinson & Company, USA).

3.3. Results and Discussion

3.3.1. Extraction and assessment of methanolic extract from *E. tinctorium* for anti-proliferative activity

The powdered *E. tinctorium* was sequentially extracted using the following solvents: 80 % ethanol, 50 % methanol, water and 5 % sodium hydroxide. We found that only the 50 %

methanol extracts exhibited anti-proliferative activity against HeLa human cervical cancer cells (Smith, 2017). Therefore, I aimed to purify, identify and characterize the anti-proliferative compound(s) from *E. tinctorium*. Fig. 3.1A summarizes the scheme taken to obtain the methanolic extract 1B which was then subjected to chloroform extraction. The aqueous phase L1 obtained, as well as the crude methanol extract 1B were lyophilized and assessed for anti-proliferative activity. As shown in Fig. 3.1B, both 1B and L1 displayed dose-dependent anti-proliferative effect on HeLa cells.

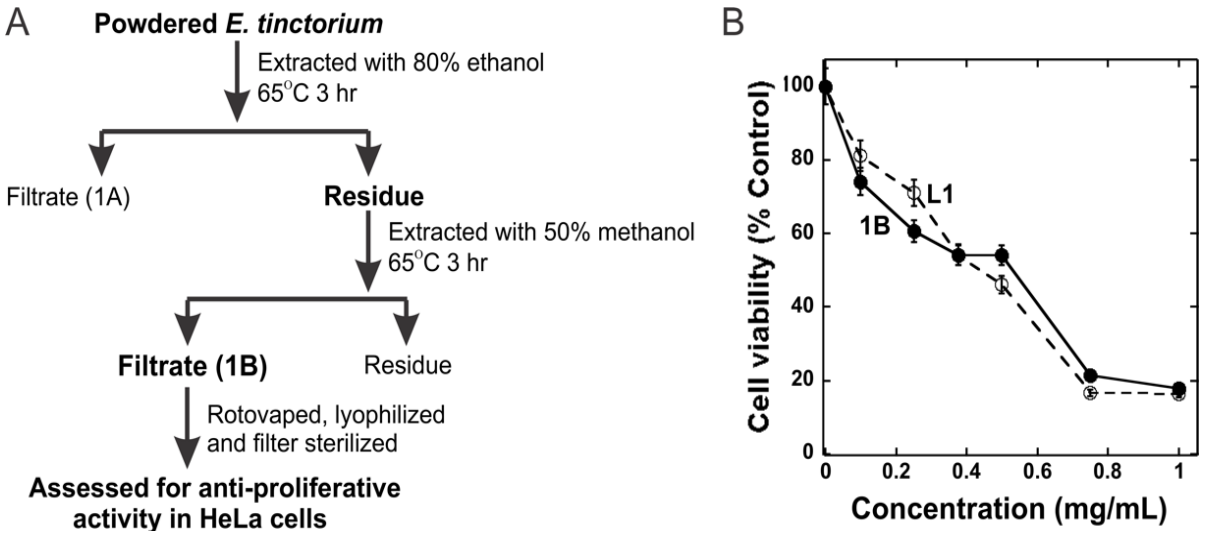

Fig. 3. 1. Chemical extraction of *E. tinctorium* and assessment of the ethanol extract 1B for anti-proliferative activity against HeLa cells. (A) Chemical extraction scheme to obtain ethanol extract from *E. tinctorium*. (B) Dose-dependent anti-proliferative MTT assay shows inhibition in HeLa cells by 1B extract and L1 from 0.1-1 mg/mL. Error bars represent S.D. Results shown are representative from three biological replicates.

3.3.2. Purification of anti-proliferative polysaccharide (EtGIPL1a) from *E. tinctorium*

The overall scheme adopted for the purification of the anti-proliferative polysaccharide from *E. tinctorium* (EtGIPL1a) is shown in Fig. 3.2A. L1 was first subjected to Sephadex LH-20 size-

exclusion chromatography designated as column-1. As shown in Fig. 3.2B, the major anti-proliferative activity was found in fractions 1-7, suggesting that the anti-proliferative compound has a relatively large molecular weight; these fractions 1-7 from column-1 were then pooled, concentrated, lyophilized, and resuspended in water. It was then subjected to column-2, DEAE-Sephadex anion exchange chromatography using L-Histidine (pH 6.2) as the buffer of choice. Optimized conditions for DEAE-Sephadex were obtained after analyzing the purification profiles with multiple buffers (Fig. S6). The flow-through and eluent from column-2 were concentrated, dialyzed, lyophilized, filter-sterilized, and assessed for anti-proliferative activity. As shown in Fig. 3.2C, the eluent referred to as 2A (but not the flow-through from DEAE-Sephadex) contains the anti-proliferative activity. This result suggested the presence of acidic groups on the compound that were effectively associated with positively charged DEAE-Sephadex resin and were eluted upon addition of salt to the mobile phase.

Eluent 2A was then subjected to column-3, Sephacryl S-500 high resolution size-exclusion chromatography. As shown in Fig. 3.3A, the anti-proliferative activity was retained in fractions 25-28 (designated L1a) and 29-31 (designated L1b). The fractions collected from column-3 were also assessed for carbohydrate (CHO) and protein contents. Results in Fig. 3.3B show that the major anti-proliferative activity L1a correlated strongly with carbohydrate content but not with the protein content. In contrast, the L1b activity appears to correlate better with the protein content (Fig. 3.3C).

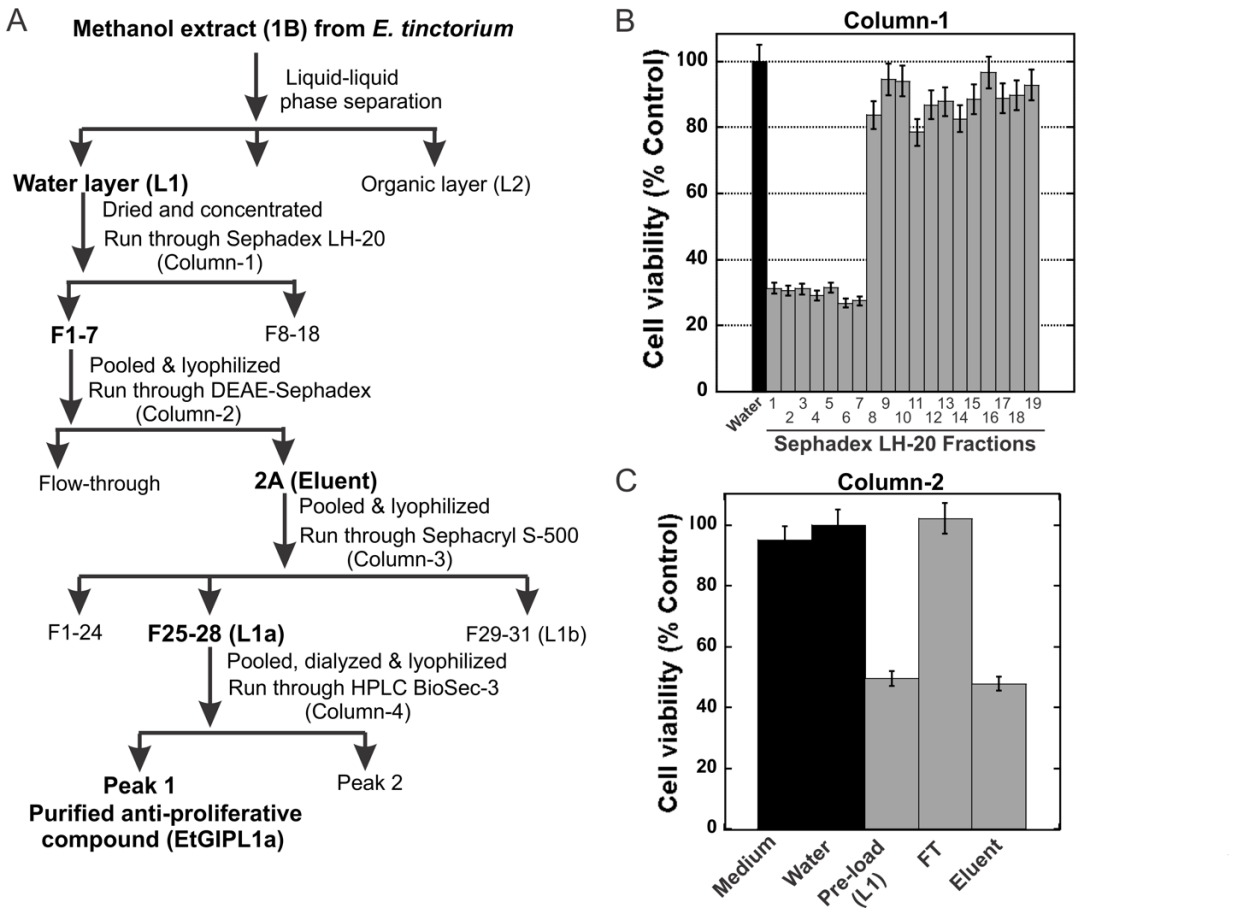

Fig. 3. 2. Purification of the anti-proliferative polysaccharide (EtGIPL1a) from *E. tinctorium*. (A) Summary of the purification scheme used. (B) 1B extract from *E. tinctorium* was purified using Sephadex LH-20 size-exclusion chromatography (column-1). Active fractions (F1-7) were pooled, lyophilized and ran through DEAE-Sephadex anion exchange chromatography (column-2) as shown in (C). The eluent (2A) showed anti-proliferative activity while the flow-through (FT) had no activity. Error bars represent S.D. Results shown are representative from three biological replicates.

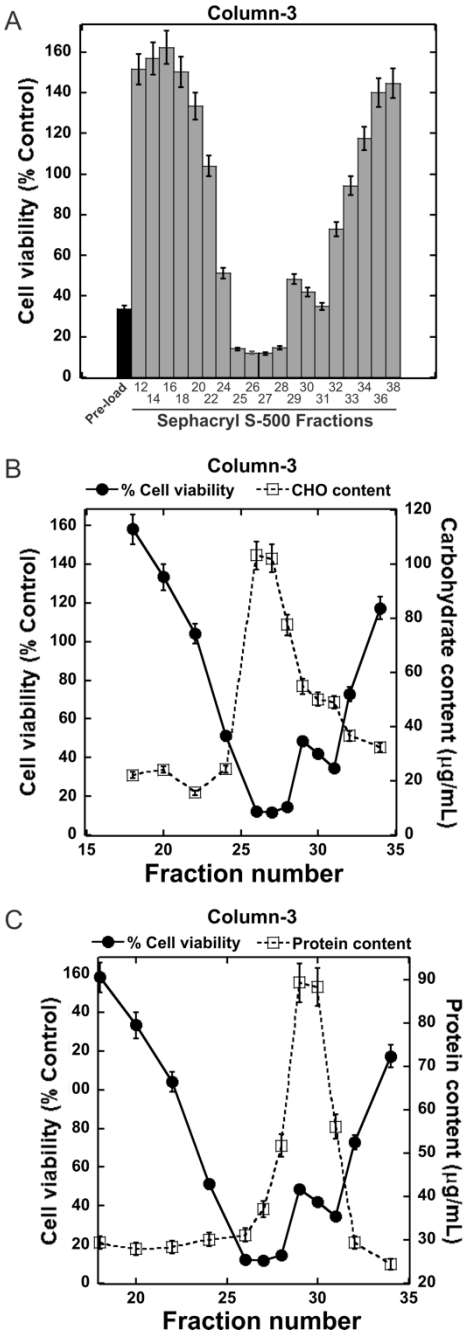

Fig. 3. 3. Purification of the anti-proliferative polysaccharide from *E. tinctorium* (EtGIPL1a) using Sephacryl S-500 (column-3). Collected fractions were assessed for cell viability (A), carbohydrate (B) and protein content (C). Error bars represent S.D. and results are representative from three separate experiments.

3.3.3. Estimation of molecular size and purification by HPLC

The major bioactive fraction L1a was further purified by HPLC using Agilent BioSEC-3 designated as column-4. As shown in Fig. 3.4A, the HPLC BioSEC-3 profile of L1a shows two peaks referred to as Peak1 and Peak 2. These were subjected to further purification by fraction collection. The collected Peak 1 and Peak 2 exhibited purity as shown in Fig. 3.4B and 3.4C respectively. Peak 1, designated as EtGIPL1a, has a retention time of 5.633 mins while Peak 2 has a retention time of 7.068 mins. Fig. 3.4D shows that both EtGIPL1a and Peak 2 dose-dependently inhibited proliferation of HeLa cells, with notable stronger effect by EtGIPL1a.

Using dextran standards on BioSEC-3 column, a standard curve was obtained (Fig. S7). Based on the standard curve, the peak maxima molecular weight (M_p) of EtGIPL1a was estimated to be 216271 g/mol (Da) or 216 kDa (Fig. S7 and Table S3). Further calculations were performed to determine the number (M_n) and weight average molecular weight (M_w) of EtGIPL1a. As shown in Table S3, the Mn and Mw of EtGIPL1a was calculated to be 232 kDa and 275 kDa respectively. The polydispersity index was calculated to be 1.18.

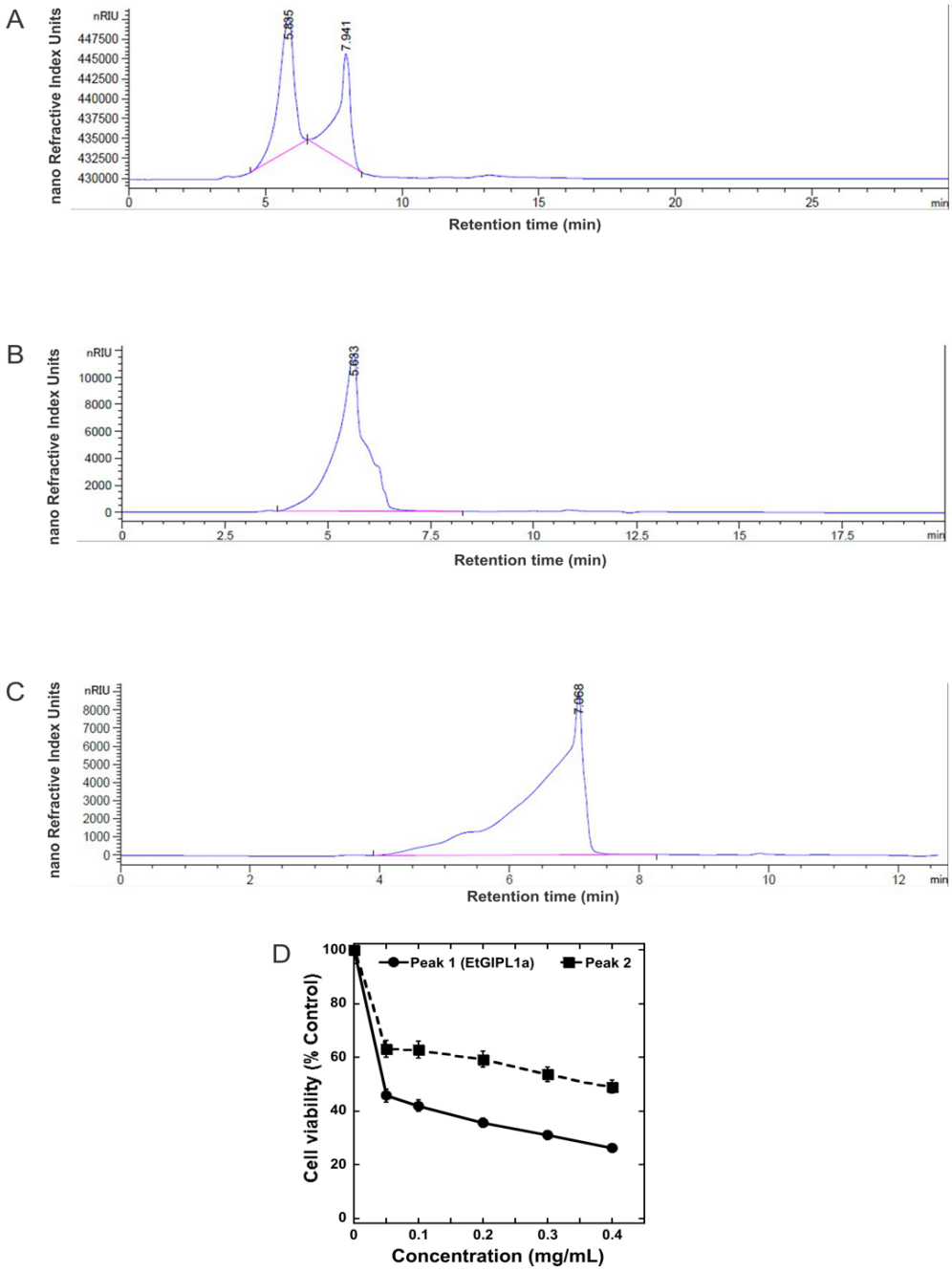

Fig. 3. 4. HPLC BioSEC-3 full elution profile of (A) L1a (B) Peak 1 (EtGIPL1a), and (C) Peak 2. The collected two peaks in (B) and (C) were assessed for anti-proliferative activity as shown in (D).

3.3.4. Assessing EtGIPL1a against a panel of human cancer cell lines

To determine whether EtGIPL1a has a broader anti-proliferative effect, we assessed it at various concentrations against a panel of human cancer cell lines. Results from the dose-dependent experiments summarized in Table 3.1 show that EtGPLL1a indeed exhibited strong anti-proliferative effect on the panel of human cancer cell lines. All the experiments shown in Table 3.1 were conducted by Dr. Lee. The purified polysaccharide was most effective against DU145 prostate cancer (IC_{50} = 50.6 nM), HCT116 colon cancer (IC_{50} = 122.2 nM) and the two glioblastoma cancer cells, U87 (IC_{50} = 136 nM) and U251 (IC_{50} = 193.2 nM). It was also effective against HeLa cervical cancer (IC_{50} = 287.9 nM), Panc-1 pancreatic (IC_{50} = 343.2 nM), MD-MB-231 breast cancer (IC_{50} = 514.3 nM), SKOV3 ovarian cancer (IC_{50} = 634.2 nM), and MCF-7 breast cancer cells (IC_{50} = 839.5 nM). EtGIPL1a is anti-proliferative on SW480 human colorectal cancer cells with an IC_{50} of 1446 nM, which is 10-fold lower than on HCT116 colon cancer cells. While both HCT116 ($KRAS^{G13D}$) and SW480 ($KRAS^{G12V}$) cells carry mutated KRAS, they have different activated cellular pathways that are related to proliferation. For example, HCT116 cells had high basal level mTORC1 activity while SW480 cells displayed low basal level mTORC1 activity (Thomas *et al*., 2014). SW480 cells showed hyperactivated mTORCs and AKT pathways leading to increased proliferation upon autophagy inhibition which was not observed in HCT116 cells (Lauzier *et al*., 2019). Whether the differential anti-proliferative effects of EtGIPL1a are due to these differentially active pathways in the cell lines will need further investigations.

Table 3. 1. IC_{50} of EtGIPL1a against human cancer cell lines

Cell lines	Types	*IC_{50} (nM)
DU145	Human prostate cancer	50.6
HCT116	Human colon cancer	122.2
U87	Human glioblastoma	136
U251	Human glioblastoma	193.2
HeLa	Human cervical cancer	287.9
Panc-1	Human pancreatic cancer	343.2
MD-MB-231	Human breast cancer	514.3
SKOV-3	Human ovarian cancer	634.2
MCF-7	Human breast cancer	839.5
SW480	Human colon cancer	1446

*IC_{50}: the data shown is an average taken from two independent experiments.

3.3.5. Growth inhibition in U251 glioblastoma cells

3.3.5.1. *Morphological changes in glioblastoma cell lines (U251)*

EtGIPL1a suppressed the growth of U251 cells *in-vitro* in a dose-dependent manner and induced morphological changes at lower doses. U251 cell morphology transformed from flat oval shape to more stellate shape with thin long processes extending from the cells as shown in Fig. 3.5. The experiments shown in Fig. 3.5 were conducted by Dr. Lee.

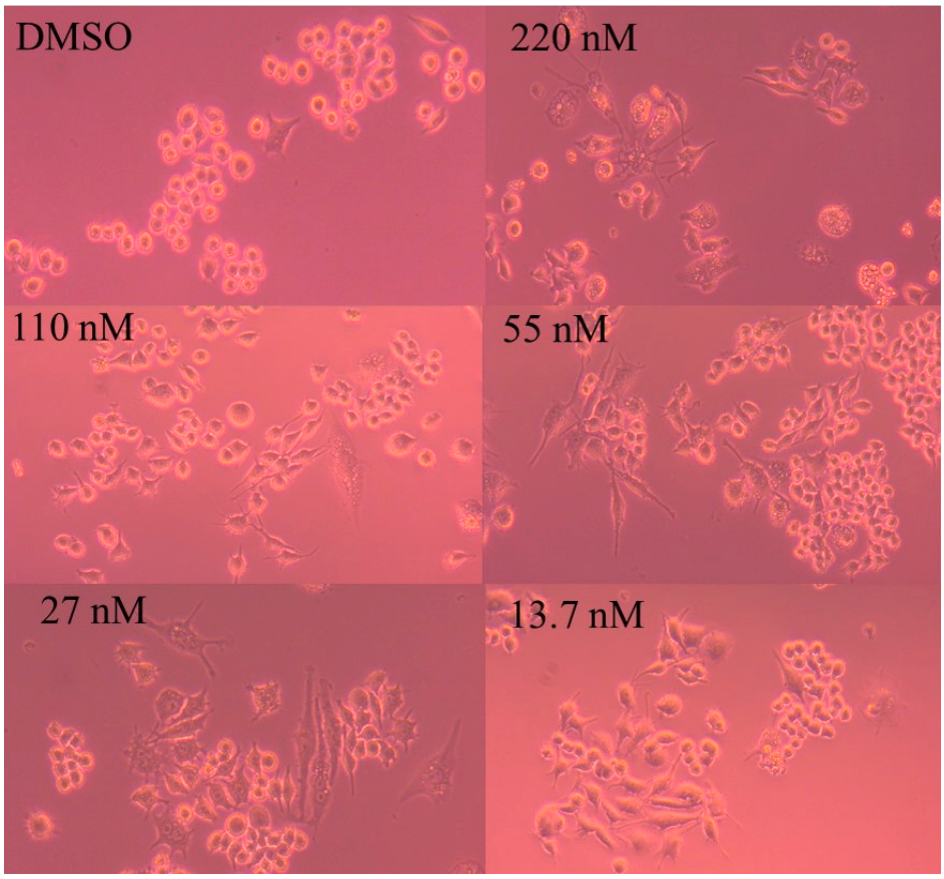

Fig. 3. 5. Morphological changes induced by EtGIPL1a after treatment at 13.7-220 nM for 48 h in U251 cells.

3.3.5.2. *Flow cytometry analysis of EtGIPL1a*

EtGIPL1a induced apoptosis in U251 cells at a concentration of 27 nM for 24-48 h (as shown in Fig. 3.6B & 3.7). A significant increase in number of cells was observed after treatment with EtGIPL1a as compared to water (negative control) and resveratrol (positive control) (Fig. 3.7). The apoptosis was not significant in SW480 cells even at very high dose (1.76 μM) when compared to U251 cells, suggesting that EtGIPL1a might be causing growth-inhibition in SW480 cells through mechanisms other than apoptosis.

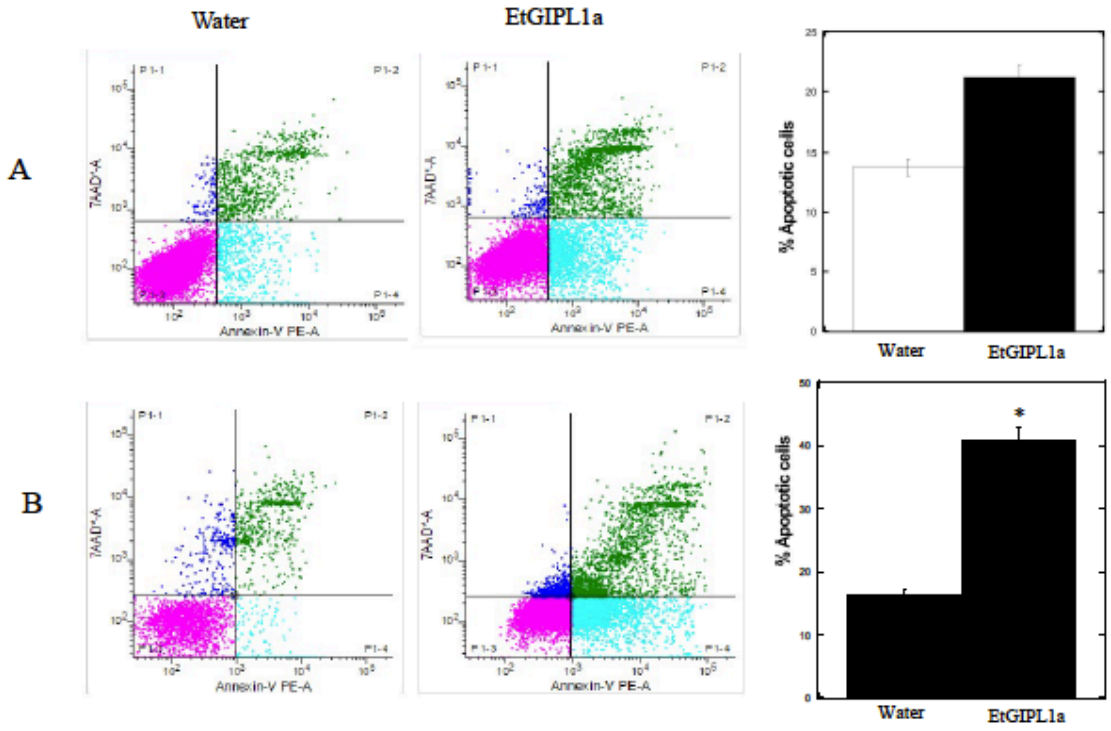

Fig. 3. 6. Flow cytometry analysis for apoptosis induced by EtGIPL1a at 1.76 µM for 48 h in SW480 cells (A) and at 27 nM for 24 h in U251 cells (B). Error bars represent standard deviation and results shown are representative from three biological replicates. One-way ANOVA was used for statistical analysis. * shows $p = 0.0046$.

EtGIPL1a showed antiproliferative effects in multiple cancer cells including U251 glioblastoma cells. Glioblastomas (GB) are generally considered very aggressive brain tumors with higher malignancy. Although quite rare, due to its malignancy, GB have been categorized as grade IV astrocytic tumor by World Health Organization (Louis *et al*., 2007). There are quite a few treatment options for the management of GB including surgery, radiotherapy and chemotherapy with Temozolomide.

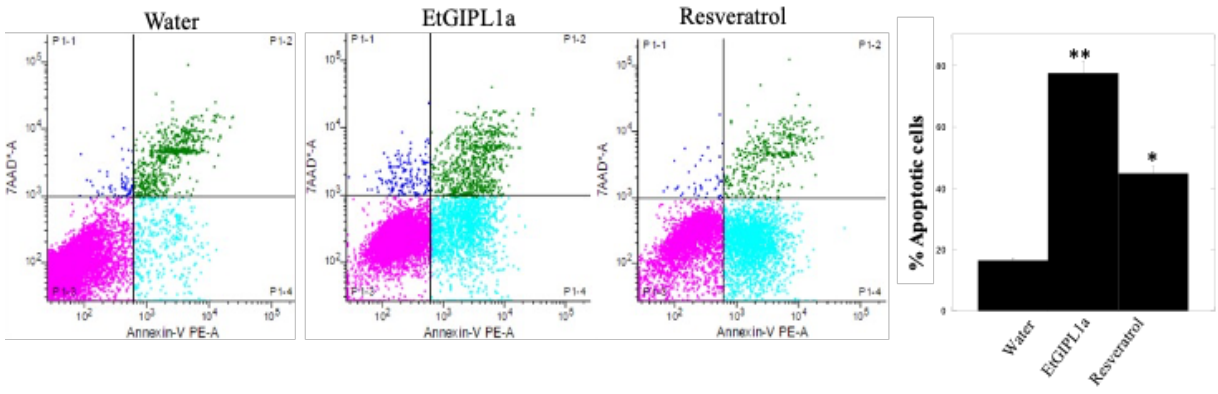

Fig. 3. 7. Apoptosis induced by treatment with 27 nM EtGIPL1a compared to 40 µM resveratrol for 48 h in U251 cells. Error bars represent standard deviation. The plots are representative of n=3. One-way ANOVA was used for statistical analysis. ** represents p = 0.0011 and * shows p= 0.0102.

The development of tumors is associated with dedifferentiation and uncontrolled growth of cells (Linskey & Gilbert, 1995), whereas normal cells are well differentiated and have a controlled differentiation, which helps us understand their morphology. EtGIPL1a caused growth-inhibition and induced differentiation in U251 glioblastoma cells. The morphological changes induced by EtGIPL1a suggested a well differentiated astrocyte-like morphology. It is known from the literature (Bovolenta *et al.*, 1984) that well differentiated astrocytes appear stellate shape with long processes, similar to what was observed with EtGIPL1a-treated U251 cells. It is believed that if cancer cells are well differentiated, the prognosis for cancer treatment is better. Astrocytes have an increased content of glial fibrillary protein (GFAP), which is exclusively expressed in mature astrocytes (Eng, 1985). A strategy proposed by researchers for limiting glial tumors is by inducing differentiation (Linskey & Gilbert, 1995).

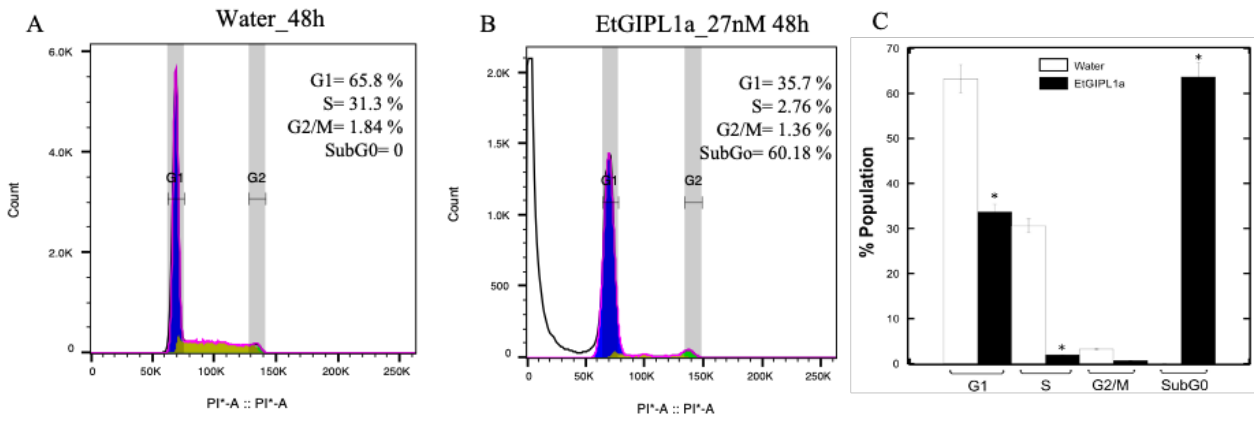

Fig. 3. 8. Cell cycle analysis of EtGIPL1a at 27 nM for 48 h on U251 cells (A & B) and % cell population in G1, S, G2/M and subG0 phases of cell cycle (C). Error bars represent S.D. Results shown are representative from three biological replicates. One-way ANOVA was used for statistical analysis. * indicates $p < 0.0001$.

Cell cycle analysis of EtGIPL1a showed a significant increase in the sub G0 population (Fig. 3.8) which is indicative of DNA fragments. The presence of high cell fractions in subG0 is indicative of cell death via apoptosis. There are few compounds from natural products that have shown cytotoxic potential against GB. A polysaccharide peptide (GL-PP) from *Ganoderma lucidum* has shown growth inhibition in U251 cells through G0/G1 cell cycle arrest and apoptosis; GL-PP has shown to induce the expression of caspase-3 in U251 cells (Wang *et al*., 2018) which is considered as an apoptotic marker. Another polyphenolic compound (hispolon) isolated from *Phellinus linteus* has been shown to induce apoptosis and G2/M phase cell cycle arrest in U87MG glioblastoma cells (Arcella *et al*., 2017). Cytotoxic triterpenoids from *Antrodia camphorata* (Li *et al*., 2020), polysaccharides from medicinal plants like *Angelica sinensis* (APs) (Zhand *et al*., 2017), *Cyclocarya paliurus* (CPP) (Du *et al*., 2020) and *Aconitum coreanum* (ACP1) (Sun *et al*., 2018) have also shown to induce apoptosis in U87MG and U251 glioblastoma cell lines.

3.3.5.3. *Molecular markers involved in differentiation and apoptosis*

Molecular markers for differentiation as well as apoptosis in U251 cells were assessed. Vimentin is a cytoskeleton dedifferentiation marker whereas GFAP indicates differentiation in astrocytes. Both protein markers were inconclusive due to the fact that the primary antibodies underwent non-specific interactions. LC3B was also assessed to determine the possibility of autophagy leading to apoptosis. Unfortunately, LC3B was not expressed to a greater extent. Another marker, cleaved caspase 3, one of the important markers for apoptosis was found to be highly expressed in U251 cells after treatment with EtGIPL1a (Fig. 3.9). The western blot analysis was performed by a former student Mr. Victor Liu.

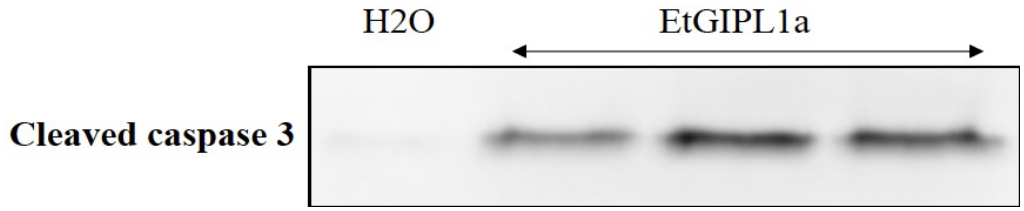

Fig. 3. 9. Western blot analysis of EtGIPL1a on expression of cleaved caspase 3 in U251 cells. The three bold bands represent three batches of EtGIL1a at 12.5 µg/mL treatment for 48 h.

3.3.6. Monosaccharide composition analysis

The monosaccharide analysis by TMS derivatization using GC-MS revealed that EtGIPL1a consisted of predominantly glucose (Glc) (54.3 %). Relatively large amounts of galactose (Gal) (19.6 %), mannose (Man) (11.1 %), and fucose (Fuc) (10.3 %) were also found in EtGIPL1a (Fig. S8 and Table 3.2). EtGIPL1a also contains glucuronic acid (GlcA) (4.0 %) and traces of rhamnose (Rha) (0.6 %). An immuno-stimulatory polysaccharide EtISPFa also isolated from *E. tinctorium* contains a higher amount of glucuronic acid (10.1 %) (Zeb *et al*., 2021). GC-MS was performed and analyzed by CCRC, USA.

3.3.7. Glycosyl linkage analysis by GC-MS

Consistent with the composition analysis, the glycosyl linkage analysis showed a majority of glucose linkages (%) in EtGIPL1a (Fig. S9 and Table 3.2). The main glucose linkages were 3-substituted, 6-substituted, and terminal. A small amount of 4-substituted glucose was also present. Galactose was found in 6- and 2,6- linkages, and GlcA was 4-substituted. Beside these, there were small amounts of terminal mannose (1.3%) as well as 3-substituted (2.5%) and terminal (0.9%) fucose. Compared with the polysaccharide EtISPFa reported previously (Zeb *et al*., 2021), 3-Fuc*p* and 6-Gal*p* were elevated, and 2,6-Gal*p* was not detected at all in the EtISPFa polysaccharide.

Table 3. 2. Monosaccharide composition of EtGIPL1a

Monosaccharide residue	Mass (µg)	Mol %
Glucose (Glc)	90.8	54.3
Galactose (Gal)	32.7	19.6
Mannose (Man)	18.6	11.1
Fucose (Fuc)	15.7	10.3
Glucuronic acid (GlcA)	7.3	4.0
Rhamnose (Rha)	0.9	0.6
Total =	165.9	100

The polysaccharide composition is known to link with bioactivity. Glucose, mannose, and galactose are amongst the commonly studied monosaccharide components of mushrooms whereas glucuronic acid, galacturonic acid, fructose, *N*-acetylglucosamine, *N*-acetyl galactosamine, and ribose are the least studied (Wang, Wang, Xu, & Ding, 2017). According to Chen et. (2005), fucose, glucose and mannose were considered essential for the anti-proliferative properties of two fungi: *Antrodia xantha* and *Rigidoporus ulmarius*; the bioactivity of these fungi

was compared with the inactive *A. cinnamomea* and *A. malicola*, which lacked the aforementioned monosaccharides in their structure (Chen, Lu, Cheng, & Wang, 2005). Another study showed the anti-proliferative effect of a fucose-containing highly branched 1,3-*β*-mannoglucan isolated from the fungus *Poria cocos*, a well-known Chinese medicine. This compound was found to inhibit lung cancer by down-regulating TGFβR signaling pathway, leading to inhibition of the migration of human metastatic lung cancer cells CL1-5 (Lin, Lu, & Chang, 2020). An anti-proliferative heterogenous polysaccharide (GIPinv) isolated from *Paxillus involutus* also contained fucose as terminal sugar (Barad *et al*., 2018). A heterogenous high molecular weight fucose-rich polysaccharide fraction FMS with fucose attached at the terminals was isolated from *Ganoderma lucidum*. FMS was found to induce production of IgM antibodies against tumor-specific glycans in Lewis lung cancer cells. FMS mediated antibody response and suppressed monocyte chemoattractant protein-1 which is an inflammatory mediator associated with cancer. Moreover, FMS suppressed Globo H, a carbohydrate antigen only found on the surface of cancer cells. This immunogenic ability of FMS was believed to be due to the presence of terminal fucose in its structure, which is capable of interacting with the surface antigens on tumor cells (Liao *et al.*, 2013). Since EtGIPL1a also contains reasonable percentage of fucose at the terminals, it will be important to investigate whether EtGIPL1a has anti-cancer activity in animal model and whether it exhibits *in vivo* properties similar to FMS.

The overall linkage analysis of EtGIPL1a showed (1→3)-linked Glc, (1→6)-linked Glc and (1→6)-linked Gal to be the major monomers, indicating that these components are the main chain of EtGIPL1a structure. *β*-glucans isolated from *Grifola frondosa* (Fang *et al*., 2012) and *Schizophyllum commune* (Klaus *et al*., 2011) share the same structural features, as their main chain is composed of (1→3)-linked Glc with branching at (1→6)-linked Glc. According to

several studies conducted on fungal polysaccharides, *β*-1→3 linkage in the major backbone with β-1→6 branching points is required for the antiproliferative activity (Wasser, 2002).

Table 3. 3. Glycosyl linkage analysis of EtGIPL1a by partially methylated alditol acetates

PMAA	**Linkage**	**Peak Area %**
1,5-Di-O-acetyl-1-deuterio-6-deoxy-2,3,4-tri-O-methylgalactitol	t-Fuc*p*	0.9
1,5-Di-O-acetyl-1-deuterio-2,3,4,6-tetra-O-methylmannitol	t-Man*p*	1.3
1,5-Di-O-acetyl-1-deuterio-2,3,4,6-tetra-O-methylglucitol	t-Glc*p*	15.3
1,3,5-Tri-O-acetyl-1-deuterio-6-deoxy-2,4-di-O-methylgalactitol	3-Fuc*p*	2.5
1,3,5-Tri-O-acetyl-1-deuterio-2,4,6-tri-O-methylglucitol	3-Glc*p*	28.9
1,5,6- Tri-O-acetyl-1-deuterio-2,3,4-tri-O-methylmannitol	6-Man*p*	2.4
1,5,6- Tri-O-acetyl-1-deuterio-2,3,4-tri-O-methylglucitol	6-Glc*p*	18.3
1,4,5- Tri-O-acetyl-1-deuterio-2,3,6-tri-O-methylglucitol	4-Glc*p*	1.7
1,4,5- Tri-O-acetyl-1,6,6'-trideuterio-2,3,6-tri-O-methylglucitol	4-Glc*p*A	9.2
1,5,6- Tri-O-acetyl-1-deuterio-2,3,4-tri-O-methylgalactitol	6-Gal*p*	3.9
1,3,5,6- Tetra-O-acetyl-1-deuterio-2,4-di-O-methylglucitol	3,6-Glc*p*	13.0
1,2,5,6- Tetra-O-acetyl-1-deuterio-3,4-di-O-methylgalactitol	2,6-Gal*p*	2.6

[a]For clarity, residues found at < 1% were omitted.

Polysaccharides isolated from basidiomycetes are known to have more complex heteroglucan structural traits as compared to ascomycetes (He *et al*., 2017; Zhang, Nie, Yin, Wang, & Xie, 2014). For instance, polysaccharides from ascomycetes contain a systematic monosaccharide chain unit such as those found in *Cordyceps* species (Lu, Gu, Hao, Jin, & Wang, 2016; Smiderle, Sassaki, Griensven, & Iacomini, 2013). In contrast, monosaccharides in polysaccharides isolated from basidiomycetes are very complex and do not have a systematic monosaccharide chain unit.

Diverse monosaccharide composition contributes to the structural complexity of polysaccharides of basidiomycetes which applies to EtGIPL1a and EtISPFa which was previously isolated immuno-stimulatory polysaccharide from *E. tinctorium* (Zeb *et al*., 2021). Despite the reported studies where β-1→3 and β-1→6 has been linked to immuno-stimulatory activity, which is true for EtISPFa but does not apply to growth-inhibitory polysaccharide EtGIPL1a. Although EtGIPL1a does have β-1→3 Glc backbone with branching at β-1→6 linked Glc, it does not possess immuno-stimulatory activity. The growth-inhibitory activity of EtGIPL1a is likely to be due to the variability in the monosaccharide composition and linkages from EtISPFa.

The presence of acidic group was also confirmed by GC-MS analysis. EtGIPL1a is an acidic polysaccharide that has a considerable amount of glucuronic acid (4 %), which is not commonly found in fungal polysaccharides. Interestingly, we also found high content of glucuronic acid (10 %) in another bioactive polysaccharide isolated from *E. tinctorium* (Zeb *et al*., 2021). Other fungi that contain acidic polysaccharides are *Pleurotus abalonus* (Shi, Zhao, Jiao, Shi, & Yang, 2013), *Fusarium* and *Gibberella* species (Ahrazem *et al*., 2000), *Plectosphaerella cucumerina*, *Verticillium dahliae*, and *V. albo-atrum* (Ahrazem *et al*., 2006).

3.3.8. Structural analysis by FTIR

FTIR showed the presence of characteristic absorption peaks for a polysaccharide (Cui, 2005) (Fig. 3.10): a broad band at 3283 cm^{-1} that referred to free hydroxyl group stretching and a weak signal at 2923 cm^{-1} for the C-H stretch. There were some other peak stretches as well: 1598 cm^{-1} for carboxyl C=O, 1383 cm^{-1} for C-H bending and 1039 cm^{-1} corresponding to pyranose ring stretching vibration. The observed functional groups present in EtGIPL1a are consistent with that of a typical polysaccharide due to the presence of free O-H groups, pyranose ring, alkanes and amine (Chen *et al.*, 2012; Liu *et al*., 2015; Wang, Wang, Xu, & Ding, 2017).

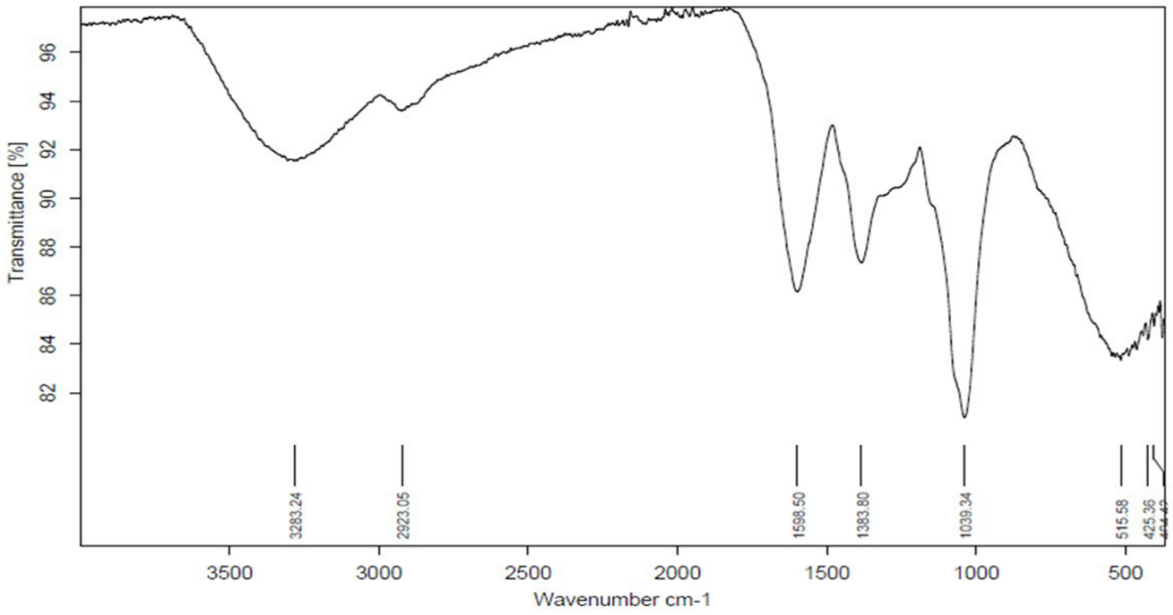

Fig. 3. 10. FTIR spectrum of EtGIPL1a.

3.3.9. NMR analyses of EtGIPL1a

To gain further structural insights, 1D and 2D NMR analyses were carried out and the data was analyzed by CCRC, USA. According to 1D proton NMR, there was a complex pattern of peaks in the 3.2-4.5 ppm region which referred to the non-anomeric proton region (H2 - H6) of carbohydrates (Fig. 3.11).

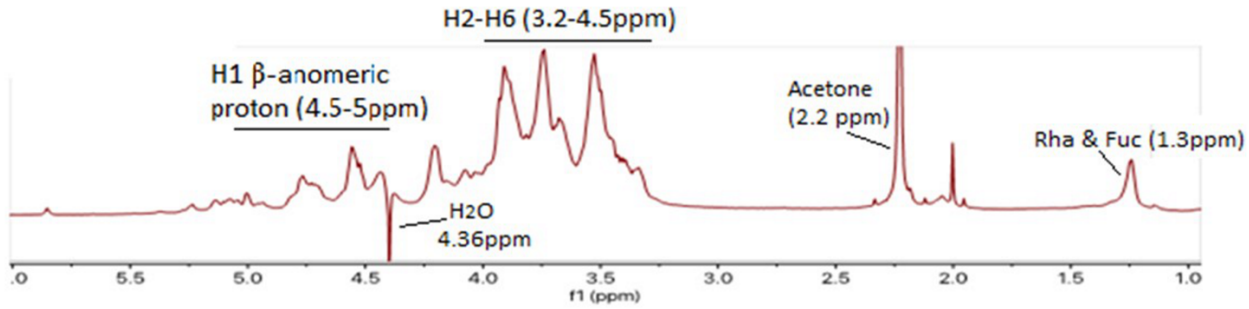

Fig. 3. 11. ^{1}H-NMR spectrum of EtGIPL1a.

H1 protons resonating at 4.5-5 ppm were referred to as β-anomeric protons. Due to the complexity of overlapping non-anomeric proton peaks, 2D NMR was conducted.

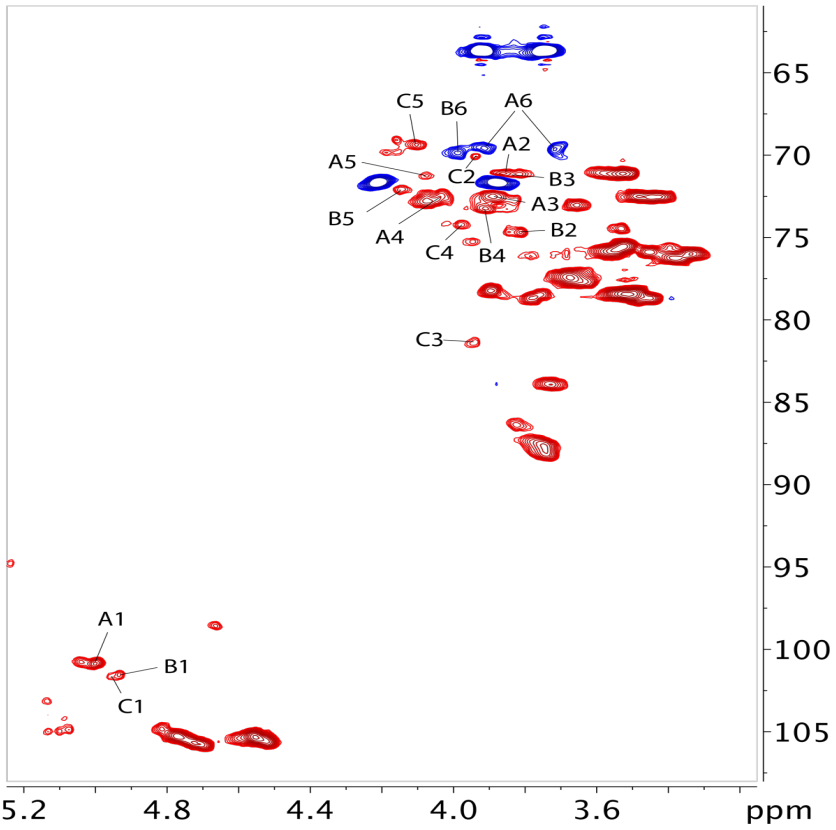

Fig. 3. 12. Partial multiplicity-edited 1H-13C-HSQC NMR spectrum of EtGIPL1a with labels indicating signals that were of much lower intensity in the EtISPFa sample (see Table 3.4). Red signals are positive and correspond to CH groups, and blue signals are negative and correspond to CH_2 groups.

The H1 signals that resonate between 5-6 ppm refer to α-anomeric protons whereas those between 4-5 ppm are β-anomeric protons. The H1 signals for EtGIPL1a were in the 4.2-5 ppm region, suggesting the polysaccharide have a β-configuration of glycosidic bond. Polysaccharide isolated from *Grifola frondosa* (Fang *et al*., 2012) and *Schizophyllum commune* (Klaus *et al*., 2011) also showed a *β*-configured glucan structure with 1→3 linked Glc as the main chain with O-6 substitution.

Table 3. 4. NMR chemical shift assignments for the residues found in EtGIPL1a that were not found in EtISPFa

No.	Residue	Chemical shift (ppm)					
		1	2	3	4	5	6
A	6-α-Gal*p*-	5.00	3.87	3.89	4.03	4.07	3.92/3.71
		101.0	71.2	72.6	72.8	71.3	69.6
B	2,6-α-Gal*p*-	4.94	3.81	3.86	3.91	4.14	3.99/3.71
		101.4	74.6	71.1	73.2	72.1	69.8
C	3-α-Fuc*p*-	4.95	3.94	3.95	3.96	4.11	1.25
		101.6	70.2	81.3	75.3	69.5	18.6

The spectra were similar to those reported for the EtISPFa polysaccharide (Zeb *et al*., 2021). The 2D NMR results were aligned with the complexity of signals seen in 1D NMR, concluding that EtGIPL1a is a complex large *β*-glucan with a 1→3 linked Glc backbone which is substituted at O-6. However, there were several additional signals indicating that the L1a polysaccharide was more complex than the EtISPFa polysaccharide sample (Chapter 2). Three additional residues were assigned (Table 3.4), confirming some of the differences observed in the linkage data in comparison with those of the EtISPFa polysaccharide. Thus, 6-substituted α-galactopyranosyl, 2,6-disubstituted α-galactopyranosyl, and 3-substituted α-fucopyranosyl residues A, B, and C were identified, which were found in lower abundance in the EtISPFa polysaccharide than in EtGIPL1a. The anomeric signals of Residues A and B showed NOE contacts only with their own H2 and one H6 (Fig. 3.4 and Table 3.4). Unlike the H1-H2 correlation, the cross peak between H1 and H6 could only arise from an inter-residue contact, suggesting that both 6-Gal and 2,6-Gal may constitute the backbone of a separate galactan polysaccharide. No NOE signals were detected from H1 of Residue C, and thus, it is unknown whether this residue belonged to the glucan or the galactan. Although it was difficult to quantify the different residues in the NMR experiments because of extensive peak overlap, the intensities

of the signals belonging to 4-substituted glucuronic acids were somewhat smaller than in the EtISPFa sample (Zeb *et al*., 2021), thus corroborating the linkage data.

Based on the chemical analyses that include monosaccharide composition, linkage analysis, FTIR, 1D and 2D NMR, a proposed backbone structure for the 275 kDa anti-proliferative EtGIPL1a (Fig. 3.13) is largely identical to that reported earlier for the 1354 kDa immuno-stimulatory EtISPFa polysaccharide (Zeb *et al*., 2021), with significantly lower proportion of GlcA. In addition to the main polysaccharide, there is a (1→6)-α-galactan with unknown side chains at O-2 of some of the Gal residues. Furthermore, there is a small amount of 3-substituted α-Fuc with an NOE correlation to a proton at 3.82 ppm (Table 3.4). This could be H3 of a β-Glc residue in the main backbone, but at the low abundance of Residue C, it is not possible to make this determination with certainty. In addition to having more 3-linked fucose (2.5 %), 6-linked mannose (2.4 %), 6-linked galactose (3.9%) and 2,6-linked galactose (2.6 %), in general. As mentioned in Chapter 2, this structure (Fig. 3.13) is an average structure with multiple possibilities. In addition to the current structure elucidation techniques, more evidence can be collected by other techniques which will confirm the monosaccharide components and linkages in EtGIPL1a. These techniques include hydrolysis of polysaccharide by acid or enzymes and then identification using MALDI-TOF-MS, capillary electrophoresis and analysis of derivatized monosaccharides on HPLC using fluorometry or UV detection. EtGIPL1a has approximately six times more fucose, three times more galactose and 2 times more mannose than EtISPFa. Therefore, it is tempting to speculate that rather than the backbone structure, the abundant fucose, mannose and galactose and their corresponding linkages distinguish EtGIPL1a from EtISPFa, and contributes to its anti-proliferative function.

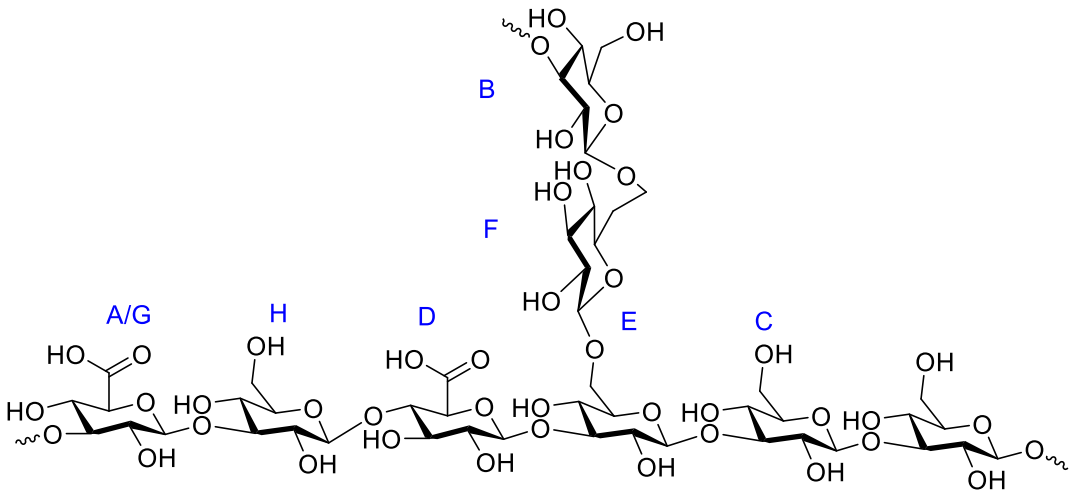

Fig. 3. 13. Proposed representative structure of the anti-proliferative polysaccharide EtGIPL1a.

3.4. Conclusion

This is the first study to describe isolation and characterization of an anti-proliferative polysaccharide from *E. tinctorium*. Using a phase separation method, Sephadex LH-20, DEAE-Sephadex, Sephacryl S-500 HR, and HPLC Bio SEC-3, we successfully isolated an anti-proliferative polysaccharide (EtGIPL1a) with weight average molecular weight (M_w) of 275 kDa from the methanol extract of *E. tinctorium*. EtGIPL1a is a complex and unique *β*-glucan polysaccharide rich in galactose (19.6 %), mannose (11.1 %), fucose (10.3 %) and glucuronic acid (4 %), along with trace amounts of rhamnose (0.6 %). The combined results from GC-MS and NMR analyses reveal that EtGIPL1a is made up mostly of a backbone consisting of *β*-(1→4)-Glc*p* residues and *β*-(1→3)-Glc*p*A residues, with branching points at *β*-(1→6)-Glc*p*. The polysaccharide is anti-proliferative against a large panel of cancer cell lines. Further biological characterization of EtGIPL1a is required to determine its mechanism of action and whether it exerts anti-cancer activity in animals.

Appendix B. Supplementary data

Supplementary material related to this chapter can be found in Appendix B.

3.5. References

Ahrazem, O., Gómez-Miranda, B., Prieto, A., Barasoaín, I., Bernabé, M., & Leal, J. A. (2000). An acidic water-soluble cell wall polysaccharide: a chemotaxonomic marker for *Fusarium* and *Gibberella*. *Mycological research*, *104*, 603-610.

Ahrazem, O., Prieto, A., Giménez-Abián, M. I., Leal, J. A., Jiménez-Barbero, J., & Bernabé, M. (2006). Structural elucidation of fungal polysaccharides isolated from the cell wall of *Plectosphaerella cucumerina* and *Verticillium* spp. *Carbohydrate research*, *341*, 246-252.

Arcella, A., Oliva, M. A., Sanchez, M., Staffieri, S., Esposito, V., Giangaspero, F., & Cantore, G. (2017). Effects of hispolon on glioblastoma cell growth. *Environmental toxicology*, *32*(9), 2113-2123.

Barad, A., Mackedenski, S., Li, W. M., Li, X. J., Lim, B. C. C., Rashid, F., Tackaberry, L.E., Massicotte, H.B., Egger, K.N., Reimer K, & Cheung, P. C. (2018). Anti-proliferative activity of a purified polysaccharide isolated from the basidiomycete fungus *Paxillus involutus. Carbohydrate polymers*, *181*, 923-930.

Blagodatski, A., Yatsunskaya, M., Mikhailova, V., Tiasto, V., Kagansky, A., Katanaev, V. L. (2018). Medicinal mushrooms as an attractive new source of natural compounds for future cancer therapy. *Oncotarget*, *9,* 29259-29274.

Bovolenta, P., Liem, R. K., & Mason, C. A. (1984). Development of cerebellar astroglia: transitions in form and cytoskeletal content. *Developmental biology*, *102*(1), 248-259.

Chen, G. T., Fu, Y. X., Yang, W. J., Hu, Q. H., & Zhao, L. Y. (2018). Effects of polysaccharides from the base of *Flammulina velutipes* stipe on growth of murine RAW264. 7, B16F10 and L929 cells. *International journal of biological macromolecules*, *107*, 2150-2156.

Chen, S. C., Lu, M. K., Cheng, J. J., & Wang, D. L. (2005). Antiangiogenic activities of polysaccharides isolated from medicinal fungi. *FEMS microbiology letters*, *249*, 247-254.

Chen, Q., Zhang, S. Z., Ying, H. Z., Dai, X. Y., Li, X. X., Yu, C. H., & Ye, H. C. (2012). Chemical characterization and immunostimulatory effects of a polysaccharide from *Polygoni Multiflori Radix Praeparata* in cyclophosphamide-induced anemic mice. *Carbohydrate polymers*, *88*, 1476-1482.

Cui, S. W. (2005). Food Carbohydrates: chemistry, physical properties, and applications (ed. Cui, S.) CRC Press. pp. 70-72.

Du, X., Guo, K., Ma, Y., & Chang, J. (2020). *Cyclocarya paliurus* Polysaccharide inhibits glioma cell U251 proliferation, migration, and invasion and promotes apoptosis via the GSK3β/β-catenin signaling pathway. *International journal of polymer science*, *2020*.

Dubey, S. K., Chaturvedi, V. K., Mishra, D., Bajpeyee, A., Tiwari, A., & Singh, M. P. (2019). Role of edible mushroom as a potent therapeutic for the diabetes and obesity. *3 Biotech, 9(12),* 450.

Eng, L. F. (1985). Glial fibrillary acidic protein (GFAP): the major protein of glial intermediate filaments in differentiated astrocytes. *Journal of neuroimmunology*, *8*, 203-214.

Fang, J., Wang, Y., Lv, X., Shen, X., Ni, X., & Ding, K. (2012). Structure of a β-glucan from *Grifola frondosa* and its antitumor effect by activating Dectin-1/Syk/NF-κB signaling. *Glycoconjugate journal*, *29*, 365-377.

Ferreira, I. C., Heleno, S. A., Reis, F. S., Stojkovic, D., Queiroz, M. J. R., Vasconcelos, M. H., & Sokovic, M. (2015). Chemical features of *Ganoderma* polysaccharides with antioxidant, antitumor and antimicrobial activities. *Phytochemistry*, *114*, 38-55.

He, X., Fang, J., Guo, Q., Wang, M., Li, Y., Meng, Y., & Huang, L. (2020). Adances in antiviral polysaccharides derived from edible and medicinal plants and mushrooms. *Carbohydrate polymers, 229,* 115548.

He, X., Wang, X., Fang, J., Chang, Y., Ning, N., Guo, H., Huang, L., Huang, X., & Zhao, Z. (2017). Polysaccharides in *Grifola frondosa* mushroom and their health promoting properties: A review. *International Journal of Biological Macromolecules*, *101*, 910-921.

Javed, S., Li, W. M., Zeb, M., Yaqoob, A., Tackaberry, L. E., Massicotte, H. B, Egger, K. N, Cheung, P.C., Payne, G.W. & Lee, C. H. (2019). Anti-Inflammatory activity of the wild mushroom, *Echinodontium tinctorium*, in RAW264. 7 macrophage cells and mouse microcirculation. *Molecules*, *24*, 3509.

Khursheed R., Singh, S. K., Wadhwa, S., Gulati, M., & Awasthi, A. (2020). Therapeutic potential of mushrooms in diabetes mellitus: role of polysaccharides. *International journal of biological macromolecules, 164,* 1194-1205.

Klaus, A., Kozarski, M., Niksic, M., Jakovljevic, D., Todorovic, N., & Van Griensven, L. J. (2011). Antioxidative activities and chemical characterization of polysaccharides extracted from the basidiomycete *Schizophyllum commune*. *LWT-Food science and technology*, *44*, 2005-2011.

Lauzier, A., Normandeau-Guimond, J., Vaillancourt-Lavigueur, V., Boivin, V., Charbonneau, M., Rivard, N., Scott, M. S., Dubois, C. M., & Jean, S. (2019). Colorectal cancer cells respond differentially to autophagy inhibition *in vivo*. *Scientific reports, 9,* 11316.

Li, B., Kuang, Y., Zhang, M., He, J. B., Xu, L. L., Leung, C. H., ... & Ye, M. (2020). Cytotoxic triterpenoids from *Antrodia camphorata* as sensitizers of paclitaxel. *Organic chemistry frontiers*, *7*(5), 768-779.

Liao, S. F., Liang, C. H., Ho, M. Y., Hsu, T. L., Tsai, T. I., Hsieh, Y. S. Y., Tsai, C.M., Li, S.T., Cheng, Y.Y., Tsao, S.M., & Lin, T. Y. (2013). Immunization of fucose-containing polysaccharides from Reishi mushroom induces antibodies to tumor-associated Globo H-series epitopes. *Proceedings of the national academy of sciences*, *110*, 13809-13814.

Linskey, M. E., & Gilbert, M. R. (1995). Glial differentiation: a review with implications for new directions in neuro-oncology. *Neurosurgery*, *36*(1), 1-22.

Louis, D. N., Ohgaki, H., Wiestler, O. D., Cavenee, W. K., Burger, P. C., Jouvet, A., ... & Kleihues, P. (2007). The 2007 WHO classification of tumours of the central nervous system. *Acta neuropathologica*, *114*(2), 97-109.

Lu, J., Gu, G., Hao, L., Jin, Z., & Wang, X. (2016). Characterization and in vitro antioxidant activity of a polysaccharide from *Cordyceps sobolifera*. *Journal of food processing and preservation*, *40*, 447-452.

Ma, G., Yang, W., Mariga, A. M., Fang, Y., Ma, N., Pei, F., & Hu, Q. (2014). Purification, characterization and antitumor activity of polysaccharides from *Pleurotus eryngii* residue. *Carbohydrate polymers*, *114*, 297-305.

Panda, M. K., Paul, M., Singdevsachan, S. K., Tayung, K., Das, S. K., Thatoi, H. (2020). Promising anticancer therapeutics from mushrooms: current findings and future perceptions. *Current pharmaceutical biotechnology,* doi: 10.2174/1389201021666201008164056.

Pires, A. D. R. A., Ruthes, A. C., Cadena, S. M. S. C., & Iacomini, M. (2017). Cytotoxic effect of a mannogalactoglucan extracted from *Agaricus bisporus* on HepG2 cells. *Carbohydrate polymers*, *170*, 33-42.

Shi, X., Zhao, Y., Jiao, Y., Shi, T., & Yang, X. (2013). ROS-dependent mitochondria molecular mechanisms underlying antitumor activity of *Pleurotus abalonus* acidic polysaccharides in human breast cancer MCF-7 cells. *PLOS ONE, 8*, e64266.

Shnyreva, A. V., Shnyreva, A. A., Espinoza, C., Padrón, J. M., & Trigos, Á. (2018). Antiproliferative activity and cytotoxicity of some medicinal wood-destroying mushrooms from Russia. *International journal of medicinal mushrooms*, *20*.

Smiderle, F. R., Sassaki, G. L., Van Griensven, L. J., & Iacomini, M. (2013). Isolation and chemical characterization of a glucogalactomannan of the medicinal mushroom *Cordyceps militaris*. *Carbohydrate polymers*, *97*, 74-80.

Smith, A. W. T. (2017). Investigating British Columbia wild mushrooms for growth-inhibitory activity (MSc thesis, University of Northern British Columbia, Prince George, BC, Canada). Retrieved from: https://unbc.arcabc.ca/islandora/object/unbc%3A54754

Souilem, F., Fernandes, Â., Calhelha, R. C., Barreira, J. C., Barros, L., Skhiri, F., Martins, A., & Ferreira, I. C. (2017). Wild mushrooms and their mycelia as sources of bioactive compounds: antioxidant, anti-inflammatory and cytotoxic properties. *Food chemistry*, *230*, 40-48.

Sun, L., Wang, Z., Wang, H., Li, J., & Liang, H. (2018). Polysaccharide sulphated derivative from *Aconitum coreanum* induces cell apoptosis in the human brain glioblastoma U87MG cell line via the NF-κB/Bcl-2 cell apoptotic signaling pathway. *Oncology reports*, *39*(3), 1469-1474.

Thomas, J. D., Zhang, Y-J., Wei, Y-H., Cho, J-H., Morris, L.E., Wang, H-Y., & Zheng, X. F. S. (2014). Rab1A is an mTORC1 activator and a colorectal oncogene. *Cancer cell, 26(5),* 754-769.

Urbancikova, I., Hudackova, D., Majtan, J., Rennerova, Z., Banovcin, P., & Jesenak, M. (2020). Efficacy of pleuran (β-glucan from *Pleurotus ostreatus*) in the management of herpes simplex virus type 1 infection. *Evidence-based complementary and alternative medicine*, *2020*, 1-8.

Venturella, G., Ferraro, V., Cirlincione, F., & Gargano, M. L. (2021). Medicinal mushrooms: bioactive compounds, use, and clinical trials. *International journal of molecular sciences, 22(2),* 634.

Wang, J., Li, W., Huang, X., Liu, Y., Li, Q., Zheng, Z., & Wang, K. (2017). A polysaccharide from *Lentinus edodes* inhibits human colon cancer cell proliferation and suppresses tumor growth in athymic nude mice. *Oncotarget*, *8*, 610-623.

Wang, C., Lin, D., Chen, Q., Lin, S., Shi, S., & Chen, C. (2018). Polysaccharide peptide isolated from grass-cultured *Ganoderma lucidum* induces anti-proliferative and pro-apoptotic effects in the human U251 glioma cell line. *Oncology letters*, *15*(4), 4330-4336.

Wang, W., Gou, X., Xue, H., & Liu, K. (2019). Ganoderan (GDN) regulates the growth, motility and apoptosis of non-small cell lung cancer cells through ERK signaling pathway *in vitro* and *in vivo*. *Oncotargets and therapy*, *12*, 8821.

Wang, Q., Wang, F., Xu, Z., & Ding, Z. (2017). Bioactive mushroom polysaccharides: a review on monosaccharide composition, biosynthesis and regulation. *Molecules*, *22*, 955.

Wasser, S. P. (2002). Medicinal mushrooms as a source of antitumor and immunomodulating polysaccharides. *Applied microbiology and biotechnology*, *60*, 258-274.

Ya, G. (2017). A *Lentinus edodes* polysaccharide induces mitochondrial-mediated apoptosis in human cervical carcinoma HeLa cells. *International journal of biological macromolecules,* 103, 676-682.

Yang, G., Yang, L., Zhuang, Y., Qian, X., & Shen, Y. (2016). *Ganoderma lucidum* polysaccharide exerts anti-tumor activity via MAPK pathways in HL-60 acute leukemia cells. *Journal of receptors and signal transduction*, *36*, 6-13.

Yaqoob, A., Li, W. M., Liu, V., Wang, C., Mackedenski, S., Tackaberry, L. E., Massicotte, H. B., Egger, K. N., Reimer, K., & Lee, C. H. (2020) Grifolin, neogrifolin and confluentin from the terricolous polypore *Albatrellus flettii* suppress KRAS expression in human colon cancer cells. *PLOS ONE, 15(5),* e0231948.

Ye, Y., Josten, I., Arnold, N., Steffan, B., & Steglich, W. (1996). Isolation of a fluorone pigment from the Indian paint fungus *Echinodontium tinctorium* and *Pyrofomes albomarginatus*. *Tetrahedron*, *52*, 5793-5798.

Zeb, M., & Lee, C. H. (2021). Medicinal properties and bioactive compounds from wild mushrooms native to North America. *Molecules, 26,* 251.

Zeb, M., Tackaberry, L. E., Massicotte, H. B., Egger, K. N., Reimer, K., Lu, G., Heiss, C., Azadi, P., & Lee, C. H. (2021). Structural elucidation and immuno-stimulatory activity of a novel polysaccharide containing glucuronic acid from the fungus *Echinodontium tinctorium*. *Carbohydrate polymers, 258,* 117700.

Zhang, W. F., Yang, Y., Li, X., Xu, D. Y., Yan, Y. L., Gao, Q., & Duan, M. H. (2017). *Angelica* polysaccharides inhibit the growth and promote the apoptosis of U251 glioma cells in vitro and in vivo. *Phytomedicine*, *33*, 21-27.

Zhang, H., Nie, S. P., Yin, J. Y., Wang, Y. X., & Xie, M. Y. (2014). Structural characterization of a heterogalactan purified from fruiting bodies of *Ganoderma atrum*. *Food hydrocolloids*, *36*, 339-347.

Zhong, K., Tong, L., Liu, L., Zhou, X., Zhang, Q., & Zhou, S. (2015). Immunoregulatory and antitumor activity of schizophyllan under ultrasonic treatment. *International journal of biological macromolecules, 80,* 302-308.

Zhuang, C., & Wasser, S. P. (2004). Medicinal value of culinary-medicinal Maitake mushroom *Grifola frondosa* (Dicks.: Fr.) SF Gray (Aphyllophoromycetideae). *International journal of medicinal mushrooms*, *6*, 1-28.

Appendix B. Supplementary data

DEAE-Sephadex Optimization

The running conditions for anion exchange chromatography using Sephadex DEAE were optimized with buffers (Fig. S1) including Bis-Tris (pH = 6.48), L-Histidine (pH 6.2), Piperazine (pH 5.3 and 9.73), and Tris (pH 8.07). The same procedure was used to obtain the optimized buffer as mentioned in Appendix A of Chapter 2. The elution and flow through were assessed for growth-inhibitory activity via MTT. L-Histidine was used as final buffer for further purification.

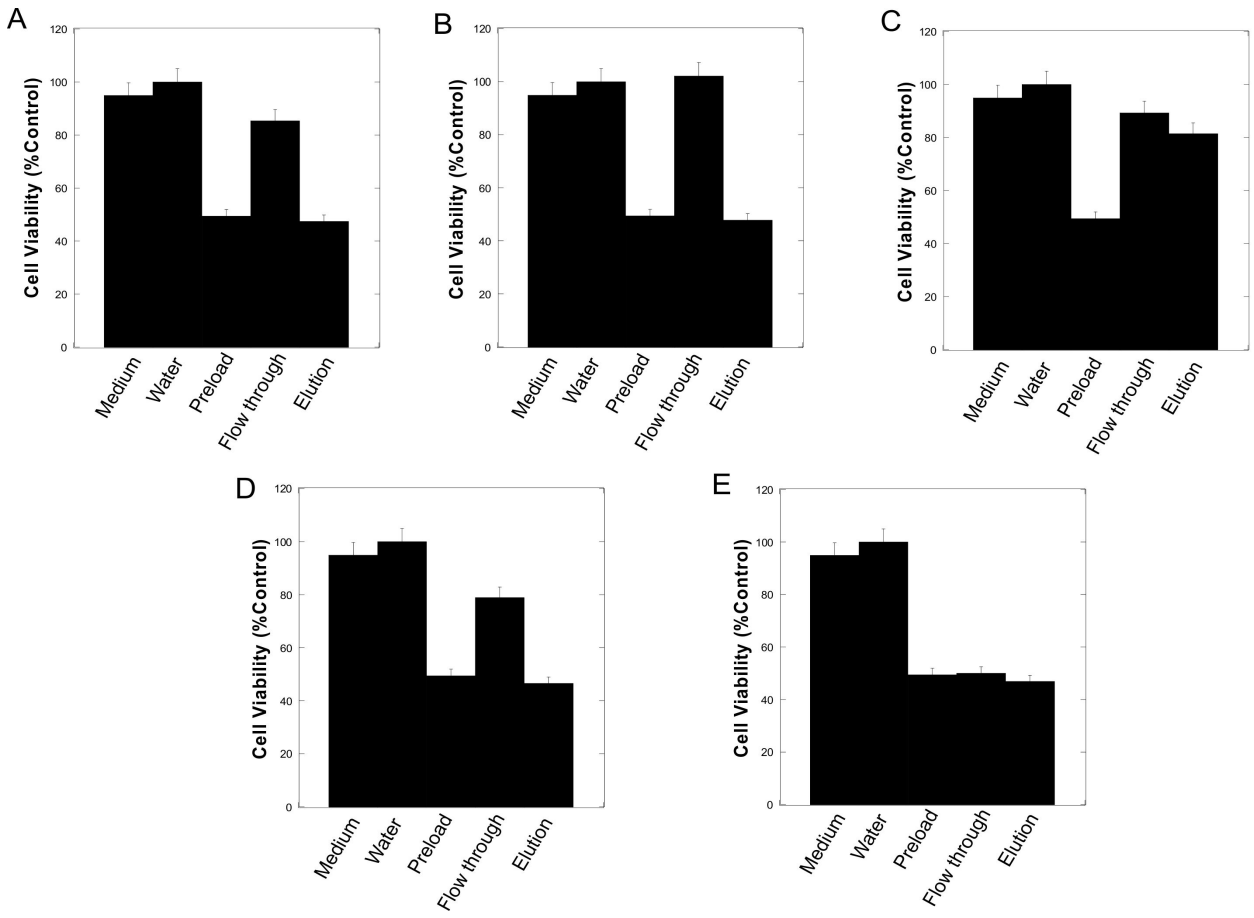

Fig. S 6. Growth-inhibitory assay for optimization of Sephadex DEAE with buffers at different pH including Bis-Tris at pH 6.48 (A), L-Histidine at pH 6.2 (B), Piperazine at pH 5.3 (C) and 9.73 (D), and Tris at pH 8.07 (E). Medium and water were used as negative controls. Error bars represent S.D.

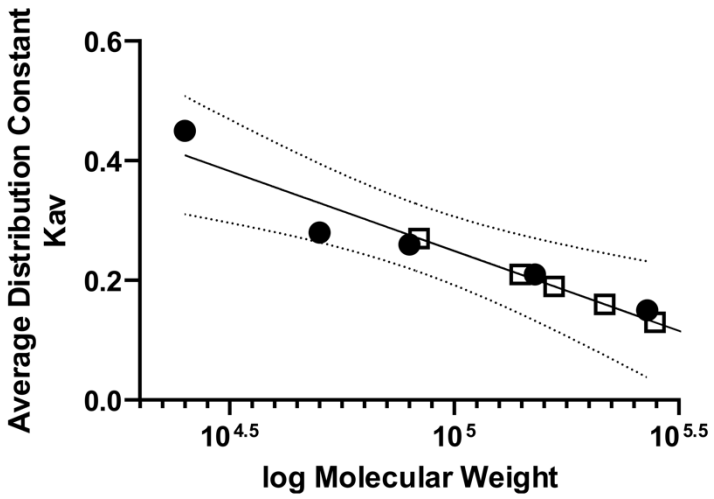

Fig. S 7. Estimating the peak maxima molecular weight (Mp) of EtGIPL1a using HPLC BioSEC-3. Dextran standards and EtGIPL1a were loaded onto BioSEC-3 at a flow rate of 1.2 mL/min. This was used to convert the retention time (Rt) to retention volume, and then to the Average Distribution Constant (Kav) as shown in Table S1. Closed circles represent the Dextran Standards used and open squares are all points of the interpolated molecular weight distribution of EtGIPL1a.

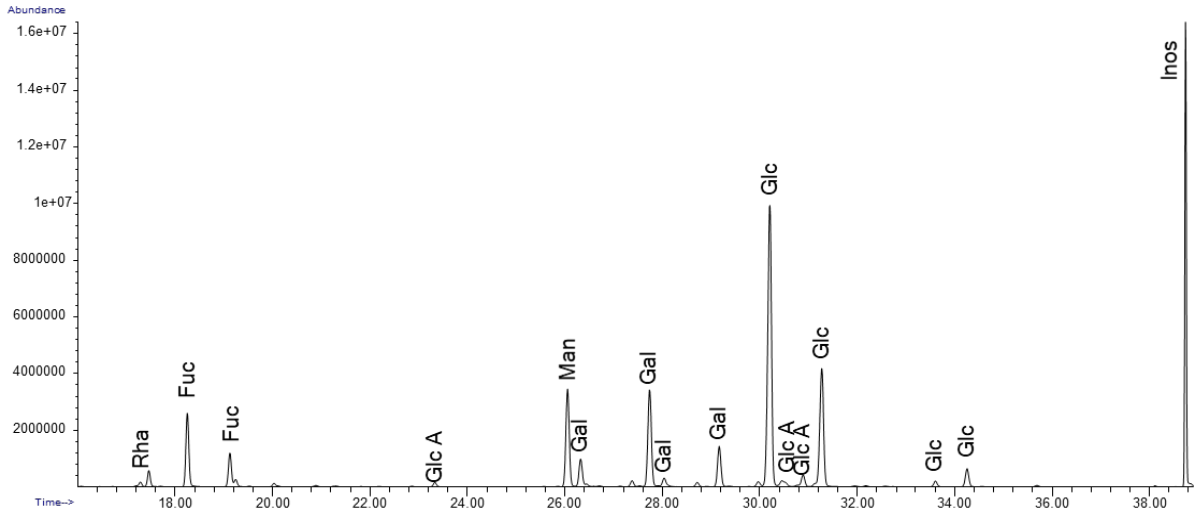

Fig. S 8. The GC-MS chromatograms from glycosyl composition analysis using TMS derivatization.

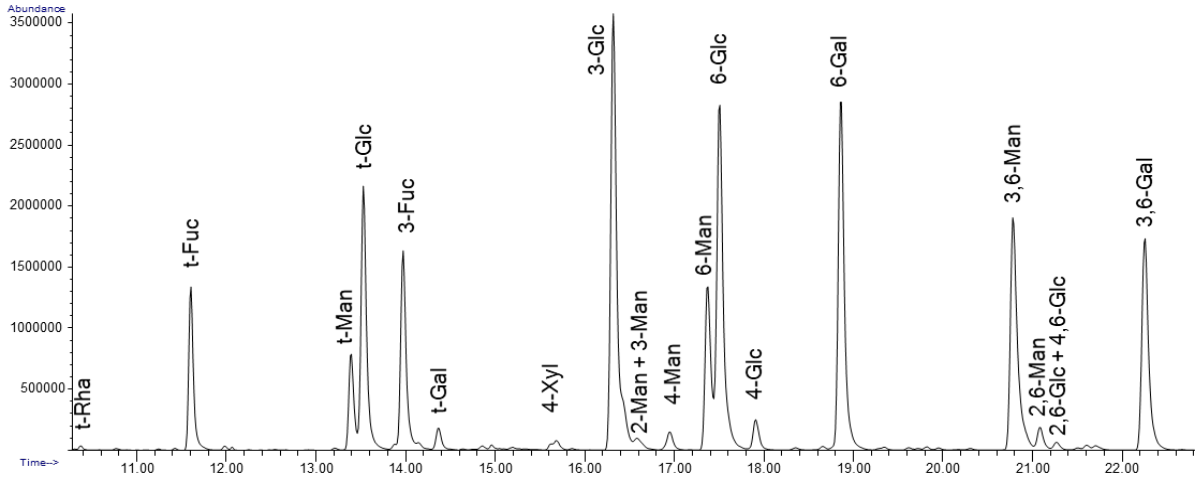

Fig. S 9. GC-MS chromatogram resulting from glycosyl linkage analysis of neutral and uronic acid residues. Glycosyl linkage analysis was performed by partially methylated alditol acetates (PMAAs). In the interest of clarity, PMAAs below 1% are not labeled.

Table S 3. Calculating the number (Mn) and weight average molecular weight (Mw) of EtGIPL1a

Rt time (min)	Rt volume (mL)	Ve-Vo	Kav=Ve-Vo/Vc-Vo	Mwt (log)	MW or Mi (g/mol)	Moles	ni (number of molecules)	niMi	wi	wiMi
5	6	0.74	0.0814978	5.635	431519	4.63479E-11	2.79107E+13	1.2044E+19	0.191902	82809.29
5.2	6.24	0.98	0.1079295	5.522	332659	6.01216E-11	3.62052E+13	1.2044E+19	0.191902	63837.87
5.4	6.48	1.22	0.1343612	5.447	279898	7.14546E-11	4.303E+13	1.2044E+19	0.191902	53712.94
5.6	6.76	1.5	0.1651982	5.335	216271[a]	9.24766E-11	5.56894E+13	1.2044E+19	0.191902	41502.8
5.8	6.96	1.7	0.1872247	5.222	166724	1.19959E-10	4.303E+13	7.1741E+18	0.114308	19057.92
6	7.2	1.94	0.2136564	5.147	140281	1.42571E-10	3.62052E+13	5.0789E+18	0.080924	11352.14
6.4	7.68	2.42	0.2665198	4.922	83560	2.39349E-10	2.79107E+13	2.3322E+18	0.03716	3105.103
						∑=	2.69981E+14	6.2761E+19		275378.1[b]

Twenty mg of EtGIPL1a was loaded onto BioSEC-3 at a flow rate of 1.2 mL/min. Vo is the void volume or Rt volume of Dextran Blue 2000 = 5.26 mL. Vc = 1 Column volume = 14.34 mL. Therefore, Vc-Vo = 9.08 mL.

[a]Molecular weight peak maxima (M_p) = 216271 g/mol.

[b]Weight average molecular weight (M_w) = 275378.1 g/mol.

Number average molecular weight (M_n) = 232465.3 g/mol. ($M_n = \Sigma niMi/\Sigma ni$)

Polydispersity index = 1.184 (PDI = M_w/M_n

Chapter 4: Lanostane triterpenoids, phenol and diphenylmethane derivatives from the fungus *Echinodontium tinctorium*

ABSTRACT

In our continuing search for bioactive metabolites from British Columbia wild mushrooms, bioassay-guided extraction, fractionation and chemical investigation of the organic extracts of the fruiting bodies from the fungus *Echinodontium tinctorium* resulted in the isolation of a new diphenylmethane derivative bis(2,4-dihydroxy-6-methylphenyl) methane (**2**), together with 5 known compounds (**1, 3-6**). The structures of **1-6** were determined by a combination of 1D and 2D NMR, ESI-MS and X-Ray crystallography. The full NMR data assignment of the known compound **(4)** and the crystal structures of **(2), (4)** and **(5)** are reported here for the first time. Furthermore, the biological activity of compounds **(2)**, **(4)** and **(5)** are shown here for the first time; they exhibited antiproliferative activity against U251 human glioblastoma cells with an IC_{50} of 85 μM, 4.6 μM, and 5.45 μM respectively. Compound **(2)** and **(4)** were also effective against HeLa cervical cancer cells with an IC_{50} > 100 μM and 1.2 μM respectively. Additionally, **(4)** also showed growth inhibition in multiple cancer cell lines with IC_{50} ranging from 2-5 μM. Flow cytometry analysis showed that compounds **(2)** and **(4)** can induce apoptosis in U251 cells.

4.1. Introduction

Glioblastoma (GB) is a highly aggressive and invasive cancer, most frequently diagnosed in adults in their mid 60's (Omuro & DeAngelis, 2013); it arises from multiple cell types with neural stem cell-like properties. Despite scientific advances, GB remains incurable with a short life expectancy of approximately 18 months post-diagnosis (Davis, 2016). Temozolomide is the only standard chemotherapeutic drug approved for the treatment of GB, with a treatment regimen that includes surgical resection, followed by radiotherapy and chemotherapy (Lim *et al*., 2018). Due to its invasiveness, chance of tumor recurrence and unwanted treatment side effects, there is a strong therapeutic need to find more effective drugs and targets. A number of promising synthetic small molecules (dos Santos *et al*., 2019) and natural products against GB have recently been tested (Erices *et al.*, 2018; Khan *et al.*, 2020).

As mentioned in the previous chapters of this thesis, *E. tinctorium* has not been studied in detail for its potential bioactive compounds. To date, 12 small molecules have been isolated from other *Echinodontium* species, which included *E. tsugicola* and *E. japonicum* (Table 4.1). Ye *et al*. (1996) and Bond *et al.* (1996) identified two small molecules (echinodol and echinotinctone) from *E. tinctorium*, but no bioactivity studies were provided for these small molecules and, as described in Chapters 2 and 3, two immuno-stimulatory and growth-inhibitory polysaccharides have been isolated and characterized from *E. tinctorium*.

Table 4.1. Small molecules isolated from *E. tinctorium* and related species

Compounds	**m/z**	**Source**	**Activity**	**Reference**
Echinotinctone	256	*E. tinctorium*	None	Ye *et al*., 1996
Echinodol	498	*E. tinctorium*	None	Bond *et al*., 1966
Tsugicolines A-E	267 (A) 351 (B) 269 (C) 249 (D)	*E. tsugicola*	A-active against *Lepidium sativum*	Arnone *et al*., 1995
Tsugicolines E-I	284 (E)	*E. tsugicola*	Antimicrobial	Arnone *et al*., 1998
Echinocidins A-D		*E. tsugicola*	None	Shiona *et al*., 2004, 2005
Echinodone	496	*E. tsugicola*	None	Kanematsu, 1972
Deacetyl-Echinotinctone	454	*E. tsugicola*	None	Kanematsu, 1972
3-Epiechinodol		*E. tsugicola*	None	Kanematsu, 1972
Deacetyl-3-epiechinodol	440	*E. tsugicola*	None	Kanematsu, 1972
Echinolactone A	245	*E. japonicum*	None	Suzuki *et al*., 2005
Echinolactone B	261	*E. japonicum*	None	Suzuki *et al*., 2005
3-Epi-illudol		*E. japonicum*	None	Suzuki *et al*., 2005

The goal of this study was to isolate and characterize small molecules from *E. tinctorium* and then assess them for growth-inhibitory activity, especially against human glioblastoma cells. To achieve this goal, multiple approaches were used which included two solvent phase separation, sequential phase separation and direct extraction of powdered mushroom. Sephadex LH-20 size exclusion chromatography (SEC), silica flash column chromatography (SFC) and high-

performance liquid chromatography (HPLC) were employed for purification. Structural elucidation was carried out with the help of electrospray ionization mass spectrometry (ESI-MS), Fourier transform infrared spectroscopy (FTIR), 1D and 2D nuclear magnetic resonance spectroscopy (NMR), and X-ray crystallography. For evaluation of biological activity, growth-inhibitory assay MTT was performed and mechanism of growth-inhibition was confirmed by apoptosis and cell cycle analyses. Potential molecular targets of isolated small molecules were also identified using the MolTarPred software.

4.2. Materials and methods

4.2.1. Materials and reagents

All reagents were of analytical grade. Eagle's Minimal Essential Medium was from LONZA (Walkersville, Maryland, USA). 3-(4,5-dimethylthiazol-2-yl)-2-5 diphenyltetrazolium bromide (MTT) and dimethylsulfoxide (DMSO) were obtained from Sigma-Aldrich (St. Louis, MO, USA). Fetal bovine serum (FBS) was from Life Technologies Inc. (Waltham, Massachusetts, USA). Sephadex™ LH-20 resin was purchased from GE Healthcare (Chicago, IL, USA). All cell lines were obtained from the American Type Culture Collection. HPLC analysis was performed on an Agilent 1260 Infinity Systems with DAD detector. Low resolution mass spectrometry was performed on an Agilent 6120 Single Quad MS. For high resolution electrospray ionization mass spectrometry (HRESIMS), an Agilent 1200 HPLC and a Bruker maXis Impact Ultra-High Resolution tandem TOF (UHR-Qq-TOF) mass spectrometer was used at the Mass Spectrometry Facility, Simon Fraser University (SFU). NMR analyses was conducted on a 600 MHz NMR spectrophotometer at University of British Columbia (UBC). HPLC grade solvents were used and were purchased from BDH (Mississauga, ON, Canada).

4.2.2. Collection and extraction of the mushroom

E. tinctorium conks were collected as described in Chapters 2 and 3. The mushroom was sequenced to confirm its identity. For isolation of small molecules from *E. tinctorium*, three different extraction approaches were used: two solvent phase separation (approach 1), sequential phase separation (approach 2), and direct extraction (approach 3).

4.2.3. Approach 1: Two solvent phase separation

4.2.3.1. Extraction and phase separation

Powdered *E. tinctorium* was sequentially extracted with 80 % ethanol (65 ºC, 3 h) followed by extraction with 50 % methanol (65 ºC, 3 h) to give crude extract E2. The crude extract E2 was reconstituted in water and partitioned with chloroform to yield two separate layers; top aqueous layer L1 and bottom organic layer L2. Both layers were dried; L1 was lyophilized whereas L2 due to high organic content was dried using a rotary evaporator.

4.2.3.2. Assessment of growth-inhibitory activity

Dried L1 and L2 were reconstituted in methanol at 20 mg/mL, filter sterilized (2 µm) and tested for growth-inhibitory activity in HeLa cells using MTT assay as described in Chapter 3. L1 and L2 were tested on HeLa cells at a final concentration of 0.1-1 mg/mL. L2 was also tested on rat intestinal epithelial cells (RIE-1) to compare the results with colorectal adenocarcinoma cells (SW480). After confirmation of biological activity, L1 and L2 were subjected to Sephadex LH-20 SEC to estimate the relative size of bioactive compound(s). As discussed in Chapter 3, L1 contained relatively large molecular weight compound while low molecular weight compound with potential growth-inhibitory activity was expected to be in L2. Therefore, L2 was further studied here.

4.2.3.3. Purification by Sephadex LH-20 SEC

Sephadex LH-20 resin was soaked in methanol for 48 h. Column was packed (2 mL/min, methanol) and equilibrated (2 CV, 1 mL/min, methanol). Initially, a 25 mL gravity drip column was used, which was then upscaled to a 80-100 mL column (mobile phase; methanol, 1 mL/min). Ten mL fractions were collected, concentrated to half the volume and tested for growth-inhibitory activity using MTT assay.

4.2.3.4. HPLC analysis and purification

Post-Sephadex LH-20 purified bioactive fractions were pooled, concentrated and subjected to HPLC analysis. A solvent gradient (Fig. 4.1) of acetonitrile and 0.2 % formic acid in water was run at 0.7 mL/min. A 10 µL sample was injected via an autosampler onto the HPLC column

(Phenomenex synergy 4µ Hydro-RP 80 Å, 150 × 4.6 mm). Once the bioactive fractions were analyzed, the most abundant peak was fraction collected, purified and re-injected into HPLC to assess for % purity.

Time [min]	A [%]	B [%]	C [%]	D [%]	Flow [mL/min]	Max. Pressure Limit [bar]
0.00	0.0	5.0	95.0	0.0	0.700	150.00
1.50	0.0	5.0	95.0	0.0	---	---
2.50	0.0	50.0	50.0	0.0	---	---
15.00	0.0	95.0	5.0	0.0	---	---
17.00	0.0	100.0	0.0	0.0	---	---
20.00	0.0	100.0	0.0	0.0	---	---
22.00	0.0	5.0	95.0	0.0	---	---
23.00	0.0	5.0	95.0	0.0	---	---

Fig. 4. 1. HPLC solvent gradient for analysis and purification. B is % of acetonitrile and C is % of 0.2 % formic acid in water.

4.2.3.5. ESI-MS analysis

HPLC-purified compound was subjected to ESI-MS (Agilent 6120 Single Quad MS) analysis using the same solvent gradient as in Fig. 4.1. Flow injection analysis (FIA) was conducted to optimize the MS conditions. The ESI-MS parameters optimized for analysis are shown in Table 4.2.

Table 4. 2. Parameters for mass spectrometry analysis

MSD signal parameters	ESI MS mode = Positive mode Scan range = 100-1000 m/z Ion source = API-ES Fragmentor = 70-400 V (100 V optimized) Gain = 1 Threshold = 150 Step size = 0.10 Speed (µL/sec) = 867
MSD spray chamber	Method spray chamber = API-ES Drying gas flow (L/min) = 12 Nebulizer pressure (psig) = 40 Drying gas temperature (°C) = 340 Capillary voltage VCap (V) = 3000 (+), 3000 (-)
MSD status	Quad temperature (°C) = 100 Capillary current (nA) = 6 Chamber current (µA) = 0.69

4.2.4. Approach 2: Sequential phase extraction

4.2.4.1. Sequential phase extraction and assessment for growth-inhibitory activity

Crude methanol extract E2 was sequentially phase-separated with multiple solvents in order of increasing polarities (Fig. 4.8A). E2 was suspended in water at a concentration of 10 mg/mL extracted 3-5 times with hexane, followed by chloroform, and ethyl acetate (EA). It was assumed that water layer retained large molecules as seen in approach 1. The other three organic layers were expected to contain small molecules. All three layers were dried, resuspended in methanol and assessed for growth-inhibitory activity at 0.4 mg/mL for 48h in HeLa cells using MTT assay.

4.2.4.2. HPLC analysis of phase separated layers

Once bioactivity was confirmed, each layer was subjected to HPLC analysis independently. HPLC method development involved optimization of column type, solvents, solvent gradients, and flow rate. HPLC analysis revealed that all the layers possess many peaks indicating the presence of many compounds. Due to many peaks in each layer, it was concluded that an additional purification step needs to be incorporated into the purification methodology.

Based on the amount of material that each layer weighed, EA layer weighed the most, followed by chloroform layer and hexane layer, therefore, EA was considered first for further purification.

4.2.4.3. Approach 2a: Purification of EA layer by Sephadex LH-20 SEC

The dried EA layer was subjected to purification by SEC using Sephadex LH-20 resin. Dried EA layer was resuspended in methanol (20 mg/mL), filtered and loaded onto the column. Methanol was used as a mobile phase and run at a flow rate of 1 mL/min. Fractions were collected (3 mL, 2-3 CV), concentrated, and tested for growth-inhibitory activity in HeLa cells using MTT assay. The Sephadex LH-20 column retained most of the compounds in EA layer as most of the preload was visible at the top of the column.

4.2.4.4. HPLC analysis of Sephadex LH-20 purified compounds

Bioactive fractions were pooled and scanned using nanodrop for optimal wavelength. Sephadex LH-20 eluted fractions were further purified by HPLC. HPLC method development

was performed for optimized conditions. A 2 mg/mL preload was run through the column (Phenomenex Luna C18(2), 5µ, 250 × 4.6 mm) at a flow rate 0.7 mL/min using acetonitrile and water gradient. Due to the fact that most of the compounds interacted and were retained by the Sephadex LH-20 resin, it was concluded that perhaps an alternative strategy is needed to resolve a range of different compounds.

4.2.4.5. Approach 2b: Purification of EA layer by silica flash column chromatography

Thin layer chromatography (TLC) was first used as a preliminary step to develop the solvent system for separating compounds in the EA layer. The optimized conditions were then used to run the column.

4.2.4.6. TLC method development

Prior to running the silica flash column, method was developed on a TLC with individual and combination of solvents. A dilute solution of EA layer was made and spotted onto aluminum baked silica plate. The best results were obtained by running hexane first which removed very non-polar compounds. Apparently, no compounds were observed to migrate on the TLC plate with hexane. It could be that those compounds were not UV active. EA was then used to run through TLC which resulted in separation of compounds that appeared under UV. There were some compounds that appeared to be still present at the origin line, indicating that a more polar solvent can be used to mobilize them from the baseline. Therefore, methanol was used to mobilize the compounds retained at the origin line. Methanol was successful in achieving further separation of more polar compounds.

4.2.4.7. Purification by Silica Flash Column (SFC)

Packing SFC: Silica was used as a stationary phase with hexane initially, followed by EA, methanol and finally chloroform were used as mobile phase. Initially, a 50-60 mL SFC was used and was later on up-scaled to a larger sized column. For stationary phase, silica powder was suspended in hexane to make a slurry. Silica slurry was poured by sliding through the side of the column to avoid entrapment of air bubbles. The column was packed by passing hexane and applying air pressure through an adaptor connected to the air hose.

Running SFC: A concentrated sample of EA layer was then applied to the column with a Pasteur pipette. Initially, hexane was allowed to run through the column. For each solvent elution, 20 fractions of 1 mL fraction size were collected and analyzed. A quadrant test was performed where each collected fraction was simultaneously spotted onto TLC plate and visualized under short and long wave UV. The hexane-eluted fractions were not visible under UV whereas the EA eluted fractions 4 to 9 were visible under UV. For methanol solvent elution, fractions 6 to 8 were visible. All the fractions from hexane, EA, and methanol were dried and re-suspended in methanol to test for growth-inhibitory activity against HeLa cells using MTT assay.

4.2.4.8. Additional purification of Post SFC fractions

The bioactive fractions from SFC were subjected to additional purification by the following approaches:

(i) SFC with solvent gradient in the elution order of 20% methanol → 60% methanol → 80% methanol → 100% methanol → 100 % acetonitrile → IPA

(ii) SFC with solvent gradient in the elution order 100 % methanol → 80 % methanol → 60 % methanol →40 % methanol → 1 % Acetic acid in water → Chloroform → EA

(iii) SFC with solvent gradient as chloroform → EA → Acetonitrile → Methanol → 1 % Acetic acid in water → Acetone → Chloroform → EA

(iv) Sephadex LH-20 using methanol as mobile phase.

Since approach (iv) gave best results therefore, it was used for further purification of compounds from EA layer.

4.2.4.9. HPLC analysis and purification of Post SFC fractions

After confirmation of growth-inhibitory activity, the bioactive fractions were subjected to HPLC analysis (Phenomenex Luna C18(2), 5µ, 250 × 4.6 mm), using acetonitrile, water, and methanol gradient (0.5-1 mL/min, λ = 260 nm) as in Fig. 4.2. The most abundant peaks were fraction collected in 6 mL vials. After collection, the peaks were concentrated and reinjected into HPLC to determine % purity. These pure peaks were designated as **(1)** and **(2)**.

Time [min]	A [%]	B [%]	C [%]	D [%]	Flow [mL/min]
0.00	0.0	20.0	60.0	20.0	0.500
14.00	0.0	40.0	20.0	40.0	0.500
15.00	0.0	50.0	0.0	50.0	1.000
20.00	0.0	50.0	0.0	50.0	1.000
23.00	0.0	20.0	60.0	20.0	0.500

Fig. 4. 2. HPLC solvent gradient for analysis and purification. B, C and D refers to acetonitrile, water and methanol.

Additionally, all the EA eluted fractions from large SFC were analyzed by HPLC. The analysis was performed on Phenomenex Luna C18(2) column at 1 mL/min using three solvent gradient (acetonitrile: water: methanol, 25.5:49:25.5 to 26:48:26 in 8 min, 100:0:0 from 10-15 min, 60:30:10 from 15-18 min, 25.5:49:25.5 from 20-25 min). Three abundant peaks containing compounds **1-3** were fraction collected and purified.

4.2.4.10. Structural elucidation of compounds from EA layer

Structural elucidation of compounds **(1-3)** purified from EA layer was performed using ESI-MS, FTIR and NMR. ESI-MS and FTIR were performed as mentioned earlier. A high resolution ESI-MS in positive scan mode (m/z 100 – 1500 Da), was performed on compound **(3)**. Acetonitrile/water (0.1 % formic acid) was used as mobile phase. For FTIR, twenty-two scans were collected to generate an IR spectrum. Further structural details of the HPLC-purified compounds **(1-3)** were obtained from NMR. 1D proton (^{1}H) and carbon (^{13}C) NMR and 2D NMR including ^{1}H-^{13}C HSQC, ^{1}H-^{13}C HMBC, ^{1}H-^{1}H COSY, and ^{1}H-^{1}H NOESY, were carried out using a 600 MHz NMR spectrophotometer.

4.2.4.11. Crystallization of compound (2)

For crystal formation of **(2)**, vapor diffusion and slow evaporation methods with multiple solvent combinations were used.

Vapor diffusion method

A saturated solution of **(2)** was made in methanol and kept in a 1.5 mL glass vial. The 1.5 mL vial was placed in a 25 mL glass vial containing hexane as the surrounding medium. The vial was capped and kept for 2 weeks to allow slow vapor diffusion of hexane into the sample vial.

Slow evaporation

Three solvent systems were used in an effort to crystallize **(2)**:

a. Saturated solution of **(2)** was made in methanol/acetonitrile and kept for slow evaporation at room temperature for 2 days in a small beaker.
b. Saturated solution of **(2)** was made in methanol/acetone and kept for slow evaporation at -20 °C and monitored at multiple time points.
c. Saturated solution of **(2)** was made in methanol/hexane and kept at -20 °C for slow evaporation overnight.

4.2.4.12. Crystallization of compound (3)

Slow evaporation

For crystal formation of **(3)**, slow evaporation with different solvents was experimented. The solvents included acetonitrile/methanol, acetone/methanol, and methanol alone. About 2 mg of **(4)** was dissolved in 100 μL of solvents to make a saturated solution and kept in a 1.5 mL glass vial at room temperature to allow slow evaporation.

Vapor diffusion

A 2 mg of **(3)** was dissolved in methanol in a 300 μL narrow glass insert which was then placed in a small beaker containing antisolvent hexane. The beaker was covered with a plastic wrap. The antisolvent was allowed to vaporize and mix with the methanol dissolved **(3)** for 2 days as well as slow evaporation of both the solvents through the plastic wrap.

Recrystallization

A saturated solution of **(3)** was made by dissolving 2 mg in minimal amount of acetonitrile. The solution was kept in a 1.5 mL glass vial and heated in a heat block (55 ºC, 5-7 min) until all dissolved. The solution was cooled on ice bath and then kept undisturbed.

4.2.4.13. Purification and HPLC analysis of phase separated hexane layer

Hexane layer was subjected to HPLC analysis on a Phenomenex Luna C18 HPLC column using acetonitrile/water gradient (20 % to 90 % acetonitrile in 10 min) at 0.8 mL/min. The absorption wavelength was set at 250 nm for analysis.

Due to the crude nature of hexane extract that contained many compounds, a small-scale gravity drip SFC was performed to purify compounds in the hexane layer. A 95:5 ratio of hexane: IPA was used as mobile phase. The solvent was optimized by method development on TLC. Twelve fractions of 1 mL each were collected. The eluted fractions from SFC were spotted onto TLC to run a quadrant test. The quadrant test confirmed the UV active compounds. The UV active fractions were then subjected to HPLC analysis (Isocratic Hexane/IPA 95/5%, 0.7 mL/min, 220 and 240 nm) on Phenomenex Luna C8(2) HPLC column.

4.2.4.14. Purification and HPLC analysis of phase-separated chloroform layer

The phase-separated chloroform layer was analyzed by HPLC on Phenomenex Luna Phenyl-Hexyl column (250 x 4.6 mm, 100 Å, 5µm) using three solvent gradient (acetonitrile: water: methanol 10:25:65 to for 10:10:80 in 10 min then 0:0:100 for an additional 5 min) at 1 mL/min flow rate.

Further purification was carried out by Sephadex LH-20 SEC and SFC. The chloroform layer was run through a medium sized SEC column (100 mL) using methanol as mobile phase at 1 mL/min. A total of 30 fractions of 5 mL each was collected. The Sephadex LH-20 collected fractions were assessed for growth inhibition in HeLa cells. The bioactive fractions were then analyzed by HPLC. Based on similar HPLC profiles, the bioactive fractions 14-16 and fractions 17-20 were pooled separately. The peaks abundant in these fractions were collected and analyzed.

Additionally, chloroform layer was also purified by another method using SFC. A solvent gradient approach was used to elute compounds starting with more non-polar hexane, followed by chloroform, acetone, ethyl acetate and finally more polar methanol. For each solvent elution 5-7 fractions of 4 mL each were collected, dried and injected into HPLC. The post SFC fractions were compared with the post-Sephadex LH-20 bioactive fractions.

4.2.5. Approach 3: Direct extraction method

4.2.5.1. Solid-liquid extraction and assessment for growth-inhibitory activity

A solid-liquid extraction of *E. tinctorium* material was performed with organic solvents as shown in Fig. 4.60. Initially, 10 g of mushroom powder was extracted with hexane (200 mL, 3 h, RT). The flask was agitated several times and supernatant was collected. The procedure was repeated twice with same conditions and the final extract was soaked in hexane (100 mL, overnight, RT). All hexane supernatants were pooled, partitioned with water to remove any polar compounds and finally dried. The dried hexane layer was reconstituted in acetonitrile and subjected to HPLC analysis. The same procedure was repeated for diethyl ether (DEE) solid-liquid extraction. The DEE dried extract was also reconstituted in acetonitrile and subjected to HPLC analysis. Moreover, hexane and DEE extracts were reconstituted in methanol at a concentration of 0.6 mg/mL and 0.7 mg/mL and assessed for growth-inhibitory activity in HeLa cells using MTT assay.

4.2.5.2. HPLC analysis and purification of hexane extract

The hexane extract was subjected to HPLC analysis using reverse phase LC column (Phenomenex Luna C18(2) 5µm, 100 Å, 250 × 4.6 mm). The following conditions were used to run the sample; mobile phase as acetonitrile: water 80:20 to 90:10 in 10 min, 90:10 from 10-20 min, 80:20 in 25 min and until 40 min, flow rate = 1 mL/min, DAD = 210, 230 nm.

The purification method for hexane layer was upscaled to semi-preparative column (Agilent Zorbax Eclipse XDB C18 9.4 × 250mm 5µ) with isocratic solvent (Acetonitrile: Water 90:10) at a flow rate 2 mL/min for 40 min.

4.2.5.3. Structural elucidation by spectroscopy

The MS analysis of compounds isolated from hexane extract was determined with positive mode ESI-MS using solvent gradient (Acetonitrile: Water 80:20 to 90:10 in 15 min, 90:10 from 15-22 min, 90:10 to 80:20 in 25 min) at 0.8 mL/min. Scan (100-1000 m/z) and SIM mode were used to confirm the mass.

The functional group analysis was performed by FTIR (Bruker ATR-FTIR spectrophotometer by Billerica, MA, USA) with a frequency range 4000-400 cm^{-1}. An IR spectrum was generated using OPUS software. A total of twenty-two scans were obtained. For more detailed structural insights, 1D and 2D NMR analyses were carried out using a 600 MHz NMR spectrophotometer at UBC.

4.2.5.4. Crystallization of compound (4)

Method 1: Compound **(4)** was dissolved in minimal volume of 90 % acetonitrile to yield a saturated solution. The solution was kept in a narrow glass insert with a 300 µL capacity and placed in a 1.5 mL glass vial with holes in the rubber cap. The vial was kept at room temperature for slow evaporation.

Method 2: A saturated solution of compound **(4)** was made with acetonitrile in a 1.5 mL glass vial for recrystallization. The vial was heated at 55 °C in a heating block for 3-4 min until all dissolved. It was then kept on an ice bath for 10 min and kept at room temperature overnight.

Method 3: Compound **(4)** saturated solution was made by adding 90 % acetonitrile and placed in a 6 mL glass vial. The solution was left for slow evaporation at room temperature.

4.2.5.5. Crystallization of compound (5)

Method 1: Vapor diffusion method was used where a saturated solution of **(5)** was made in acetonitrile and kept in a 2 mL glass vial, which was then placed in a 10 mL glass vial (screw capped) with hexane anti-solvent. The vials were placed at 2-4 ºC for a few days.

Method 2: **(5)** was dissolved in acetonitrile/methanol mix and kept for 4-5 days in a 6 mL wide glass vial (covered) for slow evaporation at room temperature.

Method 3: A saturated solution of **(5)** was made with 90 % acetonitrile/water mix in a 2 mL glass vial. The sample vial was placed open in another 6 mL glass vial (covered) and kept overnight for slow evaporation at room temperature.

4.2.5.6. Melting point determination

Melting point of compound **(2)** and **(4)** were determined using a melting point apparatus (DigiMelt MPA160, Stanford research systems, USA) with a ramp rate 2-5. Initial and final melting point range was recorded for each compound.

4.2.5.7. HPLC-MS analysis of Diethyl ether extract (DEE)

Diethyl ether extract was reconstituted in acetonitrile and subjected to HPLC analysis on Phenomenex Luna C18(2) analytical column using gradient elution (Acetonitrile 60-100 % in 25 min, 100-60 % in 30 min) at 0.8 mL/min with DAD (210, 230 nm). The ESI-MS analysis was carried out by including 0.1 % formic acid in mobile phase. The fragmentor was set to 80 V with a gain of 1.

4.2.5.8. Growth-inhibitory activity and flow cytometry analysis of purified compounds

The growth-inhibitory activity of purified compounds was first assessed on HeLa cells as well as on other cancer cell lines and normal immortalized cell lines. Percent cell viability was determined using MTT assay as described in Chapter 2.

Flow cytometry analysis was carried out on U251 glioblastoma cells using Annexin V and PI double staining analysis. Cells were plated at a seeding density of 20 x 10^4 cells/mL in 6 well plates and incubated for 24 h after which they were treated with control and purified compounds at different concentrations. For compound **(2)**, cells were treated with 50 μM and 100 μM for 24-48 h and then assessed for apoptosis and cell cycle using flow cytometry. For compound **(4)**, cells were treated with concentrations at 4.3 μM, 10 μM, 20 μM, and 40 μM for 24-48 h time intervals. After 24-48 h of treatment, cells were harvested, washed with DPBS, spin twice at 400 x g for 5 min at room temperature. Supernatant was discarded and cell pellets were resuspended in DPBS, cells were counted and spun again at 4 °C, after which the pellets were resuspended in binding buffer to achieve a cell density of 1.5 x 10^6 cells/mL. Cells were then stained with annexin V and PI and kept in the dark at room temperature for 15 min. DPBS was added and double stained cells were filtered and analyzed by flow cytometry.

4.2.5.9. Molecular target prediction of compounds (1-5)

Initially, chemical structures were drawn in Chemdraw, which were then used to generate a chemical notation, using SMILE (Simplified Molecular Input Line Entry System). SMILE format was entered into the MolTarPred program and targets were predicted in different organisms with a reliability of prediction score. Given below are the SMILE format generated for purified compounds:

Compound **(1)** OC1=CC(O)=CC(C)=C1

Compound **(2)** CC1=C(CC2=C(O)C=C(O)C+C2C)C(O)=CC(O)=C1

Compound **(4)** OC1CCC2(C)C(CCC3=C2CCC4(C)C3(C)CC5C4C(C)C(OC(C)=O)C(/C=C(C)/C)O5)C1(C)C

Compound **(5)** O=C1CCC2(C)C(CCC3=C2CCC4(C)C3(C)CC5C4C(C)C(OC(C)=O)C(/C=C(C)/C)O5)C1(C)C

4.3.Results and Discussion

4.3.1. Approach 1-Two Solvent Phase Separation

4.3.1.1. Extraction and assessment of growth-inhibitory activity

E2 was extracted from powdered *E. tinctorium* using manual extraction. L1 and L2 were obtained as a result of phase separation (Table 4.3). As shown in Fig. 4.3, L2 showed growth-inhibitory activity on HeLa, RIE-1 and SW480 cells.

Table 4. 3. Quantitative estimation of E2, L1 and L2 layers after phase separation

Exp #	E2 (mg)	L1 (H_2O layer) (mg)	% Yield	L2 (Chloroform layer) (mg)	% Yield
1	20	11	55	9	45
2	20	11.5	57.5	7.5	37.5
3	30	15	50	10.8	36

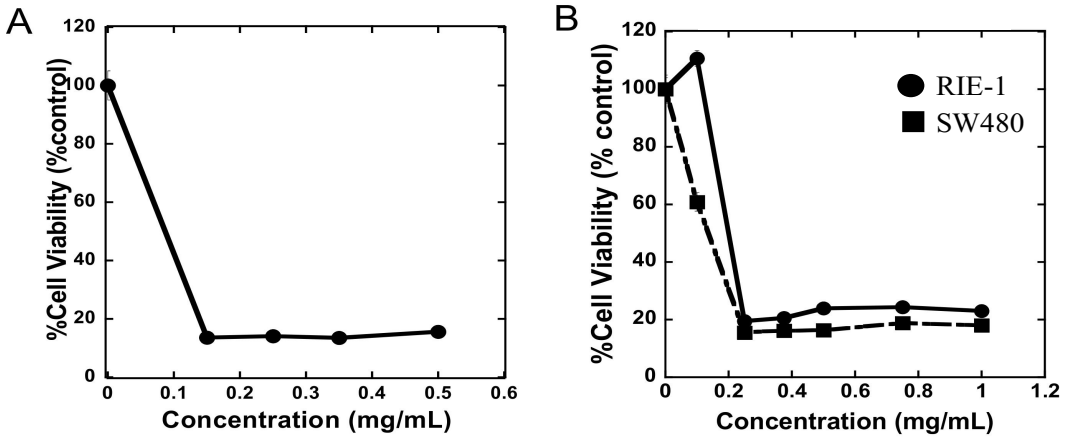

Fig. 4. 3. Dose dependent growth-inhibitory effect (n=3) of L2 at 0.1-1 mg/mL for 48 h on HeLa cells (A), RIE-1 and SW480 cells (B).

4.3.1.2. Purification by Sephadex LH-20 and HPLC

Bioactivity-guided purification (Fig. 4.4A) was done initially using Sephadex LH-20 and finally with HPLC. The Sephadex LH-20 elution profile (Fig. 4.4B) showed bioactive fractions from F17-F26, indicative of the presence of low molecular weight compounds contributing to the growth-inhibitory effects. An additional small scale liquid-liquid extraction was done and bioactive methanol layer was then subjected to HPLC analysis and purification.

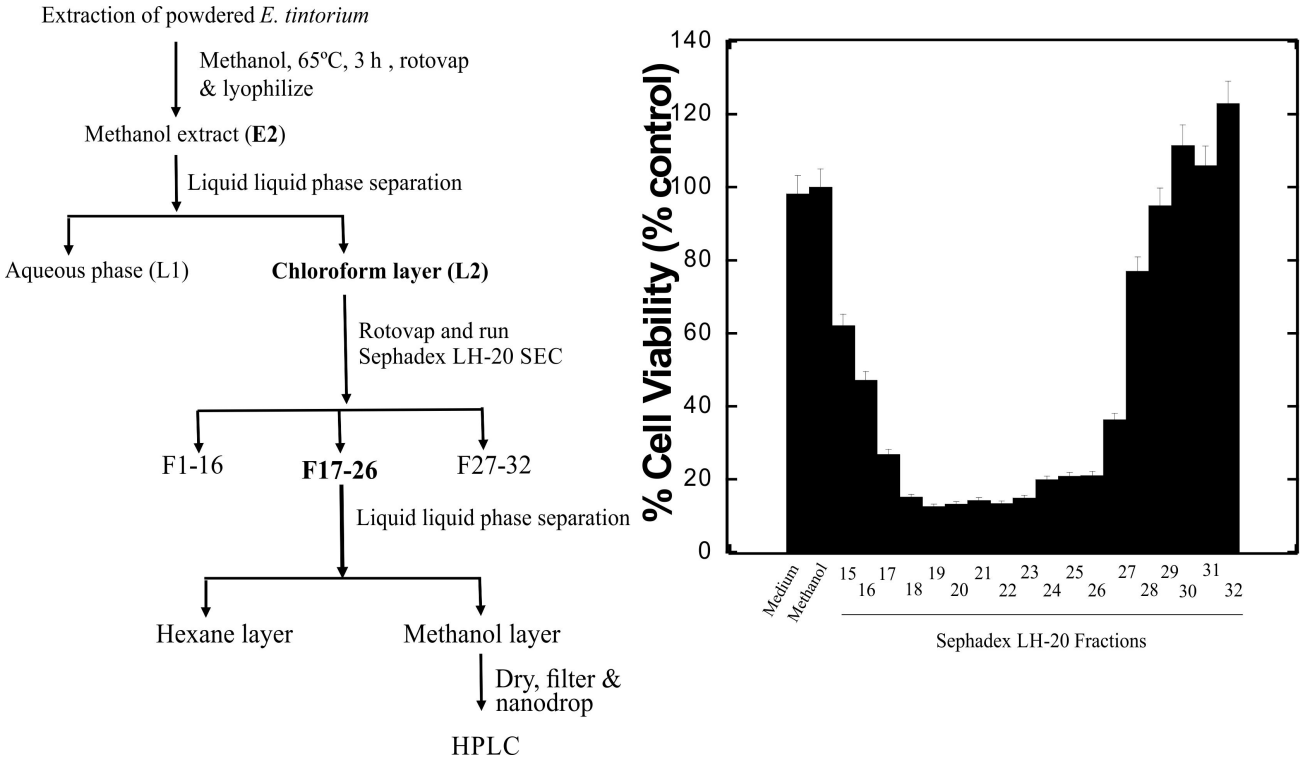

Fig. 4. 4. A) Purification strategy using two solvent phase separation. B) Sephadex LH-20 SEC elution profile for growth-inhibitory small molecule(s). A representative data from three biological replicates.

HPLC analysis of bioactive fractions on HydroRP column at 238 nm displayed one abundant peak retained at 5.9 min with some shoulder peaks (Fig. 4.5A). Purification and fraction collection of this peak resulted in a pure peak (Fig. 4.5B).

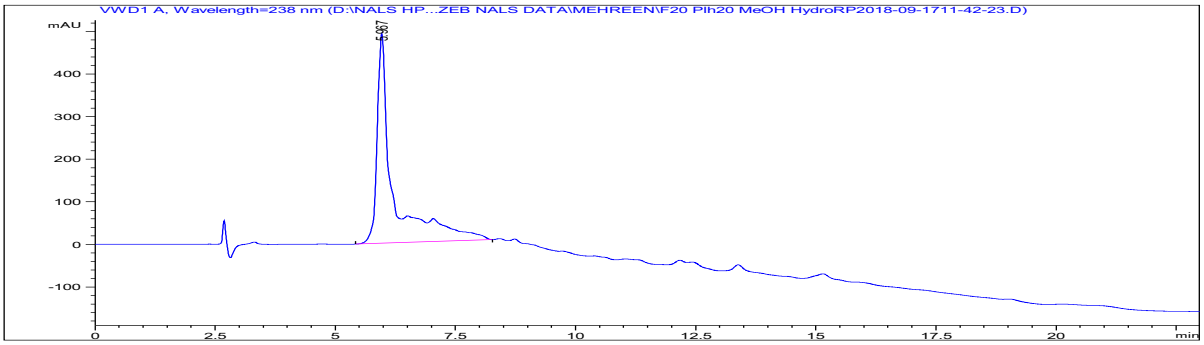

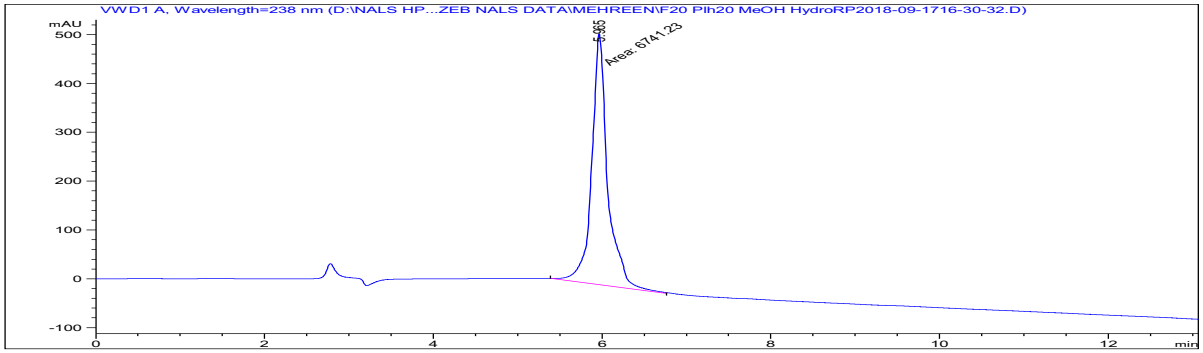

Fig. 4. 5. HPLC spectrum of Post Sephadex LH-20 purified F20 (A) and HPLC purified compound (B) at 238 nm.

4.3.1.3. Mass spectrometric analysis of HPLC-purified compound

Flow injection analysis (FIA) showed the optimum ionization conditions at fragmentor voltage 100 and 130 V (Fig. 4.6), therefore 100 V was used for further MS analysis. MS scan (Fig. 4.7A) showed the presence of three abundant MS ions at m/z 249, 251, and 293 [M + H] which were then analyzed in SIM (single ion mode). SIM (Fig. 4.7B) showed two equally abundant MS ions at m/z 249 and 293 [M + H] with a difference of -44. Such results suggest that a COO^- group came off from 293 [M + H], giving rise to its fragment 249 [M + H].

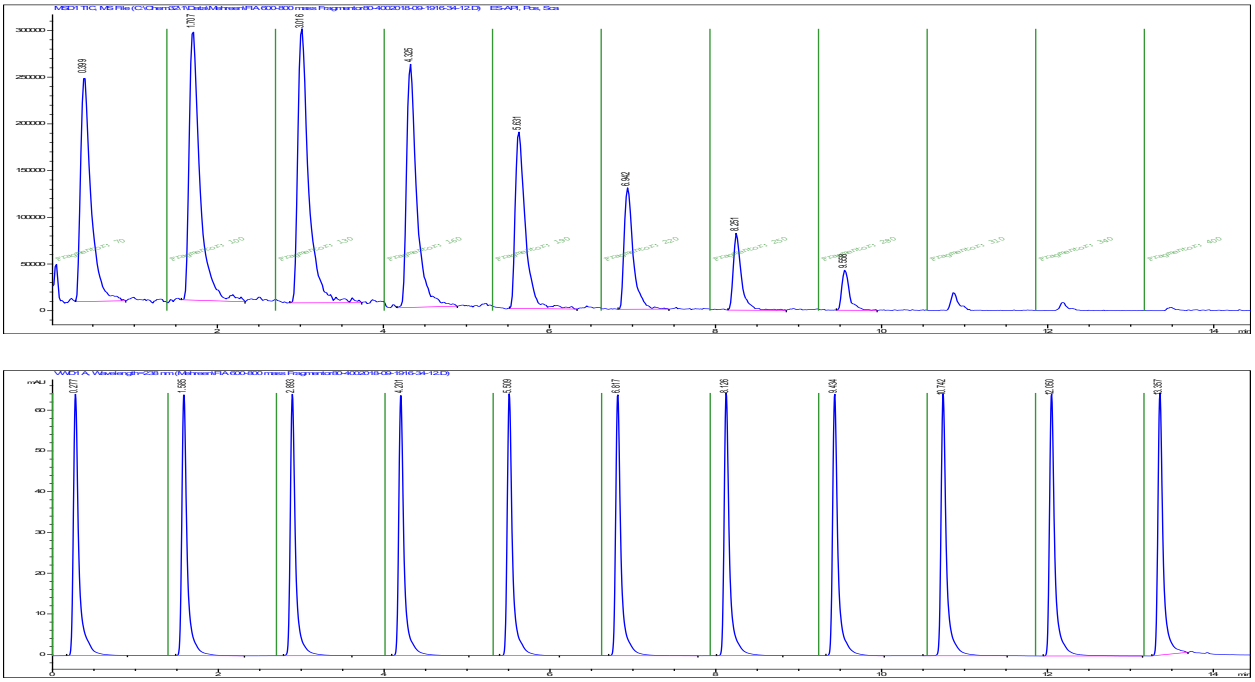

Fig. 4. 6. ESI-MS FIA of HPLC purified compound at fragmentor voltage 40-400 V in UV (A) and MSD scan signal (B).

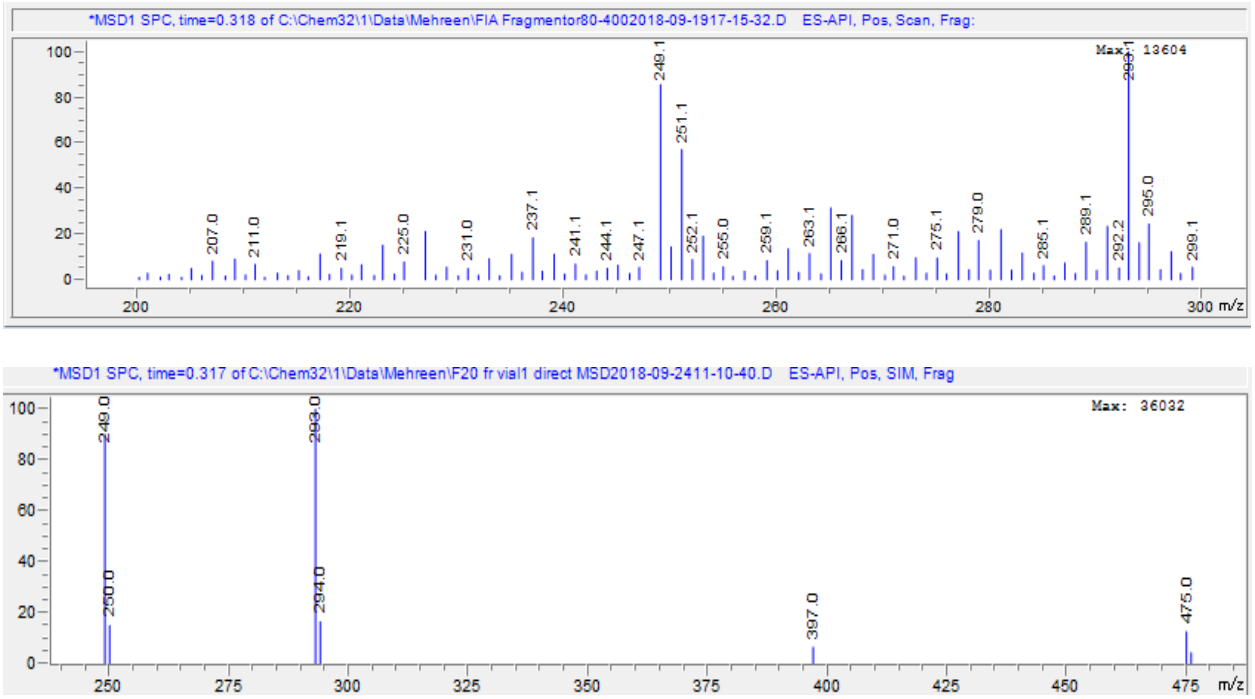

Fig. 4. 7. ESI-MS spectrum of F20 in scan mode (A) and SIM mode (B).

4.3.2. Approach 2: Sequential phase extraction

4.3.2.1. Sequential phase separation and assessment for growth-inhibitory activity

E2 was subjected to sequential phase separation in order to extract small molecules of different polarities (Fig. 4.8A). As a result of phase separation, EA layer has the highest yield followed by chloroform and hexane layers (Table 4.4). When tested on HeLa cells, all three layers exhibited growth-inhibitory activity (Fig. 4.8B).

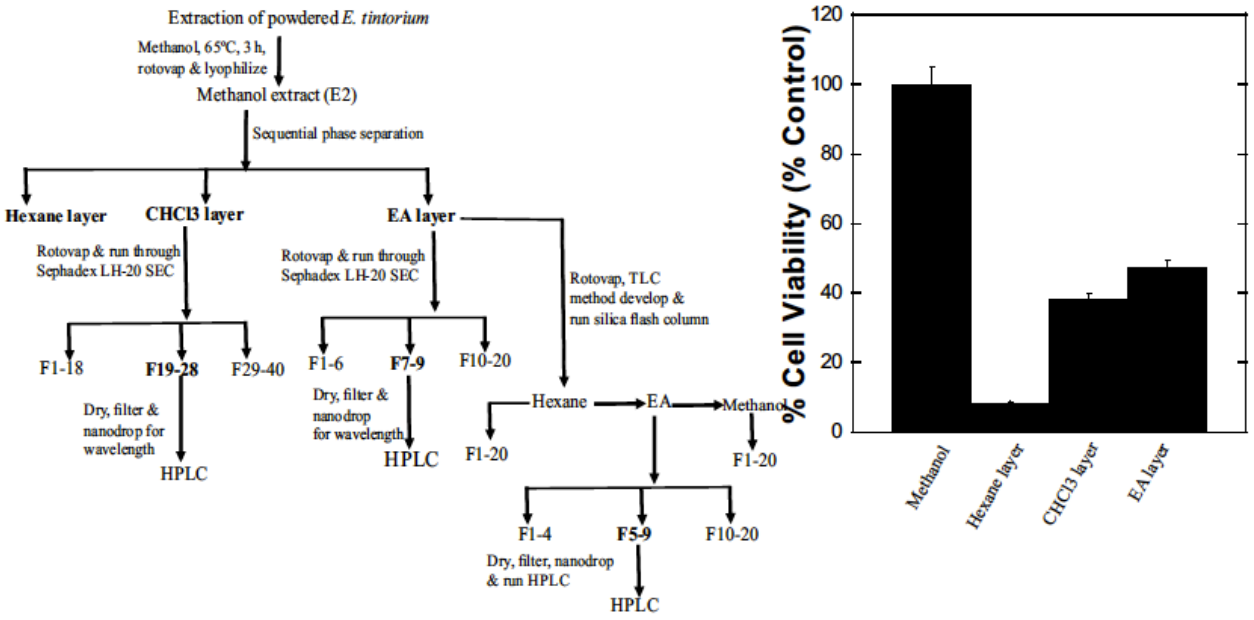

Fig. 4. 8. A) Purification methodology for sequential phase separation of *E. tinctorium*. B) Sequential phase separated layers treated at 0.4 mg/mL for 48 h were assessed for growth-inhibitory activity in HeLa cells. A representative data from three biological replicates.

Table 4. 4. Quantitative estimation of phase separated layers

Type of extract	**Amount obtained (mg)**	**% Yield**	**Solubility**
Crude methanol extract E2	400	-	Water
Hexane layer	6.4	1.6	Methanol
Chloroform layer	80	20	Methanol
EA layer	150	37.5	Methanol

4.3.2.2. Purification of EA layer by Sephadex LH-20 SEC

Bioactive compounds purified by Sephadex LH-20 column (Fig. 4.9) were present in fractions 7-9 (1 CV), suggesting that there are low molecular weight compounds contributing to the growth-inhibitory activity.

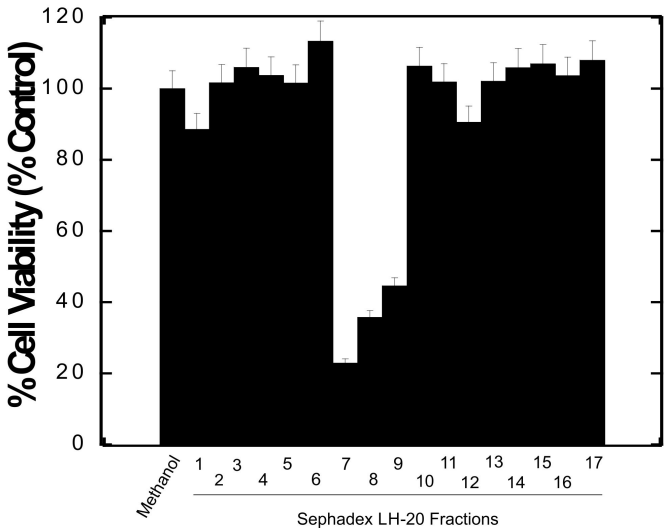

Fig. 4. 9. Sephadex LH-20 (70 mL column) elution profile of EA layer. Result shown is a representative from three biological replicates.

4.3.2.3. HPLC and ESI-MS analysis

Bioactive fractions were then analyzed on HPLC where one prominent peak was retained at 8.6 min with several least abundant peaks (Fig. 4.10A). The ESI-MS analysis of this peak showed two major mass ions with m/z 296 and 317 [M + H], along with many other ions that were less abundant (Fig. 4.10B). Therefore, further purification was done to get cleaner HPLC and MS spectra.

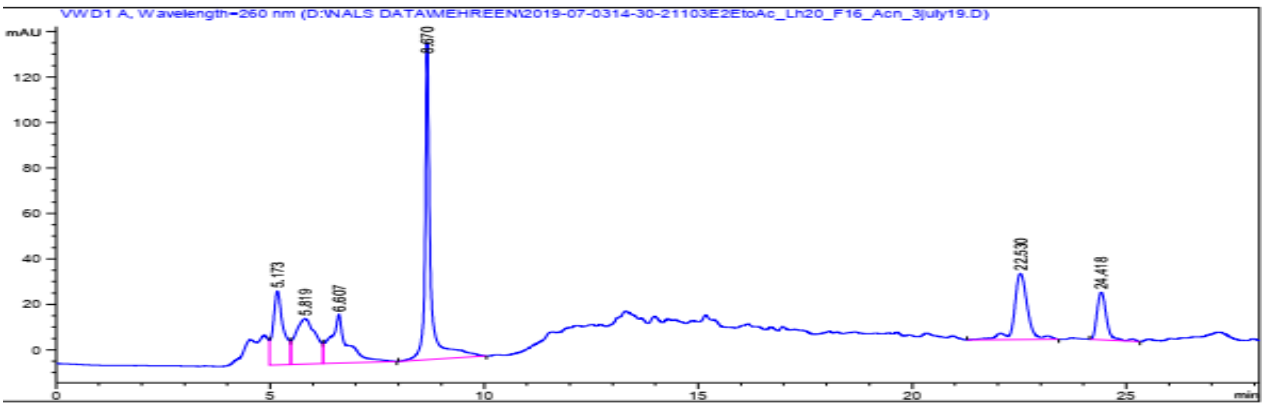

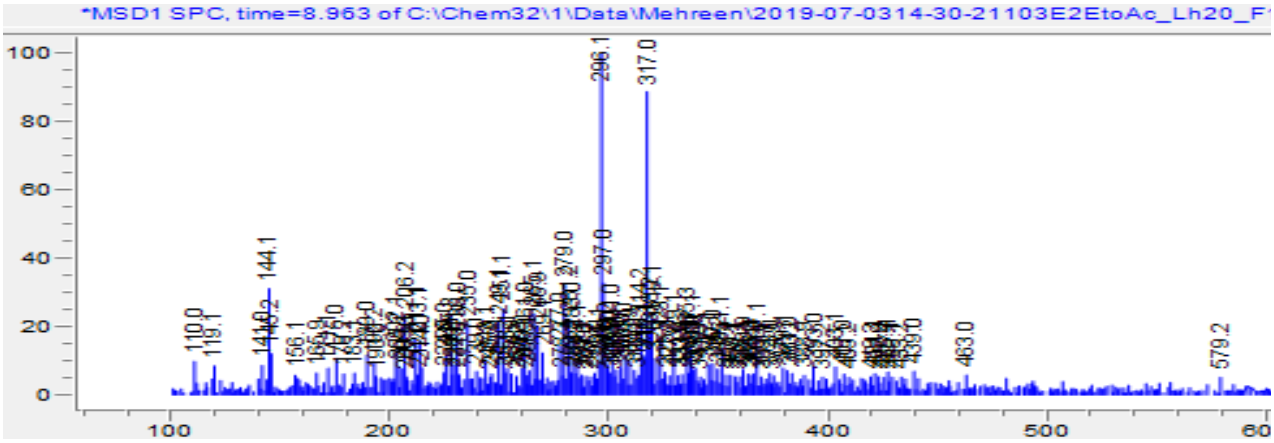

Fig. 4. 10. A) HPLC spectrum of Post Sephadex LH-20 bioactive fractions, B) ESI-MS of peak retained at 8 min.

4.3.2.4. Purification of EA layer by SFC and HPLC

TLC method was developed (Fig. 4.11) to isolate small molecules from the EA layer. The optimized solvent system was then used to run the silica column. TLC analysis showed 3 spots that were visible under short wave and long wave UV as well as with anisaldehyde stain.

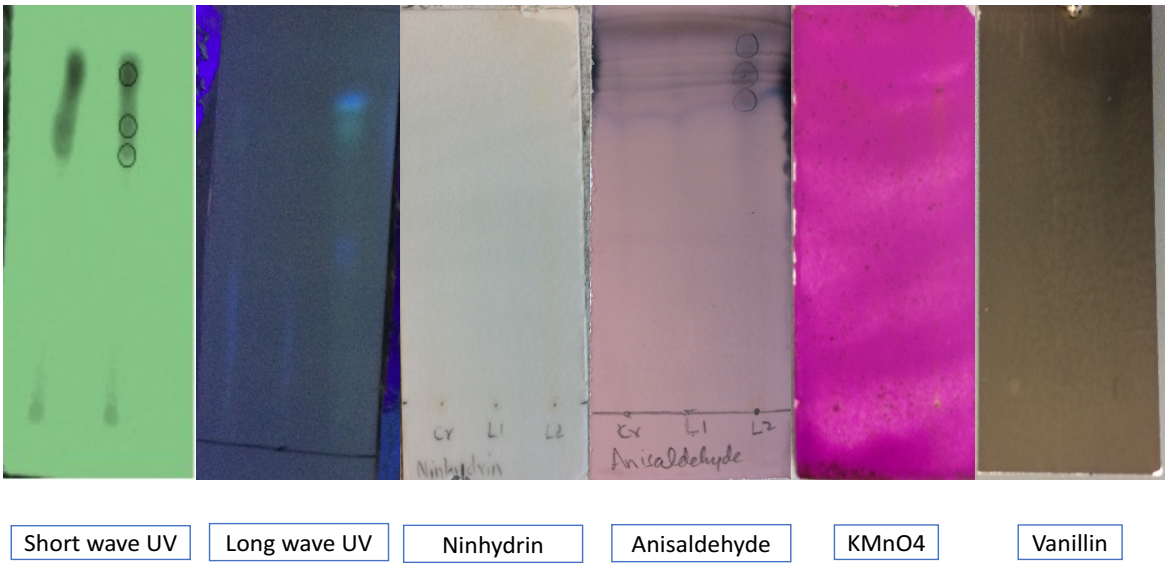

Fig. 4. 11. TLC visualization by UV and multiple stains.

The TLC quadrant test (Fig. 4.12A) showed that EA-eluted fractions 5-9 and methanol-eluted fractions 6-8 from the silica column contained UV active compounds. The UV active EA-eluted fractions 6-9 also showed growth-inhibitory activity on HeLa cells (Fig. 4.12C). These fractions were therefore further analyzed using HPLC.

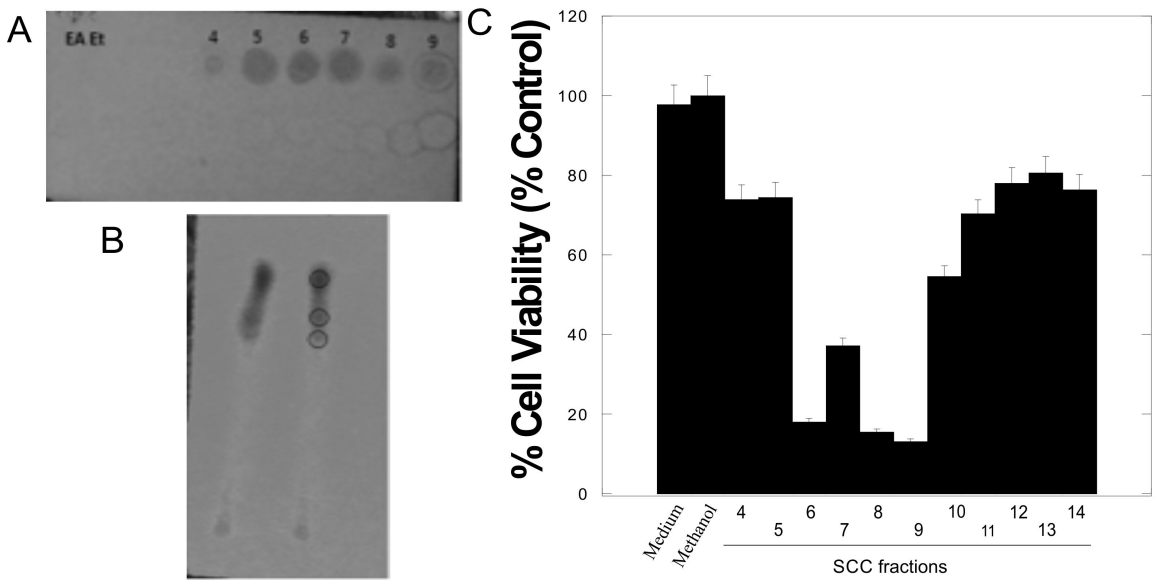

Fig. 4. 12. A) A TLC quadrant test of EA-and methanol-eluted fractions from silica column chromatography visualized under UV light, B) Full TLC on pooled UV visible fractions 4-9 visualized under UV light, C) Growth-inhibitory fractions of EA elution from silica column chromatography. Result shown is a representative of three biological replicates.

The HPLC method was successfully developed on C18 reverse phase HPLC column where bioactive fractions 6-9 showed a well resolved spectrum with multiple potential peaks (Fig. 4.13A). The abundant peaks retained at 5.2, 6.4, and 11.08 min were fraction-collected and reinjected for purity check (Fig. 4.13B, C & D).

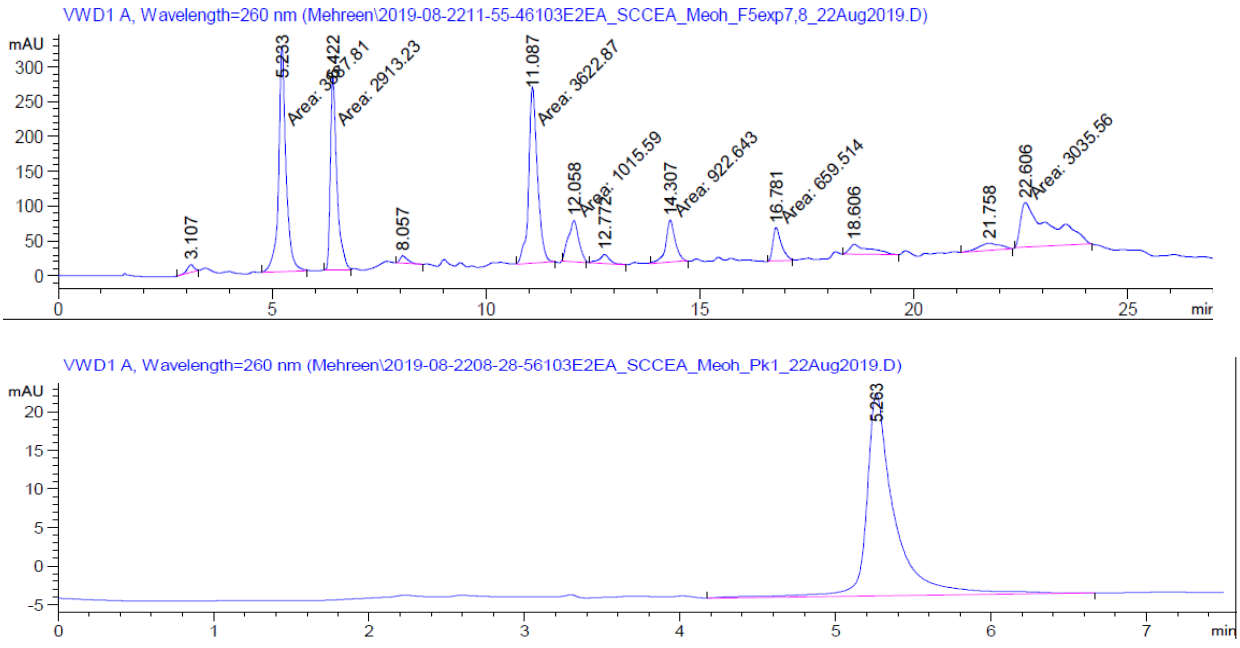

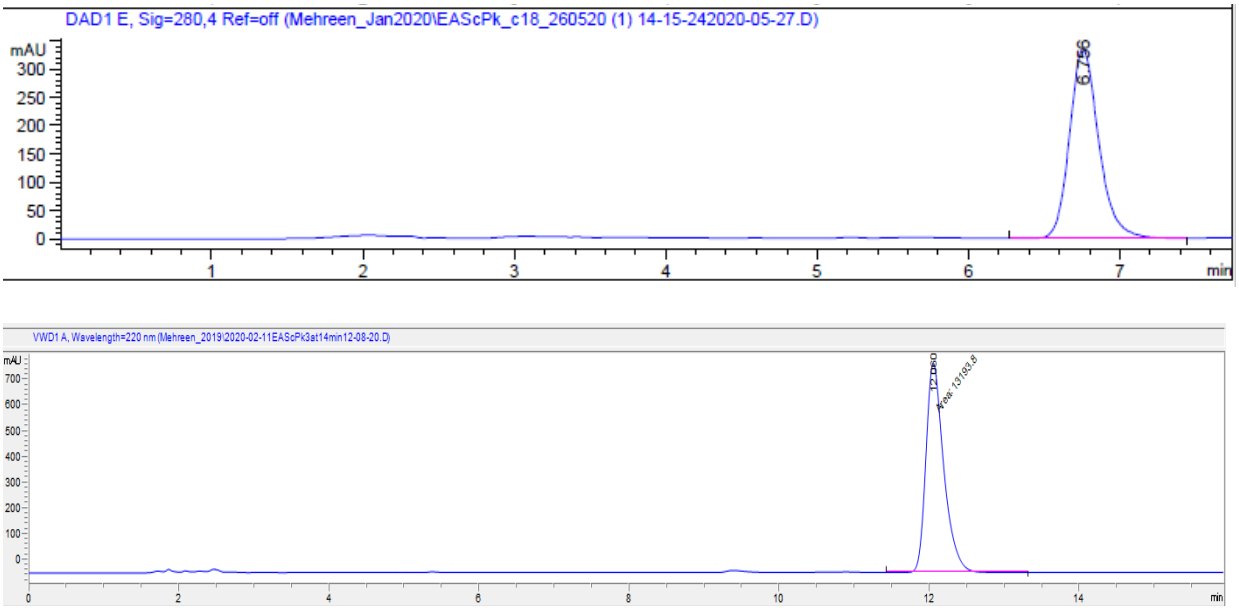

Fig. 4. 13. HPLC spectrum of SCC purified bioactive fractions 6-9 (A), and HPLC purity check of peak 1 (B), peak 3 (C) and peak 3 (D).

Additional purification of F6-9 was achieved from Sephadex LH-20 SEC (approach (iv)) that resulted in cleaner and well-resolved spectrum (Fig. 4.14). The HPLC analysis showed that initial fractions F14-16 only had peak 1, F17-18 contained both peaks 1 and 2 and F19-22 contained predominantly peak 2. These peaks were fraction-collected and analyzed. Peak 1 was designated as compound **(1)** and peak 2 was designated as compound **(2)**. Both compounds were then subjected to growth-inhibitory analysis and structural elucidation.

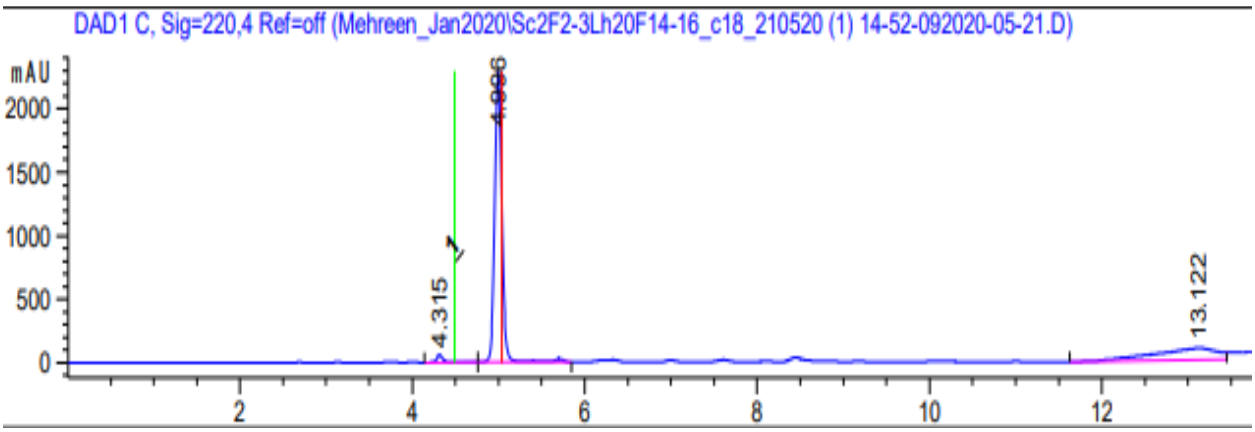

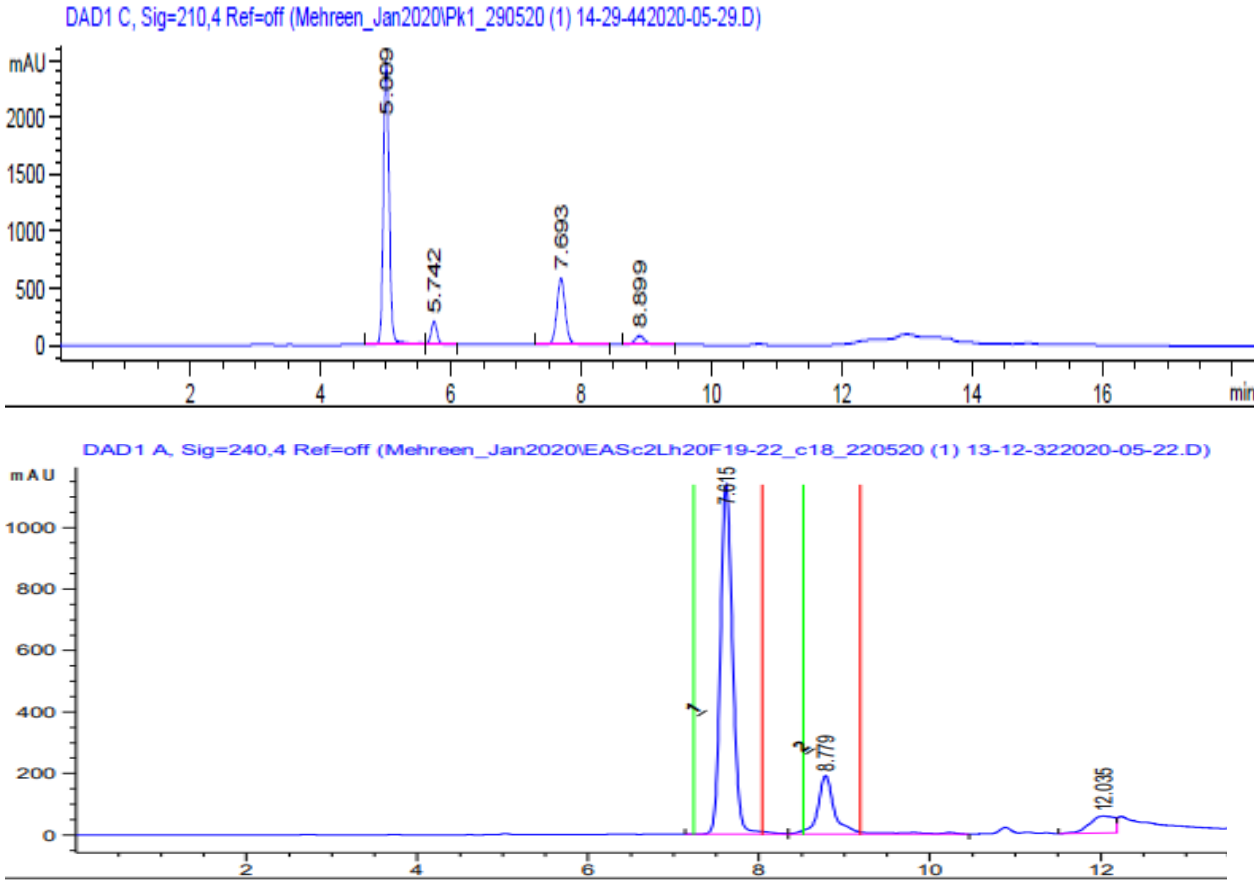

Fig. 4. 14. HPLC spectrum of approach (iv) fractions F14-16 (A), F17-18 (B), and F19-22 (C).

4.3.2.5. Chemical characterization of compound (1)

Compound **(1)** was obtained as a colorless powder, with a molecular formula $C_7H_8O_2$, confirmed from NMR data and ESI-MS ion peak at m/z 125 [M+H] as shown in Fig. 4.16.

4.3.2.6. HPLC and ESI-MS analysis of (1)

The UV diode array detector (DAD) spectrum showed **(1)** was retained at 5 min with 100 % purity and absorption maxima at 220 and 280 nm (Fig. 4.15).

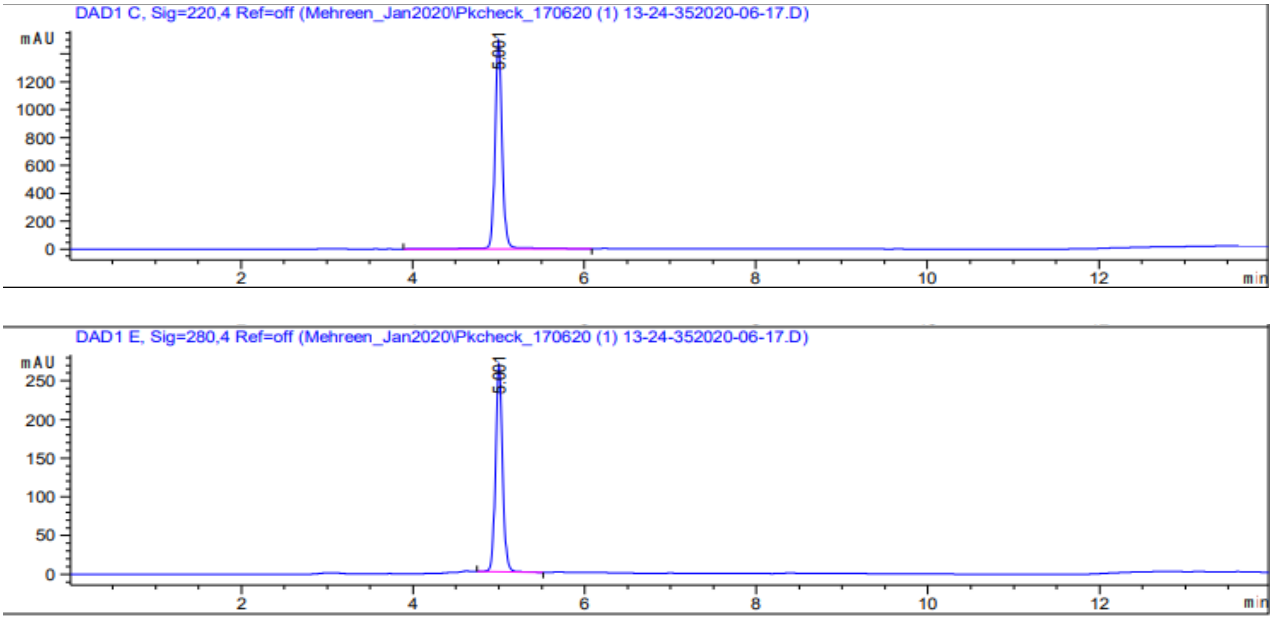

Fig. 4. 15. HPLC DAD spectrum of **(1)** at 220 (A) and 280 nm (B).

The ESI-MS spectrum (Fig. 4.16) showed a molecular ion peak at m/z 125 [M+H] in both scan mode (m/z 100 – 1000) and SIM which confirmed the molecular formula $C_7H_8O_2$ of orcinol.

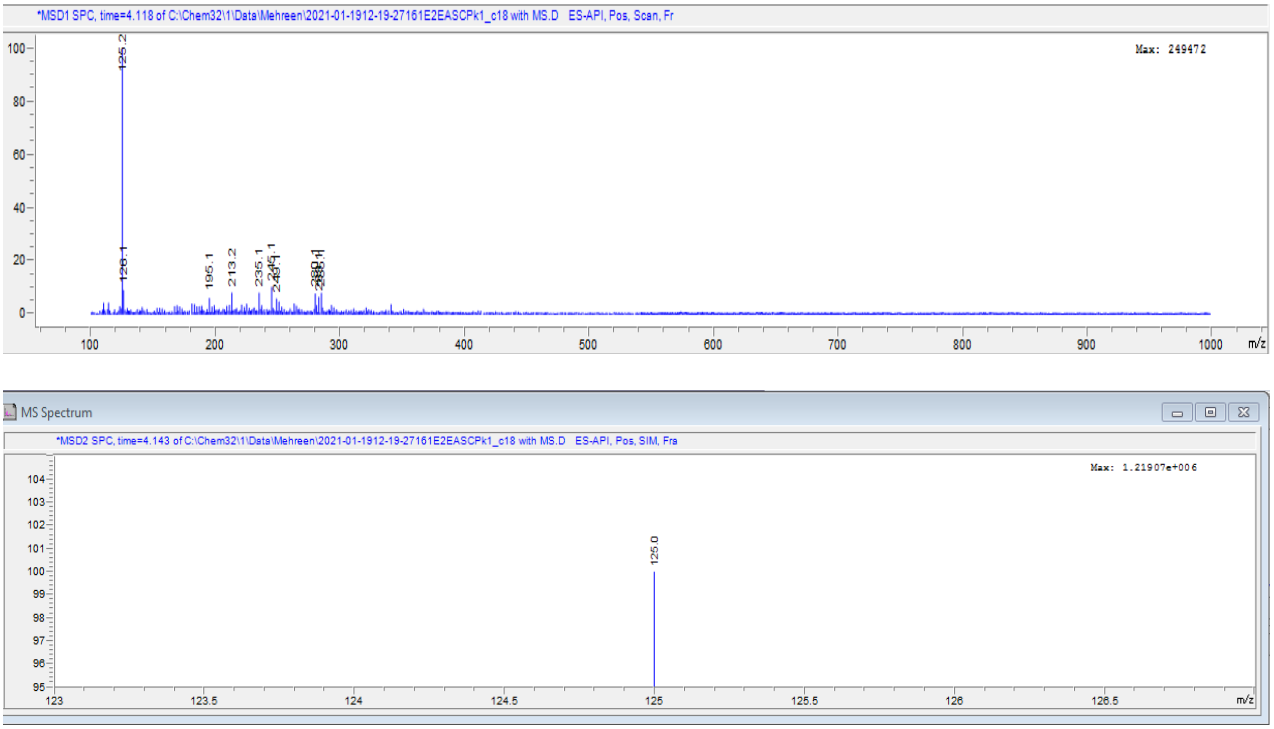

Fig. 4. 16. ESI-MS spectrum of **(1)** in scan mode (A) and SIM (B).

4.3.2.7. Structural elucidation of (1) by FTIR and NMR

IR spectrum (Fig. 4.17) showed peak stretches for OH (3286cm^{-1}) and C-H (2921 cm^{-1}) functionalities.

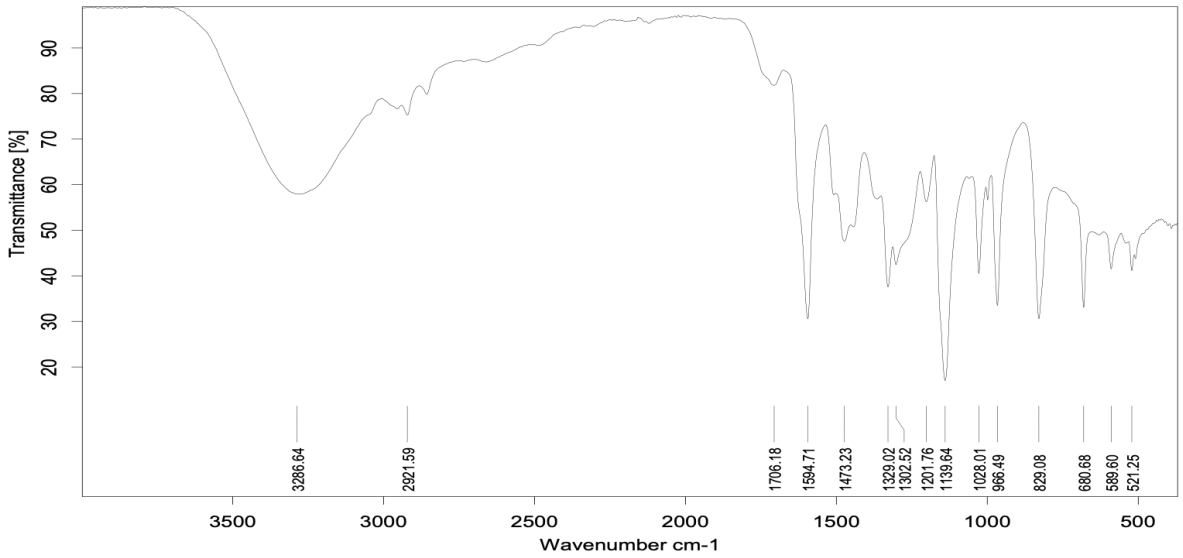

Fig. 4. 17. FTIR spectrum of **(1)**.

1D NMR data revealed that **(1)** constitutes seven carbons that include a 1, 3, 7 tri-substituted benzene ring with two hydroxy groups and a methyl group. ^{1}H NMR (Fig. 4.18 & Table 4.5) showed presence of aromatic protons (δ_H 6.08, 1H), (δ_H 6.16, 1H), (δ_H 6.16, 1H) and methyl protons (δ_H 2.19, 3H). The C-1 (δ_C 157.9) and C-3 (δ_C 157.9) were de-shielded due to their OH substituents. ^{13}C NMR (Fig. 4.19 & Table 4.5) showed three quaternary carbons (δ_C 157.9, 157.9, 140.4), three methine (δ_C 99.4, 107.5, 107.5), and a methyl group (δ_C 20.4). ^{13}C and ^{1}H signals were directly correlated in HSQC spectrum (Fig. 4.20).

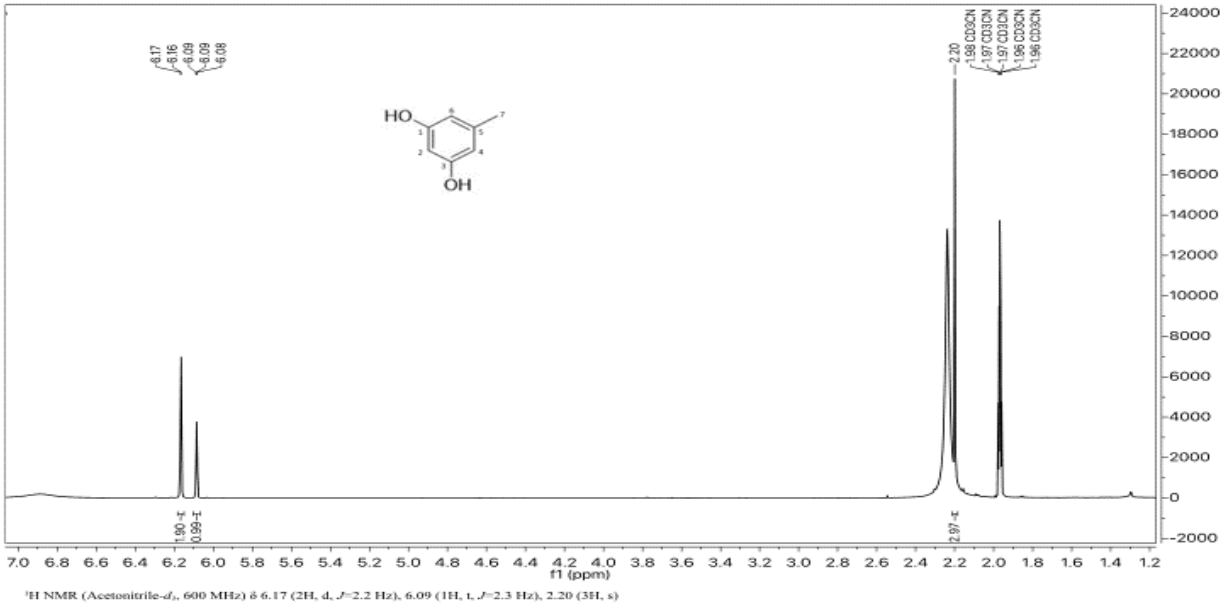

Fig. 4. 18. ^{1}H NMR spectrum of **(1)**.

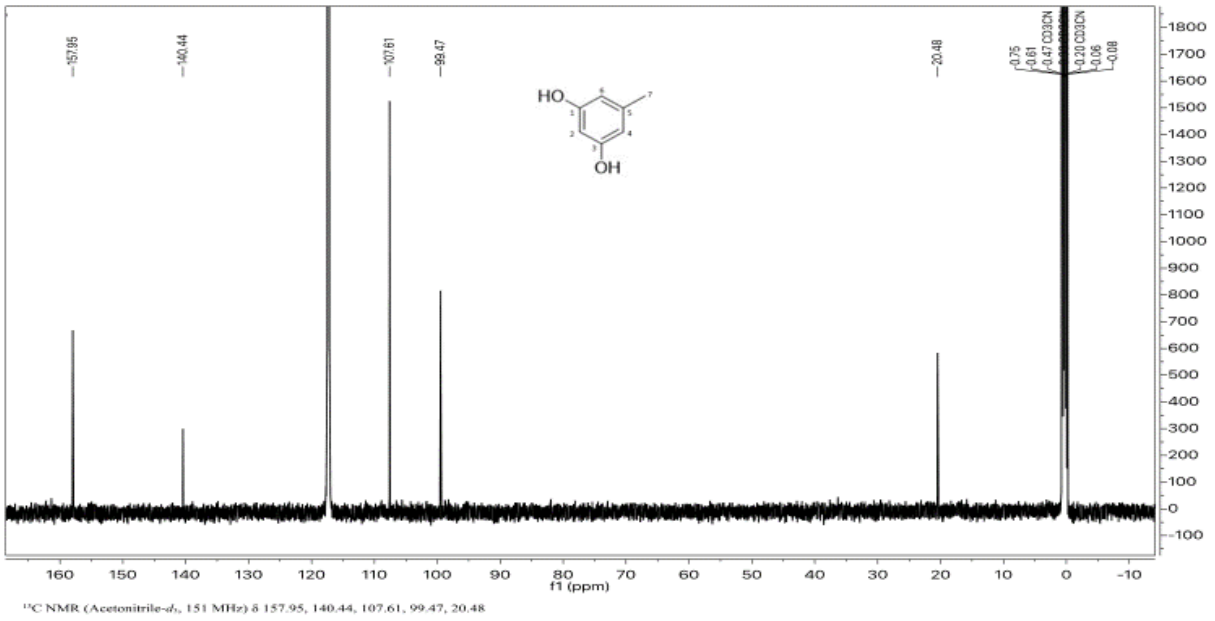

Fig. 4. 19. ^{13}C NMR spectrum of **(1)**.

Table 4. 5. ^{13}C and ^{1}H Chemical shifts of **(1)**

Number	**^{13}C Chemical shift δ ppm**	**^{1}H Chemical shift δ ppm (# H, multiplicity, *J*)**	**Chemical group**
1	157.9	-	°4 C
2	99.4	6.09 (1H, t, *J* = 2.27, 2.27)	CH
3	157.9	-	°4 C
4/6	107.5	6.17 (2H, d, *J* =2.18)	2 CH
5	140.4	-	°4 C
7	20.4	2.20 (3H, s)	CH_3

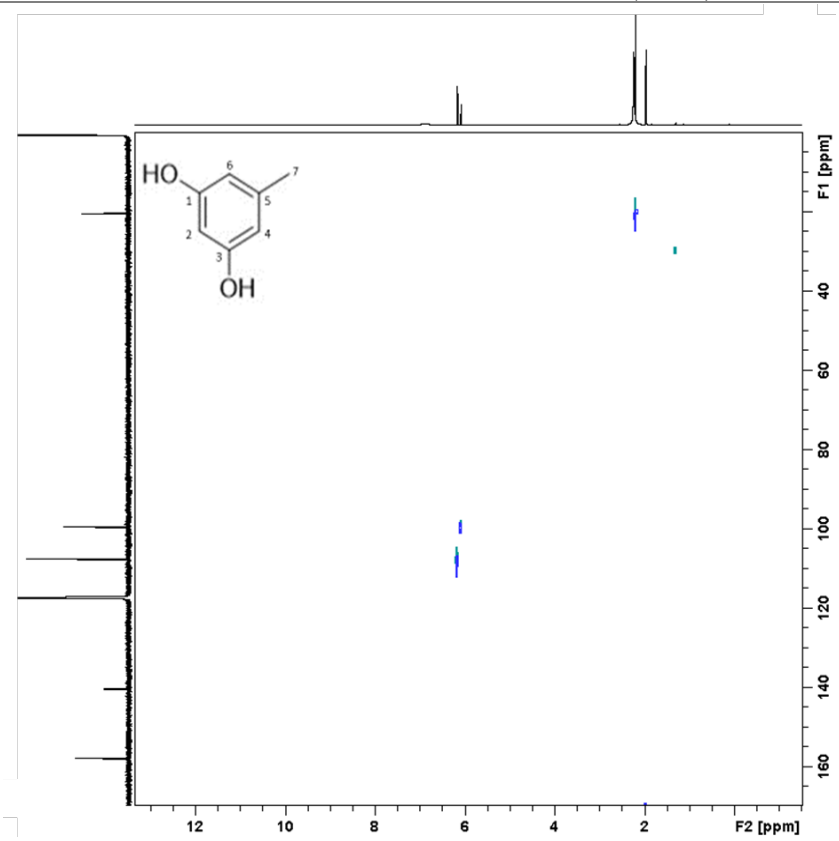

Fig. 4. 20. ^{13}C-^{1}H HSQC spectrum of **(1)**.

The ^{13}C-^{1}H HMBC cross peaks (Figs. 4.21 & 4.23) were observed between C-1/C-3 (δ_C 157.9) and H-4/H-6 (δ_H 6.16) as well as H-2 (δ_H 6.08). C-2 (δ_C 99.4) had cross peak with H-4/H-6 (δ_H 6.16), C-4 (δ_C 107.5) with H-6 (δ_H 6.16), H-2 (δ_H 6.08), and H-7 (δ_H 2.19), C-6 (δ_C 107.5) with H-4 (δ_H 6.16), H-2 (δ_H 6.08), and H-7 (δ_H 2.19), C-5 (δ_C 140.4) with H-7 (δ_H 2.19). ^{1}H-^{1}H COSY correlations (Figs. 4.22 & 4.23) were seen between H-7 (δ_H 2.19), H-4 (δ_H 6.16), and H-6 (δ_H 6.16).

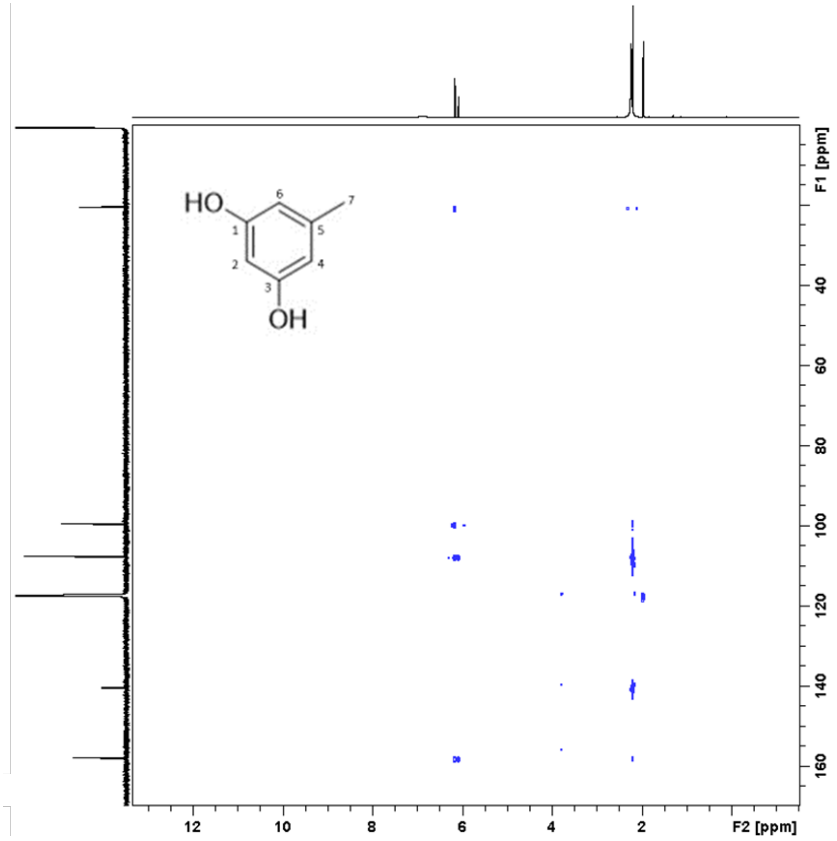

Fig. 4. 21. ^{13}C-^{1}H HMBC spectrum of **(1)**.

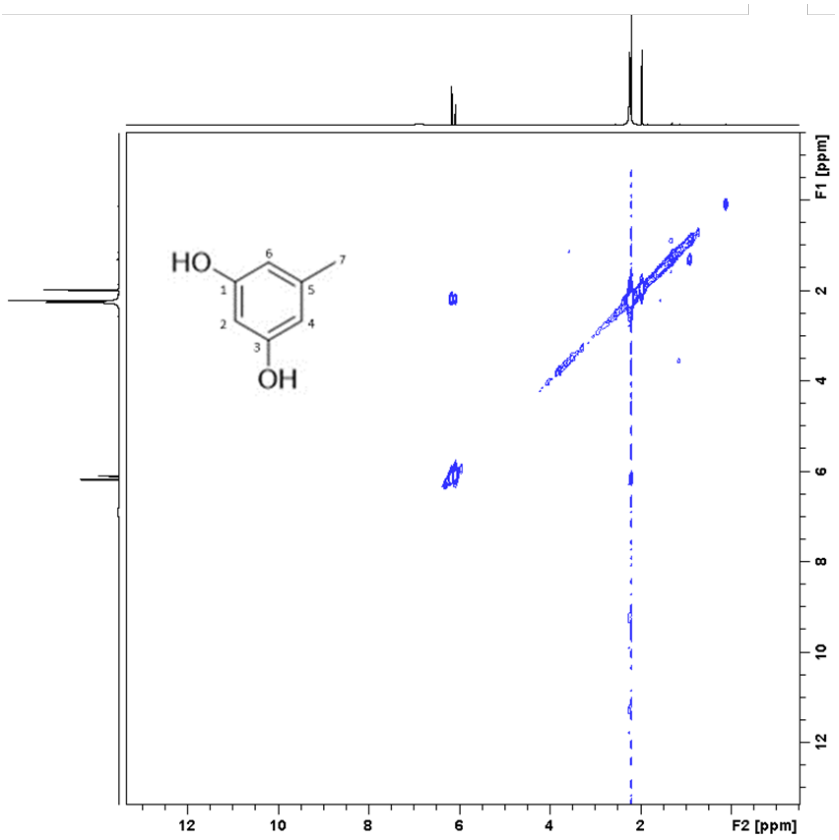

Fig. 4. 22. ^{1}H-^{1}H COSY spectrum of **(1)**.

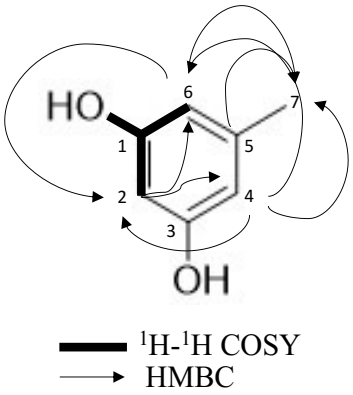

Fig. 4. 23. ^{1}H-^{1}H COSY and ^{13}C-^{1}H HMBC structural correlations.

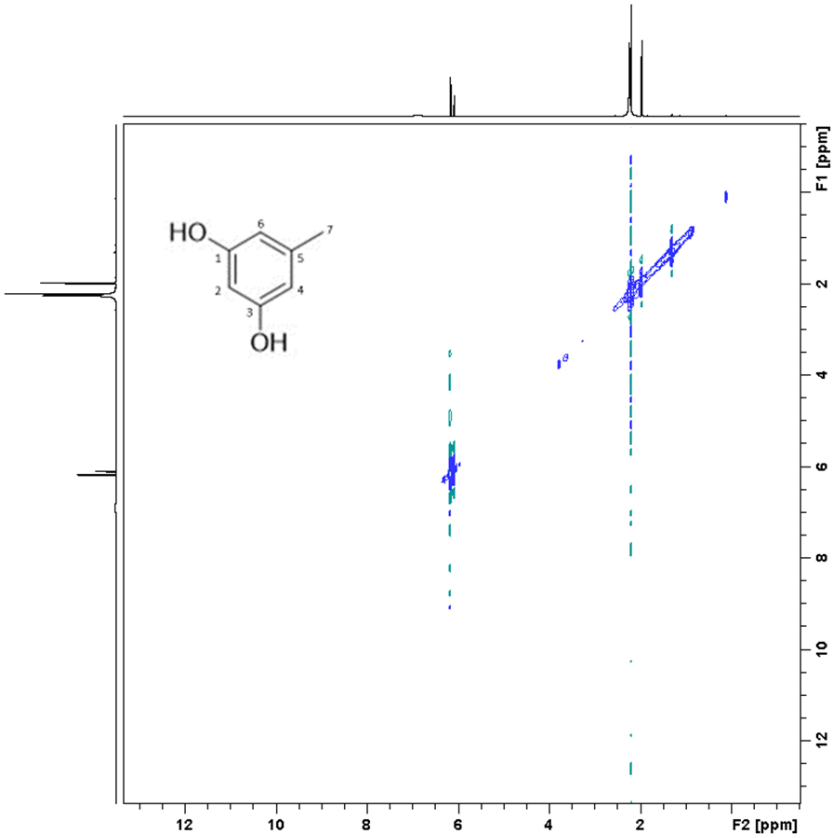

Fig. 4. 24. ^{1}H-^{1}H NOESY spectrum of **(1)**.

In summary, compound **(1)** was identified as orcinol, also called 5-methylresorcinol. Orcinol has been isolated from lichens including *Parmelia subrudecta* (Ivanova *et al*., 2010) and mold like *Aspergillus niger* (Sahasrabudhe *et al*., 1986). Some studies have described the role of orcinol as an important source of carbon and energy which is achieved by hydrolysis of benzene ring to acetate and pyruvate, which would possibly act as substrates for the energy cycles (Chapman & Ribbons, 1976, Sahasrabudhe *et al*., 1986).

4.3.2.8. Chemical characterization of compound (2)

Compound **(2)** was obtained as yellow star-shaped crystals, with a molecular formula $C_{15}H_{16}O_4$, determined from NMR data, X-ray crystal structure and ESI-MS spectrum.

4.3.2.9. HPLC and ESI-MS analysis of (2)

The UV-DAD spectrum showed maximum absorption at 220, 260 and 280 nm (Fig. 4.25). ESI-MS (Fig. 4.26) molecular ion peak at m/z 261.1 [M+H].

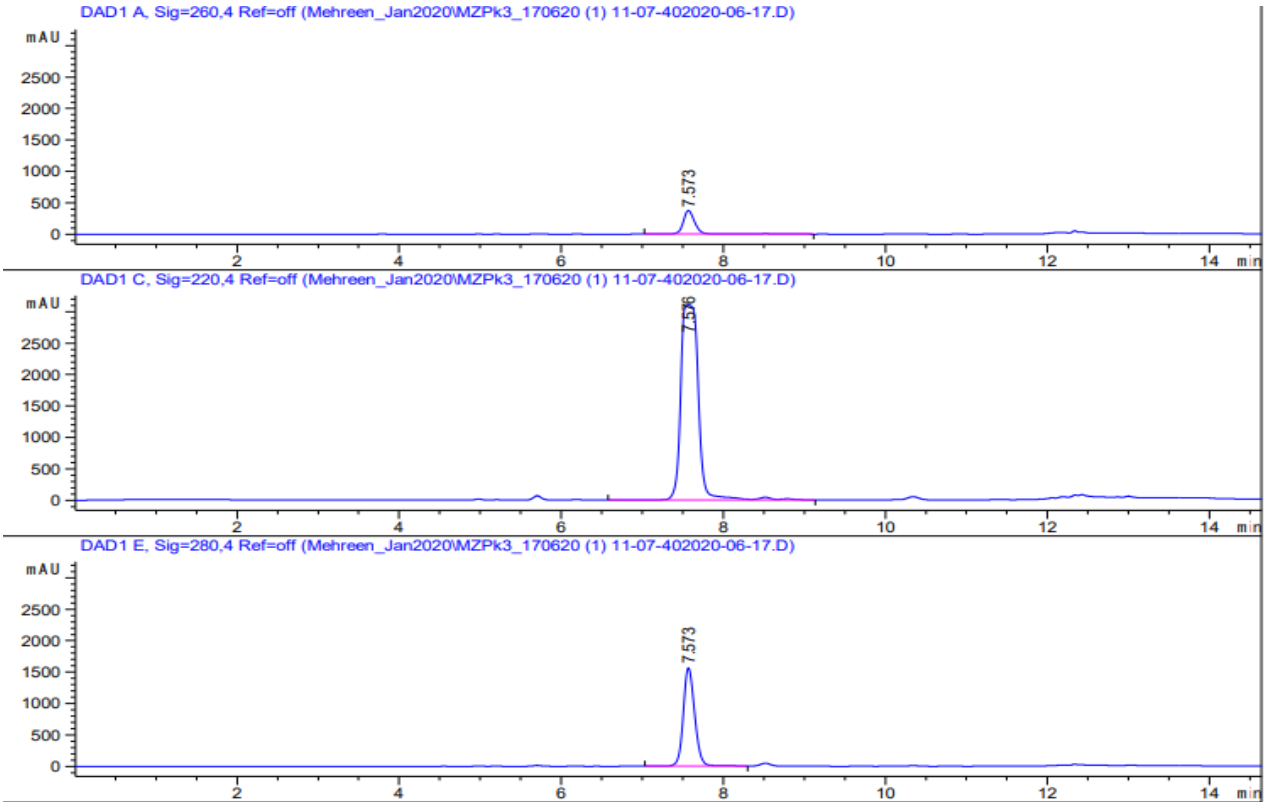

Fig. 4. 25. HPLC DAD spectrum of **(2)** at multiple wavelengths.

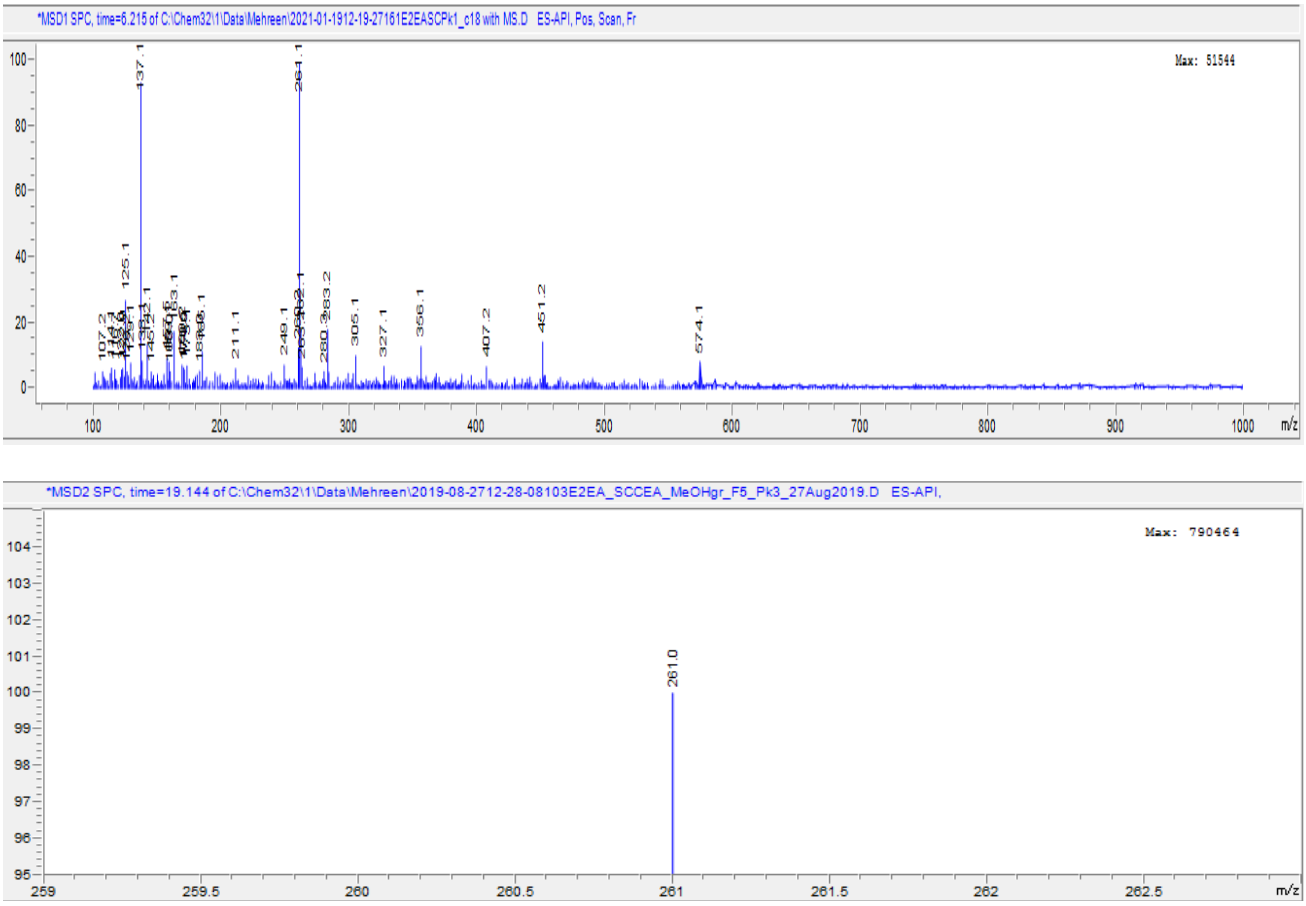

Fig. 4. 26. ESI-MS spectrum of **(2)** in scan mode m/z = 100-1000 (A) and SIM mode (B).

4.3.2.10. Structural elucidation by FTIR and NMR spectroscopy

The F TIR spectrum (Fig. 4.27) showed absorptions of hydroxy group (3233 cm^{-1}) and aliphatic CH stretches (2854, 2922 cm^{-1}) which were in agreement with the composition of compound **(2)**.

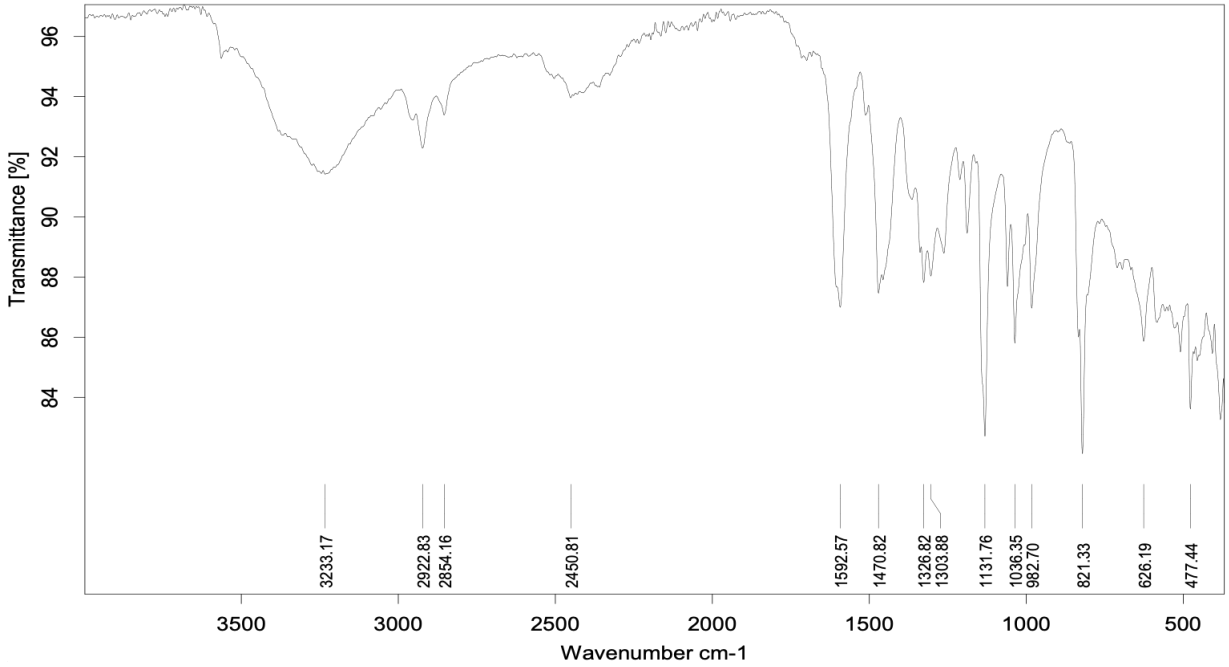

Fig. 4. 27. FTIR spectrum of **(2)**.

Data from 1D NMR revealed that **(2)** is a symmetric molecule with a total of 15 carbons (Fig. 4.28 & Table 4.6). Fourteen carbons are equally distributed on both sides of the molecule held together by another carbon. The carbons included one central methylene (δ_C 22.3), two methyl groups (δ_C 19.9), two methine (δ_C 100.7, 110.0), and four quaternary carbons (δ_C 156.0, 155.9, 155.97, 117.1). 1D NMR signals (Fig. 4.29 & Table 4.6) also revealed a substituted aromatic ring [δ_H 6.17 (4H, m), 3.78 (2H, s), 2.15 (6H, s); δ_C 100.7, 110.0, 22.3, and 19.9]. In addition to this, **(2)** also possessed four hydroxy groups which were confirmed from X-ray diffraction data (XRD). Moreover, the presence of one central methylene group was confirmed from ^{13}C NMR DEPT135 (Distortionless Enhancement of Polarization Transfer) signals that were embedded in HSQC spectrum.

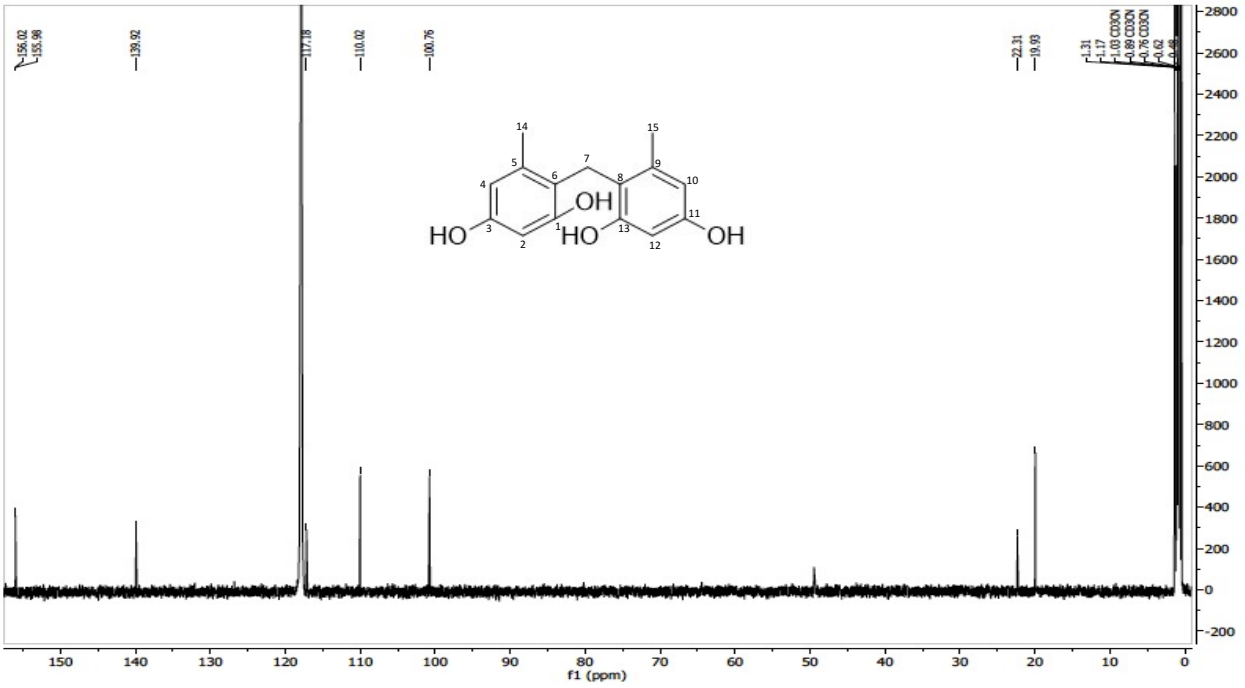

Fig. 4. 28. ^{13}C NMR of **(2)**.

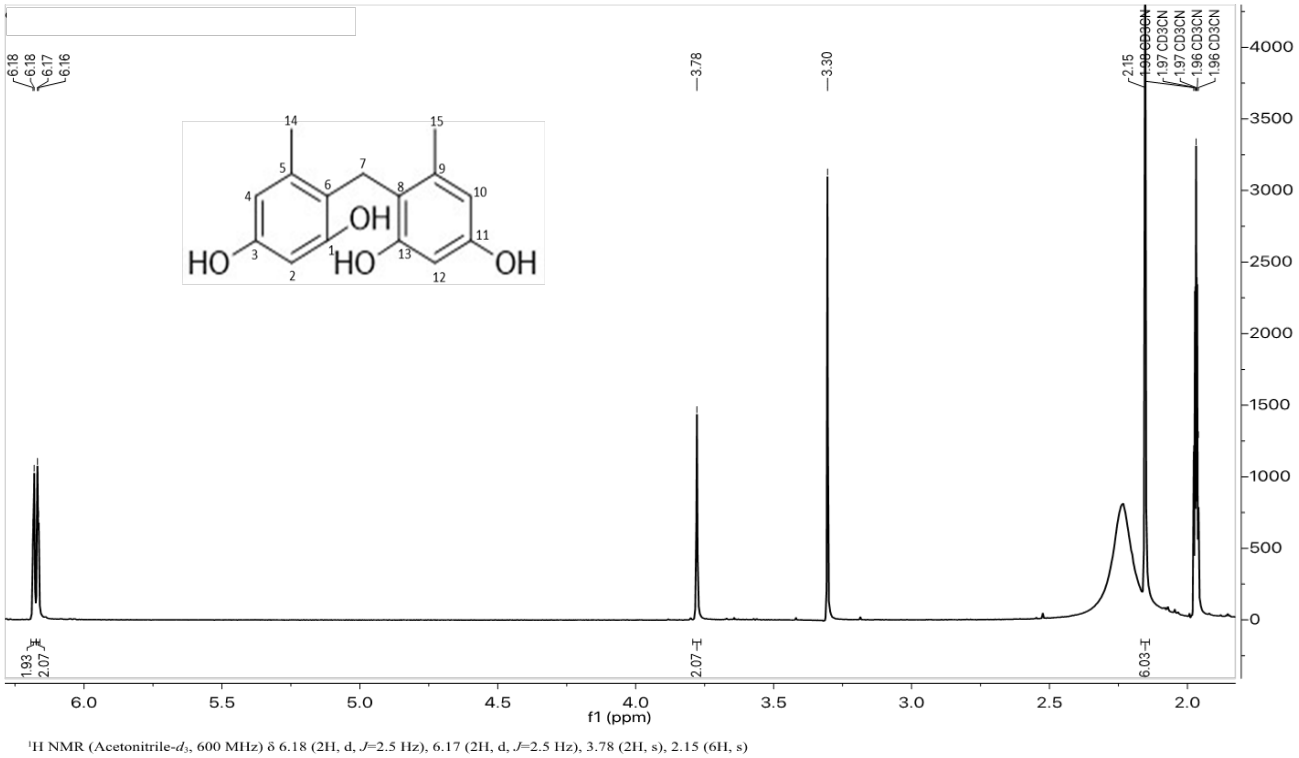

^{1}H NMR (Acetonitrile-d_3, 600 MHz) δ 6.18 (2H, d, *J*=2.5 Hz), 6.17 (2H, d, *J*=2.5 Hz), 3.78 (2H, s), 2.15 (6H, s)

Fig. 4. 29. ^{1}H NMR of **(2)**.

Table 4. 6. ^{13}C and ^{1}H NMR chemical shifts of **(2)**

Number	**^{13}C Chemical shift δ ppm**	**^{1}H Chemical shift δ ppm (# H, multiplicity, *J*)**	**Chemical group**
1/13	156.0	-	°4 C
2/12	100.7	6.17 (2H, d, *J*= 2.51)	CH
3/11	155.9	-	°4 C
4/10	110.0	6.18 (2H, d, *J*= 2.53)	CH
5/9	155.9	-	°4 C

6/8	117.1	-	°4 C
7	22.3	3.78 (2H, s)	CH_2
14/15	19.9	2.15 (6H, s)	CH_3

1D NMR peak assignments were confirmed from 2D correlations (Table 4.6 and Fig. 4.30). Cross peaks were observed between C-1/C-13 (δ_C 156.0) and H-4/H-10 (δ_H 6.18) and H-7 (δ_H 3.78). C-5/C-9 (δ_C 155.9) had cross peaks with H-2/H-12 ((δ_H 6.17) and H-7 (δ_H 3.78), C-3/C-11 (δ_C 155.9) with H-7 (δ_H 3.78) and H-14/H-15 (δ_H 2.15), C-6/C-8 (δ_C 117.1) with H-4/H-10 (δ_H 6.18), H-2/H-12 ((δ_H 6.17), H-7 (δ_H 3.77), and H-14/H-15 (δ_H 2.15), C-4/C-10 (δ_C 110.0) with H-2/H-12 (δ_H 6.17), C-2/C-12 (δ_C 100.7) with H-4/H-10 (δ_H 6.18). C-7 (δ_C 22.3) was weakly correlated to H-4/H-10 (δ_H 6.18) and H-2/H-12 (δ_H 6.17) and finally C-14/C-15 (δ_C 19.9) had cross peaks with H-4/H-10 (δ_H 6.18).

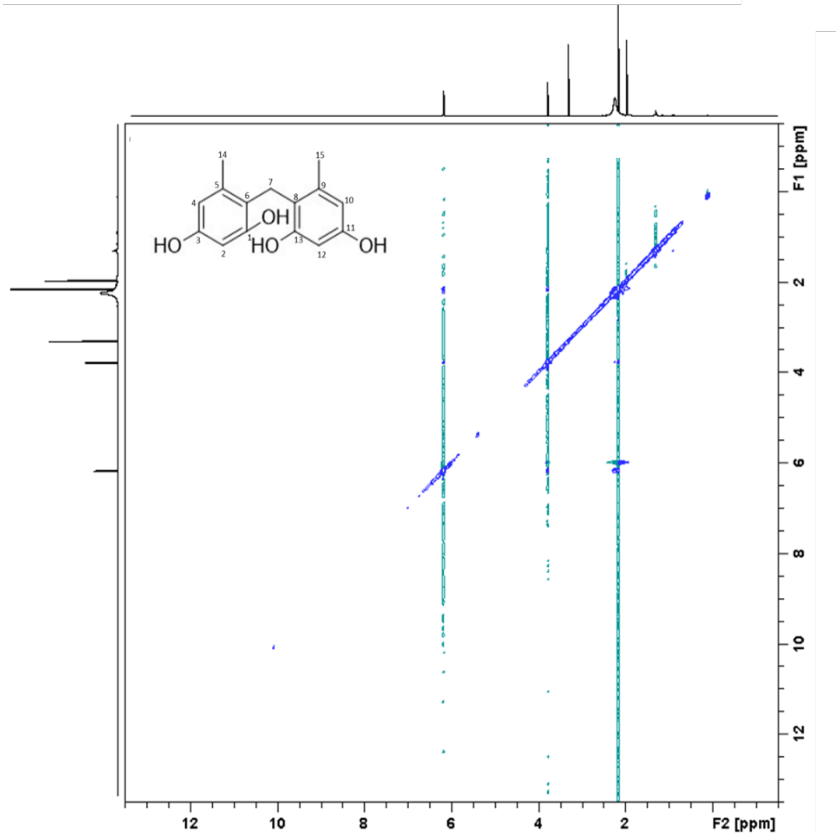

Fig. 4. 30. ^{13}C-^{1}H HSQC spectrum of compound **(2)**.

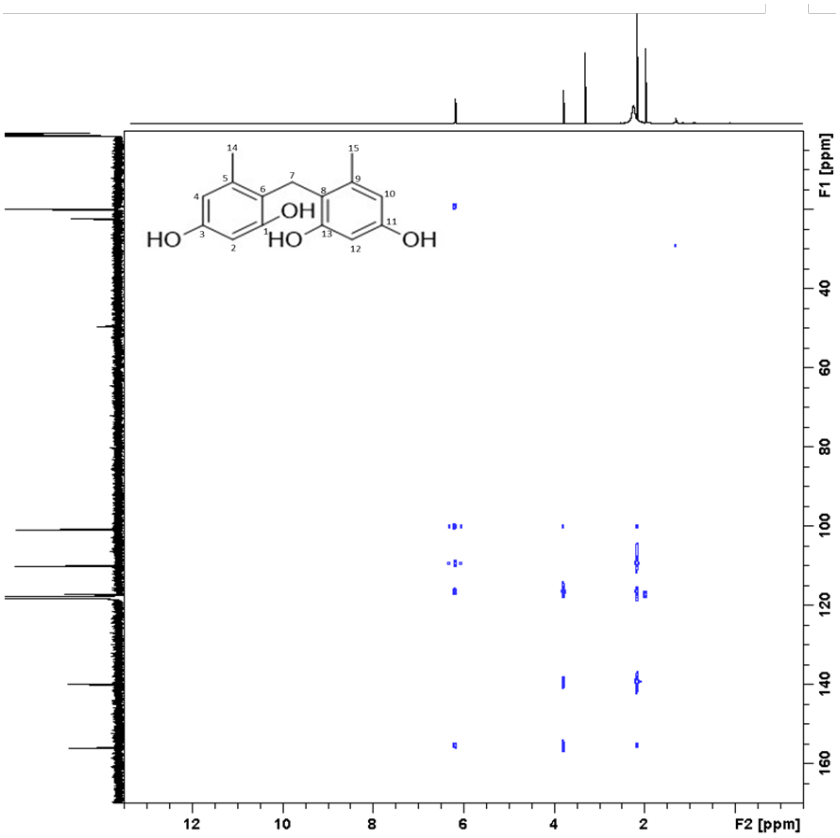

Fig. 4. 31. ^{13}C-^{1}H HMBC spectrum of compound **(2)**.

The ^{1}H-^{1}H COSY spectrum (Fig. 4.32) showed proton couplings between H-4/H-10 (δ_H 6.18) and H-14/H-15 (δ_H 2.15). H-7 (δ_H 3.78) was strongly coupled to H-2/H-12 (δ_H 6.17) and weakly to H-14/H-15 (δ_H 2.15). NOE correlations (Figs. 4.33 & 4.34) were observed between H-4/H-10 (δ_H 6.18) and H-14/H-15 (δ_H 2.15), between H-7 (δ_H 3.78) and H-14/H-15 (δ_H 2.15) and H-4/H-10 (δ_H 6.18). The long range ^{13}C-^{1}H multiple bond couplings are shown in Fig. 4.33 and Table 4.6.

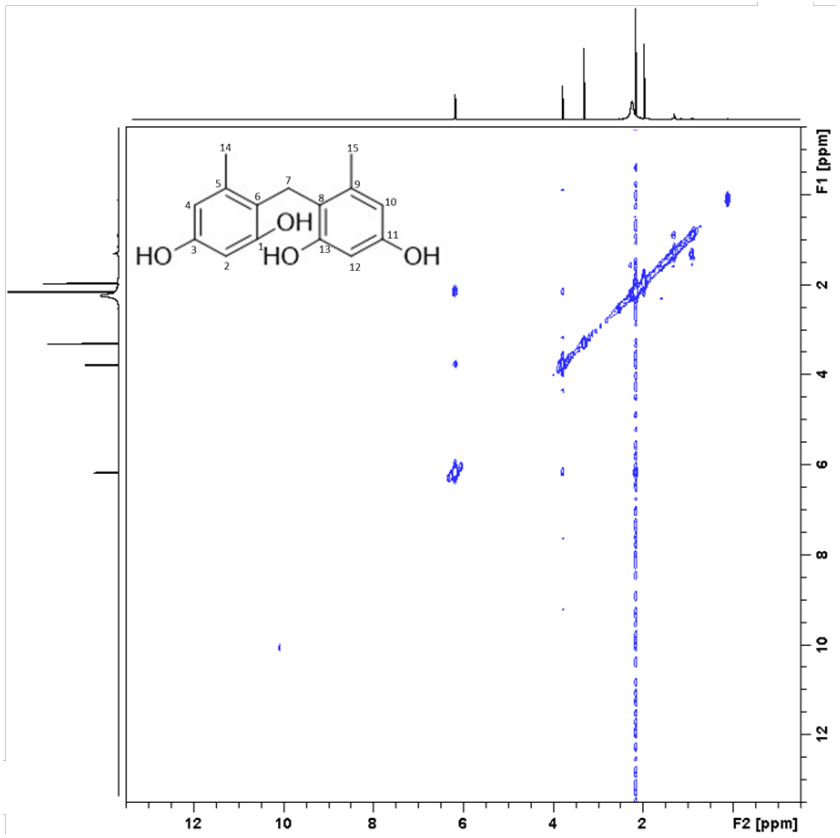

Fig. 4. 32. ^{1}H-^{1}H COSY spectrum of compound **(2)**.

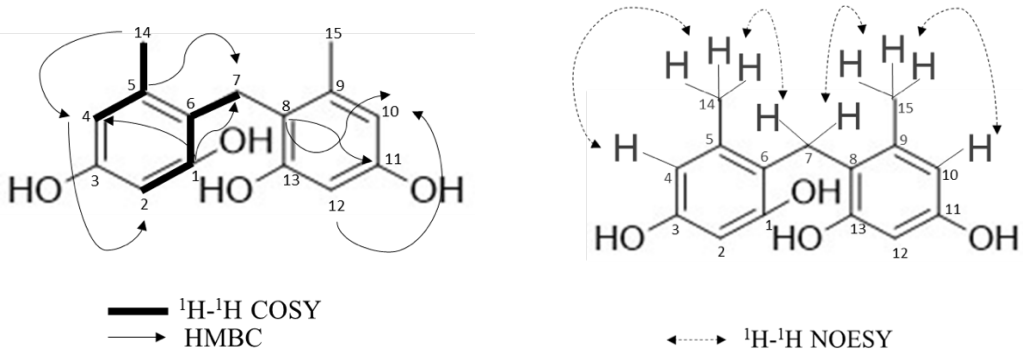

Fig. 4. 33. 2D NMR structural co-relations of compound **(2)**.

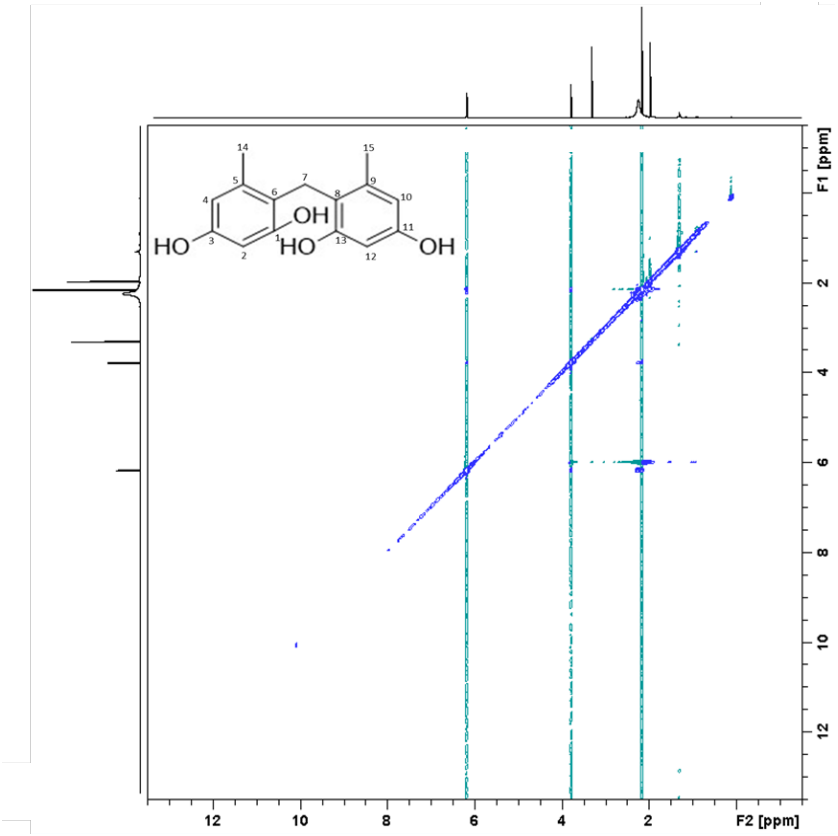

Fig. 4. 34. ^{1}H-^{1}H NOESY spectrum of compound **(2)**.

Table 4. 7. ^{13}C-^{1}H multiple bond couplings (HMBC)

# C (δ ppm)	**# H (δ ppm)**
C-1/C-13 (156.0)	H-4/H-10 (6.18), H-7 (3.78)
C-5/C-9 (155.9)	H-2/H-12 (6.17), H-7 (3.78)
C-3/C-11 (155.0)	H-7 (3.78), H-14/H-15 (2.15)
C-6/C-8 (117.1)	H-4/H-10 (6.18), H-2/H-12 (6.17), H-7 (3.78), H-14/ H-15 (2.15)
C-4/C-10 (110.0)	H-2/H-12 (6.17)
C-2/C-12 (100.7)	H-4/H-10 (6.18)
C-7 (22.3)	H-4/H-10 (6.18),
C-14/C-15 (19.9)	H-4/H-10 (6.18)

4.3.2.11. Crystallization and X-ray crystallography of (2)

The vapor diffusion method resulted in the formation of thin yellow irregular crystals whereas slow evaporation method with methanol/acetonitrile co-solvents generated star shaped yellow irregular crystals (Fig. 4.35A) which qualified for XRD analysis. None of the other methods were successful in achieving good quality crystals. Detailed crystal data can be found in supplementary data of appendix C.

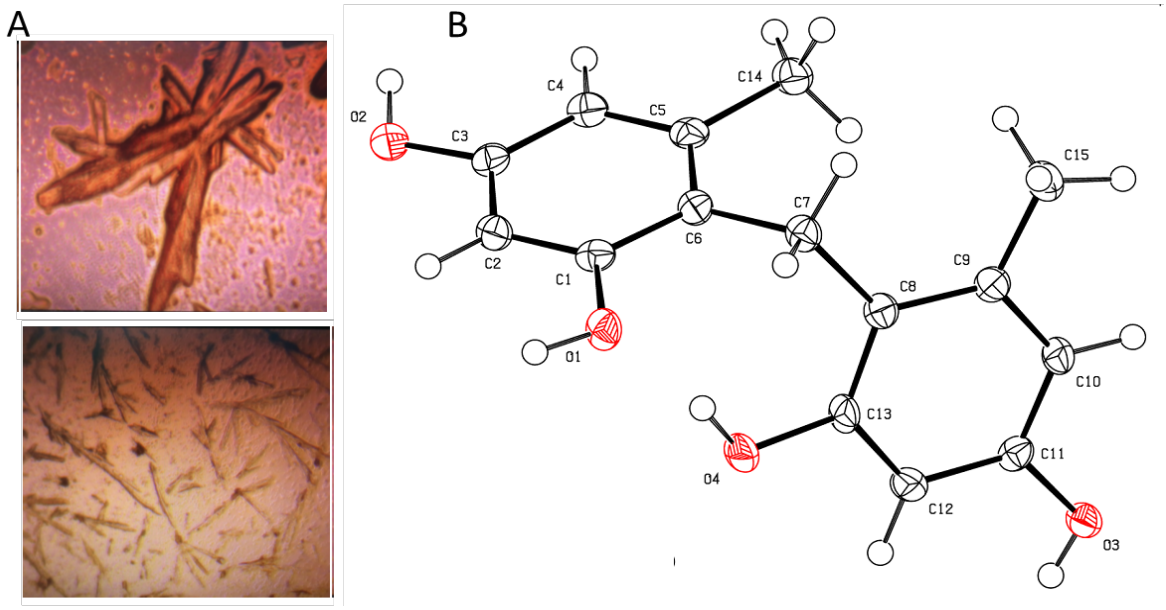

Fig. 4. 35. A) Crystals of compound **(2)** under microscope, B) ORTEP style image of compound **(2)**.

Crystal Data: $C_{15}H_{16}O_4$, triclinic, P-1 (No. 2), a=8.8847(5) Å, b=9.2916(5) Å, c= 9.4831(4) Å, α= 97.485(4)°, β= 105.756(4)°, γ= 105.320(4)°, V= 709.25(7) Å^3, T= 90(2) K, Z= 2, Z'= 1, μ(CuK$_\alpha$)= 0.838, 9454 reflections measured, 1829 unique (R_{int} = 0.0628) which were used in all calculations. The final wR_2 was 0.0968 (all data) and R_1 was 0.0378 (I > 2(I)). The XRD analysis was performed by Chemistry department, UBC. The crystal data of compound **(2)** was in agreement with the NMR data. The crystal structure of compound **(2)** is reported for the first time.

4.3.2.12. Assessment of growth-inhibitory activity of (2)

Compound **(2)** showed growth-inhibitory activity on HeLa cells and U251 cells when treated for 48 h with an IC_{50} of 195 μM ± 6.01 and 85.45 μM ± 2.8 respectively (Fig. 4.36). To further explore the mechanism for growth inhibition by **(2)** on U251 cells, apoptosis and cell cycle analyses were performed.

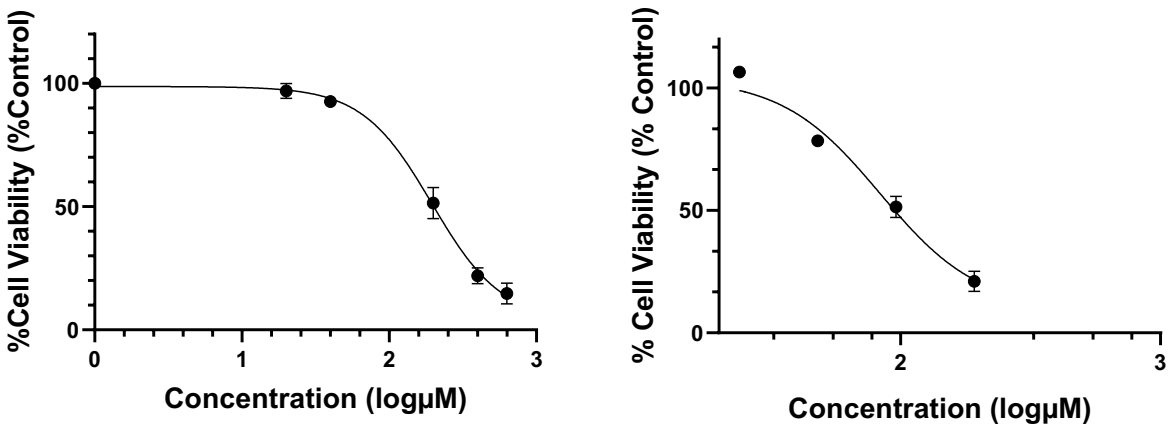

Fig. 4. 36. Growth inhibition caused by **(2)** in HeLa cells (A) and U251 cells (B). Results shown are representative from three biological replicates.

4.3.2.13. Flow cytometry analysis of compound (2)

As shown in Fig. 4.37, compound **(2)** induced significant apoptosis in U251 cells at 100 μM when cells were treated for 24 and 48 h. Twenty-four-hour treatment with 100 μM of **(2)** resulted in significant apoptosis ($p = 0.04$) with 42 % apoptotic cells as compared to 50 μM treatment and negative control methanol where there were 29 % and 26 % of apoptotic cells respectively. After 48 h treatment with 100 μM of **(2)**, the percentage of apoptotic cells also increased significantly ($p = 0.003$) to 84 % as compared to 50 μM of **(2)** and methanol with 21 % and 28 % apoptotic cells respectively (Fig. 4.37).

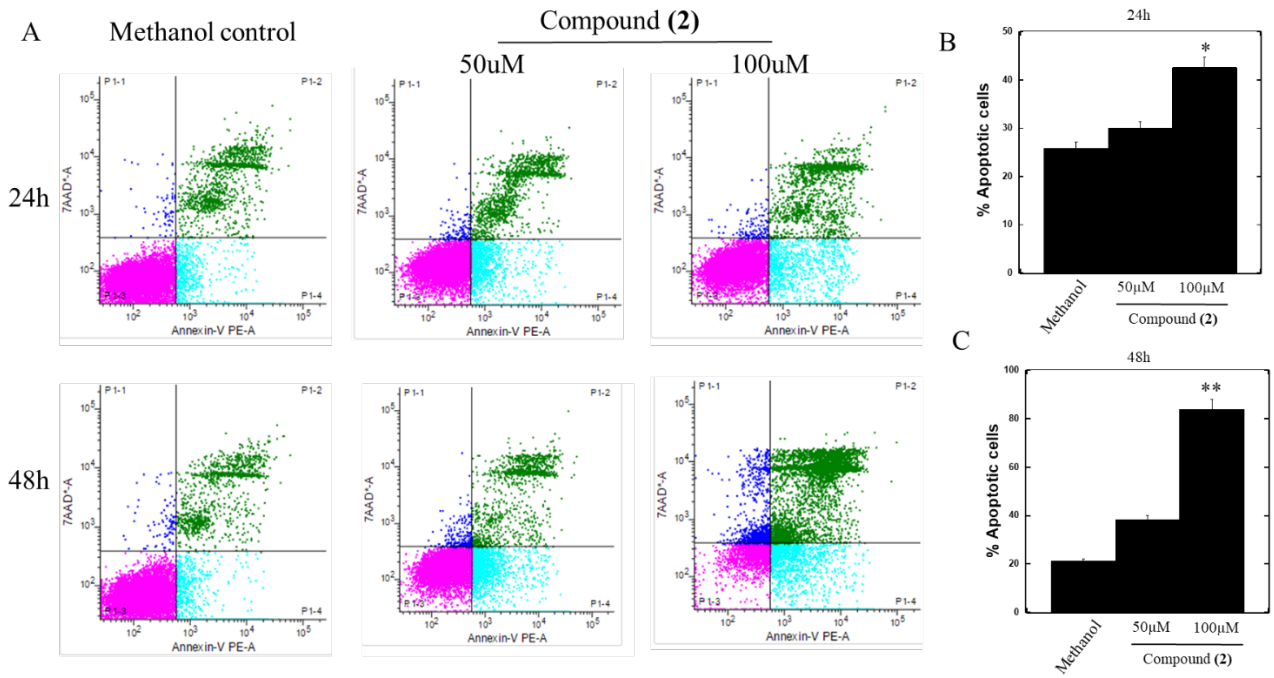

Fig. 4. 37. Apoptosis induced by 50 µM and 100 µM of compound **(2)** in U251 cells (A), and % apoptotic cells at 24 h (B) and 48 h (C) time intervals; methanol as control. Results shown are representative from 3 separate experiments (n=3). For statistical analysis, one-way ANOVA was used. * represents $p = 0.04$ and ** represents $p = 0.003$.

Cell cycle analysis of compound **(2)** showed a significant increase ($p = 0.0038$) in percentage of cells in G1 phase, suggesting that **(2)** induced G1 phase arrest in U251 cells (Fig. 4.38).

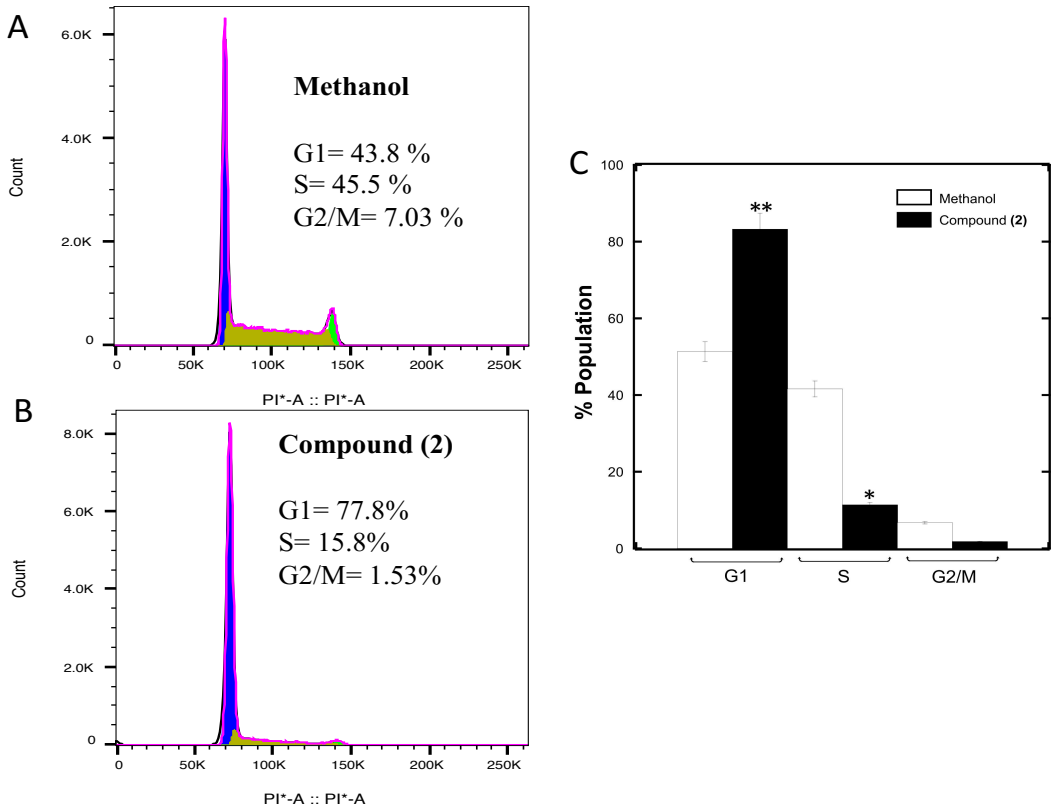

Fig. 4. 38. A) Cell cycle analysis of compound **(2)** at 100 µM for 48 h, B) % population of cells in G1, S and G2/M phase of cell cycle. Results shown are combined from three separate experiments. One-way ANOVA was performed for statistical analysis. Error bars represent standard deviation. ** and * indicates p = 0.0038 and 0.01.

Matubara *et al*. (1998) indicates that diphenylmethane derivatives had been chemically synthesized from 5-alkyl resorcinol by reacting with para-formaldehyde, dissolved in formic acid. The chemical reaction resulted in formation of multiple types of molecules; Type A (ortho-ortho), Type B (para-para), Type C (ortho-para), and Type D (xanthenes). Compound **(2)** is structurally similar to one of the type A compounds named Bis (2, 4-dihydroxy-6-methylphenyl) methane. According to the same study, this compound was tested for anti-tyrosinase activity which turned out to be negative (Matubara *et al*., 1998).

Besides the chemical synthesis described by Matsubara and coworkers, **(2)** has never been reported from any natural sources including mushrooms; therefore, this is the first description of its growth-inhibitory activity and X-ray crystal structure of **(2)**.

4.3.2.14. HPLC-MS analysis of additional fractions from SFC

HPLC analysis of fraction 9 obtained from large SFC resulted in three abundant peaks retained at 15, 16 and 18 mins (Fig. 4.39). All the peaks demonstrated maximum purity when analyzed at different wavelengths using DAD (Fig. 4.40).

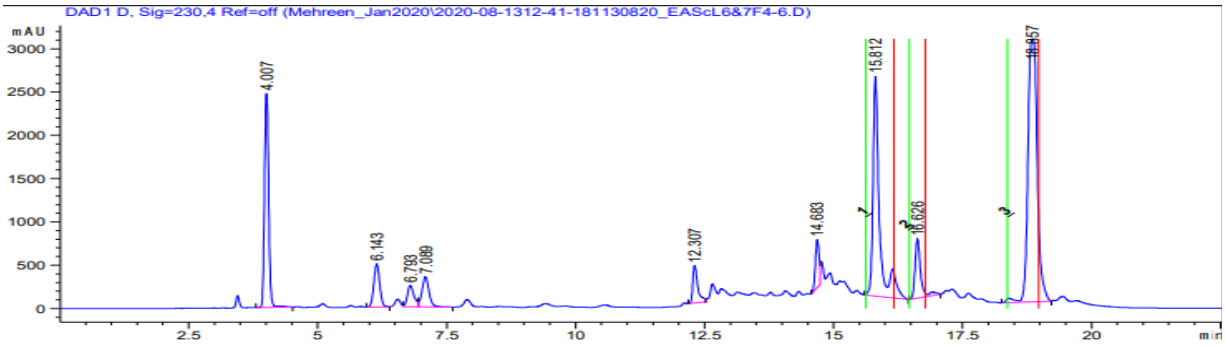

Fig. 4. 39. HPLC profile of fraction 9 of SFC.

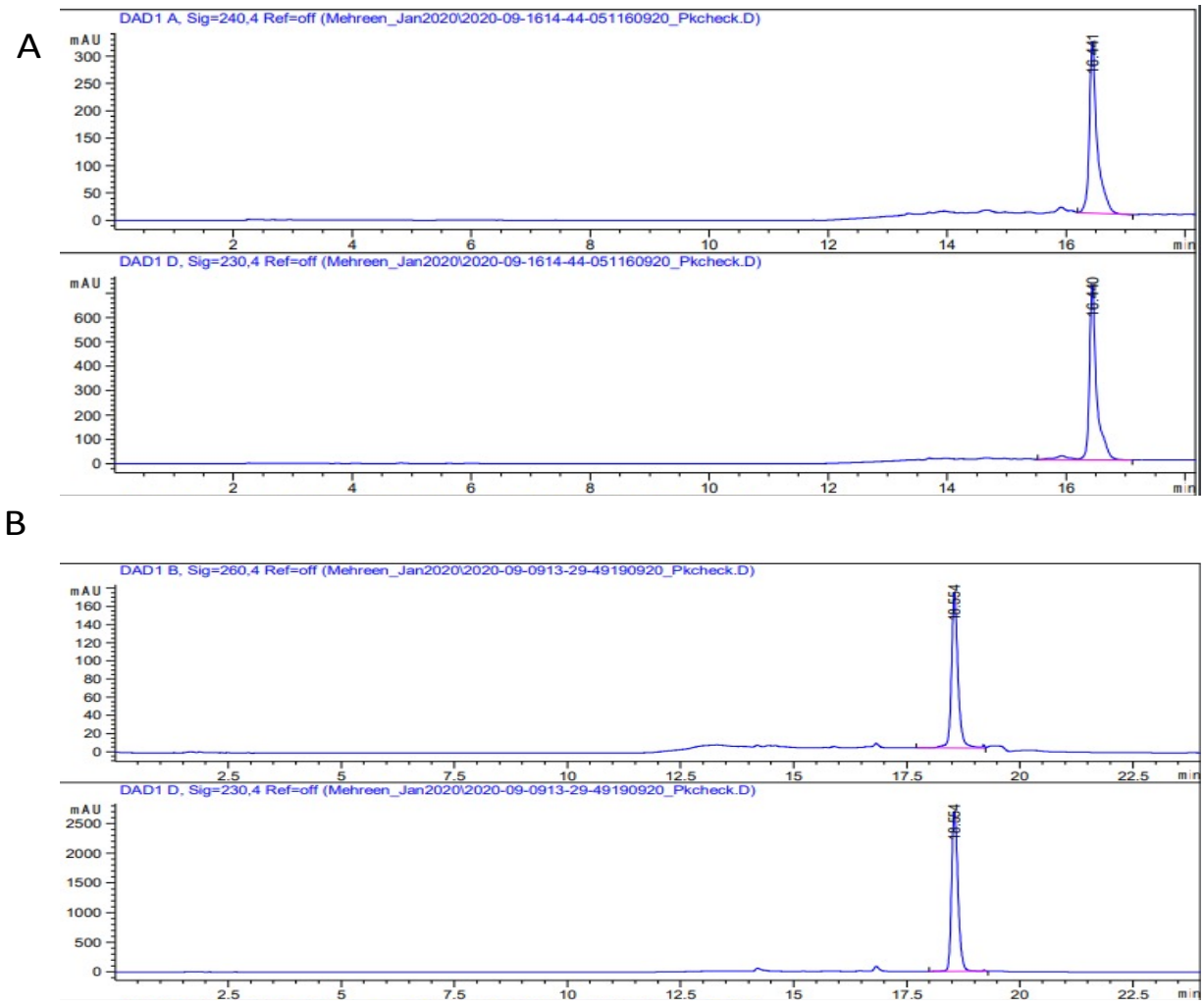

Fig. 4. 40. HPLC DAD spectrum of peaks at 16 min (A) and 18 min (B).

ESI-MS analysis of peak at 16 min showed m/z ion peak 285 [M+H] as the most abundant peak in the spectrum with few least abundant peaks of m/z 303, 407 and 447 (Fig. 4.41A). The

aforementioned ions from the MS scan mode were re-run in the SIM mode which resulted in 285 being the most abundant one (Fig. 4.41B). Since the peaks at 16 min and 18 min were purified twice to achieve maximum purity, it was deemed practically impossible to generate more material to proceed with further structural elucidation studies.

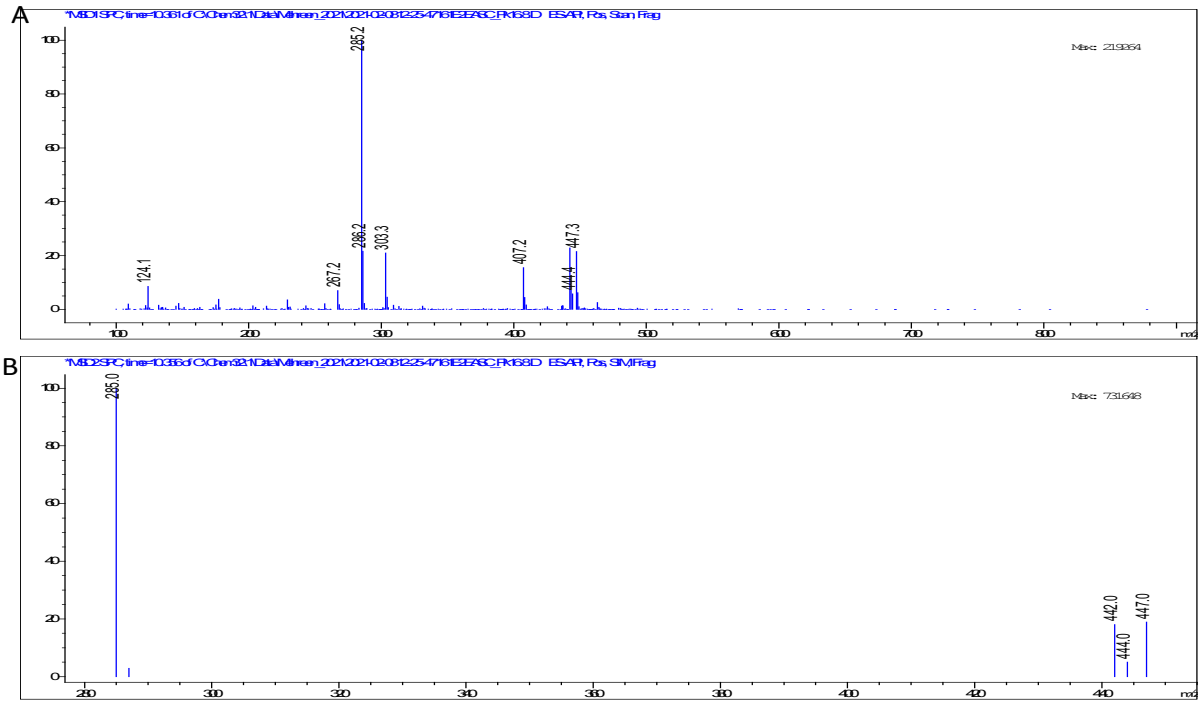

Fig. 4. 41. ESI-MS scan mode (A) and SIM (B) of peak at 16 min.

4.3.2.15. Chemical characterization of compound (3)

4.3.2.16. HPLC, ESI-MS and FTIR analysis of (3)

Further analysis was conducted on peak at 15 min, which was designated as compound **(3)**. The HPLC DAD spectrum showed that compound **(3)** was retained at 15 min with a 100 % purity at three different wavelengths; 230, 240 and 260 nm (Fig. 4.42).

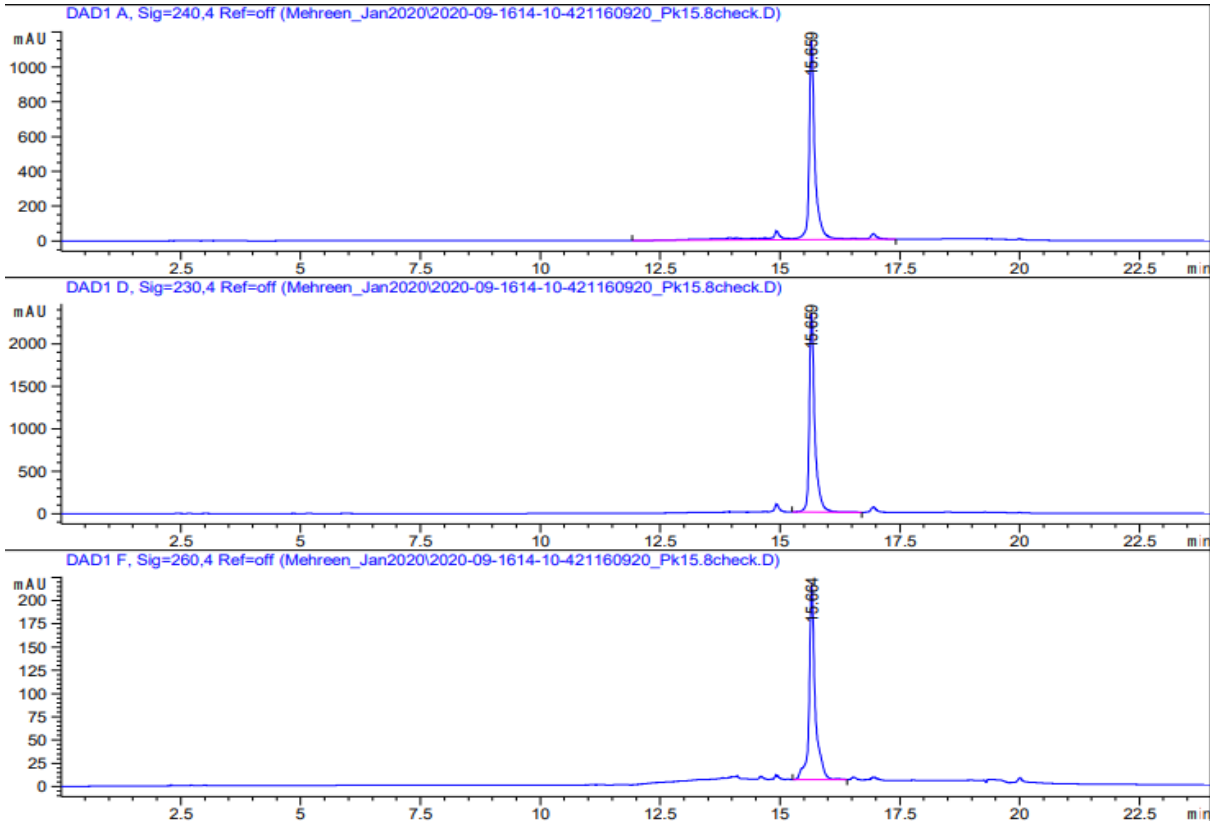

Fig. 4. 42. HPLC DAD spectrum of compound **(3)** at 230, 240 and 260 nm.

A high-resolution electrospray ionization mass spectrum (HRESI-MS) scan from 100 – 1000 m/z revealed the parent ion peak at m/z 507.2731 [M+H] and another fragment at m/z 303.2326 [M+H]. The low resolution ESI-MS scan and SIM mode were in agreement with the HRESI-MS (Fig. 4.43).

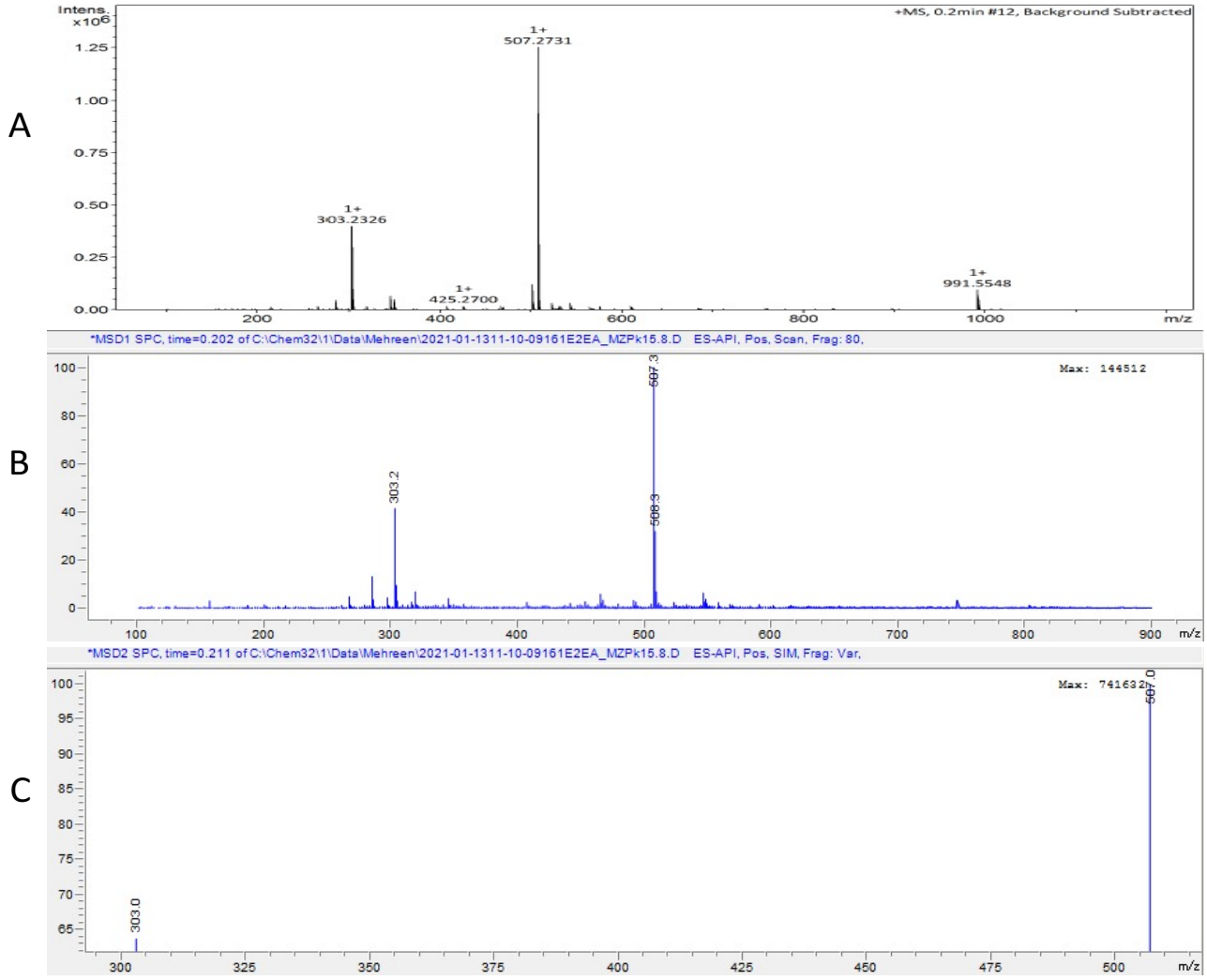

Fig. 4. 43. High resolution HRESI-MS (A) and low resolution ESI-MS (B) of compound (3) in scan mode, and SIM mode (C).

The FTIR spectrum of compound (3) showed peak stretches at 3391 cm^{-1} and 2930 cm^{-1} for hydroxyl and C-H functionalities (Fig. 4.44).

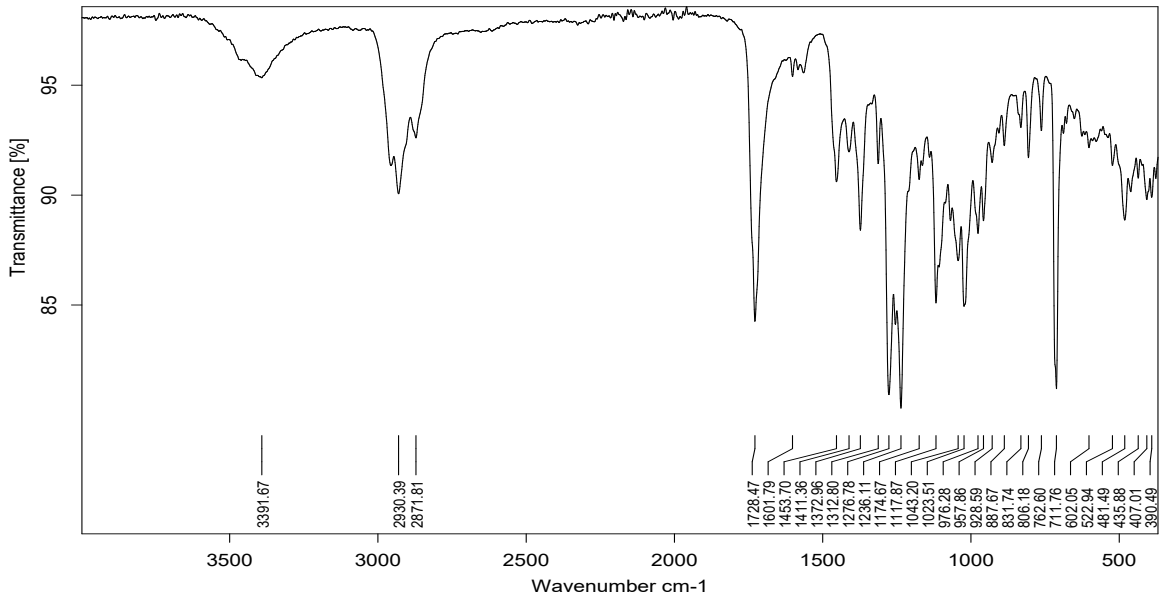

Fig. 4. 44. FTIR spectrum of compound **(3)**.

4.3.2.17. Crystallization of compound (3)

Amongst the three approaches selected (slow evaporation, vapor diffusion and recrystallization), the first two approaches successfully generated shiny white needle-shaped thin long crystals (Fig. 4.45). Methanol alone worked as a solvent for slow evaporation. Compared to slow evaporation, the crystal size was bigger with the vapor diffusion approach. Unfortunately, crystals obtained from both methods were unable to diffract light and therefore its crystal structure was unattainable.

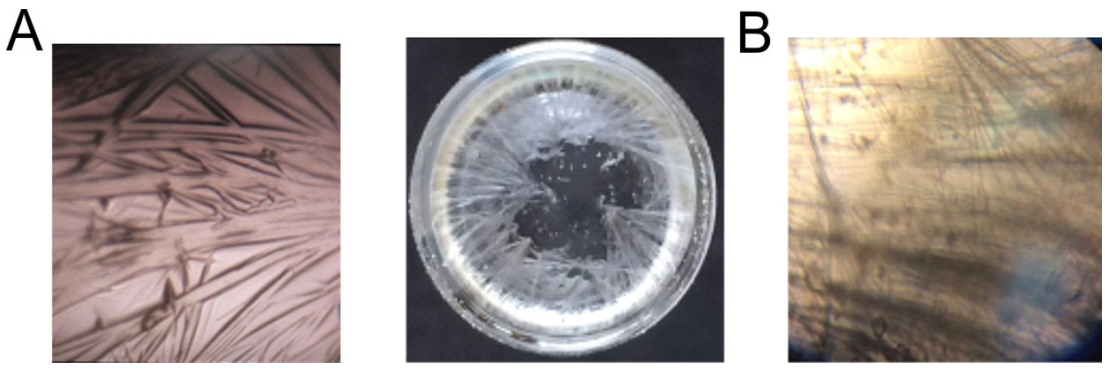

Fig. 4. 45. Crystals of compound (3) from vapor diffusion method (A) and slow evaporation (B).

4.3.2.18. HPLC analysis of hexane layer

The HPLC analysis of phase-separated hexane layer showed a very complex spectrum (Fig. 4.46) with many peaks indicating the need for further purification. Therefore, a method was successfully developed on TLC with 95:5 hexane: IPA as mobile phase. The TLC quadrant test revealed the UV active compounds in the fractions 7 to 9 (Fig. 4.47).

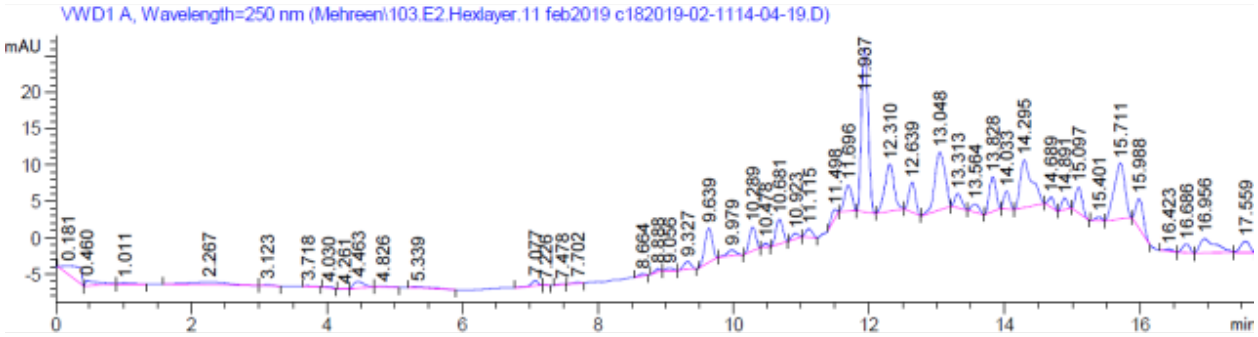

Fig. 4. 46. HPLC spectrum of phase separated hexane layer.

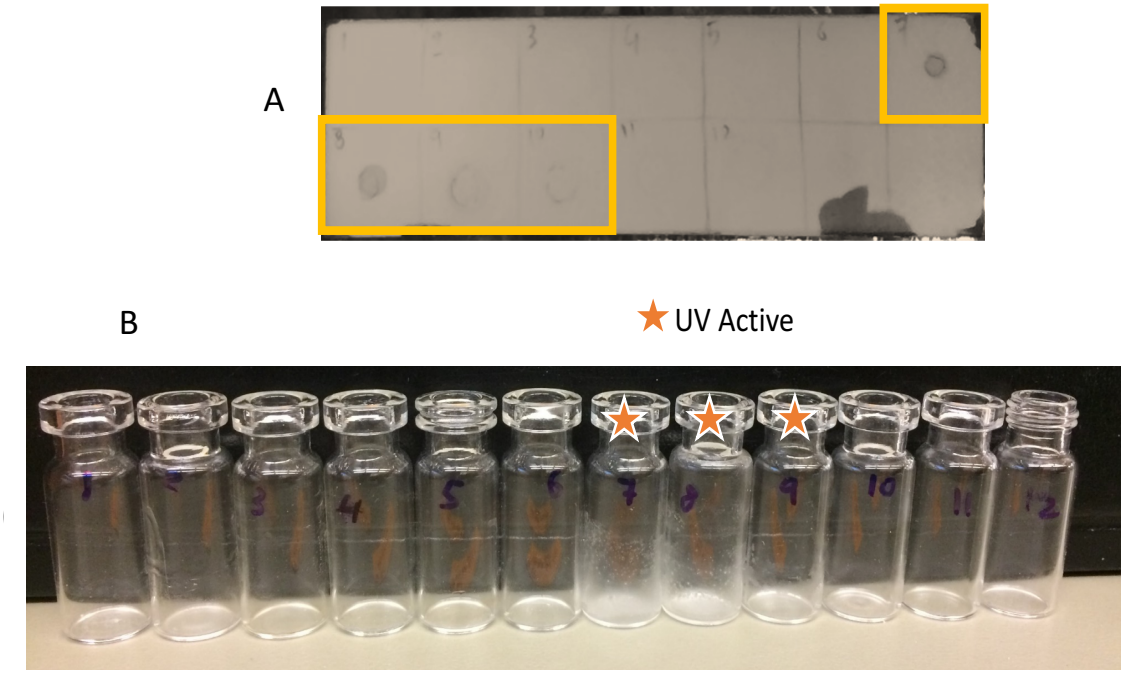

Fig. 4. 47. TLC quadrant test (A) and post SFC collected fractions (B).

4.3.2.19. Purification and HPLC analysis of compounds from chloroform layer

HPLC analysis of phase-separated chloroform layer displayed an unresolved spectrum of multiple peaks (Fig. 4.48). Therefore, further purification was carried out.

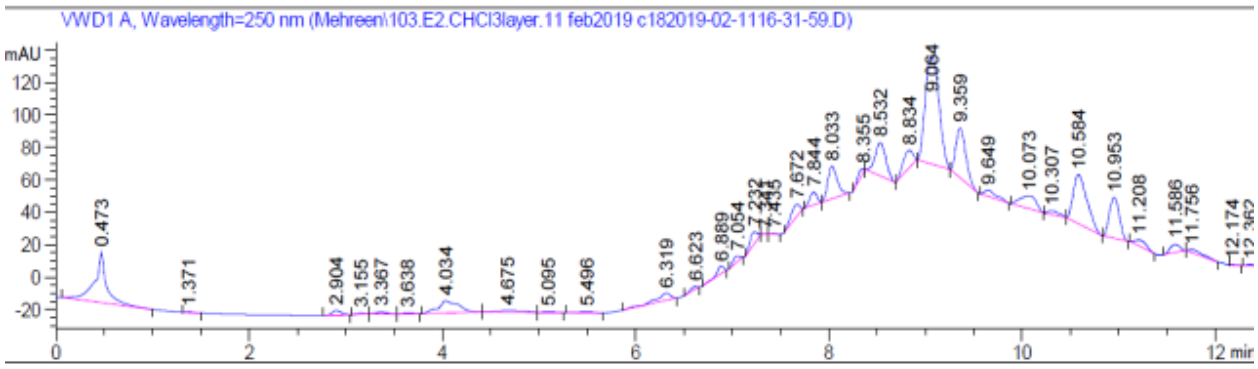

Fig. 4. 48. HPLC profile of chloroform layer.

4.3.2.20. Purification by Sephadex LH-20 SEC

The post-Sephadex LH-20 fractions 13-20 were found to contain growth-inhibitory compounds (Fig. 4.49). The bioactive fractions were analyzed by HPLC. Fractions 14-16 shared the same HPLC profile and were therefore combined for further purification (Fig. 4.50).

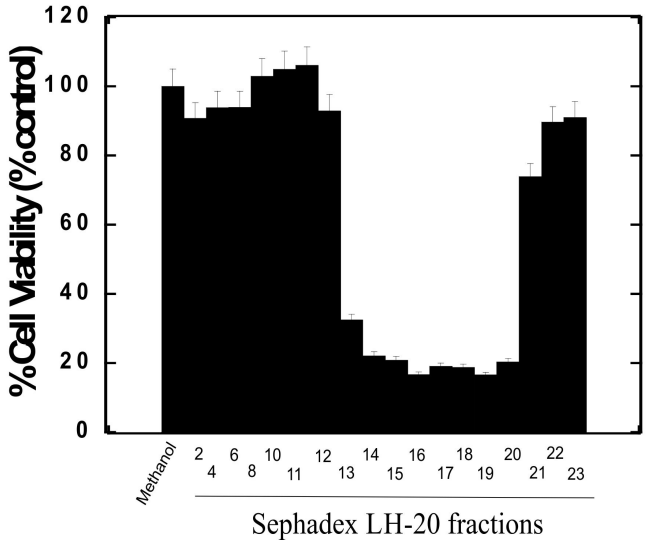

Fig. 4. 49. Sephadex LH-20 SEC profile of chloroform layer. Result shown is a representative from three biological replicates.

The fractions 4a, 4b, and 4c from chloroform elution of SFC also shared the same profile when injected into HPLC, therefore the fractions from both columns were combined and analyzed (Fig. 4.50). The peaks retained at 11.3 and 14.4 min were fraction collected and reinjected for purity check (Figs. 4.51 & 4.53).

ESI-MS analysis was carried out in positive mode for both peaks. Peak at 11.3 min showed molecular ion peak with a m/z 507 Da [M + H] in both scan (Fig. 4.52A) and SIM mode (Fig. 4.52B). In contrast, the peak at 14.4 min had a molecular ion peak of m/z 439 Da [M + H] in SIM and scan mode (Fig. 4.54).

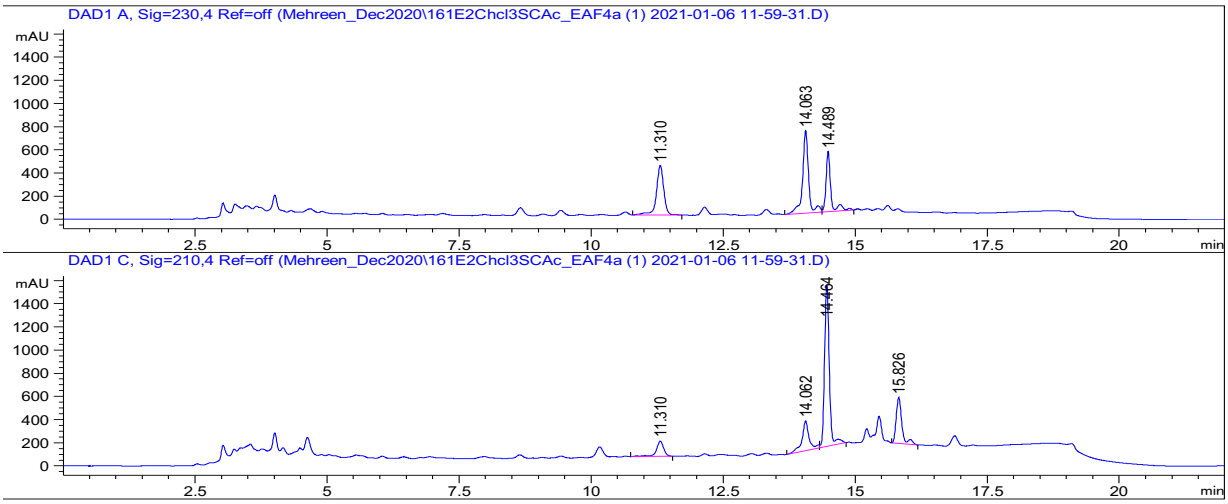

Fig. 4. 50. HPLC DAD spectrum of pooled fractions F14-16 and F4a-c.

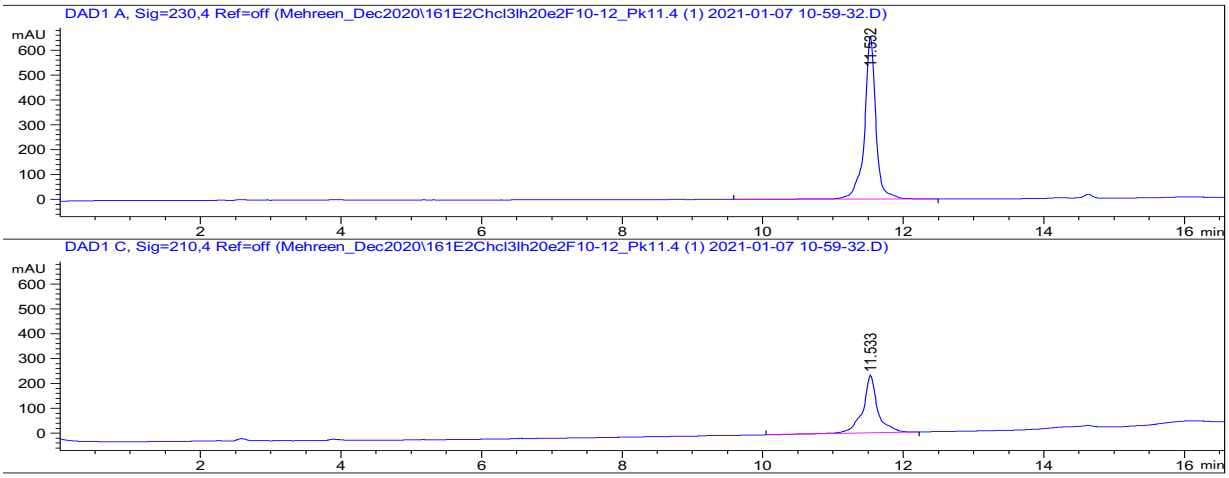

Fig. 4. 51. UV DAD spectrum of peak at 11.5 min.

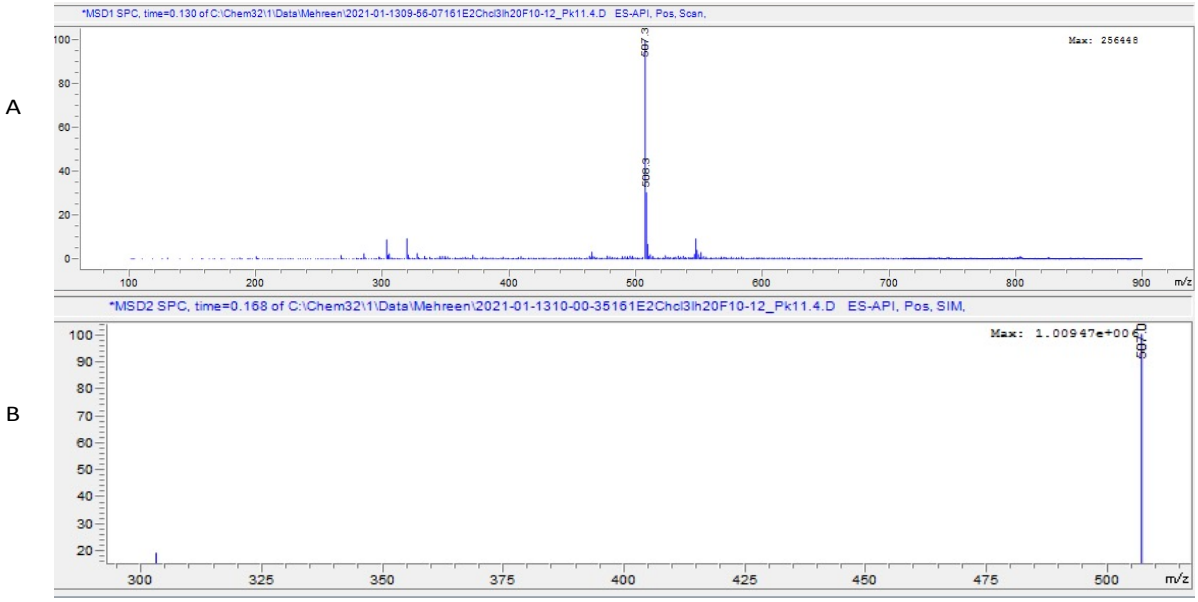

Fig. 4. 52. ESI-MS spectrum of peak at 11.3 min in scan mode (A) and SIM mode (B).

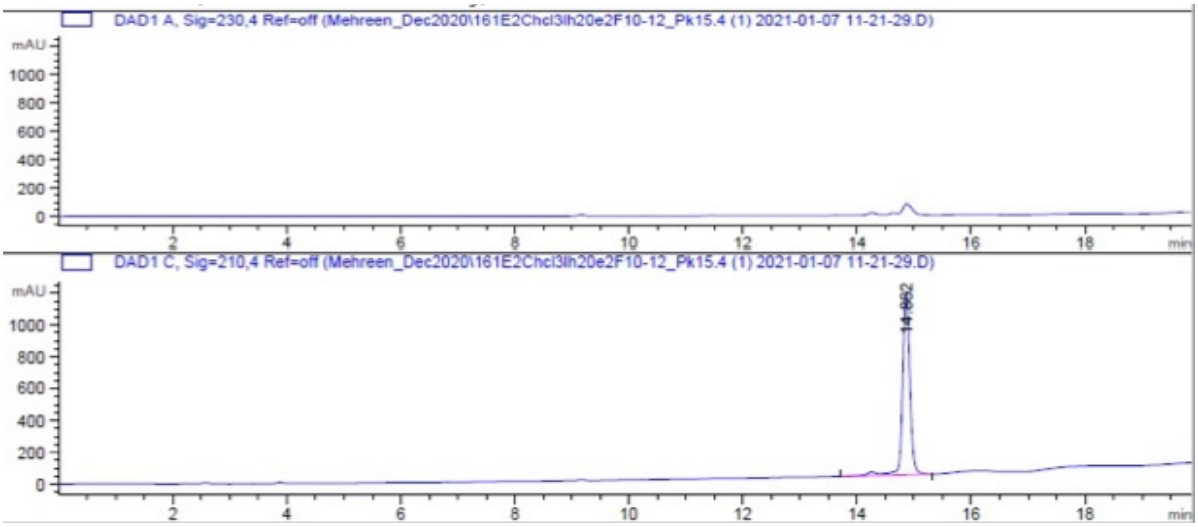

Fig. 4. 53. UV DAD spectrum of peak at 14.4 min.

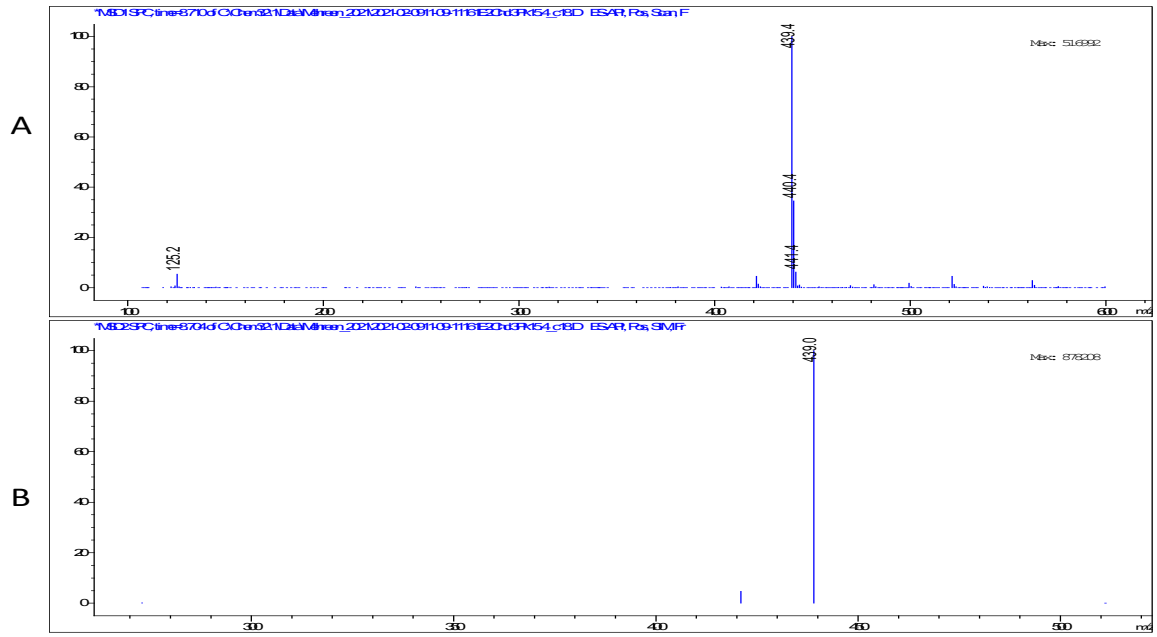

Fig. 4. 54. ESI-MS ion chromatogram of peak at 14.4 min.

In addition, HPLC analysis of the remaining bioactive fractions 17-20 from Sephadex LH-20 showed the same HPLC profile where there were two abundant peaks retained at 4.9 and 6.4 minutes (Fig. 4.55).

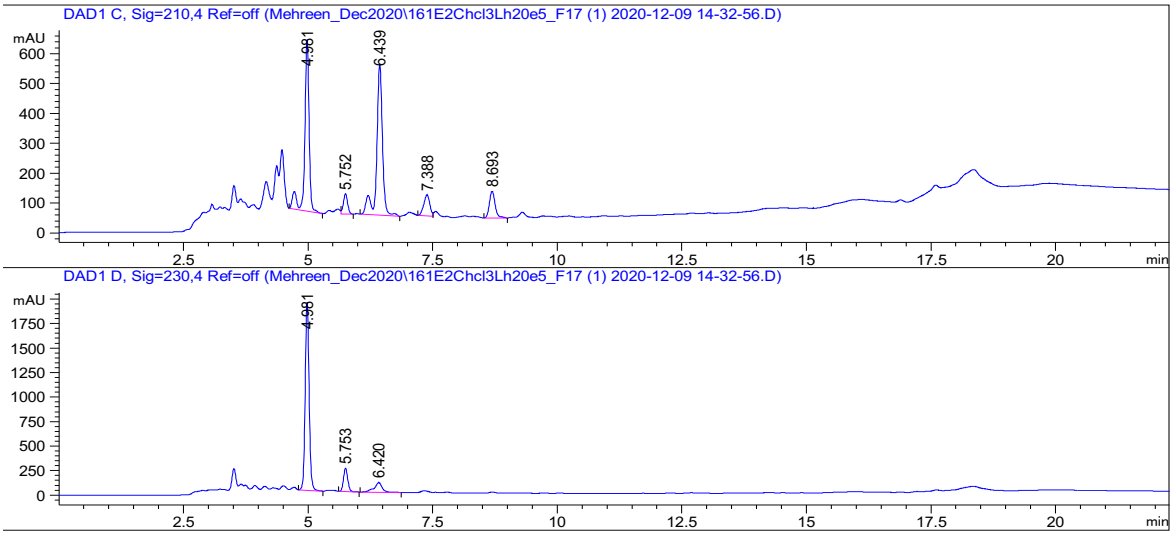

Fig. 4. 55. HPLC spectrum of bioactive fractions 17-20 of Sephadex LH-20 column.

The HPLC DAD spectrum for peak retained at 4.9 min at 210 and 230 nm was not pure (Fig. 4.56) and it was also reflected in the MS spectrum where there were multiple m/z ions, although the 271 Da peak being the dominant one (Fig. 4.57).

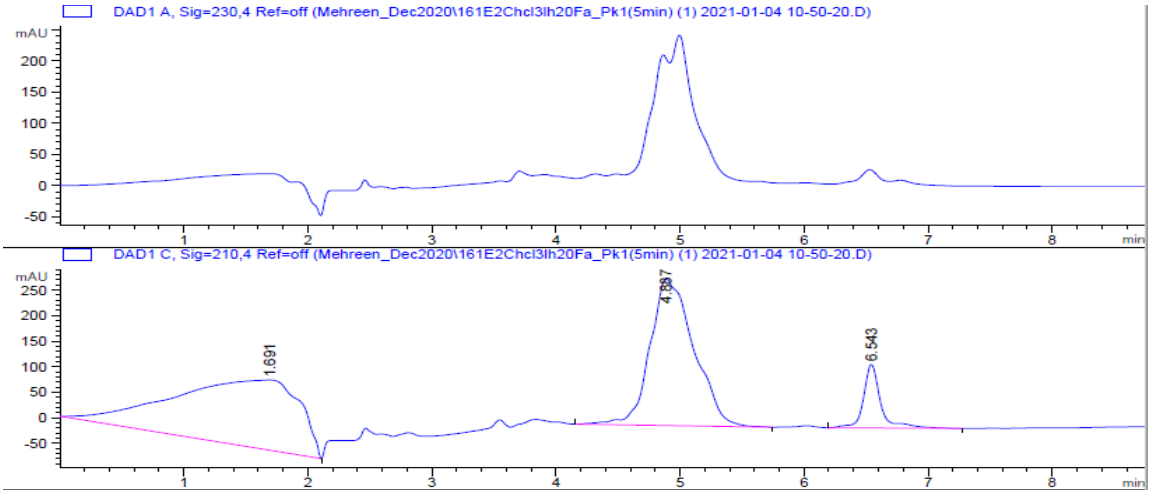

Fig. 4. 56. HPLC DAD spectrum of peak at 4.9 min at 230 and 210 nm.

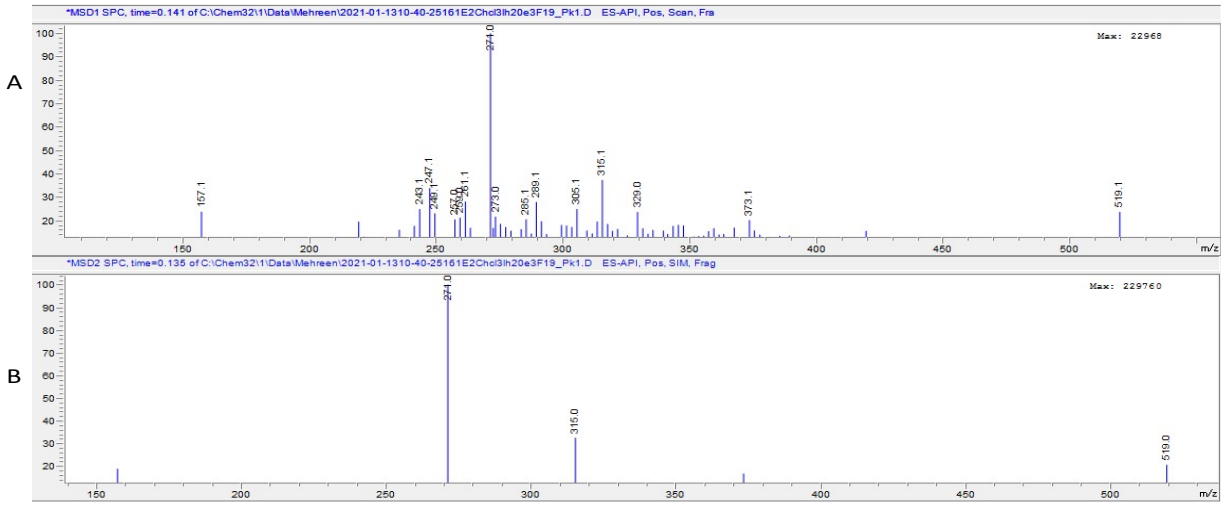

Fig. 4. 57. ESI-MS spectrum of peak at 4.9 min in scan mode (A) and SIM mode (B).

The HPLC DAD spectrum of peak at 6.4 min displayed a pure peak (Fig. 4.58) at both 210 and 230 nm. The ESI-MS showed ion peaks with m/z 543, 283 and 261 Da (Fig. 4.59). It is possible that the parent ion peak was 543 and that ion peaks 283 and 261 were its fragment ions as they both add up closely to the mass of parent ion peak.

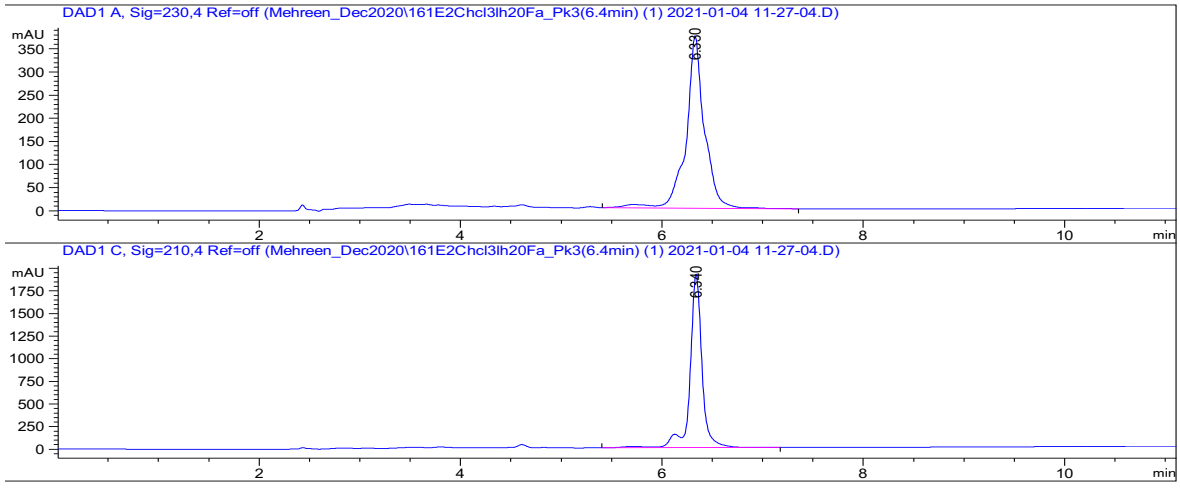

Fig. 4. 58. HPLC DAD spectrum of peak at 6.4 min.

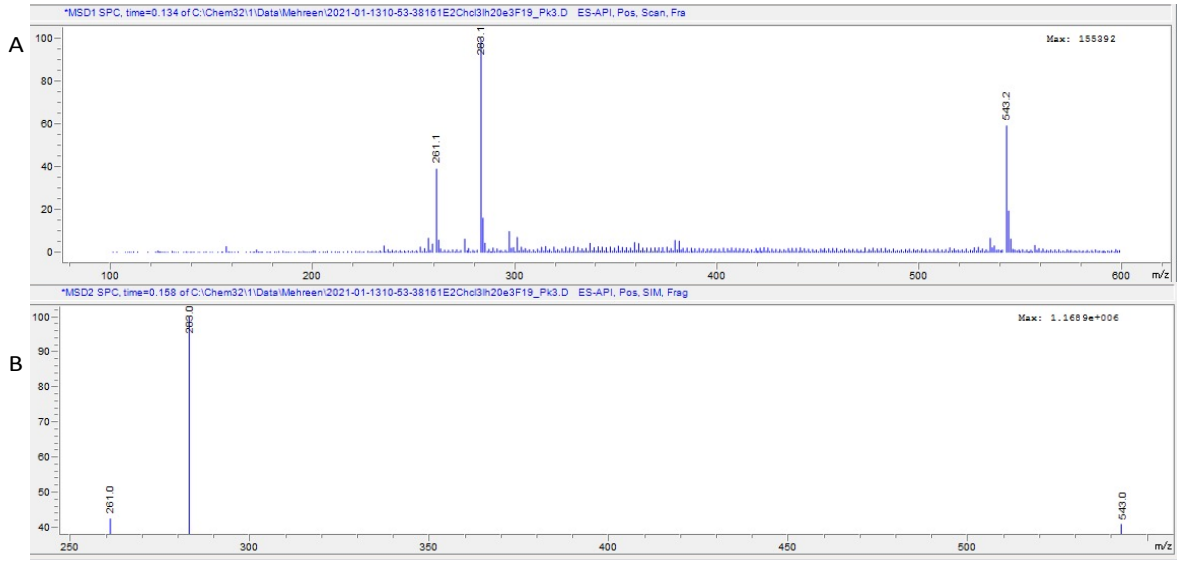

Fig. 4. 59. ESI-MS spectrum of peak at 6.4 min in scan mode (A) and SIM mode (B).

4.3.3. Approach 3: Direct extraction method

4.3.3.1. Extraction and assessment of growth-inhibitory activity of extracts

Hexane and DEE extracts were obtained from direct extraction of powdered mushroom (Fig. 4.60A) with yield of 1.8 % and 4 % respectively (Table 4.8). Both the extracts were tested for growth-inhibitory activity using MTT assay. Hexane and DEE extracts caused growth inhibition in HeLa cells with less than 20 % cell viability when treated at 0.6 mg/mL for 48 h (Fig. 4.60B).

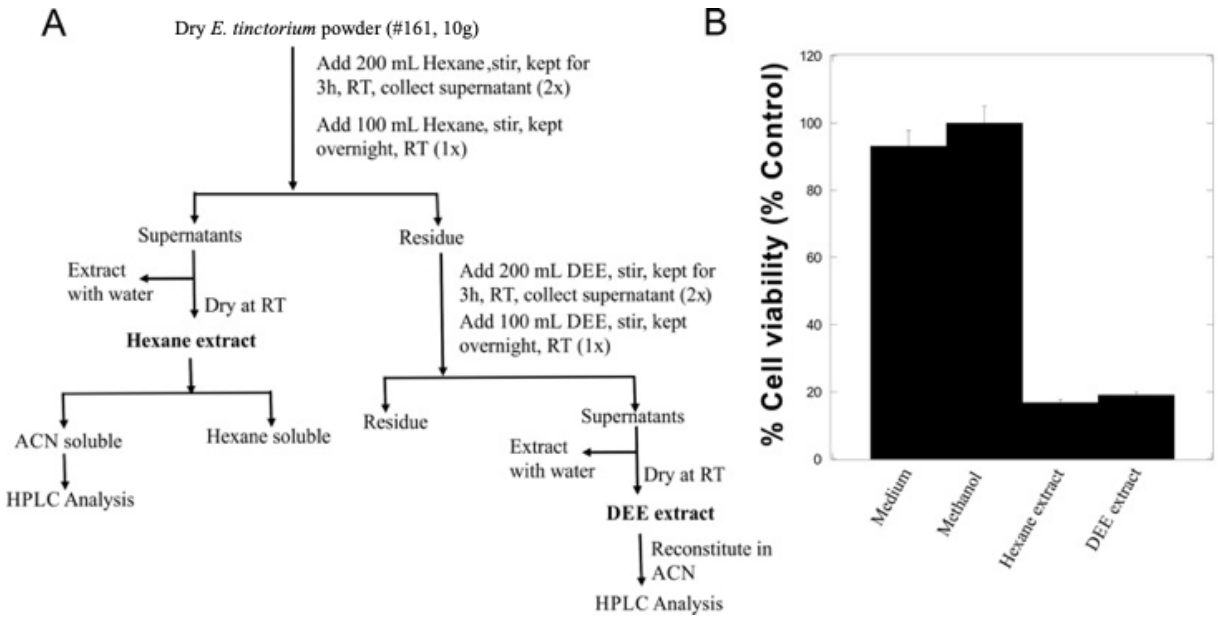

Fig. 4. 60. A) Methodology for direct extraction of small molecules from *E. tinctorium*, B) Hexane and DEE extracts at 0.6 mg/mL for 48 h were assessed for growth-inhibitory activity on HeLa cells. Result shown is a representative from three biological replicates.

Table 4. 8. Quantitative estimation of extracts and compounds from direct extraction method

Sample	Amount (mg)	% Yield	Solubility
Powdered mushroom	5000	-	Water/methanol
Hexane extract	60 (Methanol soluble) 40 (DMSO soluble)	1.8	Hexane, Acetonitrile, Methanol, DMSO
DEE extract	200	4	Acetonitrile
Hexane extract for HPLC	50	-	Methanol
PK 2	2.8*, 0.8**	5.6*, 1.6	Acetonitrile
PK 3	0.3	0.6	Acetonitrile
PK 4	3.6	7.2	Acetonitrile
PK5 (PK5a & PK5b)	1.1* (PK5a & PK5b) 0.5** (PK5a) 0.4**(PK5b)	2.2 1 (PK5a) 0.8 (PK5b)	Acetonitrile

*indicates single step purification on HPLC, **indicates two times purification on HPLC

4.3.3.2. HPLC analysis and purification

HPLC method was successfully developed using Phenomenex Luna C18 reverse phase HPLC analytical column with acetonitrile and water gradient. Some compounds had absorption maxima at 210 nm while others were more visible at 230 nm. Therefore, HPLC analysis and purification was done at both wavelengths simultaneously (Fig. 4.61).

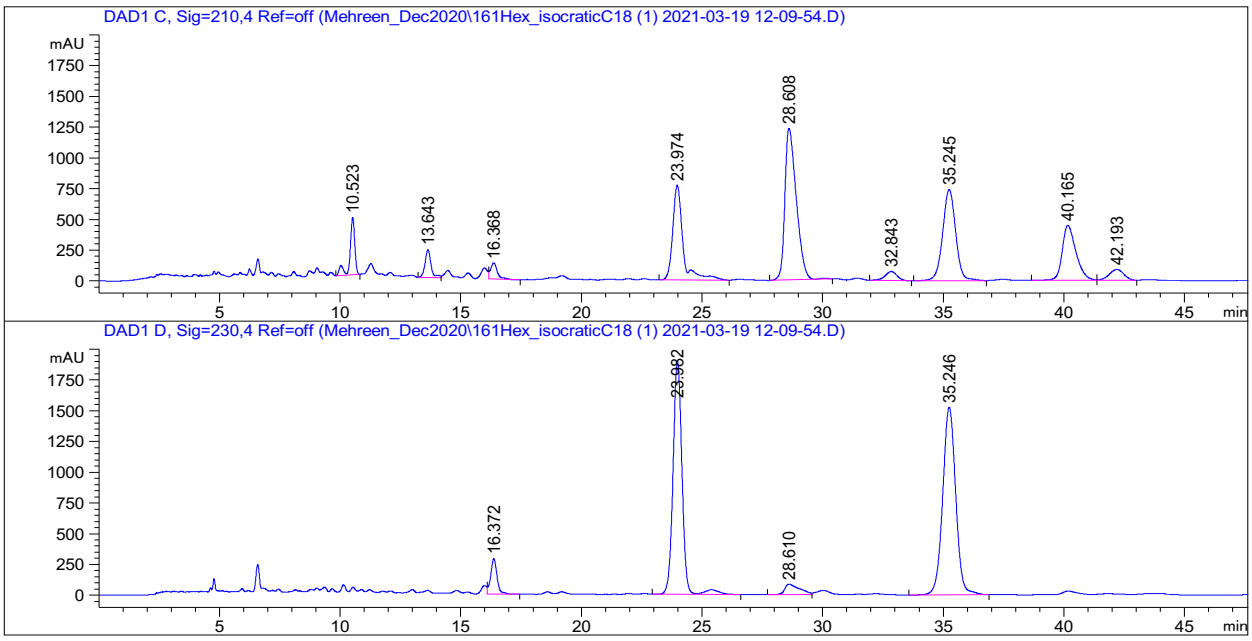

Fig. 4. 61. HPLC DAD profile of hexane layer from direct extraction method at 210 and 230 nm.

After HPLC analysis on analytical column, the method was developed on C18 reverse phase HPLC semi preparative column with acetonitrile and water gradients (Fig. 4.62). The peaks

eluting at retention times 19.3, 24.5, 26, 32 and 39.1 min were fraction collected and designated as PK1, 2, 3, 4 and 5 respectively.

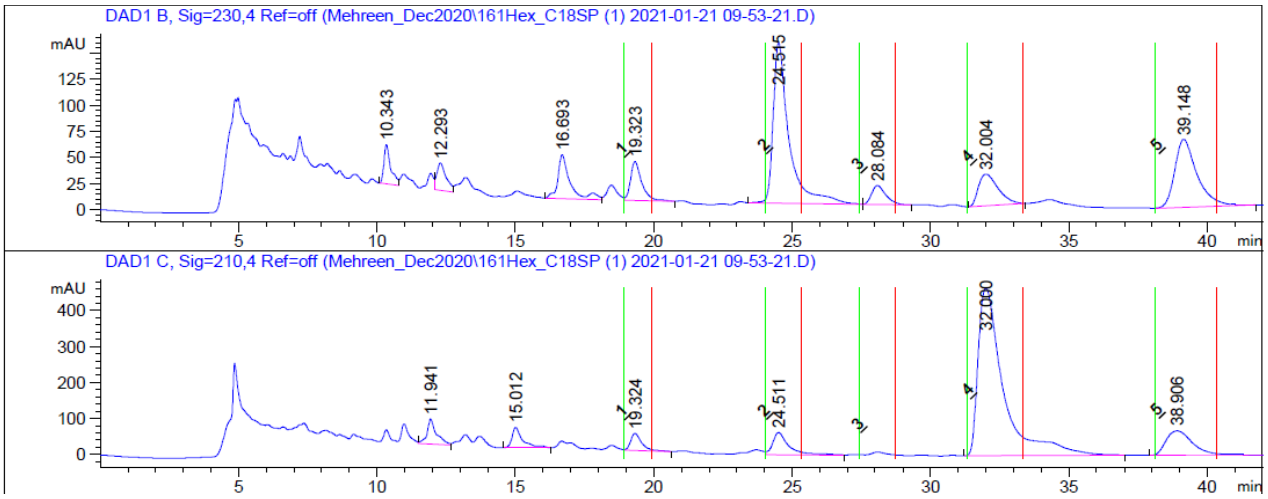

Fig. 4. 62. Semi preparative HPLC DAD profile of hexane layer.

The collected peaks were reinjected (Figs. 4.63 & 4.65) into a C18 analytical column to check for purity at multiple wavelengths using DAD (210, 230 nm). The solvent gradient (Acetonitrile: Water 80:20-90:10 in 15min, 90:10 from 15-22min, 90:10-80:20 in 25min) was used at 0.8 mL/min. All the peaks were also subjected to ESI-MS analysis to obtain the molecular mass (Figs. 4.64 & 4.69).

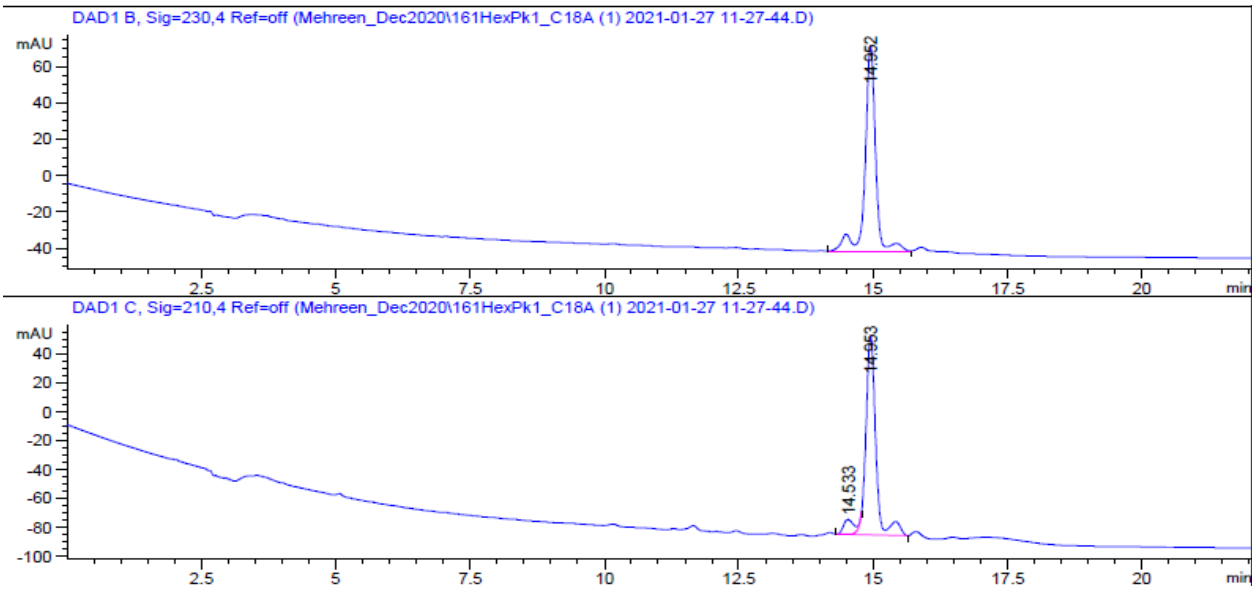

Fig. 4. 63. HPLC DAD profile of PK1.

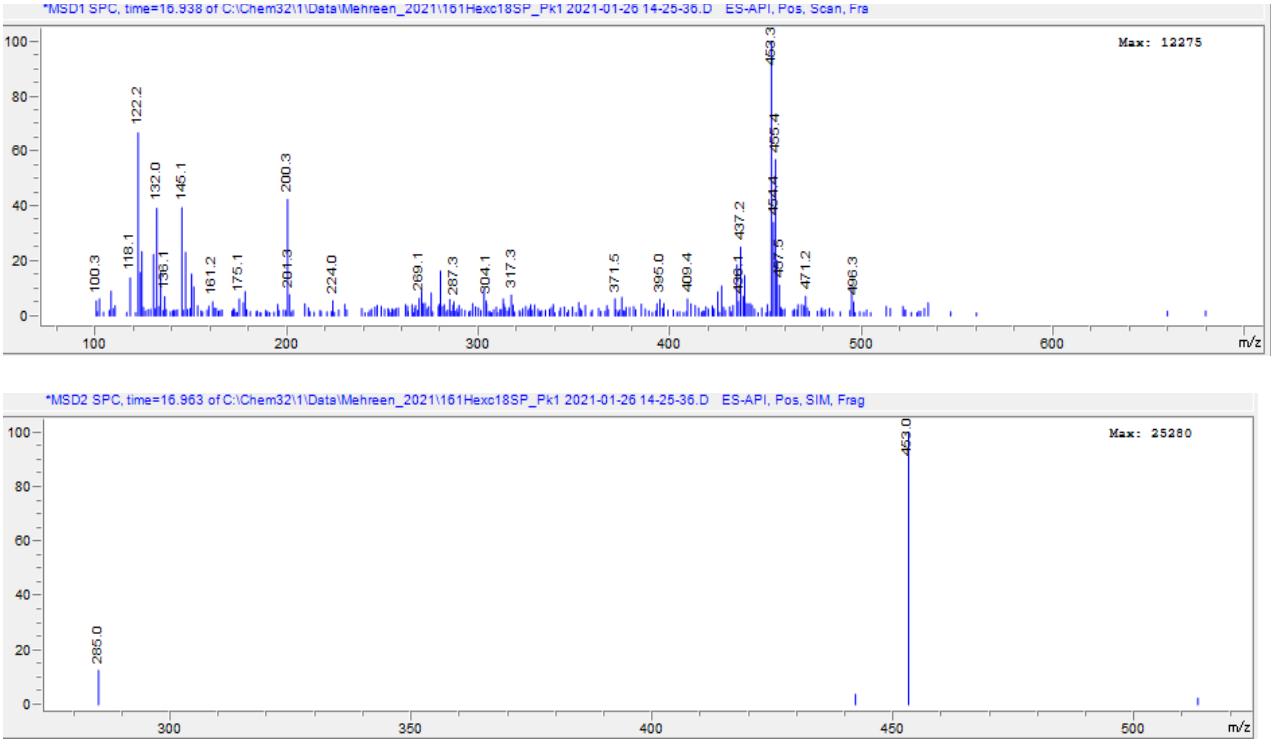

Fig. 4. 64. MSD spectrum of PK1 in scan (100-1000 m/z) and SIM mode.

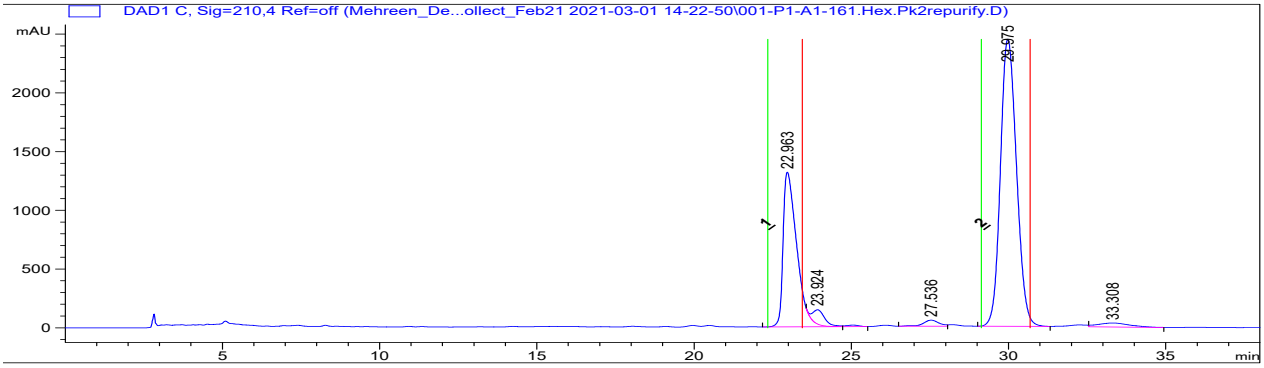

Fig. 4. 65. HPLC DAD spectrum of PK2.

When PK2 was kept over a week and reinjected again, it showed a desired peak at 29 min (named PK2b) and an unexpected peak (named PK2a) at 22 min, suggesting the unstable nature of PK2. Therefore, several attempts were taken to repurify the PK2, initially on Phenomenex Luna C18(2) (Fig. 4.66) and then on Agilent Poroshell C18 (Fig. 4.67) in order to improve the resolution of peaks (as the latter has small pore size) and shorten the time of analysis.

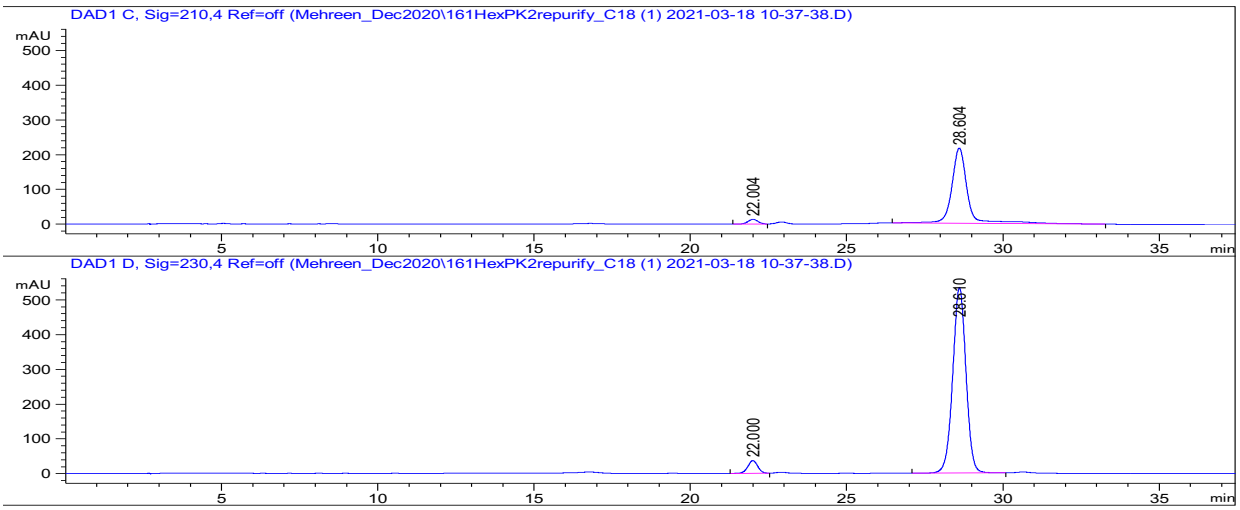

Fig. 4. 66. HPLC DAD spectrum of PK2 on Phenomenex Luna C18(2) column.

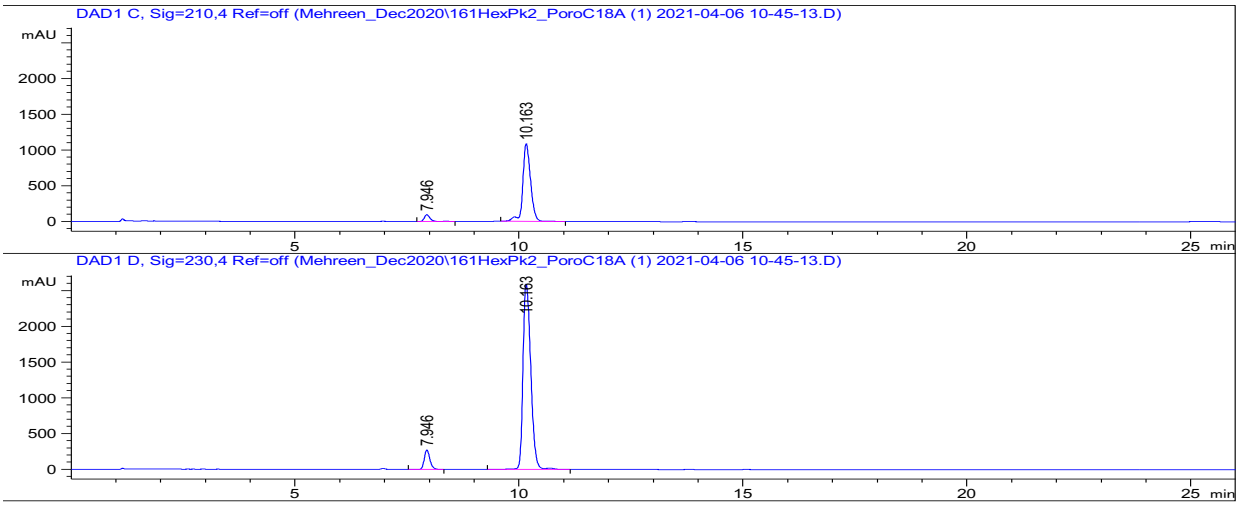

Fig. 4. 67. HPLC DAD spectrum of PK2 repurification on Agilent Poroshell C18 column.

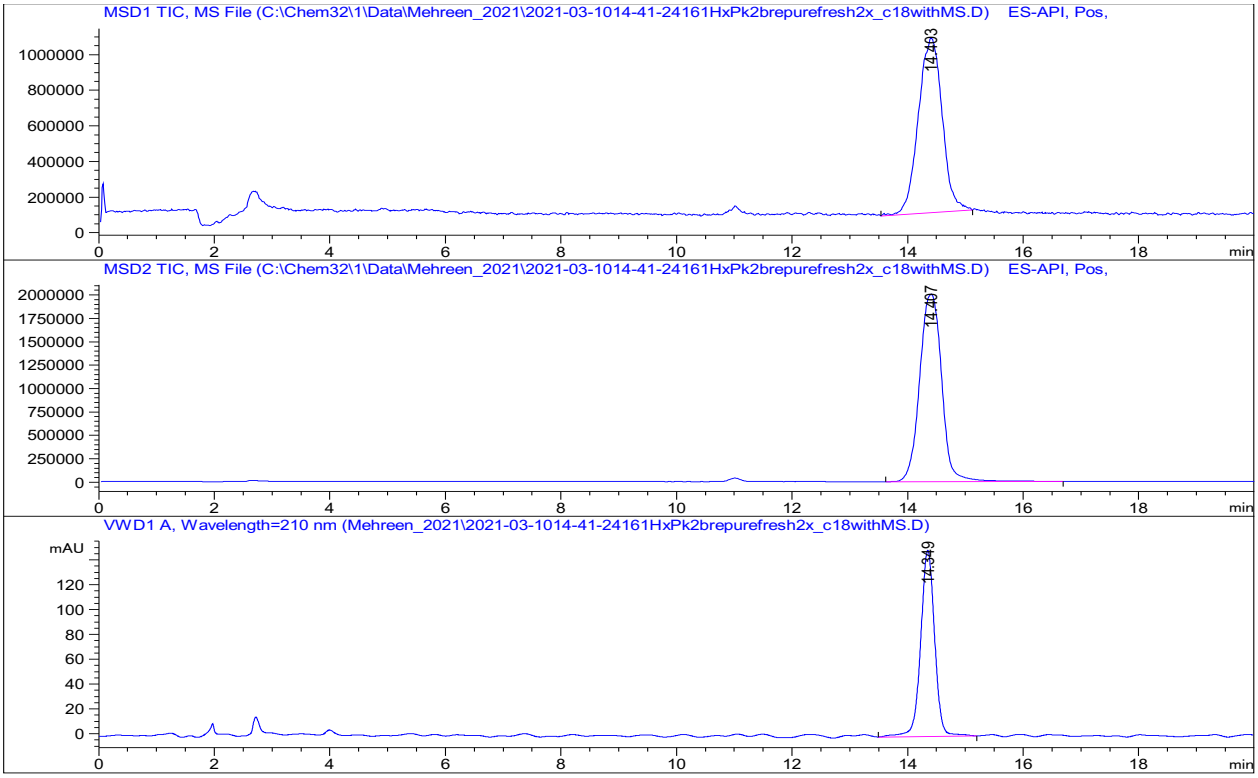

Fig. 4. 68. HPLC profile of freshly collected PK2b for purity check at MSD1 scan mode, MSD2 SIM mode and UV at 210 nm.

Fig. 4. 69. MSD spectrum of PK2 in scan mode and SIM mode.

PK3 was pure when reinjected into HPLC (Fig. 4.70). The ESI-MS analysis of PK3 revealed molecular ion peak with m/z 437 in both scan and SIM mode (Fig. 4.71). The same molecular ion peak was present in PK5b that was later identified as echinodone. PK3 had different retention time compared to PK5b which could indicate that PK3 is an isomer of PK5b. Due to

very low abundance of PK3 even after multiple rounds of purification, there was not sufficient amount of PK3 to perform further structural elucidation studies.

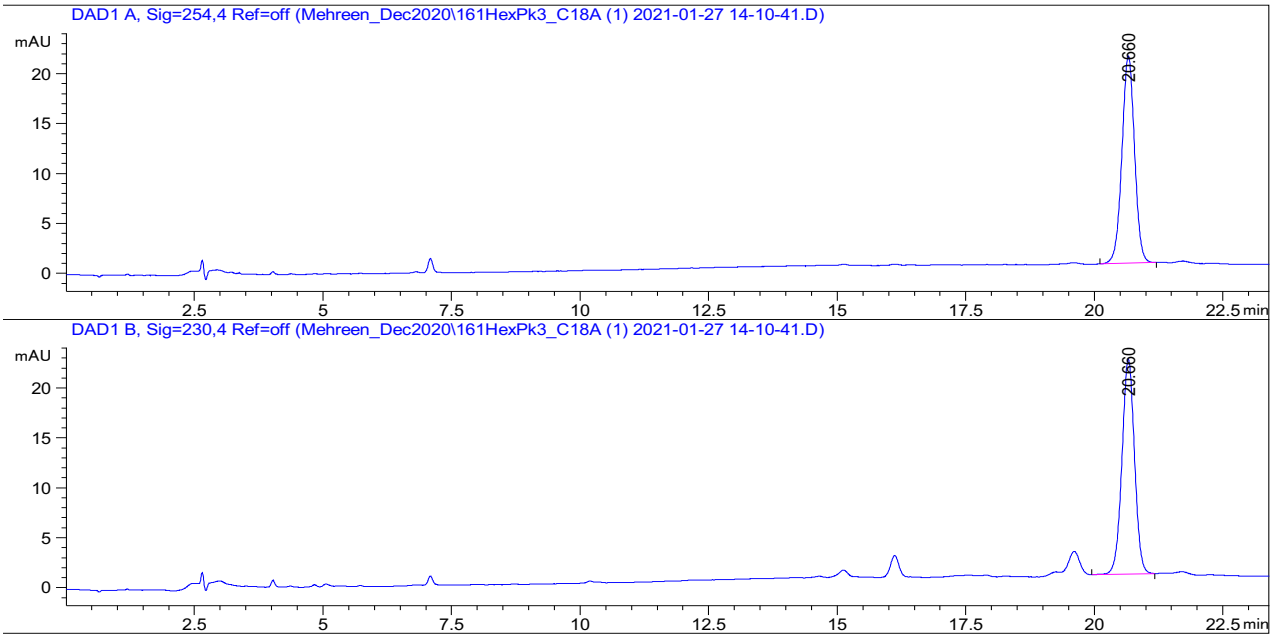

Fig. 4. 70. HPLC DAD spectrum of PK3.

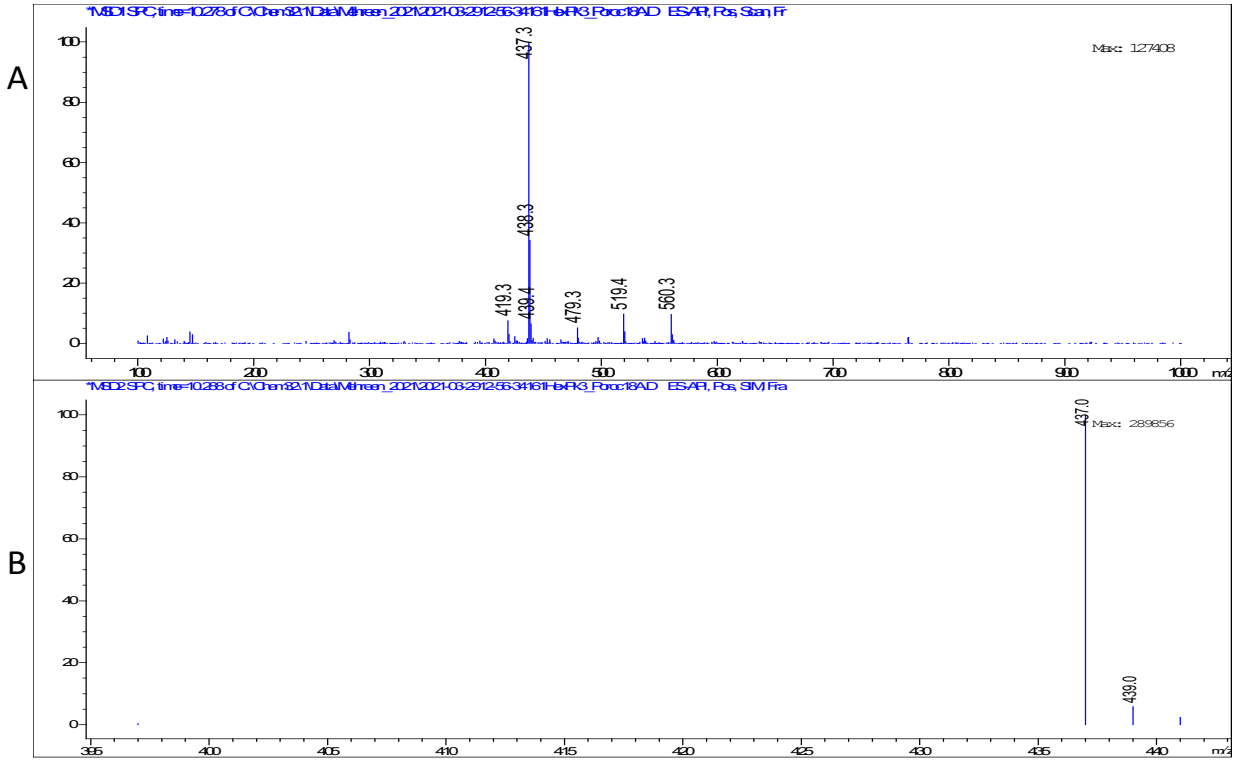

Fig. 4. 71. ESI-MS spectrum of PK3 in scan mode (A) and SIM mode (B).

4.3.3.3. Characterization of compound (4)

PK4 was designated as compound **(4)**: it was obtained as colorless needle shaped crystals, with a molecular formula of $C_{32}H_{50}O_4$ which was obtained from NMR data, X-Ray crystallography and ESI-MS ion peaks.

4.3.3.4. HPLC and ESI-MS analysis of compound (4)

The UV absorption maxima of compound **(4)** was obtained at 210 and 230 nm (Fig. 4.72).

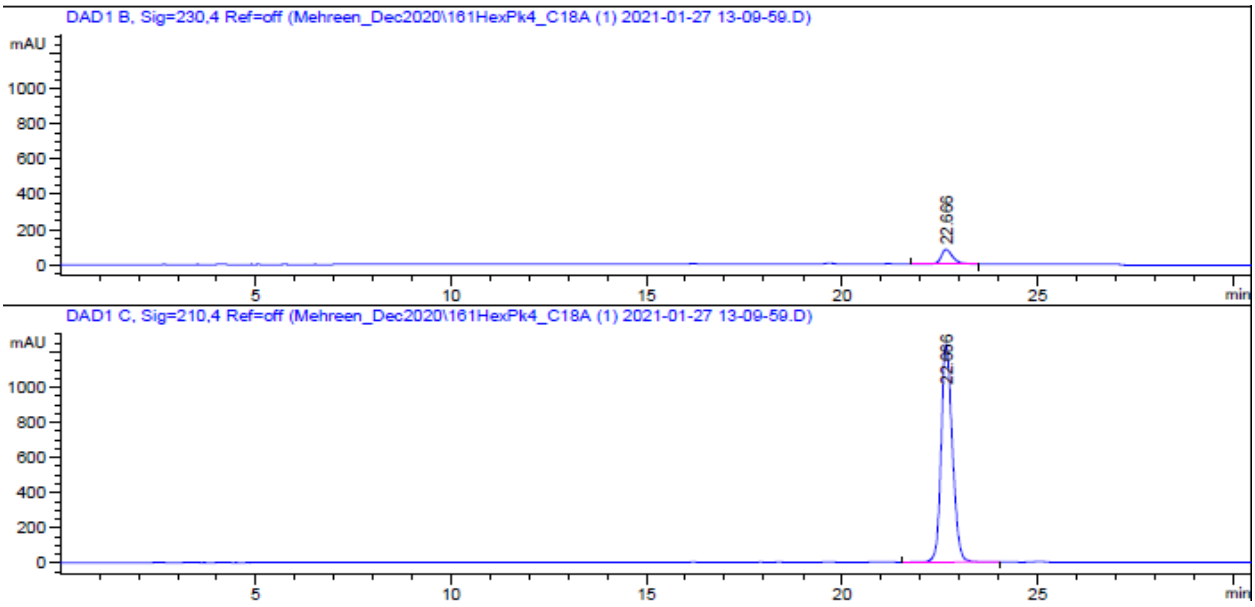

Fig. 4. 72. UV DAD profile of compound **(4)** at 210 and 230 nm.

Compound **(4)** was subjected to mass spectral analysis using scan and SIM mode. The MS spectrum (Fig. 4.73) of compound **(4)** revealed MS ion peak of m/z 439 [M+H]. The m/z 439 from the ion chromatogram represented the base peak as a major deacetylated fragment of the parent compound.

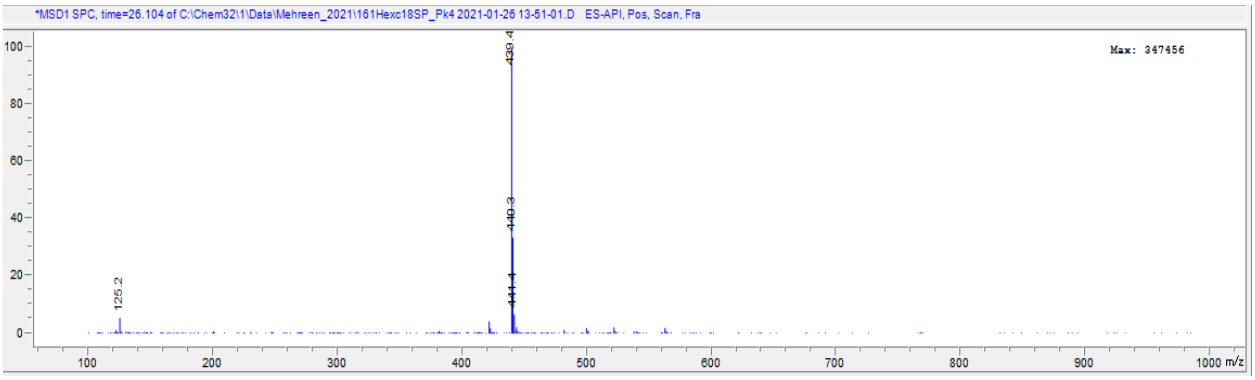

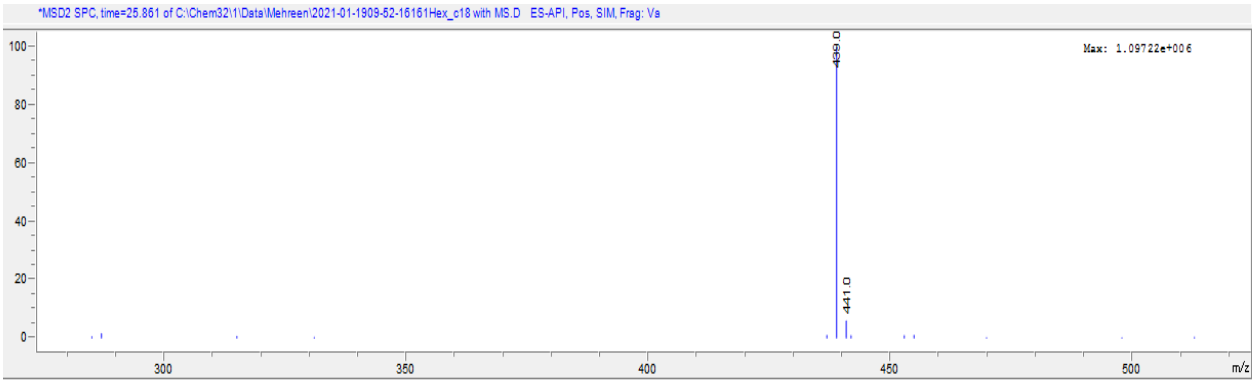

Fig. 4. 73. MS spectrum of compound **(4)** in scan mode 100-1000 m/z (A) and SIM mode (B).

4.3.3.5. Structural elucidation by FTIR and NMR spectroscopy

The IR spectrum of compound **(4)** (Fig. 4.74) showed peak stretches at 2937 cm^{-1} indicative of sp3 C-H, a weak stretch at 3273 cm^{-1} for hydroxy group and at 1738 cm^{-1} for C=O group.

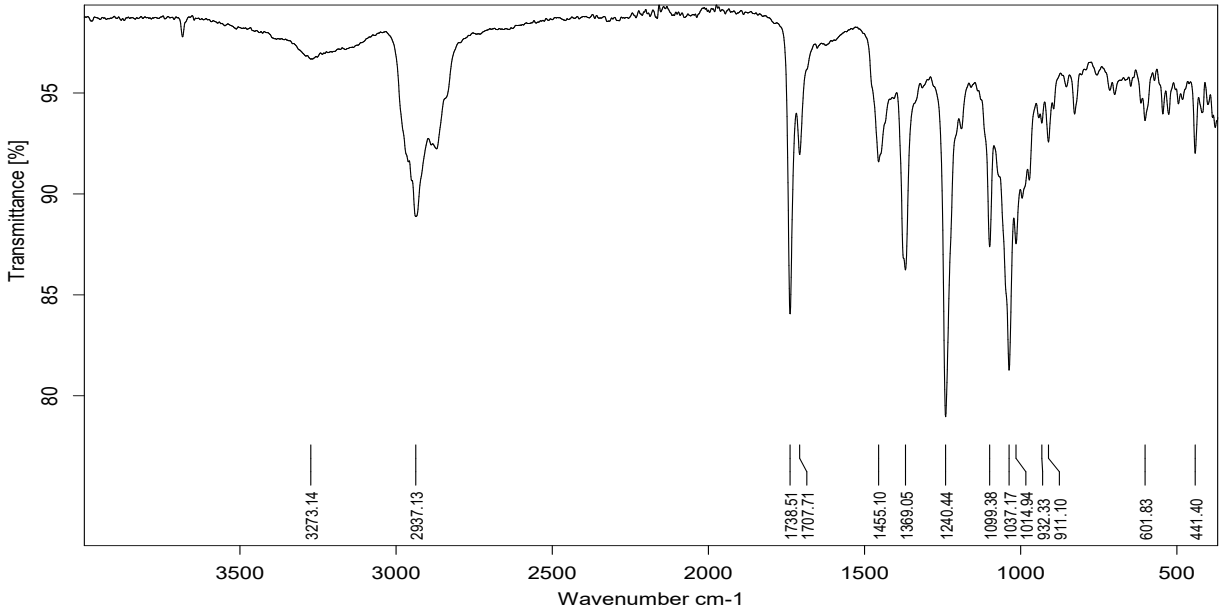

Fig. 4. 74. FTIR spectrum of compound **(4)**.

Based on the 1D NMR data, compound **(4)** possessed 32 carbons (Fig. 4.76), that included seven methylenes (δ_C 35.2, 27.5, 18.0, 26.7, 19.9, 29.7, and 35.3), nine methyl groups (δ_C 15.9, 18.3, 14.5, 24.8, 17.6, 27.4, 15.0, 27.1, and 20.0), a carbonyl (δ_C 170.2), seven quaternary carbons (δ_C 38.6, 133.9, 135.1, 37.0, 48.9, 43.5, and 37.2), eight methine groups (δ_C 50.3, 82.6, 53.2, 38.8, 77.7, 77.8, and 78.1), and vinylic carbon (δ_C 123.3).

The HSQC data showed 13C signals correlating well with the 1H NMR peaks (Table 4.9, 4.10 & Fig. 4.75). There were several methylene proton pairs (Ha and Hb) identified from HSQC signals including H-1a (δ_H 1.72, 1H) and 1-Hb (δ_H 1.22, 1H), overlapped H2-a/b (δ_H 1.57, 2H),

H-6a (δ_H 1.73, 1H) and H-6b (δ_H 1.56, 1H), H-7a (δ_H 2.17, peak hidden behind water peak) and H-7b (δ_H 2.02, 1H), overlapped H-11a/b (δ_H 2.08, 2H), H-12a (δ_H 1.84, 1H) and H-12b (δ_H 1.58, 1H), H-15a (δ_H 2.31, 1H) and H15b (δ_H 1.14, 1H). The H-24 (δ_H 5.03, 1H) attached to the unsaturated carbon was de-shielded the most. H-24 was cis-coupled to the H-26 (δ_H 1.70, 3H) and trans-coupled to H-27 (δ_H 1.69, 3H). The H-32 acetyl protons (δ_H 1.96, 3H) were overlapped by the CD3CN solvent peak. Additionally, there was also a peak for a hydroxy proton (δ_H 2.49, 1H).

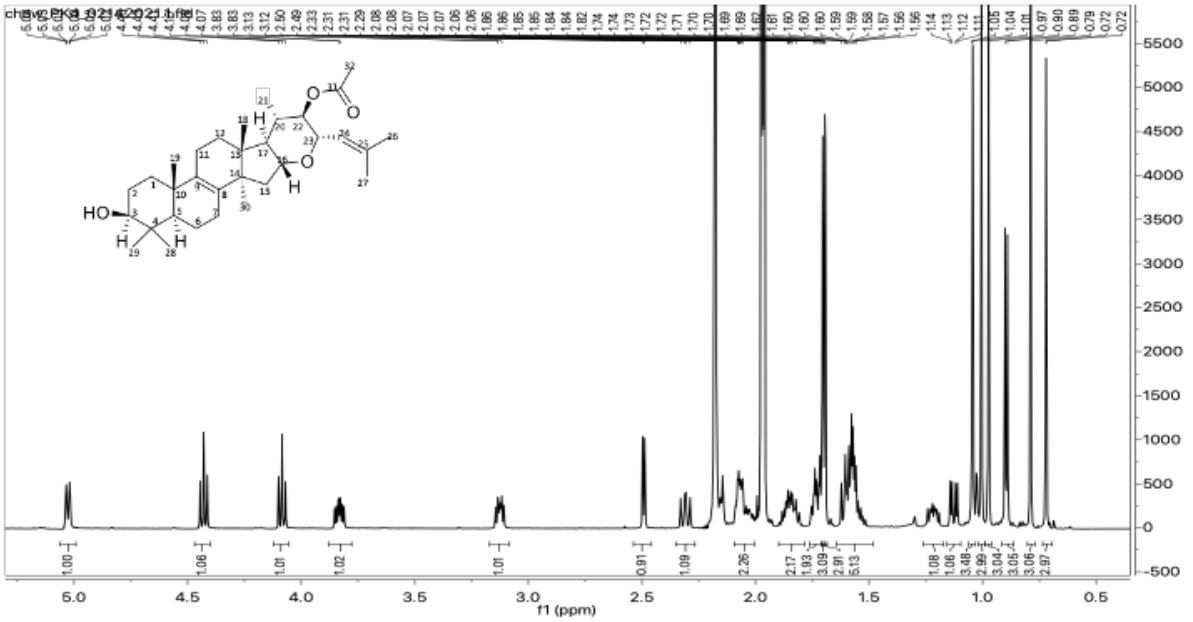

^{1}H NMR (Acetonitrile-d_3, 600 MHz) δ 5.06 – 4.99 (1H, m), 4.43 (1H, t, J=9.5 Hz), 4.08 (1H, t, J=9.1 Hz), 3.83 (1H, ddd, J=10.8, 9.4, 4.8 Hz), 3.17 – 3.09 (1H, m), 2.49 (1H, d, J=5.6 Hz), 2.31 (1H, dd, J=14.0, 10.9 Hz), 2.09 – 2.01 (2H, m), 1.90 – 1.78 (2H, m), 1.76 – 1.71 (2H, m), 1.70 (3H, d, J=1.4 Hz), 1.69 (3H, d, J=1.4 Hz), 1.64 – 1.48 (5H, m), 1.26 – 1.17 (1H, m), 1.13 (1H, dd, J=14.0, 4.8 Hz), 1.04 (3H, s), 1.01 (3H, s), 0.97 (3H, s), 0.90 (3H, d, J=6.4 Hz), 0.79 (3H, s), 0.72 (3H, d, J=1.0 Hz)

Fig. 4. 75. ^{1}H NMR of compound **(4)**.

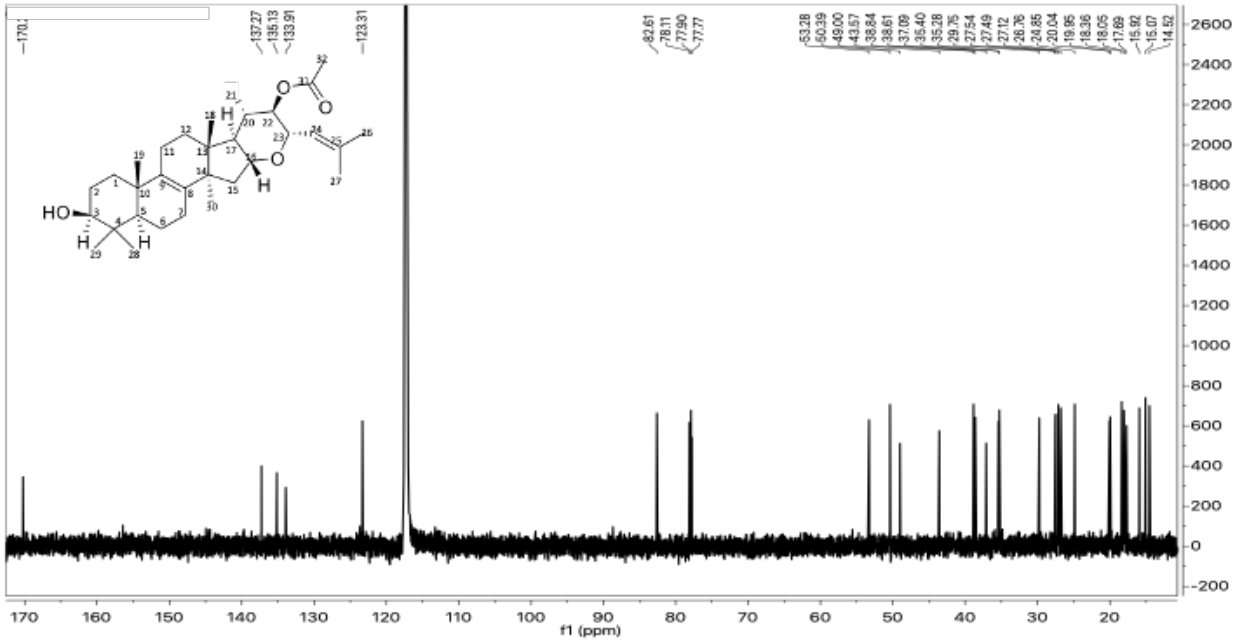

^{13}C NMR (CD$_3$CN, 151 MHz) δ 170.23, 137.27, 135.13, 133.91, 123.31, 82.61, 78.11, 77.90, 77.77, 53.28, 50.39, 49.00, 43.57, 38.84, 38.61, 37.09, 35.40, 35.28, 29.75, 27.54, 27.49, 27.12, 26.76, 24.85, 20.04, 19.95, 18.36, 18.05, 17.69, 15.92, 15.07, 14.52

Fig. 4. 76. ^{13}C NMR of compound **(4)**.

Table 4. 9. ^{13}C Chemical shift data of compound **(4)**

Number	^{13}C Chemical shift δ (ppm)	Functionality
1	35.2	CH_2
2	27.5	CH_2
3	77.8	CH
4	38.6	°4 C
5	50.3	CH
6	18.0	CH_2
7	26.7	CH_2
8	133.9	°4 C
9	135.1	°4 C
10	37.0	°4 C
11	19.9	CH_2
12	29.7	CH_2
13	48.9	°4 C
14	43.5	°4 C
15	35.3	CH_2
16	82.6	CH
17	53.2	CH
18	15.9	CH_3
19	18.3	CH_3
20	38.8	CH
21	14.5	CH_3
22	77.7	CH
23	78.1	CH
24	123.3	=CH
25	137.2	°4 C
26	27.4	CH_3
27	15.0	CH_3
28	27.4	CH_3
29	15.0	CH_3
30	27.1	CH_3
31	170.2	C=O
32	20.0	CH_3

Table 4. 10. ^{1}H Chemical shift data of compound **(4)**

Number	^{1}H Chemical shift δ ppm (#, multiplicity)	*J* value (Hz)	Comments
1a 1b	1.63-1.56 (1H, m) 1.14-1.07 (1H, m)		Signal overlap with 26 and 27
2a/b	1.57 (2H)		Signal overlap H-2a and H-2b
3	3.04-2.98 (1H, m)		
5	1.04 (1H)		Signal overlap with H-30
6a 6b	1.73 (1H, m) 1.56 (1H, m)		H-6a overlap with H-1a, H-6b overlap with H-17, H-12b, and H-2a/b
7a	2.17 (1H)		H-7a behind water peak

7b	2.02 (1H, m)		
11a/b	2.08 (2H, m)		Signal overlap between H-11a/b and H-7b
12a 12b	1.84 (1H) 1.58 (1H)		Signal overlap with H-20
15a 15b	2.31 (1H, dd) 1.14 (1H, dd)	14, 10.9 14, 4.8	
16	3.83 (1H, ddd)	10.8, 9.4, 4.8	
17	1.60 (1H, m)		Signal overlap with 2a/b, 12b and 6b
18	0.60 (3H, s)		
19	1.01 (3H, s)		
20	1.73 (1H, m)		Signal overlap with 12a
21	0.78 (3H, d)	6.4	
22	4.31 (1H, t)	9.5	
23	3.97 (1H, t)	9.1	
24	4.91 (1H, dq)	8.9, 1.4	
26 27	1.63-1.56 (7H, m)		Signal overlap with 1a
28	0.86 (3H, s)		
29	0.67 (3H, s)		
30	1.04 (3H, s)		
32	1.9 (3H)		Signal behind CD3CN solvent peak
OH	2.38 (1H, d)	5.5	

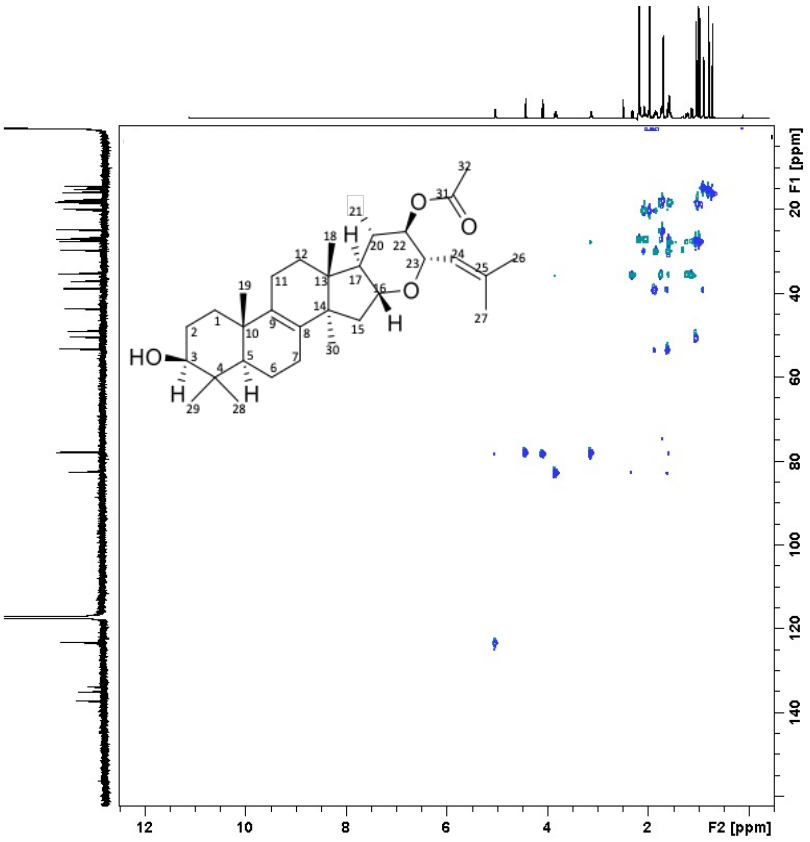

Fig. 4. 77. ^{13}C-^{1}H HSQC spectrum of compound **(4)**.

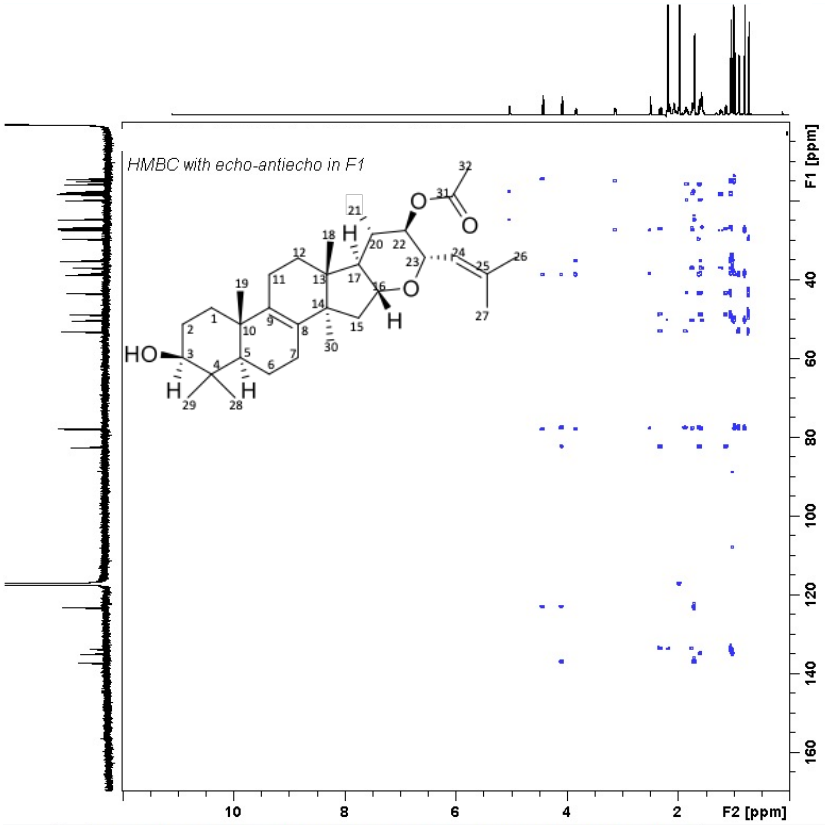

Fig. 4. 78. ^{13}C-^{1}H HMBC spectrum of compound **(4)**.

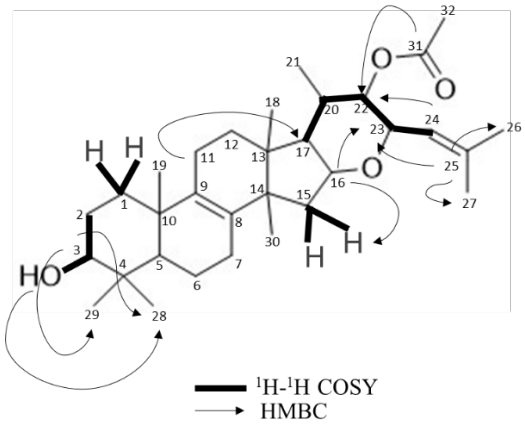

Fig. 4. 79. 2D COSY and HMBC structure correlations of compound **(4)**.

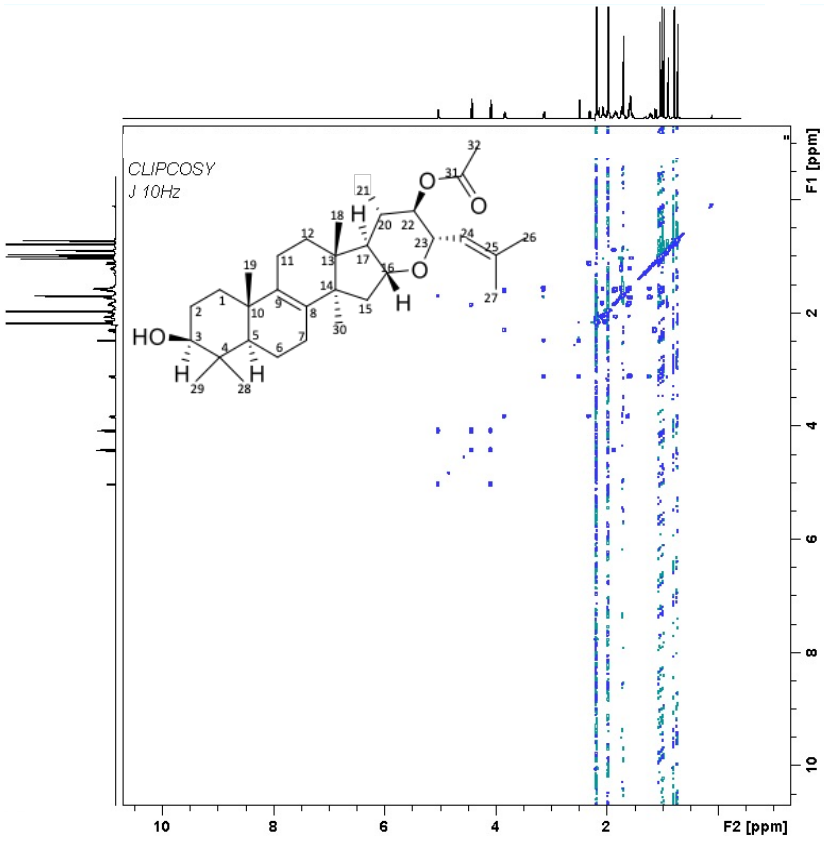

Fig. 4. 80. ^{1}H-^{1}H COSY spectrum of compound **(4)**.

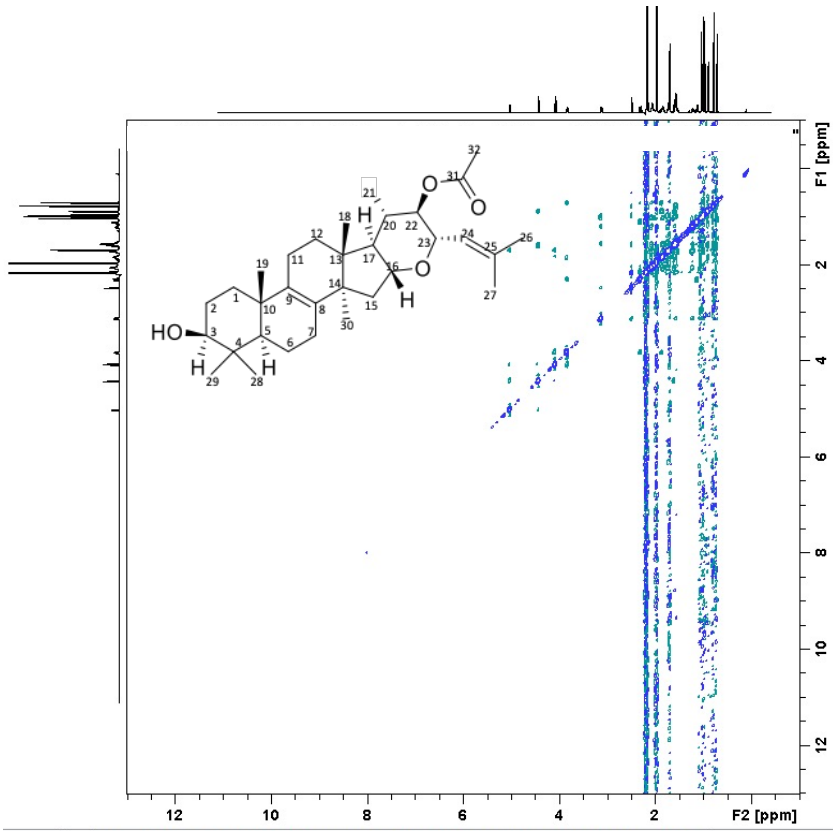

Fig. 4. 81. ^{1}H-^{1}H NOESY spectrum of compound **(4)**.

4.3.3.6. Crystallization and crystal data of compound (4)

Compound **(4)** was crystallized using three different methods. Method 1 resulted in formation of thin and small fragments of needle-like crystals that were mixed with powder (Fig. 4.82A). Method 2 resulted in the formation of bunches of white shiny crystals (Fig. 4.82B). Finally, method 3 resulted in formation of very thin and long needle-like crystals (Fig. 4.82C). Crystals obtained from method 2 were subjected to XRD analysis. For XRD analysis, the crystal with dimensions 0.24 × 0.05 × 0.05 mm^3 was selected, and it revealed a crystal structure as shown in ORTEP style, which was later identified as echinodol (Fig. 4.83). Detailed crystal data can be found in supplementary data of appendix C.

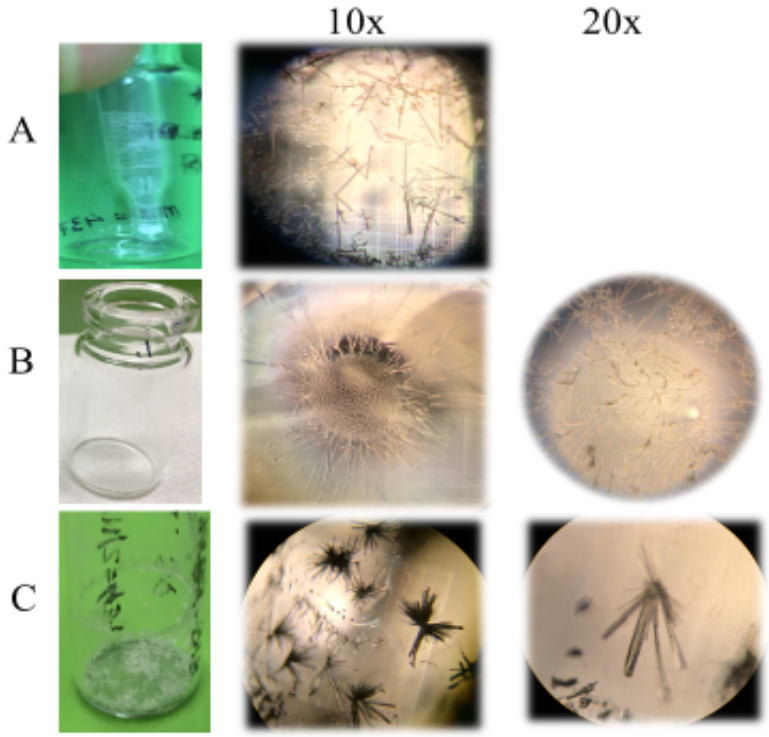

Fig. 4. 82. Crystallization of compound **(4)** using method 1 (A), method 2 (B), and method 3 (C).

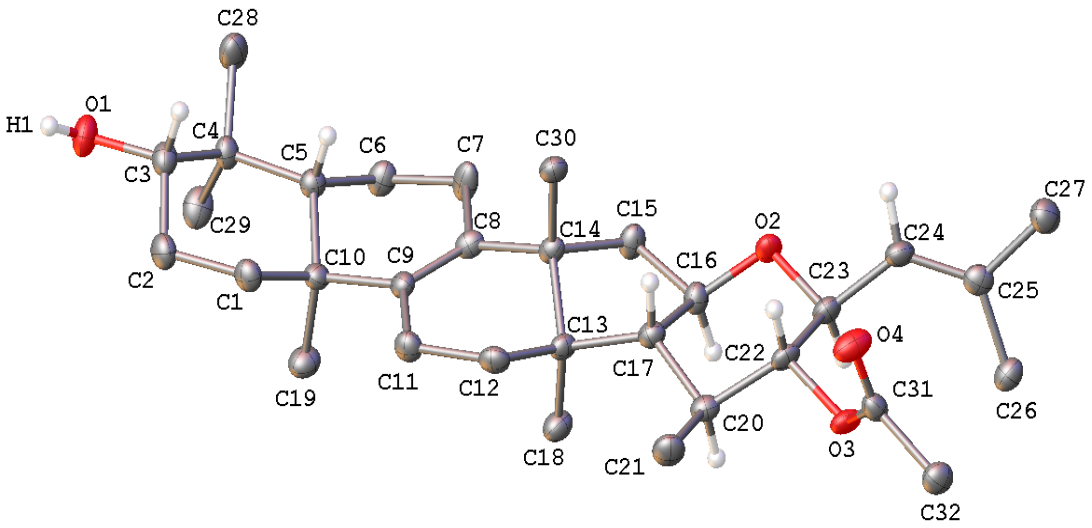

Fig. 4. 83. ORTEP style image of compound **(4)**.

X-Ray crystal data: $C_{32}H_{50}O_4$, M_r = 498.72, monoclinic, $P2_1$ (No.4), a= 7.9203(3) Å, b= 20.6269(8) Å, c= 17.4422(6) Å, β= 97.890 (2)°, α = γ = 90°, V= 2822.58(18) Å^3, T= 110(2) K, Z= 4, Z'= 2, μ(CuK_α)= 0.585, 78352 reflections measured, 8399 unique (R_{int} = 0.0722) which were used in all calculations. The final wR_2 was 0.1093 (all data) and R_1 was 0.0429 (I≥2 σ(I)).

Structural elucidation studies confirmed that compound **(4)** is echinodol, a lanostane-type triterpene acetate which has been reported together with its chemically-modified derivatives from *E. tinctorium* (Bond *et al*., 1966). To date, there is no study which has reported the crystal structure of echinodol, and no study conducted to explore its bioactive potential. Therefore, further experiments were carried out to explore the growth-inhibitory potential of echinodol.

4.3.3.7. Growth-inhibitory effects of (4) on cancer cells

Echinodol caused growth inhibition in HeLa cervical cancer cells (Fig. 4.84A) with an IC_{50} of 1.2 μM. It also showed anti-proliferative effects (Table 4.11) against U251 glioblastoma cells, SVG immortalized glial cells, RIE-1 Rat intestinal epithelial cells, U87 glioblastoma cells, HCT116 human colon cancer cells, and SW480 colorectal cancer cells with an IC_{50} of 4.6 μM, 4.09 μM, 2.28 μM, 5.41 μM, 5.37 μM, and 3.65 μM respectively. Results shown in Table 4.11 were derived from experiments performed by Dr. Chow Lee.

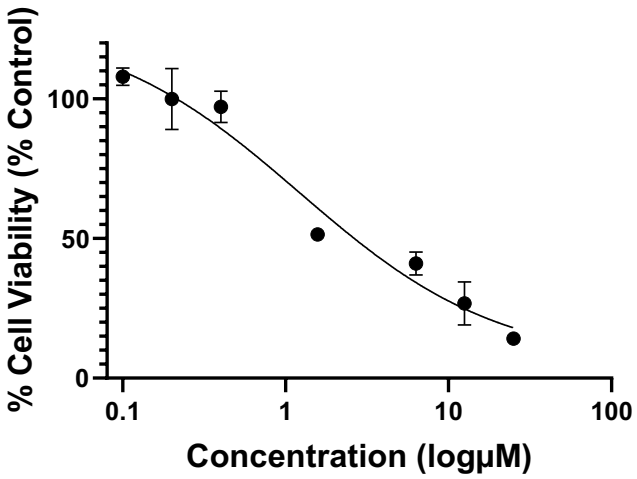

Fig. 4. 84. Effect of compound **(4)** at 48 h treatment on growth inhibition of HeLa cervical cancer cells. Result shown is a representative from three biological replicates.

Table 4. 11. IC_{50} of compound **(4)** on multiple cell lines

Cell Lines		Average IC50 (μM)*
SVG	Immortalized glial cells	4.09 ± 0.387
U251	Glioblastoma cells	4.62 ± 0.664
U87	Glioblastoma cells	5.41 ± 1.80
RIE-1	Rat intestinal epithelial cells	2.28 ± 0.496
HCT116	Human colon cancer cells	5.37 ± 1.146
SW480	Colorectal cancer cells	3.65 ± 0.961

*Results obtained from three biological replicates (n=3).

4.3.3.8. Flow cytometry analysis of compound (4)

Compound **(4)** induced apoptosis in U251 cells at 40 μM. After 24 h of treatment with 40 μM of (**4**), significant (p = 0.002) apoptosis was observed with 57 % apoptotic cells as compared to 4.6 μM and 10 μM treatments with 12.6 % and 13 % apoptotic cells respectively. After 48 h treatment with 40, 4.6 and 10 μM of compound **(4)**, there were 61, 41, and 40 % of apoptotic cells respectively (Fig. 4.85).

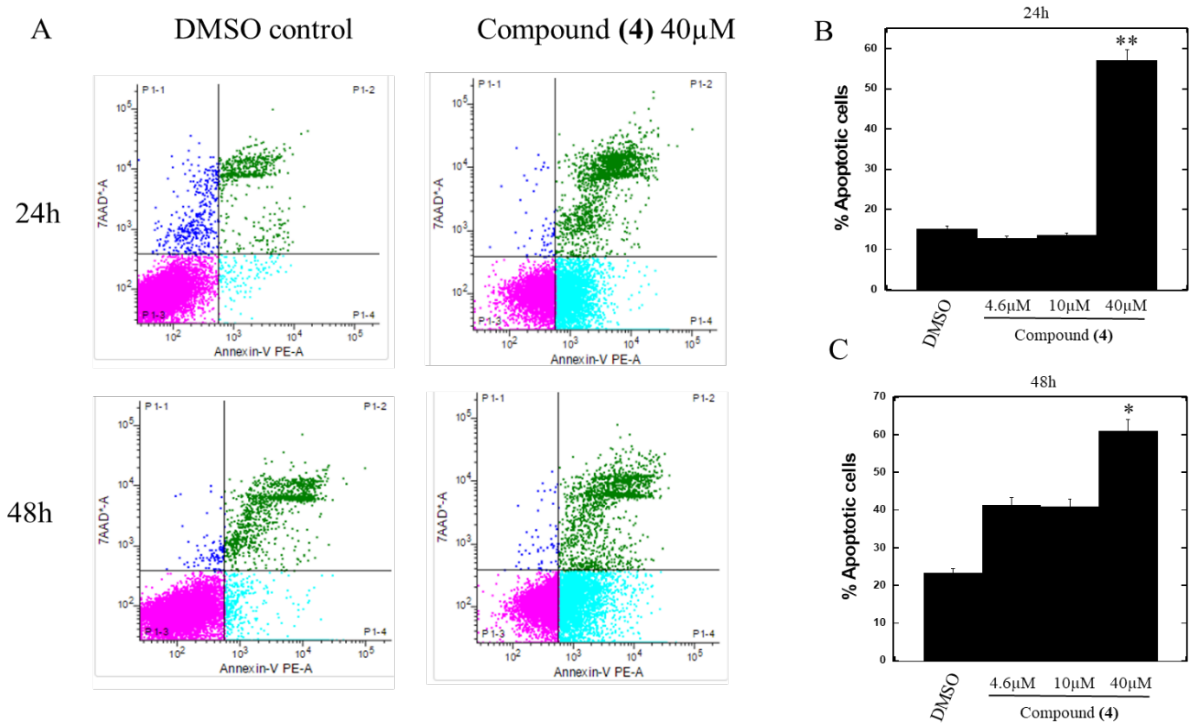

Fig. 4. 85. Apoptosis induced by compound **(4)** at 4.6, 10 and 40 µM in U251 cells (A), % apoptotic cells at 24 h (B) and 48 h (C). Results in (B) and (C) are from three biological replicates (n=3). For statistical analysis, one-way ANOVA was used. * represents $p = 0.002$ and ** shows $p < 0.0001$.

The cell cycle analysis after treatment with 40 µM of compound **(4)** for 24 h showed only a slight increase in S phase cells (Fig. 4.86A). In contrast, there was a significant increase ($p =$ 00012) in cell population in S phase (Fig. 4.86B) after treatment with 40 µM dose of compound **(4)** for 48 h. The results indicated an S phase arrest induced by compound **(4)**.

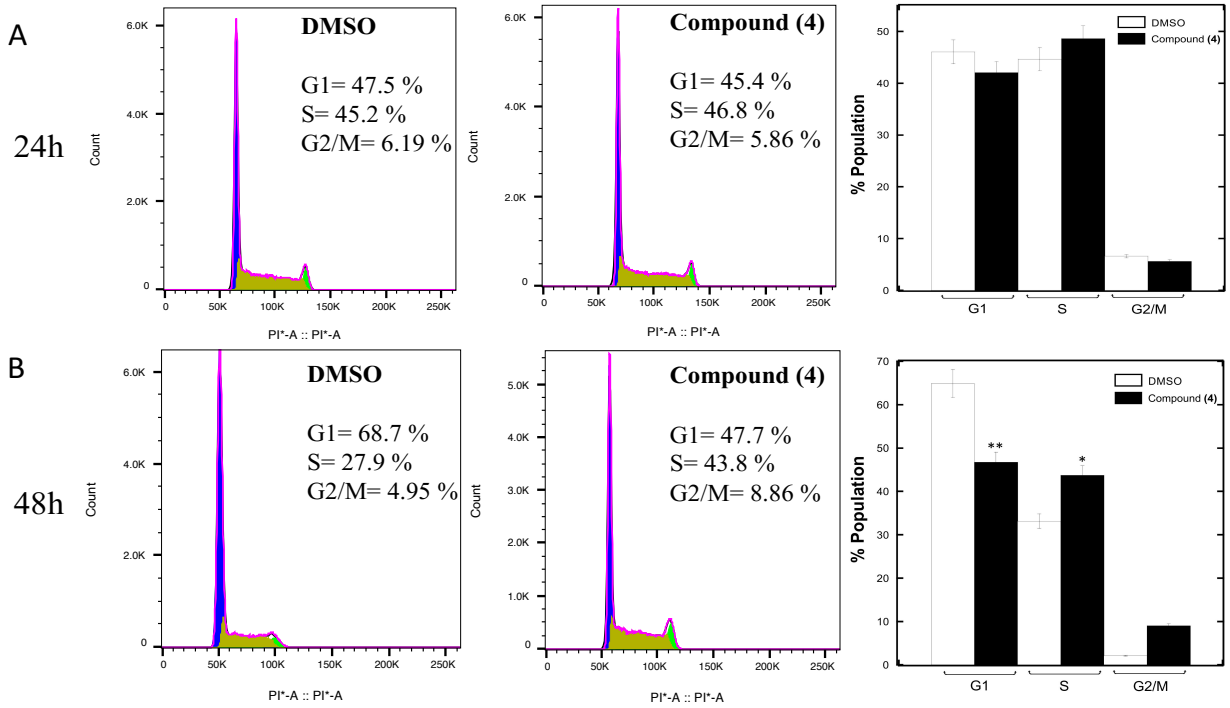

Fig. 4. 86. Cell cycle analysis of compound **(4)** at 40 µM for 24 h (A) and 48 h (B) for n=3. Error bars represent standard deviation. One-way ANOVA was used for statistical analysis. ** represent $p = 0.0002$ and * shows $p = 0.0012$.

4.3.3.9. HPLC and ESI-MS analysis of PK5

PK5 purified from hexane layer using semi-preparative HPLC column was reinjected to check purity. The analysis discovered the presence of two peaks in the purified fraction which were named as PK5a (later on renamed as compound **(6)**) and PK5b (later on renamed as compound **(5)**). Repurification of PK5 was carried out initially on Phenomenex Luna C18(2) HPLC column (Fig. 4.87) and later on method developed using Agilent Zorbax Poroshell C18 HPLC column (Fig. 4.88). Both columns were able to resolve the two peaks and Poroshell C18 column also reduced the analysis time.

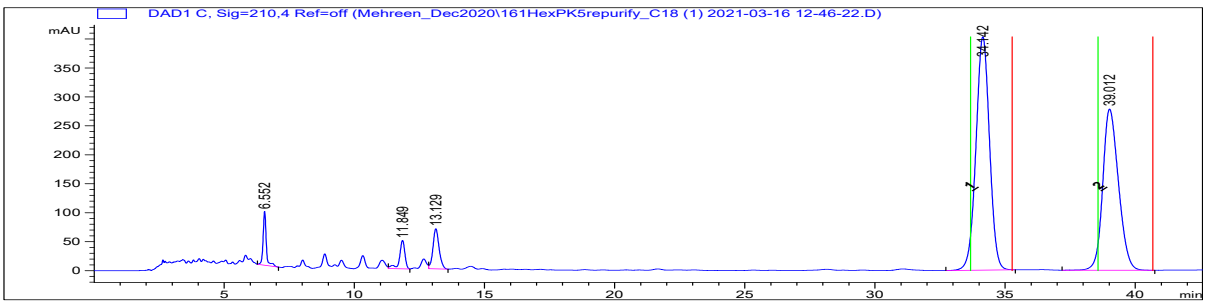

Fig. 4. 87. Repurification of PK5 on Phenomenex Luna C18(2).

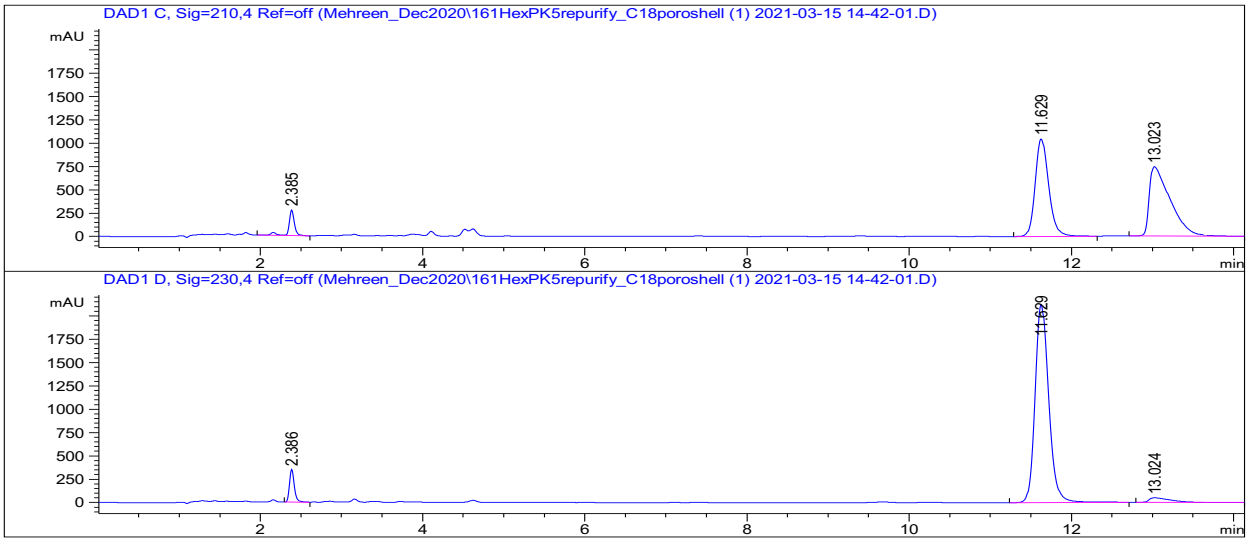

Fig. 4. 88. Repurification of PK5 on Agilent Zorbax Poroshell C18.

PK5b was renamed as compound **(5)** and was reinjected into HPLC to check for purity as well as for ESI-MS analysis. HPLC DAD spectrum showed a 100 % pure peak of compound (5) at 254 and 230 nm (Fig. 4.89). ESI-MS (Fig. 4.90) showed a small parent molecular ion peak with m/z 497 [M+H] and its fragment base peak with m/z 437 [M+H]. The fragment at 437 was possibly the deacetylated form of compound **(5)**.

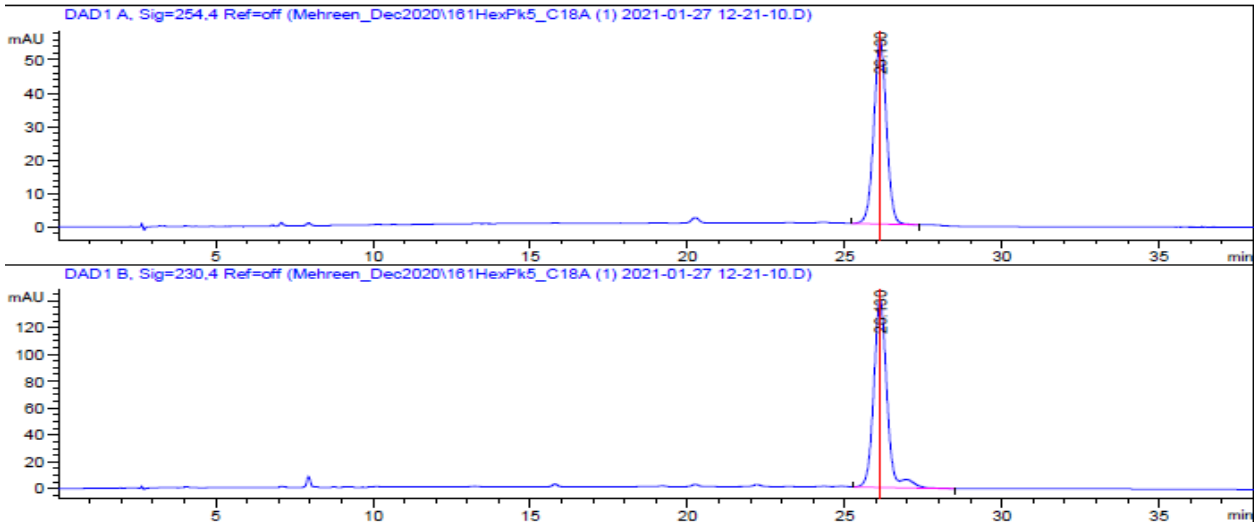

Fig. 4. 89. HPLC DAD spectrum of compound **(5)**.

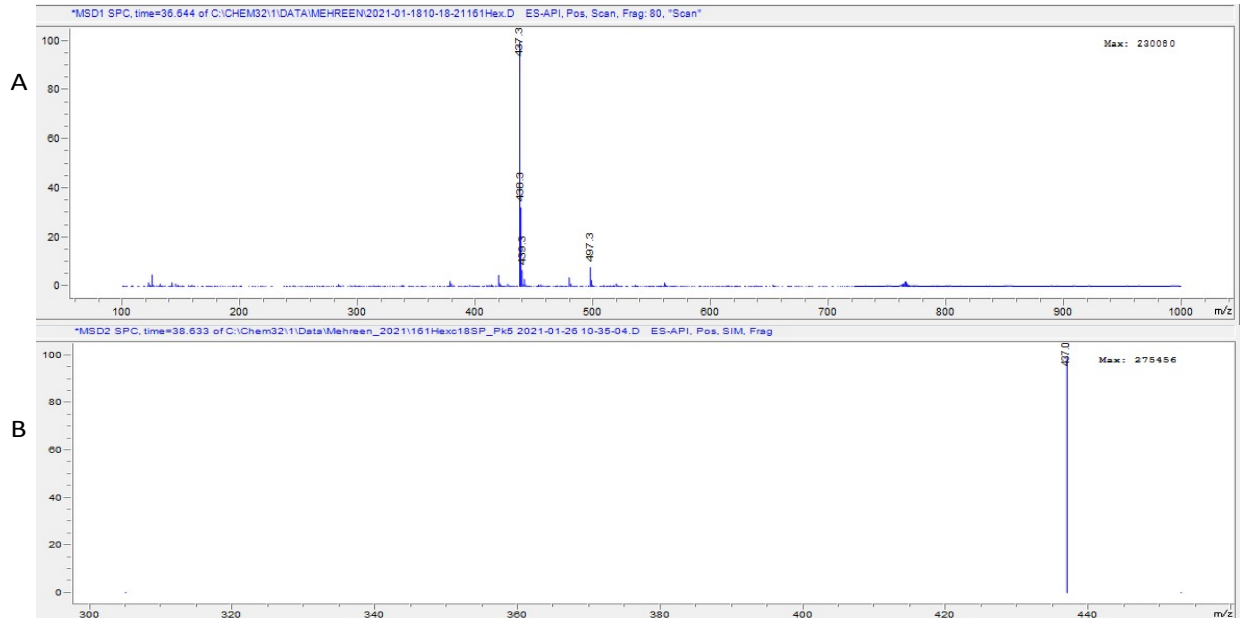

Fig. 4. 90. Positive mode ESI-MS of compound **(5)** in scan mode 100-1000 Da (A) and SIM mode (B).

4.3.3.10. Structural elucidation of (5) by NMR spectroscopy

Most of the signals from the ^{1}H NMR, ^{13}C NMR, ^{1}H-^{13}C HSQC and HMBC, ^{1}H-^{1}H COSY and NOESY of compound **(5)** shown in Figures 4.91-4.96 & Tables 4.12 & 4.13, resembled the NMR data of compound **(4)**, indicating structural similarity of both compounds. This was later confirmed from the crystal structure. Compound **(4)** has a hydroxy at carbon 3 which is replaced by a carbonyl group in compound **(5)**. Therefore, **(5)** has two carbonyl groups present which was also confirmed from the ^{13}C NMR data (Fig. 4.90 & Table 4.13).

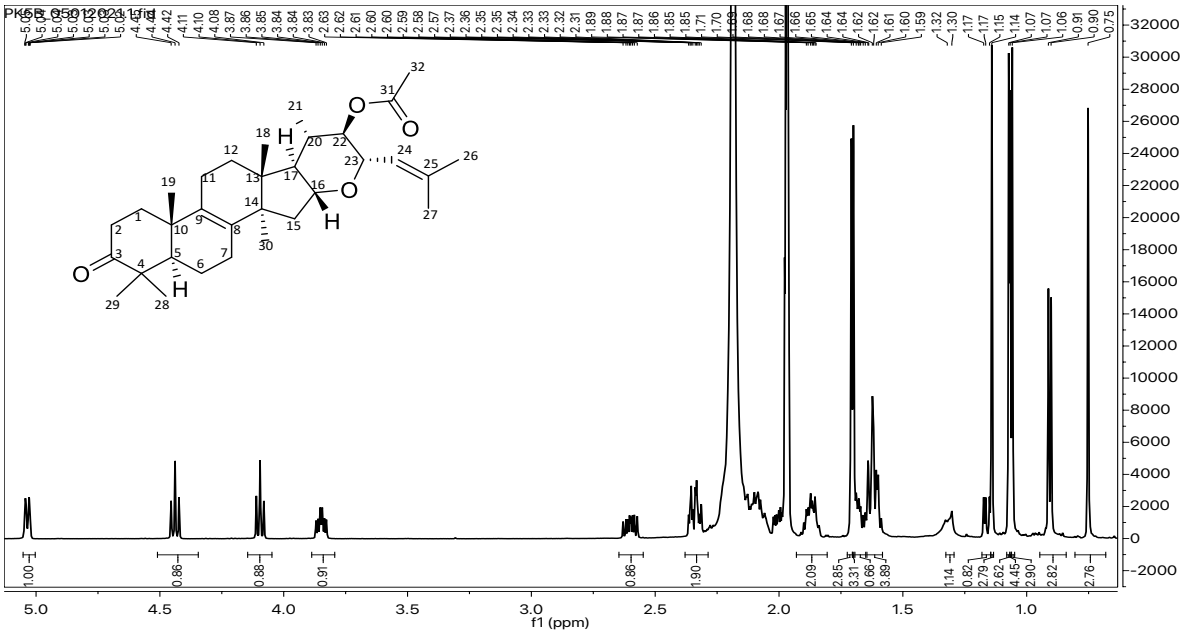

^{1}H NMR (Acetonitrile-d_3, 600 MHz) δ 5.04 (1H, dt, J=8.7, 1.5 Hz), 4.44 (1H, t, J=9.5 Hz), 4.10 (1H, t, J=9.1 Hz), 3.85 (1H, td, J=10.1, 4.8 Hz), 2.60 (1H, ddd, J=15.8, 11.5, 7.0 Hz), 2.38 – 2.29 (2H, m), 1.87 (2H, qd, J=10.1, 6.8 Hz), 1.71 (3H, s), 1.70 (3H, s), 1.69 – 1.65 (1H, m), 1.62 (4H, td, J=11.0, 3.4 Hz), 1.31 (1H, d, J=11.0 Hz), 1.18 – 1.15 (1H, m), 1.14 (3H, s), 1.07 (3H, s), 1.07 (4H, s), 1.06 (3H, s), 0.91 (3H, d, J=6.5 Hz), 0.75 (3H, s)

Fig. 4. 91. ^{1}H NMR of compound **(5)**.

Table 4. 12. ^{1}H NMR chemical shift data of compound **(5)**

Number	^{1}H Chemical shift δ ppm (#, multiplicity)	*J* value (Hz)	Comments
1a 1b	2.1 (1H, m) 1.69-1.62 (>6H, m)		Signal overlap with CD_3CN solvent peak
2a/b	1.69-1.62 (>6H, m)		Signal overlap
5	1.69-1.62 (>6H, m)		Signal overlap
6a/b	2.1-2.25 (m)		Signal overlap with H-11a/b and water peak
7a 7b	2.6 (1H, ddd) 2.3-2.29 (2H, m)	15.8, 11.5, 7	
11a/b	2.1-2.25 (m)		Signal overlap with H-6a/b and water peak
12a 12b	1.87 (2H, qd) 1.69-1.62 (>6H, m)	10.1, 6.8	Signal overlap with H-20 Signal overlap
15a 15b	2.38-2.29 (2H, m) 1.18 (1H)		
16	3.85 (1H, td)	10.1, 4.8	
17	1.69-1.62 (>6H, m)		Signal overlap
18	0.75 (3H, s)		
19	1.07 (3H, s)		
20	1.87 (2H, qd)	10.1, 6.8	Signal overlap with 12a
21	0.9 (3H, d)	6.5	
22	4.44 (1H, t)	9.5	
23	4.10 (1H, t)	9.1	
24	5.04 (1H, dt)	8.7, 1.5	
26	1.71 (3H, s)		
27	1.70 (3H, s)		
28	1.07 (3H, s)		
29	1.06 (3H, s)		
30	1.14 (3H, s)		

32	1.9 (3H)	Signal behind CD3CN solvent peak

Table 4. 13. Chemical shift data of compound **(5)** from ^{13}C NMR

Number	**^{13}C Chemical shift δ (ppm)**	**Functionality**
1	35.4	CH_2
2	19.1	CH_2
3	216.5	C=O
4	43.5	°4 C
5	51.0	CH
6	26.5	CH_2
7	34.1	CH_2
8	133.8	°4 C
9	134.8	°4 C
10	36.9	°4 C
11	19.9	CH_2
12	29.7	CH_2
13	49.1	°4 C
14	47.0	°4 C
15	35.5	CH_2
16	82.5	CH
17	53.2	CH
18	16.0	CH_3
19	25.4	CH_3
20	38.8	CH
21	14.5	CH_3
22	77.7	CH
23	78.1	CH
24	123.2	=CH
25	137.3	°4 C
26	24.8	CH_3
27	17.6	CH_3
28	27.0	CH_3
29	20.6	CH_3
30	17.7	CH_3
31	170.2	C=O
32	20.0	CH_3

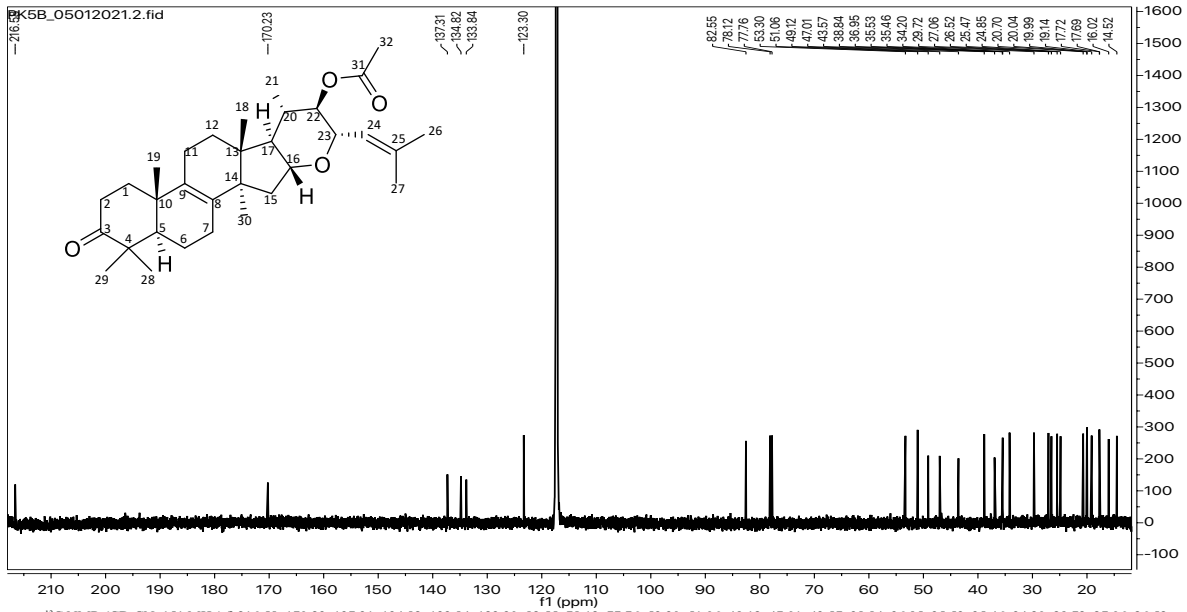

^{13}C NMR (CD_3CN, 151 MHz) δ 216.58, 170.23, 137.31, 134.82, 133.84, 123.30, 82.55, 78.12, 77.76, 53.30, 51.06, 49.12, 47.01, 43.57, 38.84, 36.95, 35.53, 35.46, 34.20, 29.72, 27.06, 26.52, 25.47, 24.85, 20.70, 20.04, 19.99, 19.14, 17.72, 17.69, 16.02, 14.52.

Fig. 4. 92. ^{13}C NMR spectrum of compound **(5)**.

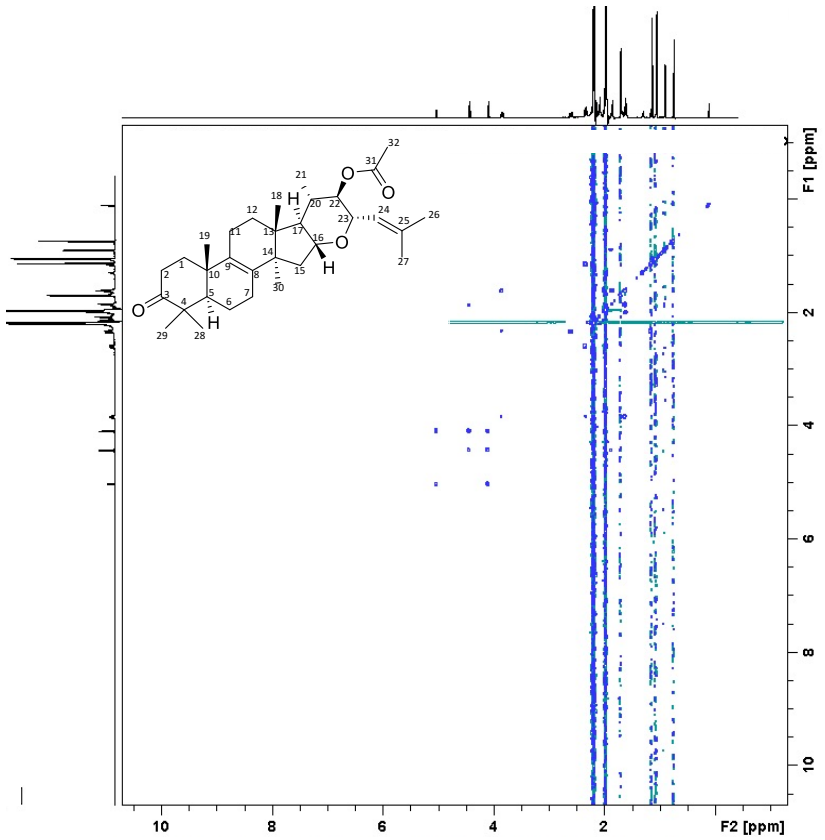

Fig. 4. 93. ^{1}H-^{1}H COSY spectrum of compound **(5)**.

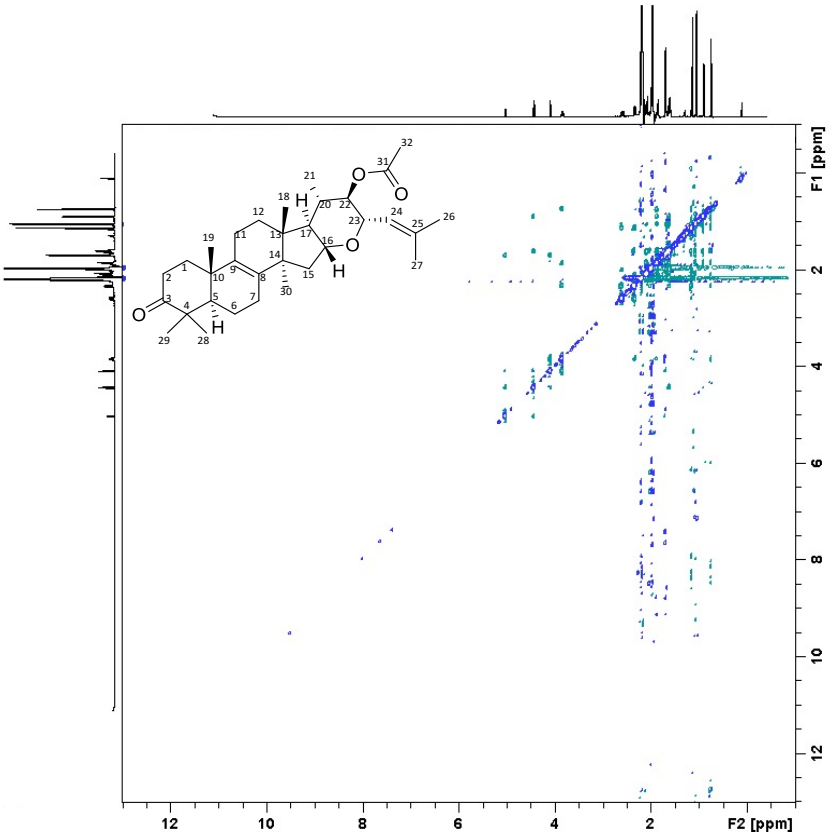

Fig. 4. 94. ^{1}H-^{1}H NOESY spectrum of compound **(5)**.

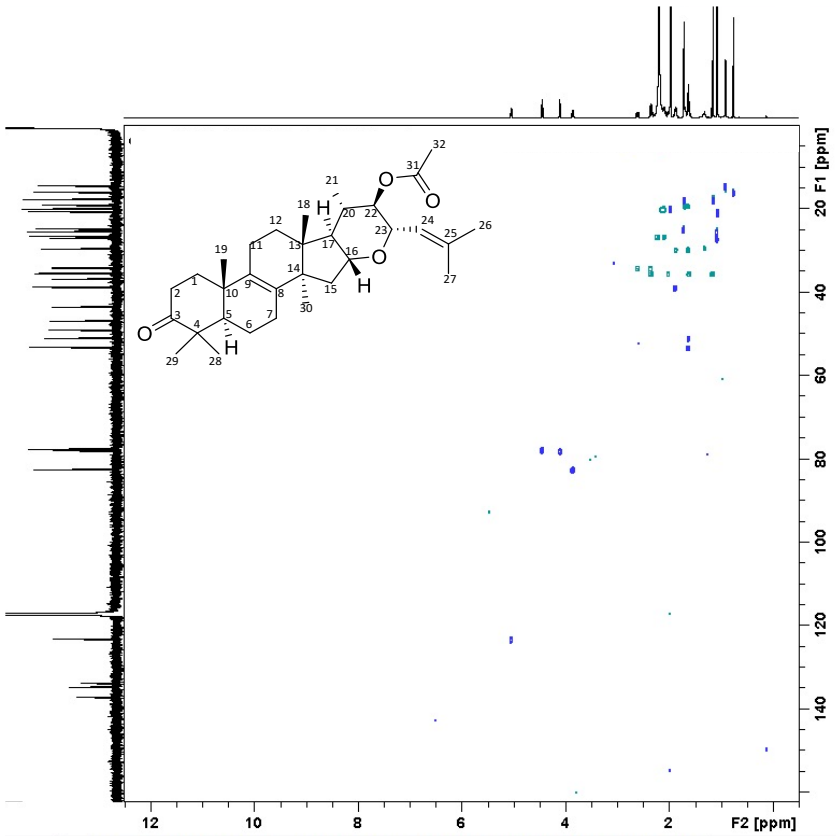

Fig. 4. 95. ^{1}H-^{13}C HSQC spectrum of compound **(5)**.

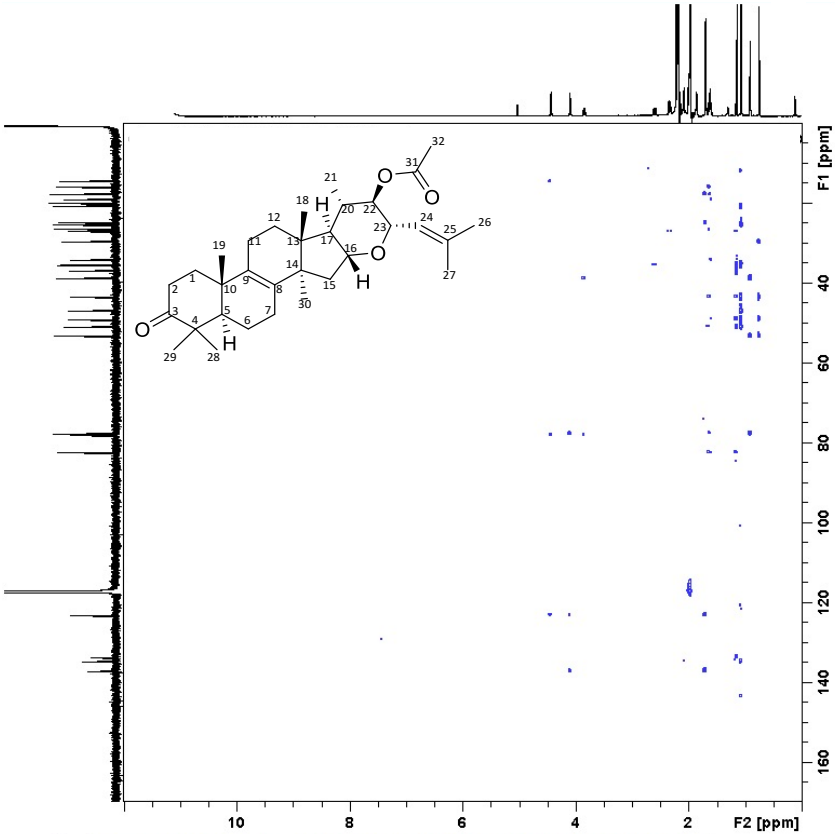

Fig. 4. 96. ^{1}H-^{13}C HMBC spectrum of compound **(5)**.

4.3.3.11. Crystallization and crystal structure of compound (5)

Colorless crystals were obtained from both method 2 and 3 (Fig. 4.97B & C). The crystals obtained from method 1 were very small (Fig. 4.97A). The crystals from method 2 and 3 qualified for XRD analysis. For XRD analysis, a single flat crystal with dimensions 0.28 × 0.24 × 0.06 mm^3 was used. The XRD analysis revealed the final crystal structure of compound **(5)** (Fig. 4.97D). Detailed crystal data can be found in supplementary data of appendix C.

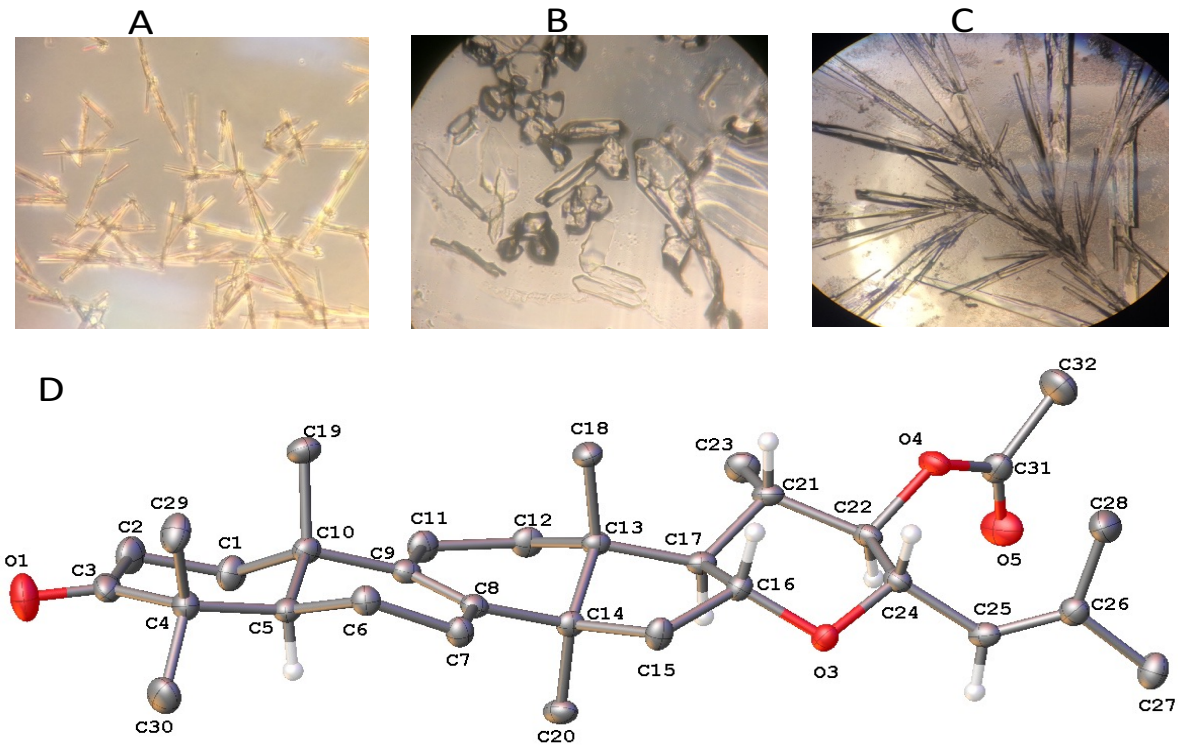

Fig. 4. 97. Crystals of **(5)** obtained from method 1 (A), method 2 (B) and method 3 (C), and ORTEP style image of **(5)** from X ray crystallography (D).

Crystal Data. $C_{32}H_{48}O_4$, M_r = 496.70, orthorhombic, $P2_12_12_1$ (No. 19), a = 8.0284(2) Å, b = 10.6283(3) Å, c = 32.8305(9) Å, $\alpha = \beta = \gamma = 90^{\circ}$, V = 2801.37(13) Å^3, T = 110(2) K, Z = 4, Z' = 1, μ(CuK$_\alpha$) = 0.589, 51100 reflections measured, 5125 unique (R_{int} = 0.0369) which were used in all calculations. The final wR_2 was 0.0725 (all data) and R_1 was 0.0281 ($I \geq 2\ \sigma(I)$).

The FTIR, NMR, ESI-MS along with the crystal data confirmed compound **(5)** to be echinodone, which is a lanostane-type triterpenoid. One of the previous studies has reported that echinodone was isolated from organic extracts of *E. tsugicola* fruiting bodies (Kanematsu *et al*., 1972). *E. tsugicola* is one of the phylogenetically related species of *E. tinctorium*. Echinodone shares the same nucleus as echinodol with the exception of a hydroxyl group replaced by a carbonyl group in the structure. To date, there is no study conducted to explore the bioactive potential of echinodone.

4.3.3.12. Growth inhibitory activity of (5)

Compound **(5)** caused growth inhibition in U251 cells with an IC_{50} of 5.45 µM $\pm$ 1.76 (Fig. 4.98). The IC_{50} of compound **(5)** was comparable to compound **(4)** in inhibiting U251 cells. Due

to their structural similarities, both molecules likely inhibit the growth of U251 cells via a similar pathway.

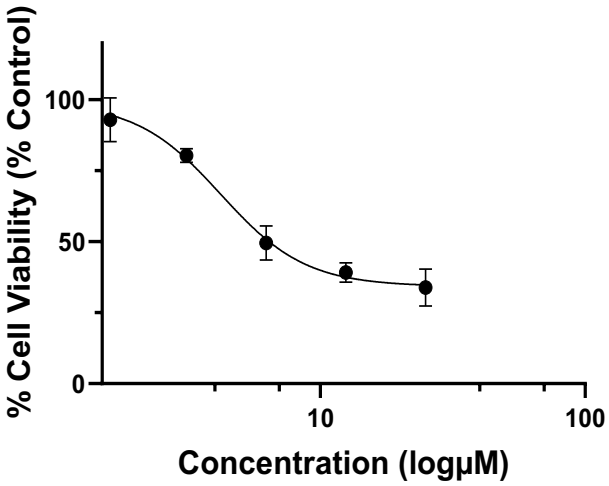

Fig. 4. 98. Growth inhibition caused by compound **(5)** after 48 h treatment in U251 cells. Result shown is a representative from three biological replicates.

4.3.3.13. HPLC analysis of PK5a

Once it was repurified from compound **(5)**, PK5a was reinjected into HPLC to determine its % purity. Fig. 4.99 shows the HPLC spectrum of **(6)** where two distinct peaks can be seen; **(6)** retained at 11.9 min and another compound retained at 2.3 min. This indicated that **(6)** was degraded into an undesirable compound probably due to its sensitivity to light, air or having been kept in liquid storage for too long.

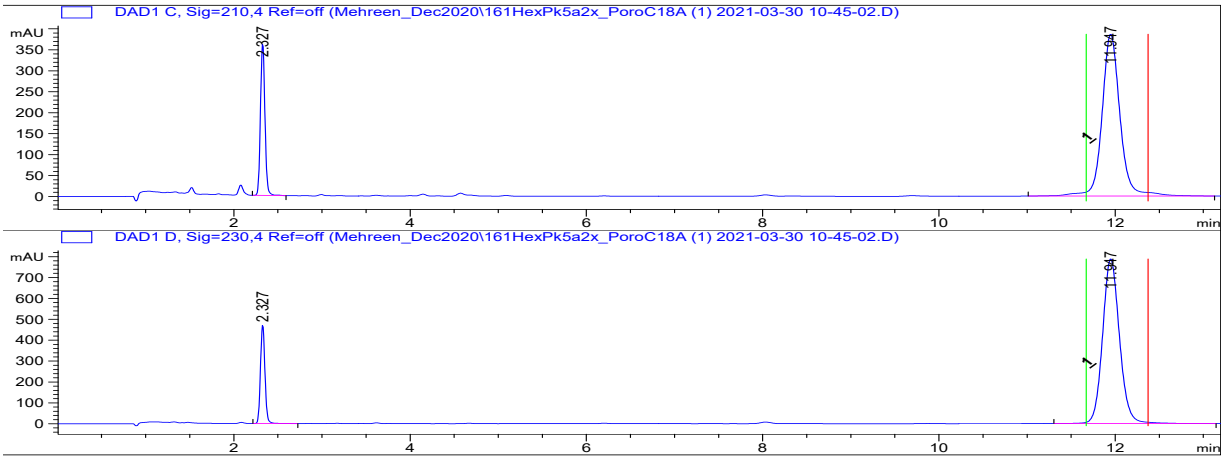

Fig. 4. 99. HPLC DAD spectrum of PK5a.

In order to determine the stability issues of **(6)**, the freshly repurified **(6)** was kept in dark (wrapped with aluminum foil), cold and lyophilized on the same day after its collection. The lyophilized **(6)** was resuspended in acetonitrile and injected into HPLC for determination of %

purity (Fig. 4.100). PK5a was then renamed as compound **(6)**. The HPLC DAD spectrum of compound **(6)** revealed a pure peak which indicated that it was a sensitive compound that might have undergone degradation. The positive mode ESI-MS indicated a molecular ion peak with m/z 441 [M+H] (Fig. 4.101). Compound **(6)** has the same mass as deacetoxyechinodol which was isolated from *E. tsugicola*, so it is likely that it is the same compound present here in *E. tinctorium*.

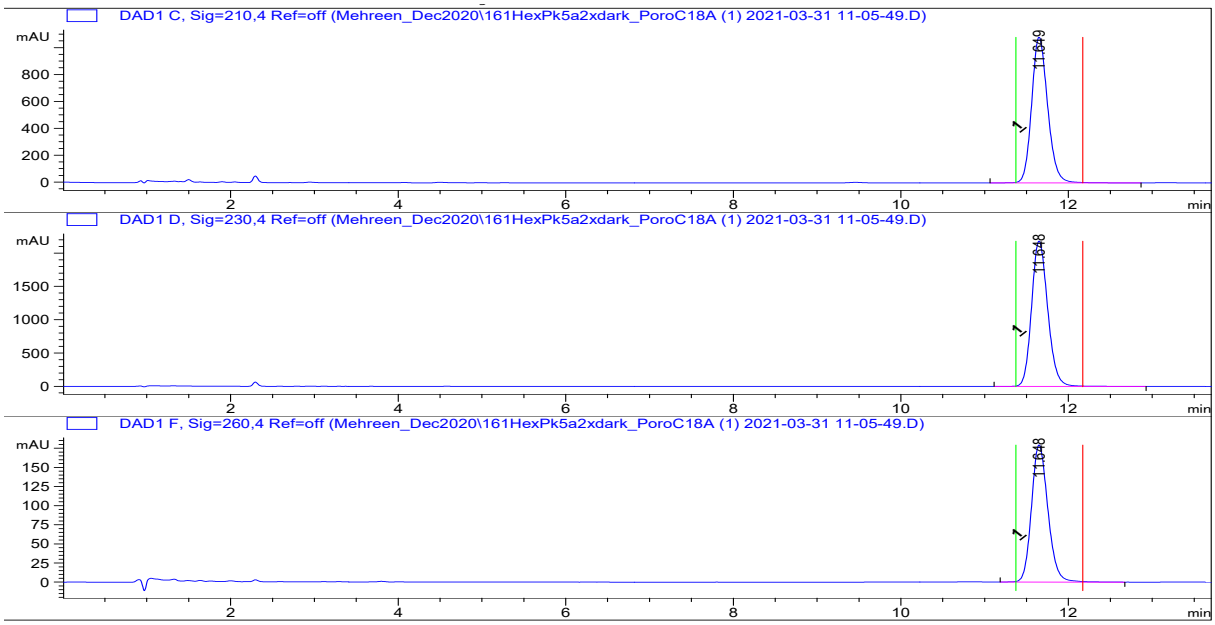

Fig. 4. 100. HPLC DAD spectrum of compound **(6)**.

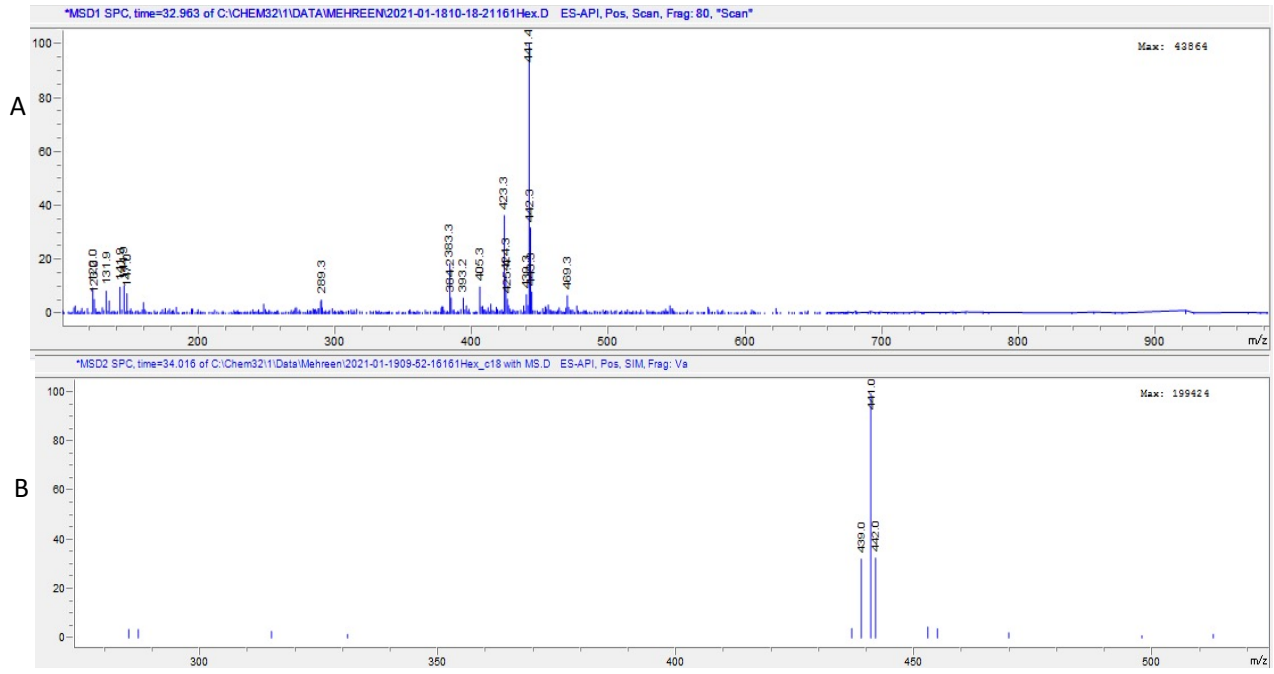

Fig. 4. 101. ESI-MS spectrum of compound **(6)** in scan mode (A) and SIM mode (B).

4.3.3.14. Melting point determination

Melting point for compound **(2)** was determined as 208.3-209.5 ºC. Compound **(4)** on the other hand had melting point of 228.5-230 ºC. Both melting points had narrow range indicating the purity of compounds. Additionally, a high melting point suggested the structural stability and complexity of compounds **(2)** and **(4)**.

4.3.3.15. HPLC and ESI-MS analysis of DEE layer

The HPLC spectrum of DEE showed several peaks (Fig. 4.102) at 230 nm. The mass of the retained peaks was determined in the positive mode ESI. The ESI-MS analysis revealed common m/z ions as that of compounds found in hexane layer which included m/z 287 Da at 14.5 min, 439 Da at 17.5 min, and 437 Da at 21.4 min. Since these compounds were also identified from the hexane layer, the DEE layer was not pursued further.

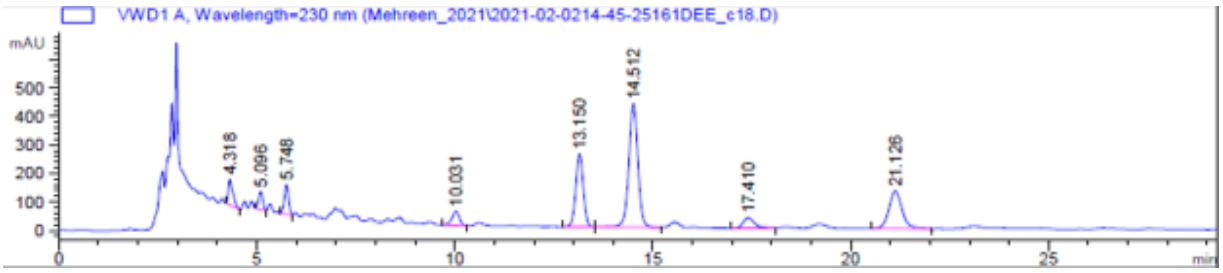

Fig. 4. 102. HPLC analysis of DEE.

A summary of all the small molecules isolated from *E. tinctorium* is shown in Table 4.14.

Table 4. 14. Small molecules isolated from *E. tinctorium*

#	Compound name	Chemical class	Molar mass (g/mol)	FTIR	NMR	Crystal structure
1	Orcinol	Phenol derivative	124	Yes	^{1}H, ^{13}C, DEPT135, ^{1}H-^{13}C HSQC, ^{1}H-^{13}C HMBC, ^{1}H-^{1}H COSY, ^{1}H-^{1}H NOESY	No
2	bis(2,4-dihydroxy-6-methylphenyl) methane	Diphenyl methane derivative	260	Yes	^{1}H, ^{13}C, DEPT135, ^{1}H-^{13}C HSQC, ^{1}H-^{13}C HMBC, ^{1}H-^{1}H COSY, ^{1}H-^{1}H NOESY	Yes
3	Unknown	NA	506	Yes	^{1}H, ^{13}C, DEPT135, ^{1}H-^{13}C HSQC, ^{1}H-^{13}C HMBC, ^{1}H-^{1}H COSY, ^{1}H-^{1}H NOESY	No

4	Echinodol	Lanostane triterpenoids	498	Yes	^{1}H, ^{13}C, DEPT135, ^{1}H-^{13}C HSQC, ^{1}H-^{13}C HMBC, ^{1}H-^{1}H COSY, ^{1}H-^{1}H NOESY	Yes
5	Echinodone	Lanostane triterpenoids	496		^{1}H, ^{13}C, DEPT135, ^{1}H-^{13}C HSQC, ^{1}H-^{13}C HMBC, ^{1}H-^{1}H COSY, ^{1}H-^{1}H NOESY	Yes
6	Deacetoxyechinodol	Lanostane triterpenoids	440			No

4.3.3.16. Target prediction of compounds 1-5

Target prediction can be done with biochemical techniques and computational tools. In the past, biochemical techniques were considered more reliable. Nowadays, computational prediction methods offer a fast, cheap and accurate target prediction. Some of the available web tools include SEA (Keiser *et al*., 2009), SwissTargetPrediction (Gfeller *et al*., 2014), HitPick (Liu *et al*., 2013), TarPred (Liu *et al*., 2015), and MolTarPred (Peon *et al.*, 2019). Amongst these, MolTarPred is the most accurate user-friendly web tool due to a large number of targets, types of organisms, and reliability score to identify the predictions (Peon *et al.*, 2019).

Due to these advantages, the MolTarPred program was used to predict the molecular targets for compounds **(1)**, **(2)**, **(4)**, and **(5)**. Generally, a score of 3 or more indicates a reliable target prediction. For compound **(1)**, 30 targets were identified by MolTarPred with a reliability score equal to and less than 2, except for one predicted target named prelamin-A/C which had a reliability score of 3. Prelamin-A/C is a protein identified in humans and is present in the nuclear lamina to promote nuclear stability (Mattioli *et al*., 2011).

For compound **(2)**, a total of 16 targets were identified by MolTarPred with a low reliability of prediction score (1-2). Surprisingly, all the identified targets had low reliability of prediction. This is likely due to the fact that compound **(2)** has not been studied before or the targets have not been identified in any organisms.

For compound **(4)**, 5 targets were identified, two of them with a reliability of prediction score 1 and one with a score 2. One predicted target, Prostaglandin E synthase enzyme, had a reliability score 3 and another protein target 7-dehydrocholesterol reductase had a reliability

score of 4. The 7-dehydrocholesterol reductase is an important terminal enzyme in biosynthesis of cholesterol. Cholesterol biosynthesis is important for neuronal development, which is sometime disrupted due to certain genetic defects. One such genetic defect is associated with Smith-Lemli-Opitz syndrome (SLOS), caused by gene mutation that encodes for 7-dehydrocholesterol reductase thereby inhibiting the conversion of 7-dehydrocholesterol to cholesterol (Horling *et al*., 2012). Compound **(4)** could be a possible lead molecule for treatment of such neurological disorders. Another reliable protein target for compound **(4)** was prostaglandin E synthase enzyme, involved in cyclooxygenase (COX)-derived prostaglandin E_2 (PGE_2) synthesis. Prostaglandins play important role in inflammation. PGE_2 has been identified as a novel target against inflammation and cancer, including brain cancers (Murakami & Kudo, 2006). Medulloblastoma (MB) is a common malignant brain cancer that occurs in children; it is associated with overexpressed COX-2 and PGE_2 synthase (Baryawno *et al*., 2008). Compound **(4)** has shown promising effect in glioblastoma cells and could be a potential target to inhibit the PGE_2 synthase and thereby address MB.

For compound **(5)**, 11 molecular targets were predicted with a reliability score 1 for 10 targets, 2 for one target and 3 for another target named Peptidyl-prolyl cis-trans isomerase NIMA-interacting 1. Peptidyl-prolyl cis-trans isomerase NIMA-interacting 1, also known as PPIase Pin1 and Rotamase Pin1, is a protein target identified in humans. Pin1 is an isomerase enzyme that catalyzes the cis/trans isomerization. Pin1 is believed to be an attractive target in cancer research due to its over expression in various cancers, especially brain cancers (Bao *et al*., 2004). The role of Pin1 in regulating cell differentiation has been identified through multiple molecular pathways (Lu, 2003). According to one study, knockdown of Pin1 reduced the tumorigenic features of glioblastoma cells through apoptosis and reduced cell migration (Atabay *et al*., 2015). Compound **(5)** has shown growth inhibition in glioblastoma cells and acting through Pin1 identified protein target could be one of the possible mechanisms for inducing apoptosis. A summary of the predicted molecular targets for compounds **(1), (2), (4)** and **(5)** is shown in Table 4.15.

Table 4. 15. Predicted molecular targets of compounds from *E. tinctorium* using MolTarPred

Compound#	Predicted molecular target	Reliability of prediction	Function
1	Prelamin-A/C	3	Nuclear stability
2	No reliable target	<3	NA
4	7-dehydrocholesterol reductase	4	Cholesterol biosynthesis
	Prostaglandin E synthase	3	COX derived PGE2 synthesis
5	Rotamase Pin1	3	Cis/trans isomerization, Regulates cell differentiation

4.4. Conclusion

Compounds (**1-6**) were successfully isolated from organic extracts of *E. tinctorium*. **(1)**, **(4)**, **(5)**, and **(6)** are known compounds previously isolated from other species. Compound **(4)** was also previously isolated from *E. tinctorium*. I report here, for the first time, the isolation of compound **(2)** from a natural origin. There were no previous reports on bioactivity analysis of molecules **(2)**, **(4)**, and **(5)**, therefore, the growth-inhibitory potential was investigated here. All the compounds were obtained with high purity at multiple wavelengths and their structure was successfully elucidated using FTIR, ESI-MS, XRD and NMR analyses. Using MolTarPred program, potential protein targets that may play a role in their growth-inhibitory activity, were identified for compounds **(1), (2), (4),** and **(5)**. Further research is clearly required to determine whether these proteins are true molecular targets for these compounds. In addition, animal studies are needed to assess the potential anti-cancer activity of these compounds, especially for compounds **(4)** and **(5)**.

Appendix C. Supplementary data

Supplementary material related to this chapter can be found in Appendix C.

4.5. References

Arnone, A., Brambilla, U., Nasini, G., & de Pava, O. V. (1995). Isolation and structure elucidation of tsugicolines AD, novel protoilludane sesquiterpenes from *Laurilia tsugicola*. *Tetrahedron*, *51*(48), 13357-13364.

Arnone, A., De Gregorio, C., Nasini, G., & de Pava, O. V. (1998). Isolation and structure elucidation of tsugicolines FH, novel furosesquiterpenes, and tsugicoline I from the fungus *Laurilia tsugicola*. *Tetrahedron*, *54*(34), 10199-10204.

Atabay, K. D., Yildiz, M. T., Avsar, T., Karabay, A., & Kiliç, T. (2015). Knockdown of Pin1 leads to reduced angiogenic potential and tumorigenicity in glioblastoma cells. *Oncology letters*, *10*(4), 2385-2389.

Bao, L., Kimzey, A., Sauter, G., Sowadski, J. M., Lu, K. P., & Wang, D. G. (2004). Prevalent overexpression of prolyl isomerase Pin1 in human cancers. *The American journal of pathology*, *164*(5), 1727-1737.

Baryawno, N., Sveinbjörnsson, B., Eksborg, S., Orrego, A., Segerström, L., Oqvist, C. O., Holm, S., Gustavsson, B., Kagedal, B., Kogner, P., & Johnsen, J. I. (2008). Tumor-growth promoting cyclooxygenase-2 prostaglandin E2 pathway provides medulloblastoma therapeutic targets. *Neuro-oncology*, *10*(5), 661-674.

Bond, F. T., Fullerton, D. S., Sciuchetti, L. A., & Catalfomo, P. (1966). The isolation and structure of echinodol, a triterpene acetate. *Journal of the American chemical society*, *88*(16), 3882-3883.

Chapman, P. J., & Ribbons, D. W. (1976). Metabolism of resorcinylic compounds by bacteria: orcinol pathway in *Pseudomonas putida*. *Journal of bacteriology*, *125*(3), 975-984.

Davis, M. E. (2016). Glioblastoma: overview of disease and treatment. *Clinical journal of oncology nursing*, *20*(5), S2.

dos Santos Fernandes, G. F., Fernandes, B. C., Valente, V., & Dos Santos, J. L. (2019). Recent advances in the discovery of small molecules targeting glioblastoma. *European journal of medicinal chemistry*, *164*, 8-26.

Erices, J. I., Torres, Á., Niechi, I., Bernales, I., & Quezada, C. (2018). Current natural therapies in the treatment against glioblastoma. *Phytotherapy research*, *32*(11), 2191-2201.

Gfeller, D., Grosdidier, A., Wirth, M., Daina, A., Michielin, O., & Zoete, V. (2014). SwissTargetPrediction: a web server for target prediction of bioactive small molecules. *Nucleic acids research*, *42*(W1), W32-W38.

Horling, A., Müller, C., Barthel, R., Bracher, F., & Imming, P. (2012). A new class of selective and potent 7-dehydrocholesterol reductase inhibitors. *Journal of medicinal chemistry*, *55*(17), 7614-7622.

Ivanova, V., Bačkor, M., Dahse, H. M., & Graefe, U. (2010). Molecular structural studies of lichen substances with antimicrobial, antiproliferative, and cytotoxic effects from *Parmelia subrudecta*. *Preparative biochemistry & biotechnology*, *40*(4), 377-388.

Kanematsu, A., & Natori, S. (1972). Triterpenoids of *Echinodontium tsugicola*. *Chemical and pharmaceutical bulletin*, *20*(9), 1993-1999.

Keiser, M. J., Setola, V., Irwin, J. J., Laggner, C., Abbas, A. I., Hufeisen, S. J., Jensen, N.H., Kuijer, M.B., Matos, R.C., Tran, T.B., & Whaley, R. (2009). Predicting new molecular targets for known drugs. *Nature*, *462*(7270), 175-181.

Khan, I., Mahfooz, S., & Hatiboglu, M. A. (2020). Herbal Medicine for Glioblastoma: Current and Future Prospects. *Medicinal chemistry*, *16*(8), 1022-1043.

Lim, M., Xia, Y., Bettegowda, C., & Weller, M. (2018). Current state of immunotherapy for glioblastoma. *Nature reviews Clinical oncology*, *15*(7), 422-442.

Liu, X., Gao, Y., Peng, J., Xu, Y., Wang, Y., Zhou, N., Xing, J., Luo, X., & Zheng, M. (2015). TarPred: a web application for predicting therapeutic and side effect targets of chemical compounds. *Bioinformatics*, *31*(12), 2049-2051.

Liu, X., Vogt, I., Haque, T., & Campillos, M. (2013). HitPick: a web server for hit identification and target prediction of chemical screenings. *Bioinformatics*, *29*(15), 1910-1912.

Lu, K. P. (2003). Prolyl isomerase Pin1 as a molecular target for cancer diagnostics and therapeutics. *Cancer cell*, *4*(3), 175-180.

Matubara, H., Miharu, K., Kinoshita, K., Koyama, K., Ye, Y., Takahashi, K., Yoshimura, I., Yamamoto, Y., Miura, Y., & Kinoshita, Y. (1998). Inhibitory effect of lichen metabolites and their synthetic analogues on melanin biosynthesis in cultured B-16 mouse melanoma cells. *Natural product sciences*, *4*(3), 161-169.

Murakami, M., & Kudo, I. (2006). Prostaglandin E synthase: a novel drug target for inflammation and cancer. *Current pharmaceutical design*, *12*(8), 943-954.

Mattioli, E., Columbaro, M., Capanni, C., Maraldi, N. M., Cenni, V., Scotlandi, K., Marino, M.T., Merlini, L., Squarzoni, S., & Lattanzi, G. (2011). Prelamin A-mediated recruitment of SUN1 to the nuclear envelope directs nuclear positioning in human muscle. *Cell death & differentiation*, *18*(8), 1305-1315.

Omuro, A., & DeAngelis, L. M. (2013). Glioblastoma and other malignant gliomas: a clinical review. *Jama*, *310*(17), 1842-1850.

Peón, A., Li, H., Ghislat, G., Leung, K. S., Wong, M. H., Lu, G., & Ballester, P. J. (2019). MolTarPred: a web tool for comprehensive target prediction with reliability estimation. *Chemical biology & drug design*, *94*(1), 1390-1401.

Sahasrabudhe SR, Lala D, Modi VV (1986). Degradation of orcinol by *Aspergillus niger*. *Canadian journal of microbiology,* 32**,** *535-538.*

Shiono, Y., Suzuki, S., Murayama, T., Ikeda, M., & Abe, Y. (2005). Protoilludane sequiterpenoids, echinocidins C and D produced by a decay causing fungal strain *Echinodontium tsugicola*. *Zeitschrift für naturforschung B*, *60*(4), 449-452.

Shiono, Y., Seto, T., Kamata, M., Takita, C., Suzuki, S., Murayama, T., & Ikeda, M. (2004). Protoilludane-type sesquiterpenes, echinocidins A and B, from a mycelial culture of *Echinodontium tsugicola*. *Zeitschrift für naturforschung B*, *59*(8), 925-929.

Suzuki, S., Murayama, T., & Shiono, Y. (2005). Illudalane sesquiterpenoids, echinolactones A and B, from a mycelial culture of *Echinodontium japonicum*. *Phytochemistry*, *66*(19), 2329-2333.

Ye, Y., Josten, I., Arnold, N., Steffan, B., & Steglich, W. (1996). Isolation of a fluorone pigment from the Indian paint fungus *Echinodontium tinctorium* and *Pyrofomes albomarginatus*. *Tetrahedron*, *52*(16), 5793-5798.

Appendix C. Supplementary data

Compound (2) Crystal Data and Experimental

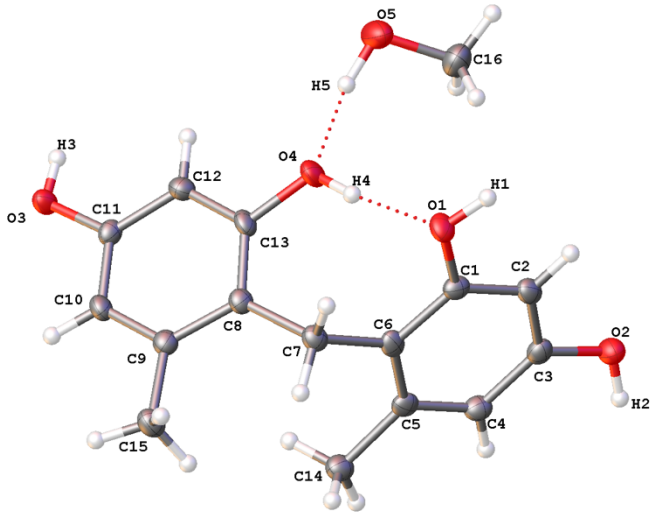

Experimental. Single yellow irregular crystals of compound **(2)** recrystallised from ethanol by slow evaporation. A suitable crystal with dimensions 0.12 × 0.10 × 0.04 mm^3 was selected and mounted on a mylar loop in oil on a Bruker APEX-II CCD diffractometer. The crystal was kept at a steady T = 90(2) K during data collection. The structure was solved with the **XT** (Sheldrick, 2015) solution program using Intrinsic Phasing methods and by using **Olex2** (Dolomanov et al., 2009) as the graphical interface. The model was refined with **XL** (Sheldrick, 2015) using full matrix least squares minimisation on F^2.

Crystal Data. $C_{16}H_{20}O_5$, M_r = 292.32, triclinic, P-1 (No. 2), a = 8.8847(5) Å, b = 9.2916(5) Å, c = 9.4831(4) Å, α = 97.485(4)°, β = 105.756(4)°, γ = 105.320(4)°, V = 709.25(7) Å^3, T = 90(2) K, Z = 2, Z' = 1, μ(CuK$_\alpha$) = 0.838, 9454 reflections measured, 1829 unique (R_{int} = 0.0628) which were used in all calculations. The final wR_2 was 0.0968 (all data) and R_1 was 0.0378 (I > 2(I)).

Compound (2)	***R*$_1$=3.78%**
Formula	$C_{16}H_{20}O_5$
$D_{calc.}$/ g cm^{-3}	1.369
μ/mm^{-1}	0.838
Formula Weight	292.32
Colour	yellow
Shape	irregular
Size/mm^3	0.12×0.10×0.04
T/K	90(2)
Crystal System	triclinic
Space Group	P-1
a/Å	8.8847(5)
b/Å	9.2916(5)
c/Å	9.4831(4)
α/°	97.485(4)
β/°	105.756(4)
γ/°	105.320(4)
V/Å^3	709.25(7)
Z	2
Z'	1
Wavelength/Å	1.54178
Radiation type	CuK$_\alpha$
Θ_{min}/°	4.965
Θ_{max}/°	56.046
Measured Refl's.	9454
Ind't Refl's	1829
Refl's with I > 2(I)	1440
R_{int}	0.0628
Parameters	213
Restraints	0
Largest Peak	0.238
Deepest Hole	-0.192
GooF	1.032
wR_2 (all data)	0.0968
wR_2	0.0880
R_1 (all data)	0.0552
R_1	0.0378

Structure Quality Indicators

Reflections:	d min (Cu) 0.93	I/σ 22.9	Rint 6.28%	complete 99%
Refinement:	Shift 0.000	Max Peak 0.2	Min Peak -0.2	GooF 1.032

A yellow irregular-shaped crystal with dimensions 0.12 × 0.10 × 0.04 mm^3 was mounted on a mylar loop in oil. Data were collected using a Bruker APEX-II CCD diffractometer equipped with an Oxford Cryosystems low-temperature device operating at T = 90(2) K.

Data were measured using ϕ and ω scans of 1.0 ° per frame for between 20 and 60 s using CuK$_\alpha$ radiation (microfocus sealed X-ray tube, 45 kV, 0.60 mA). The total number of runs and images was based on the strategy calculation from the program APEX3. The maximum resolution that was achieved was Θ = 56.046° (0.93 Å).

The unit cell was refined using **SAINT** (Bruker, V8.40A, after 2013) on 3706 reflections, 39% of the observed reflections. Data reduction, scaling and absorption corrections were performed using **SAINT** (Bruker, V8.40A, after 2013). The final completeness is 99.00 % out to 56.046° in Θ.

A multi-scan absorption correction was performed using **SADABS**-2016/2 (Bruker, 2016/2) was used for absorption correction. wR_2(int) was 0.0727 before and 0.0613 after correction. The ratio of minimum to maximum transmission is 0.8672. The $\lambda/2$ correction factor is not present. The absorption coefficient μ of this material is 0.838 mm^{-1} at this wavelength (λ = 1.54178Å) and the minimum and maximum transmissions are 0.837 and 0.967.

The structure was solved and the space group P-1 (# 2) determined by the **XT** (Sheldrick, 2015) structure solution program using Intrinsic Phasing methods and refined by full matrix least squares minimisation on $\boldsymbol{F^2}$ using version 2018/3 of **XL** (Sheldrick, 2015). All non-hydrogen atoms were refined anisotropically. Most hydrogen atom positions were calculated geometrically and refined using the riding model, but all O—H hydrogen atoms were located in difference maps and refined freely.

Table 1: Fractional Atomic Coordinates (×10^4) and Equivalent Isotropic Displacement Parameters (Å^2×10^3) for compound **(2)**. U_{eq} is defined as 1/3 of the trace of the orthogonalised U_{ij}.

Atom	x	y	z	U_{eq}
O1	580(2)	3378.3(19)	2520.0(19)	23.5(4)
O2	3683(2)	42.2(18)	1807.1(18)	24.6(4)
O3	-915(2)	2376(2)	9523.2(18)	22.3(4)
O4	-798(2)	2338.6(19)	4547.1(17)	25.5(4)
C1	1860(3)	2816(3)	3052(2)	19.1(6)
C2	2170(3)	1728(3)	2135(3)	21.1(6)
C3	3445(3)	1178(3)	2730(3)	21.2(6)
C4	4413(3)	1727(3)	4229(3)	21.2(6)
C5	4097(3)	2825(3)	5146(3)	19.8(6)
C6	2800(3)	3393(3)	4574(2)	19.6(6)
C7	2432(3)	4630(3)	5512(3)	20.4(6)
C8	1517(3)	4093(3)	6589(2)	18.9(5)
C9	2130(3)	4729(3)	8144(2)	20.0(6)
C10	1290(3)	4141(3)	9095(3)	21.0(6)
C11	-154(3)	2937(3)	8525(2)	18.7(6)
C12	-831(3)	2338(3)	6996(3)	21.8(6)
C13	-1(3)	2942(3)	6055(2)	20.4(6)

Atom	x	y	z	U_{eq}
C14	5184(3)	3420(3)	6760(3)	24.3(6)
C15	3656(3)	6104(3)	8811(3)	25.7(6)
O5	-3333(2)	-67(2)	2718(2)	36.6(5)
C16	-2582(3)	-667(3)	1755(3)	33.8(7)

Table 2: Anisotropic Displacement Parameters ($\times 10^4$) for compound **(2)**. The anisotropic displacement factor exponent takes the form: $-2\pi^2[h^2a^{*2} \times U_{11} + \ldots + 2hka^* \times b^* \times U_{12}]$

Atom	U_{11}	U_{22}	U_{33}	U_{23}	U_{13}	U_{12}
O1	26.1(10)	31.6(10)	14.3(9)	6.7(8)	4.2(7)	12.7(8)
O2	20.9(10)	28.0(10)	23.4(10)	1.5(8)	5.9(8)	8.4(8)
O3	20.4(10)	27.1(10)	15.0(9)	4.8(8)	5.2(8)	0.3(9)
O4	23.3(9)	34.0(10)	12.6(9)	2.5(8)	2.5(8)	2.8(8)
C1	16.7(13)	23.4(13)	19.1(13)	10.5(11)	6.5(11)	6.0(11)
C2	20.6(13)	25.3(14)	15.5(13)	6.4(11)	5.5(10)	3.4(11)
C3	19.5(13)	21.6(13)	22.7(14)	5.0(11)	10.3(11)	3.1(11)
C4	18.8(13)	24.5(14)	21.4(14)	9.5(11)	6.1(11)	7.1(11)
C5	17.1(13)	21.4(13)	20.4(13)	8.3(11)	7.8(11)	1.2(11)
C6	22.0(13)	19.5(13)	16.3(13)	6.2(10)	8.6(11)	1.1(11)
C7	21.7(13)	21.6(13)	16.8(13)	5.8(10)	5.3(10)	4.9(11)
C8	19.8(13)	22.4(13)	15.2(13)	6.2(10)	4.8(10)	7.4(11)
C9	19.2(13)	24.4(13)	17.7(13)	5.9(10)	5.4(10)	8.6(11)
C10	20.8(13)	27.1(14)	13.5(12)	2.5(10)	3.3(10)	7.9(11)
C11	19.6(13)	24.0(13)	16.4(13)	8.8(11)	7.5(10)	9.4(11)
C12	17.2(13)	27.4(14)	18.1(13)	4.1(11)	3.1(11)	5.3(11)
C13	21.8(14)	27.7(14)	10.7(13)	3.1(10)	1.7(11)	10.2(11)
C14	21.2(13)	31.0(15)	19.3(13)	7.8(11)	4.8(11)	6.3(11)
C15	25.5(14)	28.4(14)	18.4(13)	3.8(11)	4.5(11)	3.8(11)
O5	23.9(10)	42.9(11)	36.1(11)	-6.1(9)	7.6(9)	8.4(9)
C16	30.2(15)	40.8(16)	31.8(16)	4.2(12)	16.5(13)	8.3(13)

Table 3: Bond Lengths in Å for compound **(2)**

Atom	Atom	Length/Å
O1	C1	1.376(3)
O2	C3	1.379(3)
O3	C11	1.384(3)
O4	C13	1.376(3)
C1	C2	1.379(3)
C1	C6	1.405(3)
C2	C3	1.377(3)
C3	C4	1.391(3)
C4	C5	1.389(3)
C5	C6	1.399(3)
C5	C14	1.508(3)
C6	C7	1.520(3)
C7	C8	1.524(3)
C8	C9	1.410(3)
C8	C13	1.394(3)
C9	C10	1.395(3)
C9	C15	1.510(3)
C10	C11	1.377(3)
C11	C12	1.383(3)
C12	C13	1.387(3)
O5	C16	1.409(3)

Table 4: Bond Angles in ° for compound **(2)**

Atom	Atom	Atom	Angle/°
O1	C1	C2	121.2(2)
O1	C1	C6	116.2(2)
C2	C1	C6	122.6(2)
C3	C2	C1	119.0(2)
O2	C3	C4	121.8(2)
C2	C3	O2	117.8(2)

Atom	Atom	Atom	Angle/°
C2	C3	C4	120.3(2)
C5	C4	C3	120.5(2)
C4	C5	C6	120.4(2)
C4	C5	C14	119.4(2)
C6	C5	C14	120.2(2)
C1	C6	C7	120.0(2)
C5	C6	C1	117.3(2)
C5	C6	C7	122.6(2)
C6	C7	C8	115.51(19)
C9	C8	C7	122.6(2)
C13	C8	C7	120.5(2)
C13	C8	C9	116.9(2)
C8	C9	C15	121.1(2)
C10	C9	C8	120.4(2)
C10	C9	C15	118.4(2)
C11	C10	C9	120.4(2)
C10	C11	O3	118.0(2)
C10	C11	C12	120.5(2)
C12	C11	O3	121.5(2)
C11	C12	C13	118.7(2)
O4	C13	C8	122.2(2)
O4	C13	C12	115.1(2)
C12	C13	C8	122.8(2)

Table 5: Torsion Angles in ° for compound **(2)**

Atom	Atom	Atom	Atom	Angle/°
O1	C1	C2	C3	-178.7(2)
O1	C1	C6	C5	179.30(19)
O1	C1	C6	C7	-3.1(3)
O2	C3	C4	C5	-177.3(2)
O3	C11	C12	C13	-179.5(2)
C1	C2	C3	O2	177.21(19)
C1	C2	C3	C4	-0.6(3)
C1	C6	C7	C8	103.9(2)
C2	C1	C6	C5	0.4(3)
C2	C1	C6	C7	178.0(2)
C2	C3	C4	C5	0.5(3)
C3	C4	C5	C6	0.1(3)
C3	C4	C5	C14	-179.0(2)
C4	C5	C6	C1	-0.5(3)
C4	C5	C6	C7	-178.1(2)
C5	C6	C7	C8	-78.7(3)
C6	C1	C2	C3	0.2(3)
C6	C7	C8	C9	124.0(2)
C6	C7	C8	C13	-56.8(3)
C7	C8	C9	C10	-176.5(2)
C7	C8	C9	C15	6.6(3)
C7	C8	C13	O4	-5.6(3)
C7	C8	C13	C12	175.4(2)
C8	C9	C10	C11	-0.3(3)
C9	C8	C13	O4	173.6(2)
C9	C8	C13	C12	-5.3(3)
C9	C10	C11	O3	178.5(2)
C9	C10	C11	C12	-2.9(3)
C10	C11	C12	C13	1.9(3)
C11	C12	C13	O4	-176.7(2)
C11	C12	C13	C8	2.3(3)
C13	C8	C9	C10	4.3(3)
C13	C8	C9	C15	-172.6(2)
C14	C5	C6	C1	178.5(2)
C14	C5	C6	C7	1.0(3)
C15	C9	C10	C11	176.7(2)

Table 6: Hydrogen fractional atomic coordinates ($\times 10^4$) and equivalent isotropic displacement parameters ($Å^2 \times 10^3$) for compound **(2)**.

Atom	x	y	z	U_{eq}
H1	100(40)	2970(40)	1530(40)	62(10)
H2	4670(40)	-30(30)	2160(30)	50(9)
H3	-1750(40)	1650(40)	9080(30)	37(9)
H4	-300(40)	2860(40)	3910(40)	64(10)
H2A	1513.74	1362.92	1109.49	25
H4A	5295.44	1347.23	4628.04	25
H7A	1770.2	5112.97	4824.51	25
H7B	3486.61	5426.15	6102.02	25
H10	1716.37	4573.74	10142	25
H12	-1843.97	1528.5	6598.73	26
H14A	5966.09	2845.6	6992.88	37
H14B	4501.06	3294.83	7419.38	37
H14C	5789.11	4505.75	6915.21	37
H15A	4605.4	5838.8	8656.84	39
H15B	3850.4	6422.34	9888.59	39
H15C	3503.72	6943.8	8319.66	39
H5	-2440(50)	720(40)	3540(40)	67(10)
H16A	-1997.75	-1323.16	2235.79	51
H16B	-1797.92	174.24	1548.26	51
H16C	-3426.81	-1268.24	810.85	51

U_{eq} is defined as 1/3 of the trace of the orthogonalised U_{ij}.

Table 7: Hydrogen Bond information for compound **(2)**

D	H	A	d(D-H)/Å	d(H-A)/Å	d(D-A)/Å	D-H-A/deg
O1	H1	O3[1]	0.90(4)	1.81(4)	2.705(2)	172(3)
O2	H2	O5[2]	0.87(3)	1.72(4)	2.589(3)	173(3)
O3	H3	O2[3]	0.82(3)	1.89(3)	2.710(2)	176(3)
O4	H4	O1	0.95(4)	1.77(4)	2.695(2)	166(3)
O5	H5	O4	0.99(4)	1.74(4)	2.699(2)	163(3)

[1]+x,+y,-1+z; [2]1+x,+y,+z; [3]-x,-y,1-z

Compound (4) Crystal Data and Experimental

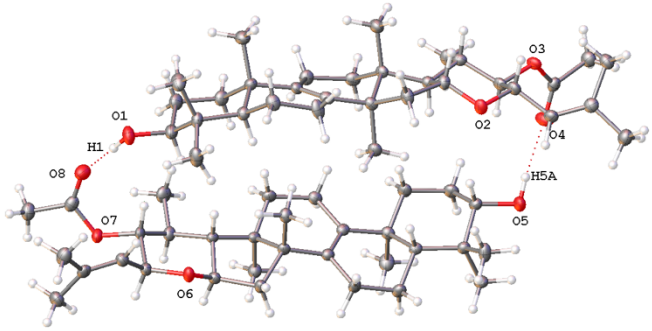

Experimental. Single colourless needle crystals of compound **(4)** recrystallised from acetonitrile by slow evaporation. A suitable crystal with dimensions 0.24 × 0.05 × 0.05 mm^3 was selected and mounted on a mylar loop in oil on a Bruker APEX II area detector diffractometer. The crystal was kept at a steady T = 110(2) K during data collection. The structure was solved with the **XT** 2018/2 (Sheldrick, 2015) solution program using Intrinsic Phasing methods and by using Olex2 (Dolomanov et al., 2009) as the graphical interface. The model was refined with **XL** (Sheldrick, 2015) using full matrix least squares minimisation on $\boldsymbol{F^2}$.

Crystal Data. $C_{32}H_{50}O_4$, M_r = 498.72, monoclinic, $P2_1$ (No. 4), a = 7.9203(3) Å, b = 20.6269(8) Å, c = 17.4422(6) Å, β = 97.890(2)°, α = γ = 90°, V = 2822.58(18) Å^3, T = 110(2) K, Z = 4, Z' = 2, μ(CuK$_\alpha$) = 0.585, 78352 reflections measured, 8399 unique (R_{int} = 0.0722) which were used in all calculations. The final wR_2 was 0.1093 (all data) and R_1 was 0.0429 (I≥2 σ(I)).

Compound (4)	***R*$_1$= 4.29 %**
Formula	$C_{32}H_{50}O_4$
$D_{calc.}$/ g cm^{-3}	1.174
μ/mm^{-1}	0.585
Formula Weight	498.72
Colour	colourless
Shape	needle
Size/mm^3	0.24×0.05×0.05
T/K	110(2)
Crystal System	monoclinic
Flack Parameter	-0.08(9)
Hooft Parameter	-0.03(7)
Space Group	$P2_1$
a/Å	7.9203(3)
b/Å	20.6269(8)
c/Å	17.4422(6)
α/°	90
β/°	97.890(2)
γ/°	90
V/Å^3	2822.58(18)
Z	4
Z'	2
Wavelength/Å	1.54178
Radiation type	CuK$_\alpha$
Θ_{min}/°	2.557
Θ_{max}/°	60.158
Measured Refl's.	78352
Indep't Refl's	8399
Refl's I≥2 σ(I)	7934
R_{int}	0.0722
Parameters	675
Restraints	1
Largest Peak	0.188
Deepest Hole	-0.202
GooF	1.131
wR_2 (all data)	0.1093
wR_2	0.1073
R_1 (all data)	0.0464
R_1	0.0429

Structure Quality Indicators

Reflections:	d min (Cu\a) 2θ=120.3° 0.89	I/σ(I) 29.2	Rint 7.22%	Full 120.3° 99.9
Refinement:	Shift 0.001	Max Peak 0.2	Min Peak -0.2	GooF 1.131	Flack -.08(9)

A colourless needle-shaped crystal with dimensions 0.24 × 0.05 × 0.05 mm^3 was mounted on a mylar loop in oil. Data were collected using a Bruker APEX II area detector diffractometer equipped with an Oxford Cryosystems low-temperature device operating at T = 110(2) K.

Data were measured using ϕ and ω scans of 1.0 ° per frame for between 10 and 30 s using CuK$_\alpha$ radiation (microfocus sealed X-ray tube, 45 kV, 0.60 mA). The total number of runs and images was based on the strategy calculation from the program APEX3. The maximum resolution that was achieved was Θ = 60.158° (0.89 Å).

The unit cell was refined using SAINT (Bruker, V8.40B, after 2013) on 9826 reflections, 13% of the observed reflections. Data reduction, scaling and absorption corrections were performed using SAINT (Bruker, V8.40B, after 2013). The final completeness is 99.90 % out to 60.158° in Θ.

A multi-scan absorption correction was performed using SADABS-2016/2 (Bruker, 2016/2) was used for absorption correction. wR_2(int) was 0.1042 before and 0.0716 after correction. The ratio of minimum to maximum transmission is 0.8207. The $\lambda/2$ correction factor is not present. The absorption coefficient μ of this material is 0.585 mm^{-1} at this wavelength (λ = 1.54178Å) and the minimum and maximum transmissions are 0.797 and 0.971.

The structure was solved and the space group $P2_1$ (# 4) determined by the **XT** 2018/2 (Sheldrick, 2015) structure solution program using Intrinsic Phasing methods and refined by full matrix least squares minimisation on $\boldsymbol{F^2}$ using version 2018/3 of **XL** (Sheldrick, 2015). The material crystallizes with two molecules in the asymmetric unit, with the two molecules forming a hydrogen bonded dimer. All non-hydrogen atoms were refined anisotropically. Most hydrogen atom positions were calculated geometrically and refined using the riding model, however the hydroxyl hydrogen in each molecule was located in a difference map and refined freely.

The value of Z' is 2. This means that there are two independent molecules in the asymmetric unit.

The Flack parameter was refined to -0.08(9) (Parsons, 2013). Determination of absolute structure using Bayesian statistics on Bijvoet differences using the Olex2 results in -0.03(7). The absolute configurations of the different stereocenters are:

C3: S, C5: R, C10: S, C13: R, C14: S, C16: R, C17: R, C20: S, C22: R, C23: S

C35: S, C37: R, C42: S, C45: R, C46: S, C48: R, C49: R, C52: S, C54: R, C55: S

Note: The Flack parameter is used to determine chirality of the crystal studied, the value should be near 0, a value of 1 means that the stereochemistry is wrong and the model should be inverted. A value of 0.5 means that the crystal consists of a racemic mixture of the two enantiomers.

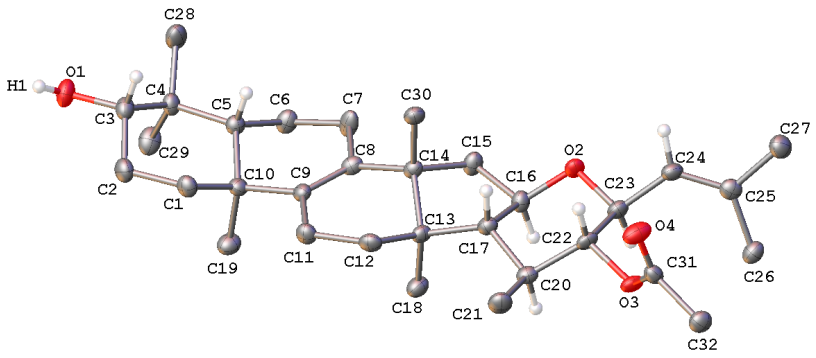

Figure 1: ORTEP-style image of one molecule in the asymmetric unit. Some hydrogen atoms removed for clarity.

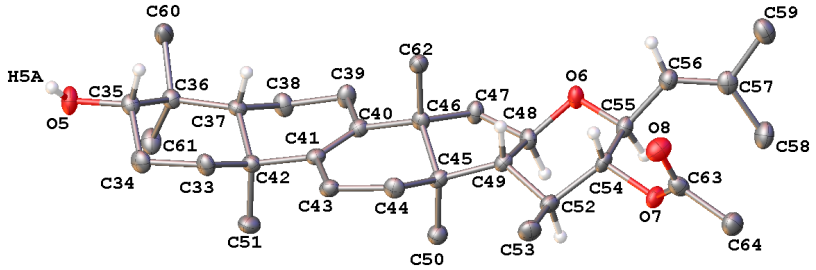

Figure 2: ORTEP-style image of the second molecule in the asymmetric unit. Some hydrogen atoms removed for clarity.

Table 8: Fractional atomic coordinates ($\times 10^4$) and equivalent isotropic displacement parameters ($Å^2 \times 10^3$) for compound **(4)**.

Atom	x	y	z	U_{eq}
O1	2760(4)	5699.0(16)	-687.3(17)	30.5(7)
O2	7599(3)	6635.9(14)	5646.1(15)	22.0(6)
O3	11982(3)	6237.2(14)	6510.8(15)	21.4(6)
O4	11784(4)	5206.7(15)	6914.5(18)	31.1(7)
C1	6511(5)	5646(2)	906(2)	22.8(9)
C2	5568(5)	5646(2)	86(2)	26.2(10)
C3	3657(6)	5700(2)	86(2)	24.3(9)
C4	3125(5)	6302(2)	497(2)	21.2(9)
C5	4185(5)	6323(2)	1324(2)	19.7(8)
C6	3759(5)	6896(2)	1811(2)	24.9(9)
C7	4418(5)	6780(2)	2660(2)	26.8(10)
C8	6126(5)	6437.2(19)	2805(2)	19.2(9)
C9	6884(5)	6178.8(19)	2234(2)	18.2(8)
C10	6154(5)	6251(2)	1376(2)	19.4(8)
C11	8590(5)	5824(2)	2399(2)	22.4(9)
C12	9400(5)	5768(2)	3253(2)	22.2(9)
C13	8842(5)	6311(2)	3743(2)	18.1(8)
C14	6828(5)	6325(2)	3640(2)	18.2(8)
C15	6482(5)	6824(2)	4260(2)	24.1(9)
C16	8027(5)	6773(2)	4895(2)	20.7(9)
C17	9175(5)	6241(2)	4631(2)	18.9(8)
C18	9594(5)	6950(2)	3482(2)	25.1(9)
C19	7057(6)	6841(2)	1059(3)	27.3(10)

Atom	x	y	z	U_{eq}
C20	10903(5)	6267(2)	5136(2)	20.1(8)
C21	12169(5)	5762(2)	4940(3)	27.9(10)
C22	10451(5)	6166(2)	5953(2)	20.1(9)
C23	9135(5)	6654(2)	6201(2)	21.6(9)
C24	8620(5)	6485(2)	6969(2)	22.6(9)
C25	9308(5)	6701(2)	7664(2)	22.7(9)
C26	10780(5)	7165(2)	7799(2)	24.3(9)
C27	8699(6)	6461(2)	8394(3)	29.5(10)
C28	1237(5)	6224(3)	593(3)	33.2(11)
C29	3299(6)	6914(2)	14(3)	30.3(10)
C30	6044(5)	5675(2)	3873(2)	22.3(9)
C31	12490(5)	5726(2)	6959(2)	21.0(9)
C32	14056(5)	5884(2)	7512(2)	26.1(10)
O5	8847(4)	4372.8(17)	6744.3(16)	28.2(7)
O6	640(3)	3941.3(14)	907.0(15)	22.5(6)
O7	2448(3)	3526.9(14)	-867.9(15)	22.4(6)
O8	3255(4)	4465.0(15)	-1367.2(17)	30.9(7)
C33	8648(5)	4034(2)	4611(2)	22.3(9)
C34	9377(5)	4032(2)	5468(2)	24.4(9)
C35	8160(5)	4359(2)	5939(2)	20.1(9)
C36	6393(5)	4030(2)	5866(2)	19.3(9)
C37	5707(5)	3973.6(19)	4988(2)	17.4(8)
C38	3965(5)	3641(2)	4824(2)	24.1(10)
C39	3155(5)	3768(2)	3992(2)	23.0(9)
C40	4398(5)	3803.0(19)	3405(2)	18.4(8)
C41	6095(5)	3786.0(19)	3608(2)	17.6(8)
C42	6926(5)	3680.1(19)	4447(2)	19.0(9)
C43	7324(5)	3823(2)	3002(2)	20.4(9)
C44	6561(5)	3863(2)	2148(2)	21.2(9)
C45	4760(5)	3583.5(19)	2014(2)	18.0(8)
C46	3655(5)	3933.1(19)	2575(2)	18.0(9)
C47	1836(5)	3684(2)	2272(2)	22.2(9)
C48	1872(5)	3568(2)	1404(2)	19.9(9)
C49	3667(5)	3734.6(19)	1238(2)	17.4(8)
C50	4861(5)	2852(2)	2153(2)	23.2(9)
C51	7233(6)	2946(2)	4541(3)	28.3(10)
C52	3918(5)	3459(2)	451(2)	20.8(9)
C53	5685(5)	3589(2)	222(3)	27.3(10)
C54	2543(5)	3807(2)	-103(2)	18.8(8)
C55	699(5)	3770(2)	114(2)	20.7(9)
C56	-414(5)	4240(2)	-370(2)	22.3(9)
C57	-1404(5)	4132(2)	-1032(2)	23.5(9)
C58	-1684(6)	3488(2)	-1421(3)	30.9(10)
C59	-2356(6)	4681(2)	-1469(3)	31.4(11)
C60	5225(5)	4493(2)	6248(2)	28.1(10)
C61	6477(6)	3391(2)	6311(2)	27.0(10)
C62	3578(5)	4675(2)	2478(2)	21.6(9)
C63	2808(5)	3905(2)	-1449(2)	23.7(10)
C64	2602(6)	3556(2)	-2209(2)	30.1(10)

U_{eq} is defined as 1/3 of the trace of the orthogonalised U_{ij}.

Table 9: Anisotropic displacement parameters ($\times 10^4$) for compound **(4)**. The anisotropic displacement factor exponent takes the form: $-2\pi^2[h^2a^{*2} \times U_{11} + \ldots + 2hka^* \times b^* \times U_{12}]$

Atom	U_{11}	U_{22}	U_{33}	U_{23}	U_{13}	U_{12}
O1	37.0(18)	33.0(19)	19.5(16)	-4.5(14)	-3.6(13)	2.3(15)
O2	13.3(14)	31.3(17)	20.7(15)	-1.8(12)	-0.6(11)	2.3(12)
O3	12.9(13)	24.0(15)	25.7(15)	3.1(13)	-3.6(11)	-2.9(12)
O4	25.4(16)	25.6(18)	39.2(18)	8.0(14)	-6.3(13)	-4.4(14)
C1	23(2)	23(2)	23(2)	-2.0(18)	5.5(17)	4.9(18)
C2	30(2)	27(2)	22(2)	-4.8(18)	5.9(18)	2(2)
C3	31(2)	23(2)	19(2)	-1.1(18)	2.3(18)	-2.3(19)
C4	23(2)	24(2)	16(2)	-0.2(17)	1.3(16)	4.6(18)
C5	19(2)	20(2)	19(2)	0.7(17)	1.6(16)	1.7(18)
C6	23(2)	24(2)	26(2)	-3.3(18)	-0.5(18)	6.8(18)
C7	23(2)	32(3)	25(2)	-11.8(19)	-0.8(18)	12.2(19)
C8	17(2)	14(2)	26(2)	-0.7(17)	0.6(17)	2.2(16)
C9	18(2)	18(2)	19(2)	-3.0(17)	2.6(16)	-2.3(16)
C10	19(2)	21(2)	19(2)	1.5(17)	3.8(16)	-1.4(17)
C11	19(2)	25(2)	23(2)	-1.6(18)	4.7(17)	4.5(18)
C12	15(2)	23(2)	29(2)	-0.3(18)	5.6(17)	2.3(17)
C13	14.3(19)	20(2)	19(2)	1.9(17)	-1.5(15)	0.2(17)
C14	14.3(19)	18(2)	22(2)	-2.8(17)	1.3(15)	2.0(17)
C15	21(2)	27(2)	23(2)	-3.8(18)	-2.0(17)	6.7(18)
C16	22(2)	21(2)	18(2)	-1.2(17)	0.5(16)	3.3(17)
C17	16(2)	19(2)	22(2)	-0.7(17)	1.7(15)	0.1(17)
C18	24(2)	25(2)	25(2)	1.0(18)	-1.7(18)	-3.8(18)
C19	28(2)	25(2)	28(2)	3.3(19)	1.0(19)	-4.4(19)
C20	17(2)	18(2)	25(2)	1.4(17)	1.3(16)	-1.1(17)
C21	17(2)	35(3)	31(2)	-2(2)	1.3(18)	4.3(19)
C22	12.4(19)	22(2)	24(2)	1.3(17)	-4.5(16)	-0.8(16)
C23	16(2)	25(2)	23(2)	-0.7(17)	-2.0(17)	-1.5(17)
C24	16(2)	27(2)	24(2)	1.7(18)	0.6(17)	-3.5(17)
C25	19(2)	23(2)	26(2)	3.1(18)	1.8(17)	4.6(17)
C26	23(2)	23(2)	26(2)	-2.6(18)	-2.0(18)	0.8(18)
C27	28(2)	36(3)	24(2)	3.3(19)	2.3(19)	0.4(19)
C28	24(2)	50(3)	25(2)	-5(2)	-1.7(18)	3(2)
C29	40(3)	23(2)	26(2)	2.1(19)	-2(2)	5(2)
C30	16(2)	27(2)	24(2)	-0.6(18)	1.6(17)	-1.1(18)
C31	18(2)	28(2)	18(2)	2.4(18)	3.7(16)	2.6(19)
C32	21(2)	30(3)	26(2)	2.2(19)	-0.6(18)	2.3(18)
O5	24.7(16)	40.4(19)	18.2(15)	0.4(13)	-2.3(12)	-9.0(15)
O6	17.7(14)	33.8(17)	15.4(14)	-2.2(12)	0.3(11)	-0.6(12)
O7	29.5(16)	23.4(15)	14.3(14)	-1.6(12)	2.7(11)	-2.6(12)
O8	38.2(18)	27.7(19)	28.2(17)	-0.5(13)	9.6(14)	-3.7(14)
C33	14(2)	30(2)	22(2)	0.5(18)	1.9(17)	-0.6(17)
C34	15(2)	30(2)	28(2)	0.2(19)	2.3(17)	-2.7(17)
C35	19(2)	22(2)	19(2)	3.5(17)	1.8(16)	-2.1(17)
C36	16(2)	22(2)	20(2)	1.6(17)	3.2(16)	-1.2(17)
C37	17(2)	16(2)	20(2)	1.8(16)	3.5(16)	1.7(16)
C38	16(2)	33(3)	23(2)	3.2(18)	4.3(17)	-3.1(18)
C39	18(2)	34(2)	17(2)	-0.8(18)	5.9(16)	-3.6(18)
C40	19(2)	17(2)	19(2)	-0.7(16)	4.3(16)	-1.6(17)
C41	20(2)	14(2)	19(2)	-0.5(16)	4.7(16)	0.2(16)
C42	16(2)	19(2)	22(2)	-0.7(16)	2.3(16)	1.0(16)

Atom	U_{11}	U_{22}	U_{33}	U_{23}	U_{13}	U_{12}
C43	18(2)	20(2)	24(2)	-3.0(17)	4.4(16)	1.0(17)
C44	15(2)	25(2)	24(2)	0.3(18)	6.8(16)	-1.9(17)
C45	18(2)	18(2)	19(2)	-2.7(16)	6.2(16)	-3.3(16)
C46	12.4(19)	23(2)	19(2)	-1.1(17)	3.8(16)	-1.1(16)
C47	17(2)	31(2)	18(2)	-2.0(17)	2.2(16)	-4.4(18)
C48	17(2)	24(2)	19(2)	0.2(17)	1.1(16)	-3.6(17)
C49	19(2)	17(2)	17(2)	-1.5(16)	5.2(16)	-3.3(16)
C50	26(2)	22(2)	21(2)	-0.6(18)	2.6(17)	0.9(18)
C51	34(3)	23(2)	27(2)	1.0(19)	1(2)	8.6(19)
C52	25(2)	20(2)	17(2)	-2.4(17)	4.1(17)	2.4(17)
C53	26(2)	33(3)	25(2)	-4.0(19)	9.4(18)	3.5(19)
C54	23(2)	21(2)	12(2)	-4.4(16)	3.7(16)	-3.5(17)
C55	22(2)	24(2)	16(2)	-2.3(17)	2.2(16)	-3.9(18)
C56	21(2)	25(2)	21(2)	-2.3(17)	2.5(18)	-2.3(17)
C57	20(2)	32(2)	20(2)	1.9(18)	7.1(18)	-3.0(18)
C58	28(2)	36(3)	27(2)	-3(2)	-1.6(19)	-8(2)
C59	25(2)	43(3)	26(2)	4(2)	2.6(19)	3(2)
C60	24(2)	40(3)	19(2)	-5.1(19)	1.0(18)	8(2)
C61	31(2)	25(2)	24(2)	5.9(18)	-0.6(18)	-8.7(19)
C62	21(2)	24(2)	20(2)	-2.2(17)	2.7(16)	2.2(18)
C63	20(2)	30(3)	22(2)	3.1(19)	5.9(17)	5.9(19)
C64	32(2)	36(3)	22(2)	-2(2)	3.0(18)	3(2)

Table 10: Bond Lengths in Å for compound **(4)**.

Atom	Atom	Length/Å
O1	C3	1.435(5)
O2	C16	1.426(5)
O2	C23	1.447(5)
O3	C22	1.453(5)
O3	C31	1.342(5)
O4	C31	1.206(5)
C1	C2	1.519(6)
C1	C10	1.540(6)
C2	C3	1.518(6)
C3	C4	1.522(6)
C4	C5	1.567(5)
C4	C28	1.536(6)
C4	C29	1.534(6)
C5	C6	1.520(6)
C5	C10	1.557(5)
C6	C7	1.520(6)
C7	C8	1.517(6)
C8	C9	1.342(6)
C8	C14	1.504(6)
C9	C10	1.536(5)
C9	C11	1.529(6)
C10	C19	1.551(6)
C11	C12	1.542(6)
C12	C13	1.511(6)
C13	C14	1.580(5)
C13	C17	1.541(5)

Atom	Atom	Length/Å
C13	C18	1.541(6)
C14	C15	1.544(6)
C14	C30	1.555(6)
C15	C16	1.536(6)
C16	C17	1.536(6)
C17	C20	1.523(5)
C20	C21	1.516(6)
C20	C22	1.532(6)
C22	C23	1.551(6)
C23	C24	1.495(6)
C24	C25	1.334(6)
C25	C26	1.502(6)
C25	C27	1.506(6)
C31	C32	1.499(6)
O5	C35	1.435(5)
O6	C48	1.437(5)
O6	C55	1.434(5)
O7	C54	1.447(5)
O7	C63	1.340(5)
O8	C63	1.211(5)
C33	C34	1.526(6)
C33	C42	1.539(6)
C34	C35	1.510(6)
C35	C36	1.544(6)
C36	C37	1.558(5)
C36	C60	1.542(6)

Atom	Atom	Length/Å
C36	C61	1.527(6)
C37	C38	1.532(5)
C37	C42	1.561(5)
C38	C39	1.527(6)
C39	C40	1.516(5)
C40	C41	1.343(6)
C40	C46	1.511(6)
C41	C42	1.536(5)
C41	C43	1.535(5)
C42	C51	1.539(6)
C43	C44	1.530(6)
C44	C45	1.527(5)
C45	C46	1.574(5)
C45	C49	1.534(6)

Atom	Atom	Length/Å
C45	C50	1.529(6)
C46	C47	1.553(5)
C46	C62	1.539(6)
C47	C48	1.537(6)
C48	C49	1.528(5)
C49	C52	1.524(5)
C52	C53	1.531(6)
C52	C54	1.531(6)
C54	C55	1.560(5)
C55	C56	1.493(6)
C56	C57	1.323(6)
C57	C58	1.495(6)
C57	C59	1.507(6)
C63	C64	1.497(6)

Table 11: Bond angles in ° for compound **(4)**.

Atom	Atom	Atom	Angle/°
C16	O2	C23	109.0(3)
C31	O3	C22	117.8(3)
C2	C1	C10	113.5(3)
C3	C2	C1	111.2(3)
O1	C3	C2	111.4(3)
O1	C3	C4	108.1(3)
C2	C3	C4	113.6(3)
C3	C4	C5	108.0(3)
C3	C4	C28	107.6(4)
C3	C4	C29	111.1(3)
C28	C4	C5	108.0(3)
C29	C4	C5	113.9(3)
C29	C4	C28	108.0(4)
C6	C5	C4	113.8(3)
C6	C5	C10	109.9(3)
C10	C5	C4	117.2(3)
C7	C6	C5	110.5(3)
C8	C7	C6	114.5(3)
C9	C8	C7	122.8(4)
C9	C8	C14	120.9(3)
C14	C8	C7	115.9(3)
C8	C9	C10	122.5(3)
C8	C9	C11	121.6(4)
C11	C9	C10	115.8(3)
C1	C10	C5	107.6(3)
C1	C10	C19	108.6(3)
C9	C10	C1	111.6(3)
C9	C10	C5	107.8(3)
C9	C10	C19	107.0(3)
C19	C10	C5	114.3(3)
C9	C11	C12	117.2(3)
C13	C12	C11	112.1(3)
C12	C13	C14	108.6(3)
C12	C13	C17	118.5(3)

Atom	Atom	Atom	Angle/°
C12	C13	C18	108.1(3)
C17	C13	C14	98.5(3)
C17	C13	C18	110.9(3)
C18	C13	C14	112.0(3)
C8	C14	C13	110.3(3)
C8	C14	C15	119.9(3)
C8	C14	C30	106.1(3)
C15	C14	C13	101.9(3)
C15	C14	C30	105.9(3)
C30	C14	C13	112.8(3)
C16	C15	C14	105.0(3)
O2	C16	C15	114.1(3)
O2	C16	C17	111.0(3)
C17	C16	C15	106.2(3)
C16	C17	C13	102.0(3)
C20	C17	C13	126.4(3)
C20	C17	C16	108.9(3)
C17	C20	C22	103.1(3)
C21	C20	C17	114.6(3)
C21	C20	C22	111.3(3)
O3	C22	C20	109.2(3)
O3	C22	C23	106.2(3)
C20	C22	C23	115.0(3)
O2	C23	C22	109.4(3)
O2	C23	C24	106.6(3)
C24	C23	C22	112.0(3)
C25	C24	C23	127.5(4)
C24	C25	C26	124.5(4)
C24	C25	C27	121.3(4)
C26	C25	C27	114.1(4)
O3	C31	C32	111.1(4)
O4	C31	O3	124.1(4)
O4	C31	C32	124.8(4)
C55	O6	C48	109.9(3)

Atom	Atom	Atom	Angle/°
C63	O7	C54	118.4(3)
C34	C33	C42	112.7(3)
C35	C34	C33	110.4(3)
O5	C35	C34	110.9(3)
O5	C35	C36	107.9(3)
C34	C35	C36	113.4(3)
C35	C36	C37	107.7(3)
C60	C36	C35	106.4(3)
C60	C36	C37	108.8(3)
C61	C36	C35	111.2(3)
C61	C36	C37	114.8(3)
C61	C36	C60	107.6(3)
C36	C37	C42	117.5(3)
C38	C37	C36	113.6(3)
C38	C37	C42	109.3(3)
C39	C38	C37	110.5(3)
C40	C39	C38	115.0(3)
C41	C40	C39	122.7(4)
C41	C40	C46	120.1(3)
C46	C40	C39	116.9(3)
C40	C41	C42	122.5(3)
C40	C41	C43	121.6(4)
C43	C41	C42	115.8(3)
C33	C42	C37	108.0(3)
C33	C42	C51	108.9(3)
C41	C42	C33	111.2(3)
C41	C42	C37	107.5(3)
C41	C42	C51	106.4(3)
C51	C42	C37	114.8(3)
C44	C43	C41	118.0(3)
C45	C44	C43	111.5(3)
C44	C45	C46	108.6(3)
C44	C45	C49	117.5(3)
C44	C45	C50	108.7(3)
C49	C45	C46	99.2(3)
C50	C45	C46	112.0(3)
C50	C45	C49	110.6(3)
C40	C46	C45	109.8(3)
C40	C46	C47	119.2(3)
C40	C46	C62	106.6(3)
C47	C46	C45	101.9(3)
C62	C46	C45	113.9(3)
C62	C46	C47	105.7(3)
C48	C47	C46	104.1(3)
O6	C48	C47	114.0(3)
O6	C48	C49	109.7(3)
C49	C48	C47	107.2(3)
C48	C49	C45	102.4(3)
C52	C49	C45	126.2(3)
C52	C49	C48	109.0(3)
C49	C52	C53	114.0(3)
C49	C52	C54	102.9(3)
C53	C52	C54	110.5(3)
O7	C54	C52	109.7(3)
O7	C54	C55	105.8(3)
C52	C54	C55	115.7(3)
O6	C55	C54	112.2(3)
O6	C55	C56	106.9(3)
C56	C55	C54	109.3(3)
C57	C56	C55	128.1(4)
C56	C57	C58	125.4(4)
C56	C57	C59	120.6(4)
C58	C57	C59	113.9(4)
O7	C63	C64	112.4(4)
O8	C63	O7	123.7(4)
O8	C63	C64	123.9(4)

Table 12: Torsion angles in ° for compound **(4)**.

Atom	Atom	Atom	Atom	Angle/°
O1	C3	C4	C5	-176.8(3)
O1	C3	C4	C28	66.9(4)
O1	C3	C4	C29	-51.1(4)
O2	C16	C17	C13	156.5(3)
O2	C16	C17	C20	-67.9(4)
O2	C23	C24	C25	-147.7(4)
O3	C22	C23	O2	177.0(3)
O3	C22	C23	C24	-65.0(4)
C1	C2	C3	O1	-179.8(3)
C1	C2	C3	C4	57.7(5)
C2	C1	C10	C5	52.3(4)
C2	C1	C10	C9	170.4(3)
C2	C1	C10	C19	-71.9(4)
C2	C3	C4	C5	-52.5(4)
C2	C3	C4	C28	-168.9(4)

Atom	Atom	Atom	Atom	Angle/°
C2	C3	C4	C29	73.1(4)
C3	C4	C5	C6	-178.9(3)
C3	C4	C5	C10	51.0(5)
C4	C5	C6	C7	163.2(4)
C4	C5	C10	C1	-50.8(4)
C4	C5	C10	C9	-171.3(3)
C4	C5	C10	C19	69.9(5)
C5	C6	C7	C8	37.6(5)
C6	C5	C10	C1	177.3(3)
C6	C5	C10	C9	56.8(4)
C6	C5	C10	C19	-62.0(4)
C6	C7	C8	C9	-8.6(6)
C6	C7	C8	C14	179.0(4)
C7	C8	C9	C10	4.6(6)
C7	C8	C9	C11	-178.8(4)
C7	C8	C14	C13	-151.2(4)
C7	C8	C14	C15	-33.3(5)
C7	C8	C14	C30	86.4(4)
C8	C9	C10	C1	-146.3(4)
C8	C9	C10	C5	-28.3(5)
C8	C9	C10	C19	95.0(4)
C8	C9	C11	C12	0.6(6)
C8	C14	C15	C16	-150.8(4)
C9	C8	C14	C13	36.3(5)
C9	C8	C14	C15	154.1(4)
C9	C8	C14	C30	-86.2(4)
C9	C11	C12	C13	-26.2(5)
C10	C1	C2	C3	-57.5(5)
C10	C5	C6	C7	-63.2(4)
C10	C9	C11	C12	177.5(3)
C11	C9	C10	C1	36.9(5)
C11	C9	C10	C5	154.9(3)
C11	C9	C10	C19	-81.8(4)
C11	C12	C13	C14	54.4(4)
C11	C12	C13	C17	165.5(3)
C11	C12	C13	C18	-67.3(4)
C12	C13	C14	C8	-59.8(4)
C12	C13	C14	C15	171.8(3)
C12	C13	C14	C30	58.6(4)
C12	C13	C17	C16	-165.2(3)
C12	C13	C17	C20	70.1(5)
C13	C14	C15	C16	-28.7(4)
C13	C17	C20	C21	-58.5(5)
C13	C17	C20	C22	-179.6(4)
C14	C8	C9	C10	176.6(4)
C14	C8	C9	C11	-6.8(6)
C14	C13	C17	C16	-48.6(4)
C14	C13	C17	C20	-173.3(4)
C14	C15	C16	O2	-124.0(4)
C14	C15	C16	C17	-1.4(4)
C15	C16	C17	C13	31.9(4)
C15	C16	C17	C20	167.6(3)
C16	O2	C23	C22	-56.8(4)

Atom	Atom	Atom	Atom	Angle/°
C16	O2	C23	C24	-178.2(3)
C16	C17	C20	C21	179.7(3)
C16	C17	C20	C22	58.6(4)
C17	C13	C14	C8	176.2(3)
C17	C13	C14	C15	47.7(4)
C17	C13	C14	C30	-65.4(4)
C17	C20	C22	O3	-174.9(3)
C17	C20	C22	C23	-55.6(4)
C18	C13	C14	C8	59.5(4)
C18	C13	C14	C15	-69.0(4)
C18	C13	C14	C30	177.9(3)
C18	C13	C17	C16	69.0(4)
C18	C13	C17	C20	-55.7(5)
C20	C22	C23	O2	56.0(4)
C20	C22	C23	C24	174.0(3)
C21	C20	C22	O3	61.7(4)
C21	C20	C22	C23	-178.9(3)
C22	O3	C31	O4	2.1(6)
C22	O3	C31	C32	-178.6(3)
C22	C23	C24	C25	92.6(5)
C23	O2	C16	C15	-175.3(3)
C23	O2	C16	C17	64.8(4)
C23	C24	C25	C26	-0.3(7)
C23	C24	C25	C27	-177.1(4)
C28	C4	C5	C6	-62.7(5)
C28	C4	C5	C10	167.1(4)
C29	C4	C5	C6	57.2(5)
C29	C4	C5	C10	-72.9(5)
C30	C14	C15	C16	89.4(4)
C31	O3	C22	C20	-119.1(4)
C31	O3	C22	C23	116.3(4)
O5	C35	C36	C37	-176.2(3)
O5	C35	C36	C60	67.3(4)
O5	C35	C36	C61	-49.6(4)
O6	C48	C49	C45	153.5(3)
O6	C48	C49	C52	-70.9(4)
O6	C55	C56	C57	-144.1(4)
O7	C54	C55	O6	171.2(3)
O7	C54	C55	C56	-70.4(4)
C33	C34	C35	O5	-178.7(3)
C33	C34	C35	C36	59.6(5)
C34	C33	C42	C37	53.0(4)
C34	C33	C42	C41	170.8(3)
C34	C33	C42	C51	-72.2(4)
C34	C35	C36	C37	-52.9(4)
C34	C35	C36	C60	-169.4(3)
C34	C35	C36	C61	73.7(4)
C35	C36	C37	C38	178.8(3)
C35	C36	C37	C42	49.5(4)
C36	C37	C38	C39	164.2(3)
C36	C37	C42	C33	-50.0(4)
C36	C37	C42	C41	-170.2(3)
C36	C37	C42	C51	71.7(4)

Atom	Atom	Atom	Atom	Angle/°
C37	C38	C39	C40	35.0(5)
C38	C37	C42	C33	178.7(3)
C38	C37	C42	C41	58.5(4)
C38	C37	C42	C51	-59.6(4)
C38	C39	C40	C41	-6.1(6)
C38	C39	C40	C46	-179.5(4)
C39	C40	C41	C42	4.6(6)
C39	C40	C41	C43	-179.9(4)
C39	C40	C46	C45	-148.1(3)
C39	C40	C46	C47	-31.2(5)
C39	C40	C46	C62	88.1(4)
C40	C41	C42	C33	-148.7(4)
C40	C41	C42	C37	-30.6(5)
C40	C41	C42	C51	92.8(4)
C40	C41	C43	C44	-1.6(6)
C40	C46	C47	C48	-151.0(4)
C41	C40	C46	C45	38.3(5)
C41	C40	C46	C47	155.2(4)
C41	C40	C46	C62	-85.5(4)
C41	C43	C44	C45	-23.6(5)
C42	C33	C34	C35	-59.6(5)
C42	C37	C38	C39	-62.5(4)
C42	C41	C43	C44	174.2(3)
C43	C41	C42	C33	35.5(5)
C43	C41	C42	C37	153.6(3)
C43	C41	C42	C51	-83.0(4)
C43	C44	C45	C46	54.0(4)
C43	C44	C45	C49	165.5(3)
C43	C44	C45	C50	-68.0(4)
C44	C45	C46	C40	-61.8(4)
C44	C45	C46	C47	170.9(3)
C44	C45	C46	C62	57.6(4)
C44	C45	C49	C48	-163.5(3)
C44	C45	C49	C52	71.5(5)
C45	C46	C47	C48	-30.0(4)
C45	C49	C52	C53	-57.1(5)
C45	C49	C52	C54	-176.8(3)
C46	C40	C41	C42	177.8(4)
C46	C40	C41	C43	-6.7(6)
C46	C45	C49	C48	-46.8(4)
C46	C45	C49	C52	-171.9(4)
C46	C47	C48	O6	-120.5(3)
C46	C47	C48	C49	1.1(4)
C47	C48	C49	C45	29.2(4)
C47	C48	C49	C52	164.9(3)
C48	O6	C55	C54	-51.9(4)
C48	O6	C55	C56	-171.8(3)
C48	C49	C52	C53	-179.3(3)
C48	C49	C52	C54	60.9(4)
C49	C45	C46	C40	175.0(3)
C49	C45	C46	C47	47.6(4)
C49	C45	C46	C62	-65.6(4)
C49	C52	C54	O7	-171.7(3)

Atom	Atom	Atom	Atom	Angle/°
C49	C52	C54	C55	-52.1(4)
C50	C45	C46	C40	58.2(4)
C50	C45	C46	C47	-69.1(4)
C50	C45	C46	C62	177.6(3)
C50	C45	C49	C48	71.0(4)
C50	C45	C49	C52	-54.1(5)
C52	C54	C55	O6	49.6(5)
C52	C54	C55	C56	168.0(3)
C53	C52	C54	O7	66.2(4)
C53	C52	C54	C55	-174.2(3)
C54	O7	C63	O8	2.2(6)
C54	O7	C63	C64	-178.1(3)
C54	C55	C56	C57	94.2(5)
C55	O6	C48	C47	-176.4(3)
C55	O6	C48	C49	63.4(4)
C55	C56	C57	C58	3.4(7)
C55	C56	C57	C59	-176.0(4)
C60	C36	C37	C38	-66.2(4)
C60	C36	C37	C42	164.5(3)
C61	C36	C37	C38	54.4(5)
C61	C36	C37	C42	-74.9(4)
C62	C46	C47	C48	89.2(4)
C63	O7	C54	C52	-117.5(4)
C63	O7	C54	C55	117.1(4)

Table 13: Hydrogen Fractional Atomic Coordinates ($\times 10^4$) and Equivalent Isotropic Displacement Parameters ($Å^2 \times 10^3$) for compound **(4)**. U_{eq} is defined as 1/3 of the trace of the orthogonalised U_{ij}.

Atom	x	y	z	U_{eq}
H1	2850(70)	5300(30)	-910(30)	41(15)
H1A	7750.99	5618.94	882.56	27
H1B	6178.58	5255.28	1178.56	27
H2A	5967.68	6015.17	-204.66	31
H2B	5826.94	5240.96	-178.43	31
H3	3277.74	5312.41	360.36	29
H5	3807.98	5933.36	1595.71	24
H6A	4282.44	7294.68	1631.98	30
H6B	2508.56	6959.47	1746.84	30
H7A	4519.69	7203.73	2929.53	32
H7B	3566.88	6519.43	2890.15	32
H11A	9413.91	6047.02	2111.05	27
H11B	8431.98	5380.19	2185.31	27
H12A	9076.71	5347.1	3463.09	27
H12B	10656.93	5776.89	3280.91	27
H15A	6383.09	7266.42	4040.16	29
H15B	5415.76	6716.88	4470.36	29
H16	8660.81	7193.76	4917.8	25
H17	8647.59	5820.05	4753.09	23
H18A	10834.47	6946.03	3623.99	38
H18B	9108.39	7315.57	3735.66	38
H18C	9316.57	6993.77	2919.04	38

Atom	x	y	z	U_{eq}
H19A	8280.44	6822.54	1247.38	41
H19B	6579.34	7242.89	1237.59	41
H19C	6883.2	6830	491.87	41
H20	11406.89	6708.31	5098.92	24
H21A	11689.41	5327.97	4985.17	42
H21B	13229.71	5802.16	5298.84	42
H21C	12406.07	5829.77	4408.74	42
H22	9999.05	5716.7	5992.88	24
H23	9626.5	7100.97	6221.71	26
H24	7695.49	6190.63	6962.34	27
H26A	11783.8	6939.12	8063.11	36
H26B	10484.97	7525.85	8120.34	36
H26C	11032.1	7331.85	7300.85	36
H27A	7686.36	6189.14	8260.1	44
H27B	8413.03	6831.66	8702.43	44
H27C	9602.42	6205.25	8693.72	44
H28A	574.38	6128.29	88.86	50
H28B	819.87	6626.54	798.74	50
H28C	1112.64	5867.24	951.81	50
H29A	4469.53	6947.37	-105.09	45
H29B	3031.56	7296.67	308.12	45
H29C	2507.5	6888.96	-468.71	45
H30A	4808.41	5682.02	3713.32	33
H30B	6282.41	5619.99	4435.19	33
H30C	6546.49	5314.82	3616.51	33
H32A	14647	6251.6	7313.31	39
H32B	14815.19	5506.43	7567.78	39
H32C	13729.8	5996.12	8017.94	39
H5A	9580(100)	4700(40)	6760(40)	90(30)
H33A	9472.54	3824.13	4311.83	27
H33B	8498.9	4488.46	4431.06	27
H34A	9576.51	3579.35	5647.06	29
H34B	10484.5	4261.93	5541.47	29
H35	7995.53	4816.72	5754.97	24
H37	5503.13	4430.32	4805.79	21
H38A	4103.54	3168.61	4908.91	29
H38B	3208.54	3807.86	5186.18	29
H39A	2319.44	3420.04	3834.14	28
H39B	2519.65	4182.46	3977.98	28
H43A	8060.94	4208.1	3121.67	24
H43B	8072.32	3437.16	3067.47	24
H44A	6531.25	4321.26	1979.17	25
H44B	7294.98	3620.2	1832.43	25
H47A	1586.5	3277.3	2536.12	27
H47B	965.29	4012.07	2354.44	27
H48	1657.75	3097.14	1291.85	24
H49	3691.31	4216.73	1180.92	21
H50A	5421.75	2645.32	1749.12	35
H50B	3707.97	2675.62	2138.62	35
H50C	5518.58	2765.06	2660.62	35
H51A	7831.57	2787.96	4122.28	42
H51B	6136.58	2722.24	4521.15	42
H51C	7927.24	2860.37	5040.73	42

Atom	x	y	z	U_{eq}
H52	3688.57	2982.21	440.57	25
H53A	5942.19	4052.72	272.31	41
H53B	5703.03	3453.37	-315.2	41
H53C	6542.26	3342.83	563.1	41
H54	2869.54	4273.56	-132.43	23
H55	241.72	3321.43	16.82	25
H56	-411.13	4671.78	-179.06	27
H58A	-1204.12	3493.47	-1910.19	46
H58B	-2908.85	3398.01	-1525.39	46
H58C	-1121.66	3149.42	-1083.53	46
H59A	-3584.96	4599.75	-1510.85	47
H59B	-2021.2	4710.2	-1987.87	47
H59C	-2082.36	5088.36	-1191.01	47
H60A	5697.49	4560.34	6791.17	42
H60B	4084.45	4302.48	6218.99	42
H60C	5150.76	4909.81	5975.72	42
H61A	7276.89	3097	6104.73	41
H61B	5342.35	3192.25	6252.46	41
H61C	6864.75	3472.91	6859.96	41
H62A	3024.44	4865.35	2893.98	32
H62B	2923.18	4783.25	1976.45	32
H62C	4736.82	4847.16	2502.59	32
H64A	2371.2	3096.88	-2125.73	45
H64B	3651	3598.28	-2444.54	45
H64C	1648.74	3745.99	-2554.13	45

Table 14: Hydrogen bond information for compound **(4)**.

D	H	A	d(D-H)/Å	d(H-A)/Å	d(D-A)/Å	D-H-A/deg
O1	H1	O8	0.91(6)	1.95(6)	2.858(4)	175(5)
O5	H5A	O4	0.88(8)	2.02(8)	2.876(4)	162(7)

Compound (5) Crystal Data and Experimental

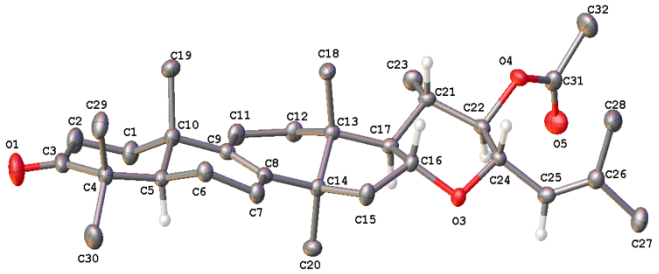

Experimental. Single colourless plate crystals of compound **(5)** recrystallised from acetonitrile by slow evaporation. A suitable crystal with dimensions 0.28 × 0.24 × 0.06 mm^3 was selected and mounted on a mylar loop in oil on a Bruker APEX II area detector diffractometer. The crystal was kept at a steady T = 110(2) K during data collection. The structure was solved with the **XT** 2018/2 (Sheldrick, 2015) solution program using Intrinsic Phasing methods and by using Olex2 (Dolomanov et al., 2009) as the graphical interface. The model was refined with **XL** (Sheldrick, 2015) using full matrix least squares minimisation on $\boldsymbol{F^2}$.

Crystal Data. $C_{32}H_{48}O_4$, M_r = 496.70, orthorhombic, $P2_12_12_1$ (No. 19), a = 8.0284(2) Å, b = 10.6283(3) Å, c = 32.8305(9) Å, α = β = γ = 90°, V = 2801.37(13) Å^3, T = 110(2) K, Z = 4, Z' = 1, μ(CuK$_\alpha$) = 0.589, 51100 reflections measured, 5125 unique (R_{int} = 0.0369) which were used in all calculations. The final wR_2 was 0.0725 (all data) and R_1 was 0.0281 (I≥2 σ(I)).

Compound (5)	R_1= 2.81 %
Formula	$C_{32}H_{48}O_4$
$D_{calc.}$/ g cm^{-3}	1.178
μ/mm^{-1}	0.589
Formula Weight	496.70
Colour	colourless
Shape	plate
Size/mm^3	0.28×0.24×0.06
T/K	110(2)
Crystal System	orthorhombic
Flack Parameter	0.03(5)
Hooft Parameter	0.04(4)
Space Group	$P2_12_12_1$
a/Å	8.0284(2)
b/Å	10.6283(3)
c/Å	32.8305(9)
α/°	90
β/°	90
γ/°	90
V/Å^3	2801.37(13)
Z	4
Z'	1
Wavelength/Å	1.54178
Radiation type	CuK$_\alpha$
Θ_{min}/°	2.692
Θ_{max}/°	68.209
Measured Refl's.	51100
Indep't Refl's	5125
Refl's I≥2 σ(I)	4993
R_{int}	0.0369
Parameters	335
Restraints	0
Largest Peak	0.165
Deepest Hole	-0.137
GooF	1.040
wR_2 (all data)	0.0725
wR_2	0.0718
R_1 (all data)	0.0290
R_1	0.0281

Structure Quality Indicators

Reflections:	d min (Cu\a) 2θ=136.4°	0.83	I/σ(I)	60.8	Rint	3.69%	Full 135.4°	100
Refinement:	Shift	-0.001	Max Peak	0.2	Min Peak	-0.1	GooF	1.040	Flack	.03(5)

A colourless plate-shaped crystal with dimensions 0.28 × 0.24 × 0.06 mm^3 was mounted on a mylar loop in oil. Data were collected using a Bruker APEX II area detector diffractometer equipped with an Oxford Cryosystems low-temperature device operating at T = 110(2) K.

Data were measured using ϕ and ω scans of 1.0 ° per frame for 10 s using CuK$_\alpha$ radiation (microfocus sealed X-ray tube, 45 kV, 0.60 mA). The total number of runs and images was based on the strategy calculation from the program APEX3. The maximum resolution that was achieved was Θ = 68.209° (0.83 Å).

The unit cell was refined using SAINT (Bruker, V8.40B, after 2013) on 9123 reflections, 18% of the observed reflections. Data reduction, scaling and absorption corrections were performed using SAINT (Bruker, V8.40B, after 2013). The final completeness is 100.00 % out to 68.209° in Θ.

A multi-scan absorption correction was performed using SADABS-2016/2 (Bruker, 2016/2) was used for absorption correction. wR_2(int) was 0.0906 before and 0.0516 after correction. The ratio of minimum to maximum transmission is 0.8607. The $\lambda/2$ correction factor is not present. The absorption coefficient μ of this material is 0.589 mm^{-1} at this wavelength (λ = 1.54178Å) and the minimum and maximum transmissions are 0.831 and 0.965.

The structure was solved and the space group $P2_12_12_1$ (# 19) determined by the **XT** 2018/2 (Sheldrick, 2015) structure solution program using Intrinsic Phasing methods and refined by full matrix least squares minimisation on F^2 using version 2018/3 of **XL** (Sheldrick, 2015). All non-hydrogen atoms were refined anisotropically. Hydrogen atom positions were calculated geometrically and refined using the riding model.

The absolute configuration was determined on the basis of the refined Flack parameter value, 0.03(5). C5, C10, C13, C14, C16, C17, C21, C22, and C24 were assigned configurations of R, S, R, S, R, R, S, R, and S, respectively. Determination of absolute structure using Bayesian statistics on Bijvoet differences using the Olex2 results in 0.04(4). Note: The Flack parameter is used to determine chirality of the crystal studied, the value should be near 0, a value of 1 means that the stereochemistry is wrong and the model should be inverted. A value of 0.5 means that the crystal consists of a racemic mixture of the two enantiomers.

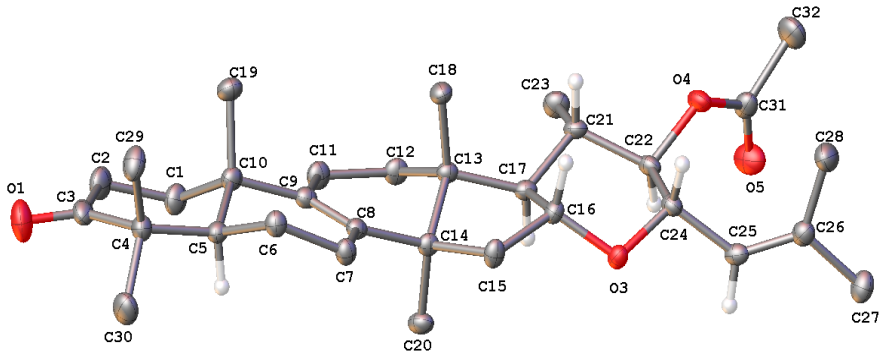

Figure 3: ORTEP-style image of compound **(5)**, with most hydrogen atoms removed, for clarity.

Table 15: Fractional atomic coordinates ($\times 10^4$) and equivalent isotropic displacement parameters ($Å^2 \times 10^3$) for compound **(5)**. U_{eq} is defined as 1/3 of the trace of the orthogonalised U_{ij}.

Atom	x	y	z	U_{eq}
O1	7721(2)	5637.3(14)	4649.5(4)	39.0(4)
O3	3937.5(14)	4951.2(11)	7990.8(3)	18.1(2)
O4	-316.4(14)	5921.3(11)	8248.7(4)	21.7(3)
O5	-144.5(17)	7553.6(13)	8686.4(4)	33.6(3)
C20	6253(2)	6624.2(17)	7067.2(5)	22.1(4)
C1	5530(2)	6963.0(17)	5529.2(5)	24.9(4)
C2	5887(3)	6736.6(18)	5077.8(5)	28.9(4)
C3	7041(2)	5667.6(17)	4979.9(5)	23.8(4)
C4	7307(2)	4584.2(16)	5283.6(5)	21.5(4)
C5	6673(2)	4887.9(15)	5722.4(5)	17.7(3)
C6	6472(2)	3716.0(15)	5986.7(5)	19.6(3)
C7	6346(2)	4086.8(15)	6433.9(5)	20.0(3)
C8	5332(2)	5255.8(14)	6508.4(5)	16.6(3)
C9	4809(2)	6024.9(15)	6211.4(5)	17.7(3)
C10	5119(2)	5742.6(15)	5758.5(5)	18.8(3)
C11	3792(2)	7210.4(16)	6297.9(5)	22.2(4)
C12	3033(2)	7357.1(16)	6730.3(5)	20.8(4)
C13	3109(2)	6121.0(14)	6964.4(5)	16.2(3)
C14	4948(2)	5625.1(14)	6946.0(5)	16.4(3)
C15	4996(2)	4594.5(15)	7283.4(5)	20.5(3)
C16	3533(2)	4908.3(15)	7566.6(4)	17.0(3)
C17	2829(2)	6169.1(15)	7428.4(5)	16.5(3)
C18	1879(2)	5185.5(16)	6768.6(5)	21.2(3)
C19	3511(2)	5160.4(18)	5586.2(5)	25.4(4)
C21	1105(2)	6321.7(15)	7619.3(5)	18.2(3)
C23	274(2)	7578.8(17)	7529.3(6)	24.9(4)
C22	1332(2)	6158.0(15)	8080.0(5)	18.0(3)
C24	2406(2)	5024.5(16)	8216.0(5)	17.5(3)
C25	2846(2)	5167.4(15)	8656.9(5)	18.7(3)
C26	2073(2)	4652.7(16)	8974.4(5)	21.0(4)
C27	2550(2)	5044.2(18)	9399.2(5)	26.3(4)
C28	664(2)	3726.9(19)	8948.4(6)	32.0(4)
C29	6479(3)	3414.1(17)	5093.1(5)	28.9(4)
C30	9194(2)	4353(2)	5306.3(6)	32.5(4)
C31	-892(2)	6679.3(17)	8546.8(5)	23.5(4)
C32	-2606(2)	6275(2)	8674.3(6)	36.5(5)

Table 16: Anisotropic displacement parameters ($\times 10^4$) for compound **(5)**. The anisotropic displacement factor exponent takes the form: $-2\pi^2[h^2a^{*2} \times U_{11} + \ldots + 2hka^* \times b^* \times U_{12}]$

Atom	U_{11}	U_{22}	U_{33}	U_{23}	U_{13}	U_{12}
O1	49.3(9)	40.6(8)	26.9(7)	8.6(6)	14.5(6)	3.4(7)
O3	16.5(6)	22.4(5)	15.3(5)	-1.4(5)	0.5(4)	4.0(5)
O4	13.6(5)	29.0(6)	22.6(6)	-5.2(5)	2.5(5)	-0.9(5)
O5	28.6(7)	36.3(7)	35.8(7)	-15.0(6)	4.7(6)	2.8(6)
C20	15.0(8)	26.8(8)	24.6(8)	-4.8(7)	-1.5(7)	0.8(7)
C1	31.8(10)	21.8(8)	21.1(9)	4.9(7)	0.3(7)	2.2(7)

Atom	U_{11}	U_{22}	U_{33}	U_{23}	U_{13}	U_{12}
C2	35.6(10)	28.6(9)	22.4(9)	9.4(7)	0.2(8)	0.4(8)
C3	25.0(9)	26.7(9)	19.8(8)	2.2(7)	1.0(7)	-9.2(7)
C4	22.1(9)	24.2(9)	18.0(8)	1.4(7)	1.5(7)	-1.3(7)
C5	16.9(8)	19.6(8)	16.8(7)	0.3(6)	-0.8(6)	-1.9(6)
C6	21.6(8)	17.6(8)	19.8(8)	0.6(6)	1.7(7)	2.4(7)
C7	21.1(8)	20.4(8)	18.6(8)	2.7(6)	1.5(6)	3.7(7)
C8	14.5(7)	16.5(7)	18.9(8)	1.5(6)	-0.4(6)	-1.4(6)
C9	15.3(7)	17.4(7)	20.4(8)	1.4(6)	-1.0(6)	-1.0(6)
C10	18.9(8)	19.0(8)	18.6(7)	2.7(6)	-1.7(6)	0.6(7)
C11	25.0(9)	19.3(8)	22.3(8)	5.0(6)	-0.7(7)	4.1(7)
C12	21.2(9)	18.4(8)	22.9(8)	2.5(6)	-1.3(7)	6.2(7)
C13	14.8(8)	15.3(7)	18.5(8)	0.6(6)	-1.5(6)	0.6(6)
C14	16.5(8)	14.6(7)	18.0(7)	1.5(6)	-1.1(6)	2.5(6)
C15	23.6(9)	20.2(8)	17.6(8)	2.2(6)	1.2(7)	7.7(7)
C16	19.3(8)	17.3(7)	14.5(7)	-0.3(6)	-0.8(6)	1.0(6)
C17	14.4(8)	15.4(7)	19.7(8)	-1.2(6)	-2.4(6)	0.1(6)
C18	19.0(8)	26.0(9)	18.5(7)	-2.3(7)	-1.8(6)	-3.6(7)
C19	19.7(9)	32.7(9)	23.8(8)	0.2(7)	-4.9(7)	0.3(7)
C21	13.6(8)	20.2(8)	20.8(8)	-3.2(6)	-2.2(6)	-0.2(6)
C23	20.2(9)	26.7(9)	27.7(9)	-0.8(7)	-0.2(7)	6.4(7)
C22	12.4(8)	20.8(8)	20.8(8)	-3.8(6)	2.3(6)	-0.5(6)
C24	14.8(8)	19.2(8)	18.4(7)	-2.3(6)	1.8(6)	-1.4(6)
C25	15.6(8)	19.6(8)	21.1(8)	-5.8(6)	-1.3(6)	1.9(6)
C26	19.0(8)	23.9(8)	19.9(8)	-2.2(7)	0.5(7)	3.4(7)
C27	33.7(10)	25.6(9)	19.7(8)	-3.0(7)	1.7(7)	4.0(8)
C28	29.5(10)	40.9(11)	25.7(9)	5.8(8)	0.1(8)	-8.5(9)
C29	43.1(11)	24.4(9)	19.1(8)	-2.4(7)	2.3(8)	-1.8(8)
C30	25.5(10)	44.2(11)	27.7(9)	0.9(8)	6.6(8)	6.6(9)
C31	18.4(8)	31.3(9)	20.9(8)	-1.6(7)	0.8(7)	7.2(8)
C32	22.9(10)	51.7(13)	34.9(10)	-2.8(9)	9.2(8)	4.1(9)

Table 17: Bond lengths in Å for compound **(5).**

Atom	Atom	Length/Å
O1	C3	1.215(2)
O3	C16	1.4310(18)
O3	C24	1.4369(19)
O4	C22	1.457(2)
O4	C31	1.349(2)
O5	C31	1.197(2)
C20	C14	1.544(2)
C1	C2	1.529(2)
C1	C10	1.536(2)
C2	C3	1.501(3)
C3	C4	1.538(2)
C4	C5	1.562(2)
C4	C29	1.543(2)
C4	C30	1.536(3)
C5	C6	1.527(2)
C5	C10	1.548(2)
C6	C7	1.524(2)
C7	C8	1.506(2)
C8	C9	1.340(2)
C8	C14	1.521(2)
C9	C10	1.537(2)
C9	C11	1.528(2)
C10	C19	1.539(2)
C11	C12	1.553(2)
C12	C13	1.523(2)
C13	C14	1.569(2)
C13	C17	1.541(2)
C13	C18	1.542(2)
C14	C15	1.558(2)
C15	C16	1.534(2)
C16	C17	1.523(2)
C17	C21	1.528(2)
C21	C23	1.522(2)
C21	C22	1.533(2)
C22	C24	1.547(2)
C24	C25	1.498(2)

Atom	Atom	Length/Å
C25	C26	1.331(2)
C26	C27	1.505(2)
C26	C28	1.502(3)
C31	C32	1.501(3)

Table 18: Bond Angles in ° for compound **(5).**

Atom	Atom	Atom	Angle/°
C16	O3	C24	107.94(11)
C31	O4	C22	118.94(13)
C2	C1	C10	112.49(14)
C3	C2	C1	116.25(15)
O1	C3	C2	119.24(16)
O1	C3	C4	119.77(17)
C2	C3	C4	120.92(15)
C3	C4	C5	113.44(14)
C3	C4	C29	106.31(14)
C29	C4	C5	113.58(14)
C30	C4	C3	106.74(15)
C30	C4	C5	108.06(14)
C30	C4	C29	108.41(16)
C6	C5	C4	112.96(13)
C6	C5	C10	110.51(13)
C10	C5	C4	117.06(13)
C7	C6	C5	110.11(13)
C8	C7	C6	113.94(13)
C7	C8	C14	118.42(13)
C9	C8	C7	123.70(14)
C9	C8	C14	117.80(14)
C8	C9	C10	122.30(15)
C8	C9	C11	122.36(15)
C11	C9	C10	115.28(13)
C1	C10	C5	106.53(13)
C1	C10	C9	110.12(13)
C1	C10	C19	109.89(14)
C9	C10	C5	108.59(12)
C9	C10	C19	107.37(13)
C19	C10	C5	114.32(14)
C9	C11	C12	117.55(13)
C13	C12	C11	111.04(13)
C12	C13	C14	107.94(13)
C12	C13	C17	117.68(13)
C12	C13	C18	108.67(13)
C17	C13	C14	100.74(12)
C17	C13	C18	109.91(13)
C18	C13	C14	111.71(13)
C20	C14	C13	113.43(13)
C20	C14	C15	106.47(13)
C8	C14	C20	106.46(13)
C8	C14	C13	108.30(13)
C8	C14	C15	119.02(13)
C15	C14	C13	103.41(13)
C16	C15	C14	105.01(13)
O3	C16	C15	115.01(13)
O3	C16	C17	110.24(12)
C17	C16	C15	107.13(13)
C16	C17	C13	102.20(12)
C16	C17	C21	107.89(13)
C21	C17	C13	122.75(13)
C17	C21	C22	106.54(13)
C23	C21	C17	114.25(14)
C23	C21	C22	110.07(14)
O4	C22	C21	106.66(13)
O4	C22	C24	105.18(13)
C21	C22	C24	116.06(13)
O3	C24	C22	111.74(13)
O3	C24	C25	107.51(13)
C25	C24	C22	109.35(13)
C26	C25	C24	127.26(15)
C25	C26	C27	119.55(16)
C25	C26	C28	125.18(16)
C28	C26	C27	115.20(15)
O4	C31	C32	110.19(16)
O5	C31	O4	124.70(17)
O5	C31	C32	125.10(17)

Table 19: Torsion angles in ° for compound **(5)**.

Atom	Atom	Atom	Atom	Angle/°
O1	C3	C4	C5	167.76(16)
O1	C3	C4	C29	-66.7(2)
O1	C3	C4	C30	48.9(2)
O3	C16	C17	C13	159.20(12)
O3	C16	C17	C21	-70.16(15)
O3	C24	C25	C26	-141.94(17)
O4	C22	C24	O3	165.24(12)
O4	C22	C24	C25	-75.85(15)

Atom	Atom	Atom	Atom	Angle/°
C20	C14	C15	C16	98.72(15)
C1	C2	C3	O1	-160.60(18)
C1	C2	C3	C4	22.3(3)
C2	C1	C10	C5	61.22(18)
C2	C1	C10	C9	178.79(15)
C2	C1	C10	C19	-63.13(19)
C2	C3	C4	C5	-15.2(2)
C2	C3	C4	C29	110.37(19)
C2	C3	C4	C30	-134.06(18)
C3	C4	C5	C6	163.39(14)
C3	C4	C5	C10	33.3(2)
C4	C5	C6	C7	163.70(14)
C4	C5	C10	C1	-56.02(18)
C4	C5	C10	C9	-174.60(13)
C4	C5	C10	C19	65.56(19)
C5	C6	C7	C8	39.36(19)
C6	C5	C10	C1	172.78(13)
C6	C5	C10	C9	54.20(17)
C6	C5	C10	C19	-65.65(17)
C6	C7	C8	C9	-10.4(2)
C6	C7	C8	C14	172.76(14)
C7	C8	C9	C10	3.5(3)
C7	C8	C9	C11	-179.50(15)
C7	C8	C14	C20	97.32(16)
C7	C8	C14	C13	-140.39(14)
C7	C8	C14	C15	-22.8(2)
C8	C9	C10	C1	-141.46(17)
C8	C9	C10	C5	-25.2(2)
C8	C9	C10	C19	98.92(18)
C8	C9	C11	C12	-13.4(2)
C8	C14	C15	C16	-141.16(14)
C9	C8	C14	C20	-79.68(18)
C9	C8	C14	C13	42.61(19)
C9	C8	C14	C15	160.19(15)
C9	C11	C12	C13	-13.4(2)
C10	C1	C2	C3	-46.5(2)
C10	C5	C6	C7	-62.98(17)
C10	C9	C11	C12	163.79(14)
C11	C9	C10	C1	41.36(19)
C11	C9	C10	C5	157.65(14)
C11	C9	C10	C19	-78.26(17)
C11	C12	C13	C14	51.80(17)
C11	C12	C13	C17	164.82(14)
C11	C12	C13	C18	-69.52(18)
C12	C13	C14	C20	50.23(17)
C12	C13	C14	C8	-67.71(15)
C12	C13	C14	C15	165.13(13)
C12	C13	C17	C16	-162.53(14)
C12	C13	C17	C21	76.6(2)
C13	C14	C15	C16	-21.07(16)
C13	C17	C21	C23	-65.25(19)
C13	C17	C21	C22	172.99(13)
C14	C8	C9	C10	-179.65(14)

Atom	Atom	Atom	Atom	Angle/°
C14	C8	C9	C11	-2.7(2)
C14	C13	C17	C16	-45.56(14)
C14	C13	C17	C21	-166.40(14)
C14	C15	C16	O3	-130.26(14)
C14	C15	C16	C17	-7.35(17)
C15	C16	C17	C13	33.39(16)
C15	C16	C17	C21	164.02(13)
C16	O3	C24	C22	-55.80(16)
C16	O3	C24	C25	-175.79(13)
C16	C17	C21	C23	176.62(13)
C16	C17	C21	C22	54.86(16)
C17	C13	C14	C20	-73.71(15)
C17	C13	C14	C8	168.35(12)
C17	C13	C14	C15	41.18(14)
C17	C21	C22	O4	-163.17(12)
C17	C21	C22	C24	-46.39(18)
C18	C13	C14	C20	169.64(13)
C18	C13	C14	C8	51.70(17)
C18	C13	C14	C15	-75.47(16)
C18	C13	C17	C16	72.41(15)
C18	C13	C17	C21	-48.43(19)
C21	C22	C24	O3	47.64(18)
C21	C22	C24	C25	166.55(14)
C23	C21	C22	O4	72.45(16)
C23	C21	C22	C24	-170.76(14)
C22	O4	C31	O5	0.3(3)
C22	O4	C31	C32	179.72(14)
C22	C24	C25	C26	96.6(2)
C24	O3	C16	C15	-169.67(13)
C24	O3	C16	C17	69.11(16)
C24	C25	C26	C27	-171.68(16)
C24	C25	C26	C28	5.3(3)
C29	C4	C5	C6	41.8(2)
C29	C4	C5	C10	-88.22(18)
C30	C4	C5	C6	-78.47(18)
C30	C4	C5	C10	151.46(16)
C31	O4	C22	C21	-123.96(15)
C31	O4	C22	C24	112.24(15)

Table 20: Hydrogen fractional atomic coordinates ($\times 10^4$) and equivalent isotropic displacement parameters ($Å^2 \times 10^3$) for compound **(5)**. U_{eq} is defined as 1/3 of the trace of the orthogonalised U_{ij}.

Atom	x	y	z	U_{eq}
H20A	7372.64	6266.48	7041.18	33
H20B	6064.44	6884.24	7349.85	33
H20C	6149.19	7356.23	6887.43	33
H1A	4582.14	7552.98	5555.19	30
H1B	6515.41	7362.26	5656.52	30
H2A	4813.76	6582.29	4937.91	35
H2B	6365.32	7517.17	4962.05	35
H5	7594.83	5376.68	5852.34	21

Atom	x	y	z	U_{eq}
H6A	5455.27	3254.61	5904.47	24
H6B	7440.28	3152.17	5946.83	24
H7A	5842.76	3381.04	6587.44	24
H7B	7483.54	4221.19	6542.09	24
H11A	2869.48	7245.2	6098.26	27
H11B	4515.48	7947.83	6246.22	27
H12A	3652.8	8012.15	6881.85	25
H12B	1858.85	7632.83	6706.85	25
H15A	4858.77	3746.34	7163.37	25
H15B	6063.77	4623.25	7433.81	25
H16	2652.38	4254.22	7526.62	20
H17	3561.69	6845.68	7541.22	20
H18A	736.93	5420.65	6841.16	32
H18B	2112.99	4334.48	6868.26	32
H18C	2006.25	5206.6	6471.75	32
H19A	2580.1	5741.81	5629.04	38
H19B	3280.84	4364.35	5725.95	38
H19C	3648.82	5004.11	5293.96	38
H21	369.26	5631.85	7516.71	22
H23A	1018.85	8265.24	7610.08	37
H23B	-769.95	7639.95	7682.78	37
H23C	37.59	7640.28	7237.12	37
H22	1796.18	6949.77	8199.18	22
H24	1759.65	4229.22	8176.88	21
H25	3780.91	5683.08	8716.58	22
H27A	3553.75	5568.29	9388.45	39
H27B	2771.52	4294.13	9564.16	39
H27C	1637.02	5525.18	9521.56	39
H28A	-341.39	4098.61	9067.64	48
H28B	958.95	2961.34	9098.36	48
H28C	454.14	3516.42	8662.37	48
H29A	5270.53	3537.76	5082.26	43
H29B	6732.34	2672.38	5259.28	43
H29C	6909.12	3288.74	4816.65	43
H30A	9612.77	4128.27	5035.57	49
H30B	9420.57	3664.86	5496.97	49
H30C	9751.89	5119.66	5400.87	49
H32A	-3149.93	5836.02	8447.91	55
H32B	-3263.58	7016.75	8749.13	55
H32C	-2524.26	5708.39	8908.88	55

Citations of crystal data

O.V. Dolomanov and L.J. Bourhis and R.J. Gildea and J.A.K. Howard and H. Puschmann, Olex2: A complete structure solution, refinement and analysis program, *J. Appl. Cryst.*, (2009), **42**, 339-341.

Parsons, S., Flack, H.D., and Wagner, T., *Acta Cryst*., (2013), **B69** 249-259

Sheldrick, G.M., XT, *Acta Cryst.*, (2015), **A71**, 3-8.

Sheldrick, G.M., XL, *Acta Cryst.*, (2015), **C71**, 3-8.

Software for the Integration of CCD Detector System Bruker Analytical X-ray Systems, Bruker AXS., Madison, WI (after 2013).

Chapter 5: Discussion

5.1. Overview of *Echinodontium tinctorium*

Echinodontium tinctorium (E. tinctorium) is a wood-decaying fungus from the western US and Canada that colonizes aged and decayed trees. It is found growing as a hoof-shaped conk on trees, mostly hemlocks (Ye *et al.,* 1996). Like many other North American mushrooms, *E. tinctorium* has not been explored much for its bioactivities and bioactive compounds. At the outset of this research, only two small molecules, echinotinctone and echinodol (Ye *et al*., 1996), and one polysaccharide (AIPetinc, Javed *et al*., 2019) had been isolated from *E. tinctorium*. AIPetinc was isolated from the alkali extracts of *E. tinctorium* (Javed *et al*., 2019). Echinotinctone and echinodol had never been reported to have any bioactivity, whereas AIPetinc is a large polysaccharide isolated from alkali extracts, and has anti-inflammatory activity (Javed *et al*., 2019). Due to the limited prior studies, *E. tinctorium* was therefore considered a good resource for the potential discovery of novel bioactive compounds. In addition, based on the literature review described in chapter 1, there is high potential in discovering novel compounds in mushrooms native to North America.

5.2. Overview of project

The current research carried out in this thesis was aimed at providing scientific evidence of the presence of immuno-stimulatory and growth-inhibitory compounds in *E. tinctorium*. The project was mostly based on using bioactivity-guided fractionation approach. Initially, a group of compounds were isolated from the powdered mushroom via extraction. Small molecules were then mostly obtained from the organic extracts 80% ethanol and 50% methanol, while polysaccharides were mainly extracted using water or 5% sodium hydroxide. Further separation of compounds was achieved using several purification techniques. The separation of compounds

was based on size, polarity and charge. High-resolution chromatographic techniques were then employed to achieve purity. At each step of purification, bioactivity was confirmed and bioactive fractions were subjected to the next purification steps. Once pure compounds were obtained, bioactivity was again confirmed, structure was elucidated and molecular targets for small molecules were predicted, when possible.

The hypothesis proposed at the start of the research project was tested with the help of several research objectives, sub-divided into three (Chapters 2, 3 and 4) experimental chapters.

5.3. Key findings of the biomolecules isolated from *E. tinctorium*

In chapter 2, a novel immuno-stimulatory large molecular weight polysaccharide (EtISPFa) with an estimated molecular weight of 1354 kDa was isolated from the aqueous extracts of *E. tinctorium* mushroom. EtISPFa was successfully purified using Sephadex LH-20 SEC, Sephadex DEAE AEC, Sephacryl S-500 HR SEC and HPLC BioSEC-5. Chemical characterization of EtISPFa was carried out by GC-MS for monosaccharide content and linkage analysis, FTIR for presence of functional groups and NMR for absolute configuration. EtISPFa comprises of a high abundance of glucose (66.2%) and glucuronic acid (10.1%) and a relatively lower percentage of mannose (6.7 %), galactose (6.4 %), xylose (5.6 %), and rhamnose (3.1 %), and traces of fucose (1.8 %) and arabinose (0.2 %). EtISPFa had abundant 3-linked glucose (19.8 %), 4-linked glucuronic acid (10.8 %), 6-linked glucose (10.7 %) and 3,6-linked glucose which suggested the main backbone to be of 3-linked glucose residues; NMR confirmed the linkages and final ß-configuration of EtISPFa. EtISPFa was capable of inducing the production of several cytokines. This chapter was published in early 2021 in *Carbohydrate Polymers* (Zeb *et al*., 2021).

In chapter 3, a growth-inhibitory polysaccharide EtGIPL1a with a weight average molecular weight of 275 kDa was isolated from the methanol extracts of *E. tinctorium*. EtGIPL1a was

successfully purified by multiple size exclusion and ion exchange chromatographic techniques. Structural elucidation was accomplished by GC-MS, NMR and FTIR. GC-MS revealed the monosaccharide content as well as linkages present in EtGIPL1a. The most prominent monosaccharides present in EtGIPL1a included glucose (54.3 %), galactose (19.6 %), mannose (11.1 %), fucose (10.3 %), along with small amounts of glucuronic acid (4 %) and rhamnose (0.6 %). The most abundant glycosidic linkages in EtGIPL1a were 3-linked glucose (28.9 %), 6-linked glucose (18.3 %) and galactose (3.9 %), 3,6-linked glucose (13 %) and 2, 6-linked galactose (2.6 %), 4-linked glucuronic acid (9.2 %) and glucose (1.7 %), 3-linked fucose (2.5 %) and 6-linked mannose (2.4 %). Most of the terminal sugars comprised of glucose (15.3 %), mannose (1.3 %) and fucose (0.9 %). The final *β*-configuration of EtGIPL1a was confirmed from NMR. Chemical characterization data altogether suggested that EtGIPL1a constitutes a sugar backbone of *β*-1-3-linked glucose. Biological characterization of EtGIPL1a included growth-inhibition against multiple cancer cell lines with IC_{50} ranging from 50.6-1446 nM. EtGIPL1a showed promising effects against U251 glioblastoma cells with an IC_{50} of 193 nM and was further investigated for mechanism. Flow cytometry analysis revealed that EtGIPL1a induced apoptosis in U251 glioblastoma cells and showed significant DNA fragmentation in cell cycle analysis which is considered a hallmark of apoptosis. This was further confirmed with the increased expression of apoptosis protein marker cleaved caspase-3 in U251 cells after treatment with EtGIPL1a. This paper will be submitted shortly to *Scientific Reports*.

In chapter 4, six small molecules **(1-6)** were isolated and characterized from organic extracts of *E. tinctorium*. Isolation and purification were achieved through multiple purification strategies including phase separation, Sephadex LH-20 SEC, thin layer chromatography, silica column chromatography and HPLC. Structural elucidation was carried out by ESI-MS, FTIR, NMR and

X-Ray crystallography. Compounds **(1)**, **(4)**, **(5)** and **(6)** were known compounds identified as orcinol, echinodol, echinodone, and deacetoxyechinodol respectively. Compound **(2)** turned out to be a new compound which has never been isolated from natural sources. Other than **(4),** previously isolated from *E. tinctorium*, three other compounds (**1, 5, 6**) have been reported from other mushroom species. Despite the identification of **(4)** and the three compounds from other species, their bioactivity have never been previously reported and were therefore investigated. Compounds (**2, 4, 5**) exhibited growth-inhibitory activity against HeLa human cervical cancer cells and U251 human glioblastoma cells. Compound **(4)** also showed promising effects against other cancer cell lines. Additionally, compounds **(2)** and **(4)** induced apoptosis in U251 cells. X-Ray crystal structures of compounds **(2),** (**4)** and **(5**) were reported for the first time.

In order to facilitate the final discussion of my thesis findings, I am providing in the following paragraphs the context on advances in the metabolism of sugar chemistry, biosynthetic gene clusters for enzymes involved in biosynthesis of polysaccharides and small molecules, chemical synthesis of isolated molecules, bioactive compounds produced by phylogenetically related and unrelated fungi, structure comparison of isolated molecules to existing drugs, possible molecular pathways of apoptosis in glioblastoma and approaches to molecular target prediction of compounds.

5.4. Biosynthesis of molecules using biosynthetic gene cluster

Bioactive compounds including polysaccharides and lanostane-type triterpenes have been identified from mushrooms, however the molecular understanding of biosynthesis for these molecules at the molecular level remains limited. Advances in the genome and transcriptome sequencing as well as functional annotation tools has enabled researchers to predict the gene clusters for biosynthesis of bioactive molecules from mushrooms. Gene clusters for bioactive

compounds have recently been investigated for secondary metabolites from *Aspergillus fumigatus* (Lind *et al*., 2017), *Ganoderma lucidum* (Ye *et al*., 2018)*, Flammulina filiformis* and *Hericium erinaceus* (Zhang *et al*., 2019) for triterpenoid biosynthesis.

To further understand the molecular basis of bioactive potential of isolated compounds, the genome of the targeted mushroom would need to be sequenced, after which transcriptome sequencing is carried out. RNA sequence reads are mapped to the respective genome using TopHat software. Functional annotation of predicted genes can be performed in NCBI Non-Redundant Protein Sequence Database (NR), Kyoto Encyclopedia of Genes and Genomes (KEGG), Gene Ontology (GO), SwissProt, and Clusters of Orthologous Groups (COG) (Chen *et al*., 2020). Gene clusters for biosynthesis can be reliably predicted by antiSMASH 3.0 and SMURF software and the genes for the enzymes related to biosynthesis of bioactive compounds were identified by homology searches using the genomes of respective mushrooms using BlastP (Chen *et al*., 2020). Medema *et al* (2011) gave a more accurate software strategy using software for identification and analysis of gene clusters for secondary metabolites. Based on the given strategy, genes were predicted by Glimmer 3 by employing genome sequence data (FASTA, GBK or EMBL files) and gene clusters were identified. HMMer3 was used to generate profile Hidden Markov Models (pHMMs) based on amino acid sequences of all protein encoding genes. A pHMMs library was generated for signature genes involved in biosynthesis of bioactive compounds (Medema *et al*., 2011). This suggests that genome sequencing of bioactive mushrooms will provide detailed insights into the genetic basis of therapeutic potential contained in those mushrooms.

Another interesting combinatorial biosynthesis approach has been employed for generation of new bioactive compounds against cancers, where selected genes are inactivated giving rise to

mutant strains, which then undergo muta-synthesis to generate new product. Alternatively, genes of a biosynthetic pathway are expressed in a producer of a structurally related compound to generate a new compound. Olano and others (2009) reviewed biosynthetic gene clusters of antitumor compounds isolated from actinomycetes. Some of the common compounds included Actinomycin D, Bleomycin A, Doxorubicin, Daunorubicin, and many others.

5.4.1. Biosynthesis of isolated polysaccharides

Polysaccharides are structurally complex molecules and understanding the structure-activity relationship is challenging. Structurally, polysaccharides are condensation polymers of varying monosaccharides. The biosynthesis of polysaccharides involves formation of nucleotide sugar precursors, assembly of monosaccharide residues and polymerization of repeating units. The biosynthesis starts with the phosphorylation of glucose to glucose-6-phosphate (Glc-6-P) which then isomerizes to Fructose-6-phosphate (Fru-6-P). Fru-6-P phosphorylates to fructose-1,6-Bisphosphate and continues with the metabolic cycle. Fru-6-P isomerizes to mannose-6-phosphate and Glc-6-P is converted to Glc-1-P. After multiple steps of conversions with isomerases, epimerases, mutases and dehydratases, as shown in Fig.1, the monosaccharides are added and, after repeating units of monosaccharides, the polysaccharide molecule is formed. The enzymes critical for polysaccharide biosynthesis are phosphoglucomutases (PGM), UDP-Glucopyrophosphorylase (UGP) and phosphoglucoisomerase (PGI). PGM catalyzes the conversion of Glc-6-P to glucose-1-phosphate (Glc-1-P), UGP catalyzes conversion of Glc-1-P to UDP-Glucose and PGI isomerizes Glc-6-P to Fru-6-P. These enzymes were identified by homology sequence search using BLAST and are mentioned in previously published studies (Zhang *et al*., 2019). This biosynthesis has been deduced by researchers (Wang *et al*., 2017; Ye *et al*., 2018; Zhang *et al*., 2019) for polysaccharides from other mushroom species and can be

applied to the existing polysaccharides isolated form *E. tinctorium*. The scheme for biosynthesis mentioned by multiple researchers (Wang *et al*., 2017; Ye *et al*., 2018; Zhang *et al*., 2019) has been combined and summarized in Fig. 5.1. It has been reported that changes in the enzymes critical for biosynthesis of polysaccharides including PGM, UGP and PGI, was correlated with the mole percentage of galactose and mannose in *Ganoderma lucidum* (Peng *et al*., 2015). It is likely that the upregulation or down regulation of genes involved in biosynthesis of polysaccharides generates diverse polysaccharides with variable length and monosaccharide composition. Unlike small molecules, to the best of my knowledge, the biosynthesis of bioactive polysaccharides has never been described in literature. The inability to abundantly produce bioactive polysaccharides with little variability and high purity has in large part impeded the advancement of polysaccharide science and adoption of complex carbohydrate in Western medicine (Persin *et al*., 2011).

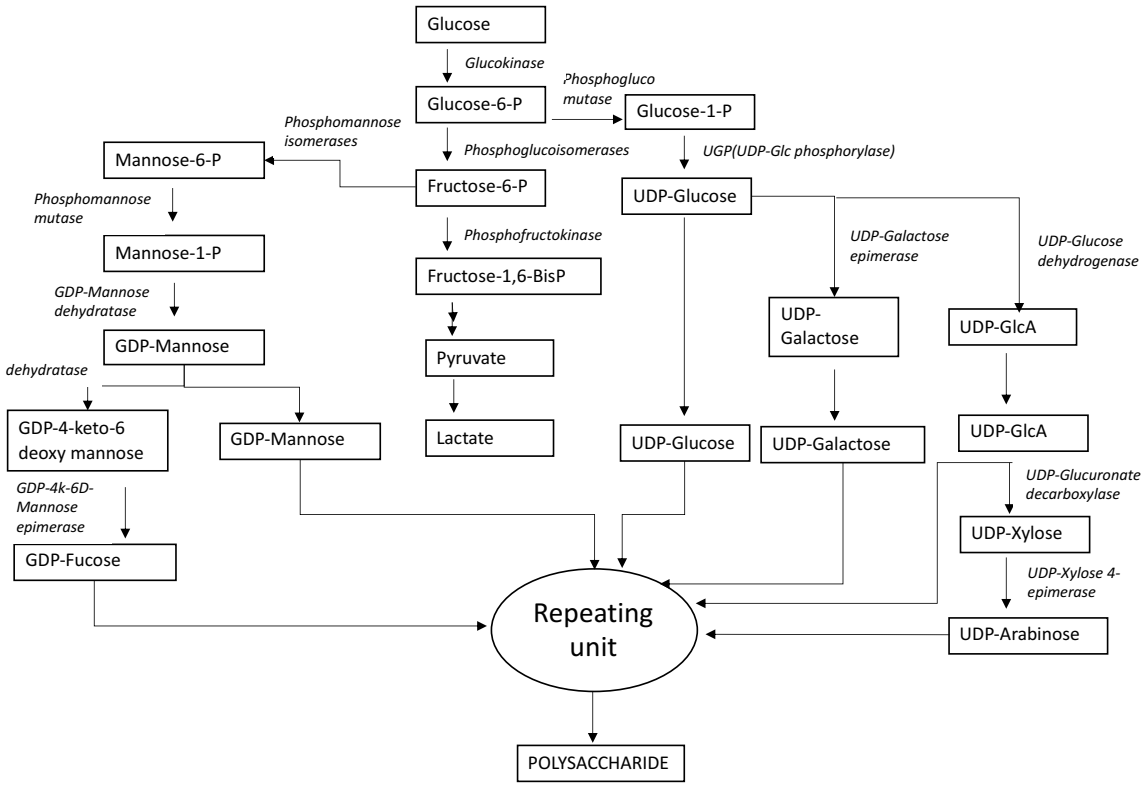

Fig. 5. 1. Schematic representation of biosynthesis of polysaccharides (Summarized from Wang *et al.*, 2017; Ye *et al*., 2018; Zhang *et al*., 2019)

5.4.2. Biosynthesis of small molecules isolated from *E. tinctorium*

5.4.2.1. Biosynthesis of Orcinol (1)

Compound **(1)** identified as orcinol is one of the small molecules isolated from *E. tinctorium*. Biosynthesis of orcinol has been proposed in literature where it can be biosynthesized by sequential condensations of malonyl-CoA and acetyl-CoA. The scheme was given by Taura and others (Taura *et al*., 2016). Orcinol synthase was identified as novel plant type III polyketide synthase (PKS) and considered essential in biosynthesis of orcinol. After multiple sequential condensations, a tetraketide-CoA (methyl tetra-ß-ketide CoA) is formed which then spontaneously or non-enzymatically undergoes cyclization in a step wise manner by thioester hydrolysis, aldol condensation, decarboxylation and aromatization (Fig. 5.2).

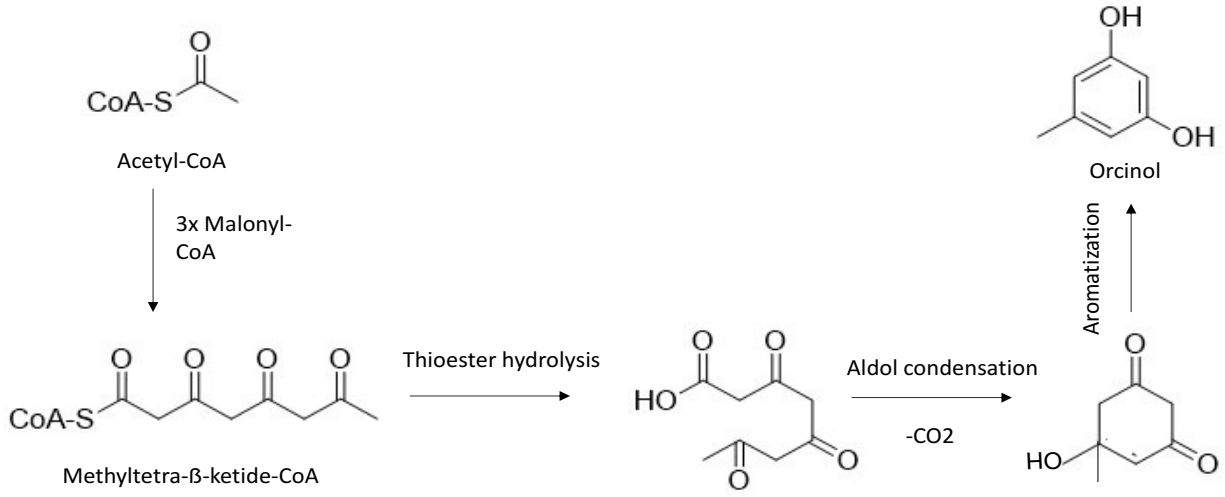

Fig. 5. 2. Biosynthesis of orcinol **(1)** (Taura *et al*., 2016)

Another study identified the gene clusters for synthesis of orcinol from a pathogenic fungus *Fusarium graminearum* (Jørgensen *et al*., 2014). The PKS14 gene cluster was identified to be responsible for producing orsellinic acid and orcinol. It was also hypothesized that orcinol is produced from orsellinic acid by decarboxylation (Fig. 5.3). According to Jørgensen *et al*. (2014), there were seven genes identified near PKS14, amongst which one gene encoded for a carboxylase, enzyme likely to catalyze conversion of orsellinic acid to orcinol. Since, polyketides including orcinol can be biosynthesized by iterative decarboxylative Claisen condensation in the presence of polyketide synthases (PKS), an alternate synthesis strategy was proposed where polyketide backbone could be synthesized by non-decarboxylative Claisen condensation in the presence of polyketoacyl-CoA thiolases (PKTs) (Tan *et al*., 2020).

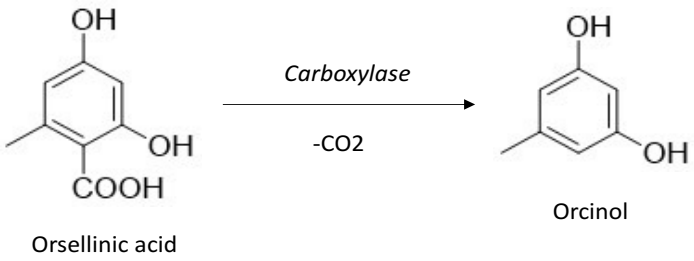

Fig. 5. 3. Biosynthesis of orcinol from decarboxylation of orsellenic acid (Jørgensen *et al*., 2014)

5.4.2.2. Biosynthesis of diphenylmethane derivative (2)

Biosynthesis of compound **(2)** has never been investigated due to the fact that it is isolated for the first time from a natural source. Therefore, gene clusters for its biosynthesis need to be identified from the genome of *E. tinctorium*. It is likely that PKS14 gene cluster is involved. It is also possible that both orsellinic acid and orcinol are biosynthesized and combined to give a keto dimer which is then reduced via some reductases enzymes to give compound **(2)**.

5.4.2.3. Biosynthesis of lanostane-type triterpenes

Biosynthesis of triterpenoids takes place by cyclization of squalene. Studies have shown that triterpene backbone can be biosynthesized through two major pathways in plants: the mevalonic acid (MVA) pathway and the methyl erythritol 4-phosphate (MEP) pathway. The MEP pathway does not exist in fungi (Shi *et al*., 2010). Genetic analysis of *G. lucidum* has revealed genes involved in MVA pathway (Liu *et al*., 2012), suggesting that triterpenoids from *G. lucidum* are biosynthesized via MVA pathway. From the genetic investigation and KEGG gene functional analysis, triterpenoid biosynthesis pathway was summarized (Fig. 5.4) for ganoderic acids isolated from *G. lucidum*. Likewise, the gene clusters for the enzymes involved in triterpenes biosynthesis were also identified in *Flammulina filiformis* (Chen *et al.*, 2020) and *Wolfiporia cocos* (Shu *et al*., 2013). Compound **(4)**, **(5)** and **(6)** are lanostane-type triterpenes isolated from *E. tinctorium* with structural resemblance to ganoderic acids. It is likely that the isolated compounds are biosynthesized via the MVA pathway to obtain the backbone of triterpenoid structure.

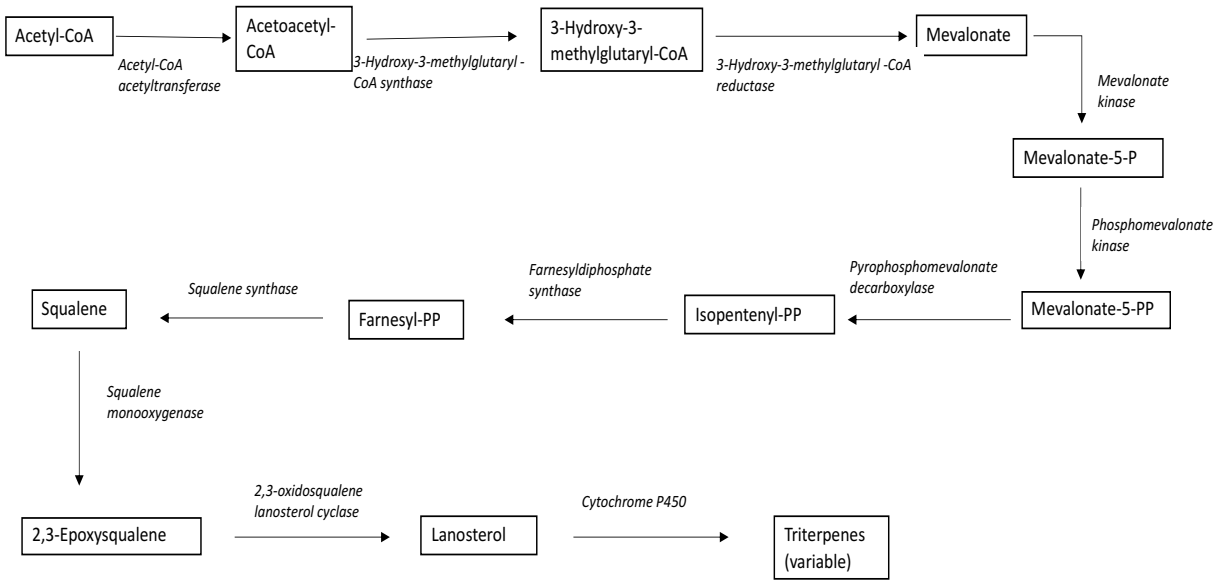

Fig. 5. 4. Mevalonic acid pathway for biosynthesis of triterpenes (adapted from Liu *et al*., 2012)

5.5. Chemical synthesis of isolated molecules

5.5.1. Chemical synthesis of isolated small molecules

For compound **(1)** identified as orcinol, Collie proposed a scheme for chemical synthesis of orcinol (Staunton, J., & Weissman, 2001), involving hydrolysis of dihydro acetic acid to an intermediate that undergoes cyclization and rearrangement to give orcinol as shown in Fig. 5.5.

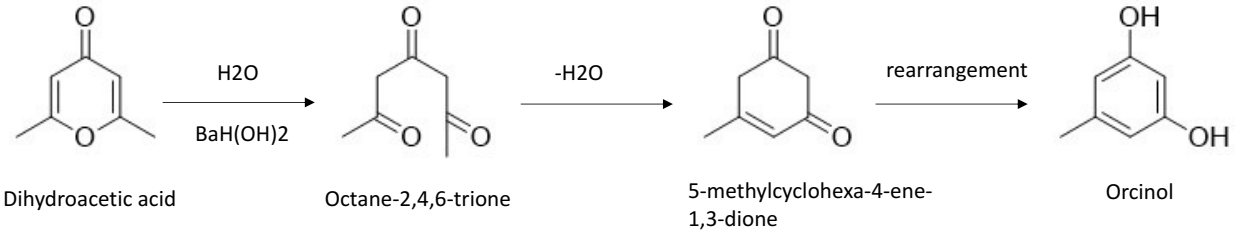

Fig. 5. 5. Collie's synthesis scheme for orcinol **(1)**

For compound **(2)**, several diphenylmethane derivatives were chemically synthesized (by reaction of 5-methylresorcinol with para-formaldehyde in the presence of formic acid. This resulted in formation of *ortho-ortho* form type A, *para-para* from type B, *ortho-para* type C and xanthene type D products (Fig. 5.6). Compound **(2)** was categorized as *ortho-ortho* type A

product. The resulting products were separated by silica column chromatography and HPLC (Matubara *et al*., 1998).

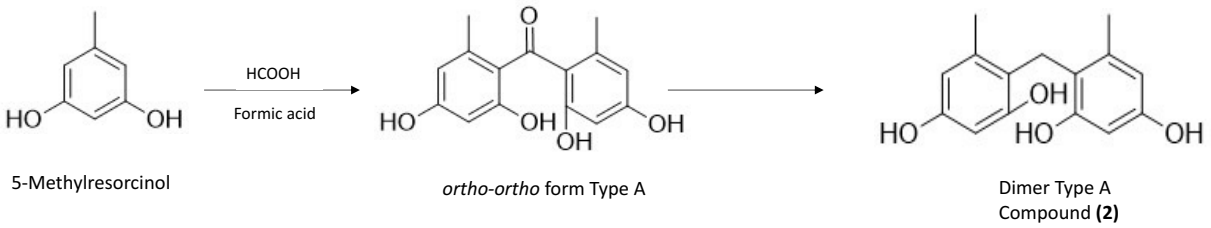

Fig. 5. 6. Chemical synthesis of diphenylmethane derivative compound **(2)**

5.5.2. Chemical synthesis of polysaccharides

Researchers have attempted to synthesize simple carbohydrates although they have faced challenges: lower yields, longer reaction times even for single coupling and finding a single strategy for synthesis. In addition to this, there are also challenges associated with regioselective protection and stereoselective glycosylation for synthesizing complex carbohydrates (Guo, 2008; Kulkarni *et al*., 2018). This shows the complexity of chemical synthesis for small and simple carbohydrates, making it almost impossible to predict the chemical synthesis outcome of a complex polysaccharide. Several attempts have been made in the past to synthesize polysaccharides by self-condensation and have resulted in low yield and degree of polymerization due to some side reactions that caused chain termination (Schuerch, 1973). One of the reviews highlights the use of one-pot protection glycosylation strategies to obtain complex carbohydrates (Kulkarni *et al*., 2018). Chemoenzymatic synthesis is another approach that has come forward in recent years for synthesis of complex sugars which occurs in the presence of enzymes (Li *et al*., 2019). In addition to the aforementioned challenges, there is high molecular weight, variable monosaccharide composition, complex hyper-branched structures, protecting multiple reactive hydroxyl groups, and difficulty in defining the absolute structure of polysaccharides that limits researchers to chemically synthesize complex carbohydrates.

5.6. Compounds produced by phylogenetically related versus unrelated fungi

Researchers have paid attention to the study of bioactive compounds from fungi and often neglected the importance of fungal hosts which might be a significant source of these bioactive compounds. Fungi have a symbiotic relationship with their hosts (or substrates), whereby the host provides the fungus a suitable habitat with plentiful resources and in return, the fungi produce bioactive compounds that may help the host against biotic and abiotic stresses and also supplements growth. It is most likely that the compounds produced by phylogenetically unrelated fungi are similar to that of its host (Kanematsu & Natori, 1972; Xia *et al.,* 2014). This is based on the examples found in the literature of the different fungi growing on the same host plant, as described in detail in the next few paragraphs.

5.6.1. Phylogenetically unrelated fungi

During evolutionary history, fungi have undergone molecular changes in order to adapt to the microenvironments of their habitats. Many studies on endophytic fungi isolated from the same plant host have revealed the presence of the same type of compounds; these have the ability to fight cancer and include paclitaxel, vincristine, vinblastine, camptothecin, and podophyllotoxin, as summarized in Table 5.1. Zhao *et al*. (2010) have reported 19 taxonomically different classes of fungi having the ability to produce the same bioactive compound “Paclitaxel”, a well-known anticancer drug; most of these fungi are hosted by the same plant genus *Taxus* (yew) (Zhao *et al.,* 2010; Kumara *et al.,* 2014). Another study conducted on numerous phylogenetically different fungi isolated from *Nothapodytes nimmoniana* (Icacinaceae) host plant was found to produce the same anticancer compound “camptothecin” (Gurrudatt *et al.,* 2010; Shweta *et al.,* 2010). Other examples include Echinolactone A and D produced by two wood-decaying fungi, *Echinodontium japonicum* and *Granulobasidium vellereum* (Nord, 2014; Suzuki *et al.,* 2005).

One possible reason why endophytic fungi of different lineages produce similar compounds on the same host might be due to the relationship between these fungi and their host, (whether mutualistic or symbiotic) and could be related to some evolutionary molecular mechanisms. There are two possible mechanisms. The first mechanism is the acquisition of gene clusters or DNA segments from the host plant by the resident fungus. It is important to note that when a fungus establishes a relationship with a host, it usually extends its network and become part of the host. As a result of this, the fungal resident acquires the gene clusters present on plasmids of its host, which are responsible for producing those bioactive compounds. Over time, those plasmids containing gene clusters carry the information for biosynthesis of bioactive compounds in the fungi (Kumara *et al.,* 2014). Staniek *et al*. (2009) identified the presence of two genes; *txs* and *baps*, which were involved in the biosynthesis of Taxol (Staniek *et al.,* 2009). The second mechanism could be the independent evolution of genes that are responsible for the production of bioactive compounds. Based on a study conducted on three endophytic fungi, it was revealed that certain genes have independently evolved in the fungi that have a low homology with the *txs* and *baps* genes in Taxol biosynthesis (Xiong *et al.,* 2013).

E. tinctorium, a wood-rotting fungus native to western US and Canada causes decay of living trees (*Abies grandis*) and other conifers such as Western hemlock (*Tsuga heterophylla*) (Ye *et al.,* 1996). Ye *et al*. (1996) have isolated an orange pigment named echinotinctone from *E. tinctorium*, which is also isolated from another fungus *Pyrofomes albomarginatus* (Ye *et al.,* 1996). The common fact to note is that both fungi are isolated from the wood-rotting polypores found on the same host tree, *Abies grandis.* In the light of the above-presented evidence, it is possible that the compounds produced from both of these fungi are a contribution from the genetic machinery of the host. In this case, the compounds produced could be “host-derived”.

Table 5. 1. Host-derived compounds from phylogenetically unrelated fungi

Compound	Fungi	Host	Reference
Paclitaxel	*Cladosporium cladosporioides, Taxomyces andreanae, Taxomyces sp., Alternaria sp., Aspergillus niger var. taxi, Botrytis sp., Botryodiplodia theobromae, Fusarium mairei, Fusarium solani, Metarhizium anisopliae, Papulaspora sp., Pestalotiopsis microspora*	*Taxus* (Yew)	Staniek *et al.,* 2009; Zhao *et al.,* 2010
Podophyllotoxin	*Alternaria sp., Penicillium sp., Phialocephala fortinii, Trametes hirsuta*	*Sinopodophyllum*	Yang *et al.,* 2003; Zhao *et al.,* 2010
Camptothecin	*Neurospora sp., Entrophospora infrequens*	*Nothapodytes*	Rehman *et al.,* 2008; Puri *et al.,* 2005
Gibberellic acid	*Fusarium proliferatum*	Orchid roots	Bomke and Tudzynski, 2009
Vincristine Vinblastine	*Alternaria sp., Fusarium oxysporum*	*Catharanthus roseus*	Guo *et al.,* 1998; Zhang *et al.,* 2000
Huperzine A	*Blastomyces sp., Botrytis sp.*	*Phlegmariurus cryptomerianus*	Ju *et al.,* 2009
Echinotinctone	*E. tinctorium, Pyrofomes albomarginatus*	*Abies grandis*	Ye *et al.,* 1996

5.6.2. Phylogenetically related fungi

Phylogenetically related fungi share a close resemblance to each other based on morphological and molecular characters. Because they are genetically close to each other, they might have the ability to produce similar compounds. However, reports in the literature are not numerous. For instance, *G. lucidum* and other species in the same genus produce the same type of polysaccharides, FIPs and small molecules. The triterpenes and polysaccharides are deemed to be the primary bioactive compounds of *Ganoderma* (Xia *et al.,* 2014). Another example is *Hypomyces subiculosus (*Reeves *et al*., 2008) and *Hypomyces trichothecoides* (Nair *et al.,* 1980), where both species produce the same compound, Hypothemycin.

E. tsugicola is found in Japan and is placed in the same phylogenetic group as *E. tinctorium*. From my investigation on small molecules described in chapter 4, *E. tinctorium* contained three lanostane-type triterpenes: echinodol, echinodone and deacetoxyechinodol. It is interesting to note that the latter two compounds have also been isolated from *E. tsugicola* providing evidence that the same genus produce some similar sets of compounds. In contrast to this, echinodol identified from *E. tinctorium* is not produced by *E. tsugicola* (Kanematsu & Natori, 1972). These examples show that phylogenetically-related fungi can also produce the same compounds and, in that case, these are "fungal-derived compounds".

5.7. Future studies on isolated compounds

Given the large number of bioactive compounds found in *E. tinctorium*, it would be profitable to investigate related species. Based on the phylogenetic classification mentioned in Chapter 1, species within the same genus as *E. tinctorium* can be potential source of similar compounds. These include *E. tsugicola* on *Tsuga* and *Abies* in Japan that shares many similarities with *E. tinctorium* found on western hemlock (Tsuga) and grand fir (Abies) in Western America. This study has already confirmed the presence of echinodone and deacetoxyechinodol from both species. Other members of the same genus including *E. ballouii* on *Chamaecyparis* in Eastern North America and *E. ryvardenii* on *Juniperus* in Europe are found on different hosts. These species may produce interesting compounds on alternate coniferous hosts. In contrast to this, *Echinodontiellum japonicum* is the only member of the Echinodontiaceae on a hardwood host (*Quercus*) so it is likely to produce different compounds. Species representatives of *Amylostereum* and *Larssoniporia*, placed in the Echinodontiaceae by Liu *et al*. (2017), also deserve further investigation. Finally, although two species included in the Echinodontiaceae by Gross (1964) have since be placed in other genera in the separate family

Bondarzewiaceae, *Lauriliella taxodii* and *Laurilia sulcata*, their occurrence of conifer hosts may make them worthy of further study.

The anti-proliferative compounds including EtGIPL1a and small molecules **(2)**, **(4)**, and **(5)** isolated from *E. tinctorium* have already shown promising effects against cancer cell lines. Compound **(2)** is a diphenylmethane derivative. An anticancer small molecule A-007 (4,4'-Dihydroxybenzophenone-2,4-dinitrophenylhydrazone) for advanced breast cancer melanomas and non-Hodgkin's lymphoma showed promising results in phase I clinical trials (Morgan *et al.,* 2003). A-007 structure was compared with Tamoxifen, a well-known drug for treatment of breast cancer. Both molecules have similarities in the skeletal backbones of their chemical structure. Both A-007 and tamoxifen contain diphenylmethane chemical moiety and therefore compound **(2)** can be related with these molecules for its anticancer potential. Structural comparison of both molecules with compound **(2)** is shown in Fig. 5.7.

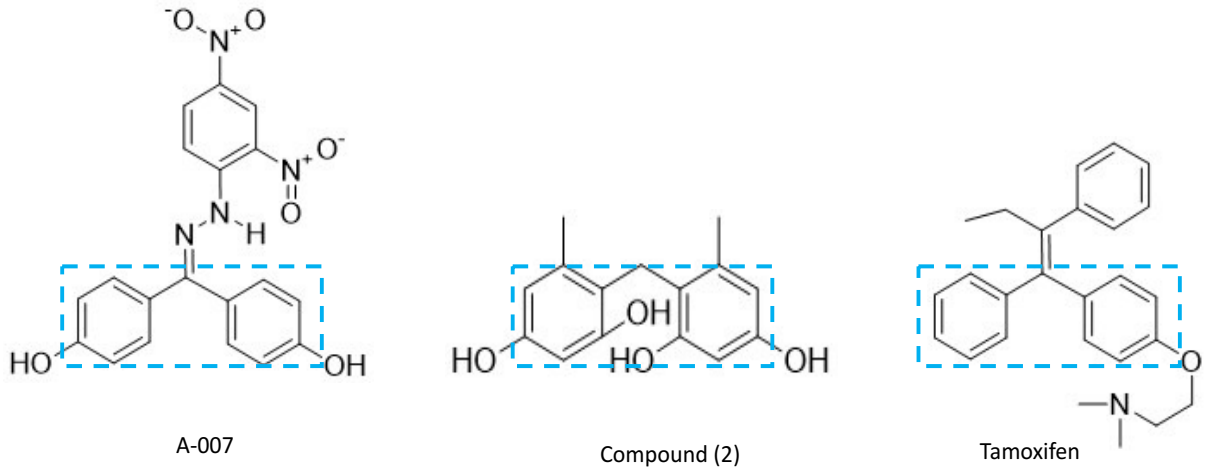

Fig. 5. 7. Structure comparison of A-007, Tamoxifen and compound **(2)**

Some of the well-known antihistamines are also diphenylmethane derivatives. These include hydroxyzine, diphenhydramine, orphenadrine, cetirizine and ebastine. These drugs share the same basic structural unit (Fig. 5.8). It is possible that compound **(2)** might also possess other

biological activities in addition to growth-inhibitory activity. Therefore, it will be interesting to test compound **(2)** for action on histamine receptors.

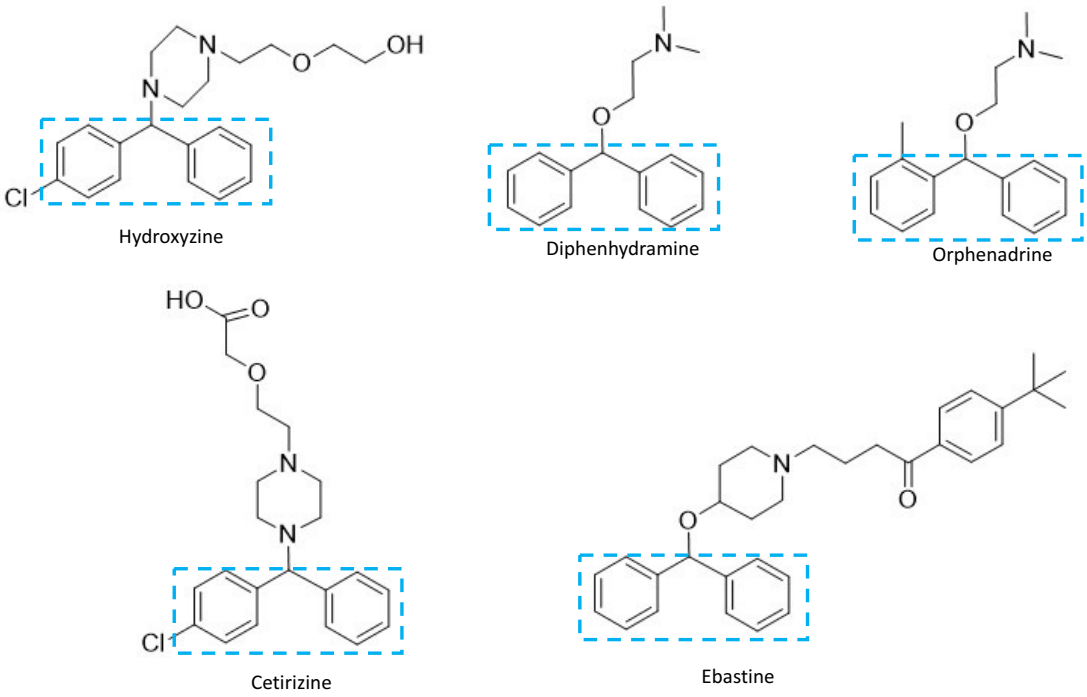

Fig. 5. 8. Structures of anti-histamine drugs with diphenylmethane backbone

From flow cytometry analysis, compounds **(2)** and **(4)** have shown ability to induce apoptosis in U251 glioblastoma cells. Further investigations are clearly required to determine the specific proteins and the molecular pathways involved in their induction apoptosis in U251 cells. The next section focuses on the known possible pathways as well as targets of apoptosis in glioblastoma. The proteins upregulated in those pathways can be investigated in order to determine the molecular pathway that is targeted by EtGIPL1a and small molecules **(2)**, **(4)** and **(5)**.

5.8. Glioblastoma and molecular mechanisms of apoptosis

Glioblastoma is a very aggressive primary malignant tumor of the brain and it accounts for 16 % of the primary central nervous system tumors. Apoptosis, programmed cell death, is essential in maintaining homeostasis between cell survival and cell death. A number of molecular pathways have been reviewed for apoptosis in glioblastoma (Fig. 5.9). Apoptosis can occur through the extrinsic pathway (TRAIL/FasL death receptor cascade) or the intrinsic pathway (mitochondrial pathway). The major molecular targets of bioactive molecules against glioblastoma have been identified by multiple studies (Eisele & Weller, 2013; dos Santos Fernandes *et al*., 2019; Pearson & Regad, 2017; Trjo-Solis *et al*., 2018; Valdes-Rives *et al*., 2017) and includes death receptors DR4/DR5 and FasR, TGF-ß, p53, tyrosine kinase receptors (TKR), P13k/Akt/mTOR, and NF-kB. TRAIL-DR4/5 pathway is targeted by Taxol and TKR pathway is targeted by Axitinib, Imatinib, Niclosamide, NVP-BKM120A, CCT128930. NF-kB is a target for Bortezomib, DHNEQ and BAY-11-7082. Finally, mTOR is a target for Everolimus, Sirolimus, Temsirolimus, and Lonafarnib.

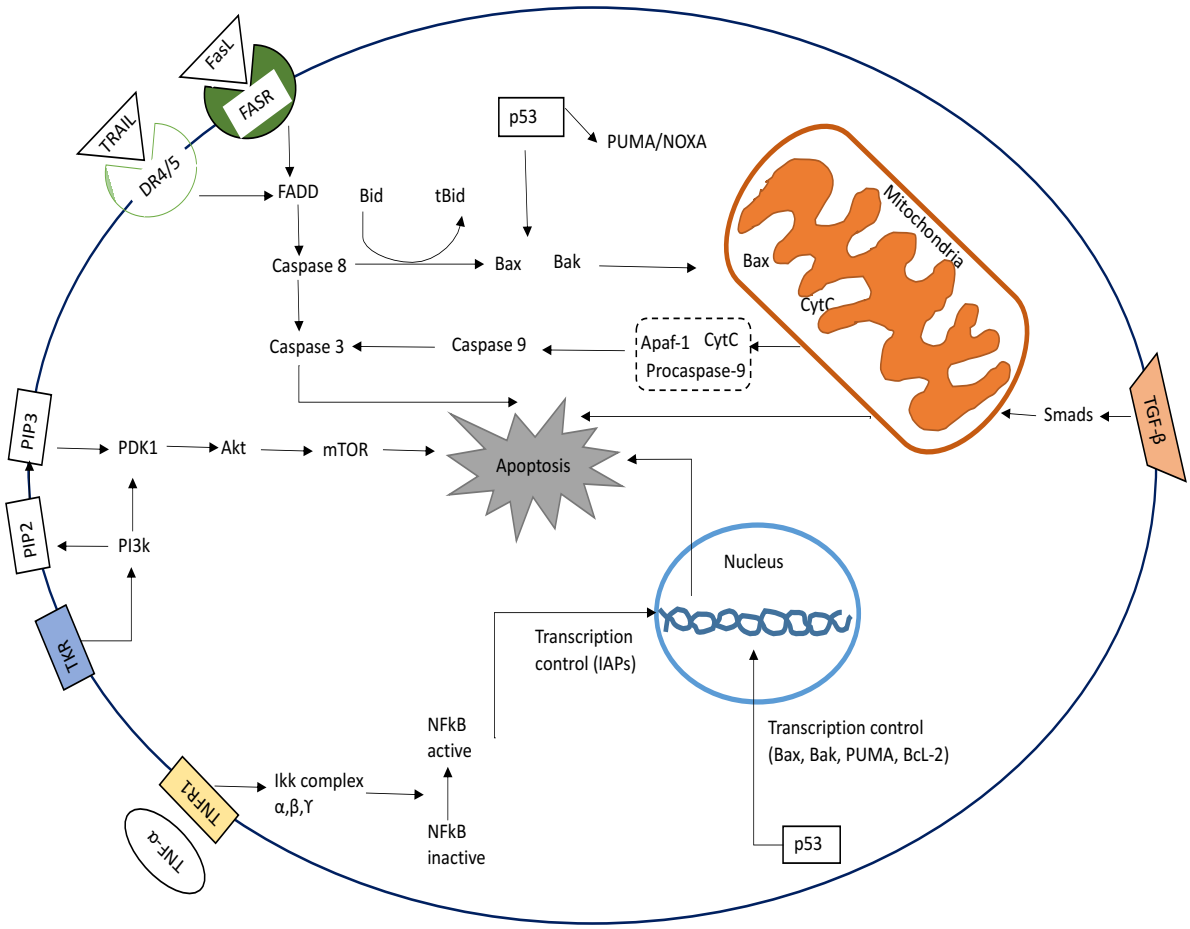

Fig. 5. 9. Molecular targets of bioactive molecules for apoptosis in glioblastoma

5.9. Molecular target prediction and their importance

Drug-target interaction has been predicted by biochemical and computational tools, where computational target deconvolution is considered faster, cost effective and considerably reliable in the current era. Predicting targets for the lead molecules is one of the essential steps in drug discovery process. The importance of predicting drug targets is to identify the receptors that a drug molecule will effectively bind to produce a response. It can also determine whether the drug has the ability to associate with multiple targets for producing multiple effects. The common computational tools currently available for target prediction include TarPred, MolTarPred, SEA, HitPick and SwissTargetPrediction with varying target coverage in their database. TarPred offers

target coverage of 533 whereas MolTarPred 4553, SEA 1400, HitPick 1375, and SwissTargetPrediction have 2686 targets (Peon *et al.*, 2019). MolTarPred is a more user-friendly computational tool for molecular target prediction with large target coverage and also offers reliability of prediction score, ensuring how accurate a predicted target is.

Therefore, for the small molecules **(1), (2), (4)** and **(5)** isolated from *E. tinctorium*, MolTarPred program was used to predict their molecular targets. A summary of isolated compounds with their predicted targets and reliability of prediction score is shown in chapter 4 Table 16. Interestingly, compound **(2)** did not have a reliable predicted target. This could be due to the fact that it has not been isolated before and therefore the database did not have structurally-related molecules which could interact the same way with the targets as **(2)**. In contrast, it could also be that **(2)** in its current form does not have an effective target and it is possible that it will bind more effectively to predicted targets after chemical modification. This approach is also used to generate more effective and less toxic drug alternatives.

Molecular targets predicted for lanostane-type triterpenes **(4)** and **(5)** were different although the structure of **(4)** and **(5)** differ by only one functional group, suggesting that structurally-related compounds can have diverse interactions with the target receptors. Compound **(4)** also has structural similarity to cholesterol and, not surprisingly the predicted target was 7-dehydrocholesterol reductase, a terminal enzyme for biosynthesis of cholesterol. The structural resemblance to cholesterol explains the high prediction score of compound **(4)** towards this enzyme. The other predicted targets for **(4)** and **(5)** have been linked to brain cancers which to some extent could explain the growth-inhibitory effects of both compounds in U251 glioblastoma cells. The results of molecular target prediction using computational tools can then

be used to confirm whether or not these results can be reproduced and confirmed by biochemical testing.

5.10. Experimental approaches to identify molecular targets of isolated compounds

Small molecule drug development involves two main strategies: target-based drug discovery and phenotype-based drug discovery (Kubota *et al*., 2019; Shangugguan, 2021; Wilkinson, 2020). Target-based drug discovery is also recognized as "bottom-up strategy" and is a traditional approach where target is identified first followed by small molecule screening. Phenotype-based drug discovery also known as "target deconvolution strategy" has gained more popularity recently in the drug discovery process as it starts with small molecules screening through assays and, once a lead molecule is selected, the molecular targets are then identified (Kubota *et al*., 2019; Shangugguan, 2021; Wilkinson, 2020).

Experimental profiling of predicted targets of compounds can be done by using the assays which can confirm the binding of isolated molecules to its predicted target molecule. For target deconvolution, target prediction is either indirectly assessed via gene expression profiling using microarrays, RNA sequencing and connectivity maps (Kubota *et al*., 2019; Wilkinson, 2020) or by directly finding the targets that bind to the small molecules which is achieved by chemical proteomics, cloning-based methods (phage display) and protein microarrays (Kubota *et al*., 2019). For target prediction, small molecules are derivatized with chemical or radioactive labels, probes with or without photo-crosslinking, drug target databases (therapeutic target database, ChEMBL database, BindingDB database, PharmGKB database, canSAR database, DrugBank), biological assays (DNA microarray, RT-PCR, RNA sequencing, and gene knockout), and machine-based methods (support vector machine and random forest algorithm) are employed (Shangugguan, 2021).

These approaches have been successful in identifying targets for small molecules like Dasatinib a protein tyrosine kinase inhibitor, Orlistat as an anti-obesity drug, Paraglycine for Parkinson's disease, Showdomycin, a nucleoside antibiotic (Shu et al., 2013) and therefore, these target deconvolution approaches can be used in the future to experimentally determine the molecular targets of small molecules **(1-6)** isolated from *E. tinctorium* as described in this thesis.

5.11. References

Bömke, C., & Tudzynski, B. (2009). Diversity, regulation, and evolution of the gibberellin biosynthetic pathway in fungi compared to plants and bacteria. *Phytochemistry*, *70*(15), 1876-1893.

Chen, J., Li, J. M., Tang, Y. J., Ma, K., Li, B., Zeng, X., ... & Guo, S. X. (2020). Genome-wide analysis and prediction of genes involved in the biosynthesis of polysaccharides and bioactive secondary metabolites in high-temperature-tolerant wild *Flammulina filiformis*. *BMC genomics*, *21*(1), 1-16.

Eisele, G., & Weller, M. (2013). Targeting apoptosis pathways in glioblastoma. *Cancer letters*, *332*(2), 335-345.

dos Santos Fernandes, G. F., Fernandes, B. C., Valente, V., & Dos Santos, J. L. (2019). Recent advances in the discovery of small molecules targeting glioblastoma. *European journal of medicinal chemistry*, *164*, 8-26.

Gross, H. L. (1964). The Echinodontiaceae. *Mycopathologia et mycologia applicata*, *24*(1), 1-26.

Guo, B., Li, H., & Zhang, L. (1998). Isolation of a fungus producing Vinblastine. *Journal of Yunnan university (Natural Sciences)*, *20*(3), 214-215.

Guo, Z. (2008). Chemical Synthesis of Complex Carbohydrates. In *carbohydrate chemistry, biology and medical applications* (pp. 59-83). Elsevier.

Gurudatt, P. S., Priti, V., Shweta, S., Ramesha, B. T., Ravikanth, G., Vasudeva, R., & Puri, S. (2010). Attenuation of camptothecin production and a negative relation between hyphal biomass and camptothecin content in endophytic fungal strains isolated from *Nothapodytes nimmoniana* Grahm (Icacinaceae). *Current science*, *98*(8), 1006-1010.

Javed, S., Li, W. M., Zeb, M., Yaqoob, A., Tackaberry, L. E., Massicotte, H. B.,Egger, K. N., Cheung, P. C., Payne, G. W., & Lee, C. H. (2019). Anti-inflammatory activity of the wild mushroom, *Echinodontium tinctorium*, in RAW264. 7 macrophage cells and mouse microcirculation. *Molecules*, *24*(19), 3509.

Jørgensen, S. H., Frandsen, R. J. N., Nielsen, K. F., Lysøe, E., Sondergaard, T. E., Wimmer, R., Giese, H., & Sørensen, J. L. (2014). *Fusarium graminearum* PKS14 is involved in orsellinic acid and orcinol synthesis. *Fungal genetics and biology*, *70*, 24-31.

Ju, Z., Wang, J., & Pan, S. L. (2009). Isolation and preliminary identification of the endophytic fungi which produce Hupzine A from four species in Hupziaceae and determination of Huperzine A by HPLC. *Fudan university journal of medical sciences*, *4*, 017.

Kanematsu, A., & Natori, S. (1972). Triterpenoids of *Echinodontium tsugicola*. *Chemical and pharmaceutical bulletin*, *20*(9), 1993-1999.

Kubota, K., Funabashi, M., & Ogura, Y. (2019). Target deconvolution from phenotype-based drug discovery by using chemical proteomics approaches. *Biochimica et biophysica acta)-proteins and proteomics*, *1867*(1), 22-27.

Kulkarni, S. S., Wang, C. C., Sabbavarapu, N. M., Podilapu, A. R., Liao, P. H., & Hung, S. C. (2018). "One-pot" protection, glycosylation, and protection–glycosylation strategies of carbohydrates. *Chemical reviews*, *118*(17), 8025-8104.

Kumara, P. M., Shweta, S., Vasanthakumari, M. M., Sachin, N., Manjunatha, B. L., Jadhav, S. S., & Shaanker, R. U. (2014). Endophytes and plant secondary metabolite synthesis: molecular and evolutionary perspective. In *advances in endophytic research* (pp. 177-190). Springer India.

Lind, A. L., Wisecaver, J. H., Lameiras, C., Wiemann, P., Palmer, J. M., Keller, N. P., Rodrigues, F., Goldman, G. H., & Rokas, A. (2017). Drivers of genetic diversity in secondary metabolic gene clusters within a fungal species. *PLoS biology*, *15*(11), e2003583.

Liu, D., Gong, J., Dai, W., Kang, X., Huang, Z., Zhang, H. M., Liu, W., Liu, L., Ma, J., Xia, Z., & Xiong, X. (2012). The genome of *Ganoderma lucidum* provide insights into triterpense biosynthesis and wood degradation. *PloS one*, *7*(5), e36146.

Liu, S. L., Zhao, Y., Dai, Y. C., Nakasone, K. K., & He, S. H. (2017). Phylogeny and taxonomy of *Echinodontium* and related genera. *Mycologia*, *109*(4), 568-577.

Li, W., McArthur, J. B., & Chen, X. (2019). Strategies for chemoenzymatic synthesis of carbohydrates. *Carbohydrate research*, *472*, 86-97.

Matubara, H., Miharu, K., Kinoshita, K., Koyama, K., Ye, Y., Takahashi, K., Yoshimura, I., Yamamoto, Y., Miura, Y., & Kinoshita, Y. (1998). Inhibitory effect of lichen metabolites and their synthetic analogues on melanin biosynthesis in cultured B-16 mouse melanoma cells. *Natural product sciences*, *4*(3), 161-169.

Medema, M. H., Blin, K., Cimermancic, P., De Jager, V., Zakrzewski, P., Fischbach, M. A., Weber, T., Takano, E., & Breitling, R. (2011). antiSMASH: rapid identification, annotation

and analysis of secondary metabolite biosynthesis gene clusters in bacterial and fungal genome sequences. *Nucleic acids research*, *39* (suppl. 2), W339-W346.

Morgan, L. R., Thangaraj, K., LeBlanc, B., Rodgers, A., Wolford, L. T., Hooper, C. L., Fan, D., & Jursic, B. S. (2003). Design, Synthesis, and Anticancer Properties of 4, 4'-Dihydroxybenzophenone-2, 4-dinitrophenylhydrazone and Analogues. *Journal of medicinal chemistry*, *46*(21), 4552-4563.

Newman, D. J., & Cragg, G. M. (2007). Natural products as sources of new drugs over the last 25 years. *Journal of natural products*, *70*(3), 461-477.

Nair, M. S. R., and S. T. Carey. (1980). Metabolites of Pyrenomycetes. XIII. Structure of (+) hypothemycin, an antibiotic macrolide from *Hypomyces trichothecoides*. *Tetrahedron letters,* 21**:**2011-2012.

Nord, C. (2014). Secondary metabolites from the saprotrophic fungus *Granulobasidium vellereum*. *Acta universitatis agriculturae sueciae,* (Vol. 2014, No. 88).

Olano, C., Méndez, C., & Salas, J. A. (2009). Antitumor compounds from marine actinomycetes. *Marine drugs*, *7*(2), 210-248.

Pearson, J. R., & Regad, T. (2017). Targeting cellular pathways in glioblastoma multiforme. *Signal transduction and targeted therapy*, *2*(1), 1-11.

Peón, A., Li, H., Ghislat, G., Leung, K. S., Wong, M. H., Lu, G., & Ballester, P. J. (2019). MolTarPred: a web tool for comprehensive target prediction with reliability estimation. *Chemical biology & drug design*, *94*(1), 1390-1401.

Peng, L., Qiao, S., Xu, Z., Guan, F., Ding, Z., Gu, Z., Zhang, L., & Shi, G. (2015). Effects of culture conditions on monosaccharide composition of *Ganoderma lucidum* exopolysaccharide and on activities of related enzymes. *Carbohydrate polymers*, *133*, 104-109.

Puri, S. C., Verma, V., Amna, T., Qazi, G. N., & Spiteller, M. (2005). An endophytic fungus from *Nothapodytes foetida* that produces camptothecin. *Journal of natural products*, *68*(12), 1717-1719.

Reeves, C. D., Hu, Z., Reid, R., & Kealey, J. T. (2008). Genes for the biosynthesis of the fungal polyketides hypothemycin from *Hypomyces subiculosus* and radicicol from *Pochonia chlamydosporia*. *Applied and environmental microbiology*, *74*(16), 5121-5129.

Rehman, S., Shawl, A. S., Kour, A., Andrabi, R., Sudan, P., Sultan, P., & Qazi, G. N. (2008). An endophytic *Neurospora* sp. from *Nothapodytes foetida* producing camptothecin. *Applied biochemistry and microbiology*, *44*(2), 203-209.

Schuerch, C. (1973). Systematic approaches to the chemical synthesis of polysaccharides. *Accounts of chemical research*, *6*(6), 184-191.

Shangguan, Z. (2021). A Review of Target Identification Strategies for Drug Discovery: from Database to Machine-Based Methods. In *Journal of physics: conference series* (Vol. 1893, No. 1, p. 012013). IOP Publishing.

Shi, L., Ren, A., Mu, D., & Zhao, M. (2010). Current progress in the study on biosynthesis and regulation of ganoderic acids. *Applied microbiology and biotechnology*, *88*(6), 1243-1251.

Shweta S, Züehlke S, Ramesha BT, Priti V, Mohana Kunar P, Ravikanth G, Spiteller M, Vasudeva R, Shaanker RU. Endophytic fungal strains of *Fusarium solani*, from *Apodytes dimidiata* E. Mey. ex Arn (Icacinaceae) produce camptothecin, 10-hydroxycamptothecin and 9-methoxycamptothecin. *Phytochemistry*. 2010; 71: 117-122.

Shu, S., Chen, B., Zhou, M., Zhao, X., Xia, H., & Wang, M. (2013). De novo sequencing and transcriptome analysis of *Wolfiporia cocos* to reveal genes related to biosynthesis of triterpenoids. *PLoS One*, *8*(8), e71350.

Staniek, A., Woerdenbag, H. J., & Kayser, O. (2009). *Taxomyces andreanae*: a presumed paclitaxel producer demystified? *Planta medica* 75:1561-1566.

Staunton, J., & Weissman, K. J. (2001). Polyketide biosynthesis: a millennium review. *Natural product reports*, *18*(4), 380-416.

Su, Y., Ge, J., Zhu, B., Zheng, Y. G., Zhu, Q., & Yao, S. Q. (2013). Target identification of biologically active small molecules via in situ methods. *Current opinion in chemical biology*, *17*(5), 768-775.

Suzuki, S., Murayama, T., & Shiono, Y. (2005). Illudalane sesquiterpenoids, echinolactones A and B, from a mycelial culture of *Echinodontium japonicum*. *Phytochemistry*, *66*(19), 2329-2333.

Tan, Z., Clomburg, J. M., Cheong, S., Qian, S., & Gonzalez, R. (2020). A polyketoacyl-CoA thiolase-dependent pathway for the synthesis of polyketide backbones. *Nature catalysis*, *3*(7), 593-603.

Taura, F., Iijima, M., Yamanaka, E., Takahashi, H., Kenmoku, H., Saeki, H., Morimoto, S., Asakawa, Y., Kurosaki, F., & Morita, H. (2016). A novel class of plant type III polyketide synthase involved in orsellinic acid biosynthesis from *Rhododendron dauricum*. *Frontiers in plant science*, *7*, 1452.

Trejo-Solís, C., Serrano-Garcia, N., Escamilla-Ramírez, Á., Castillo-Rodríguez, R. A., Jimenez-Farfan, D., Palencia, G., Calvillo, M., Alvarez-Lemus, M. A., Flores-Najera, A., Cruz-Salgado, A., & Sotelo, J. (2018). Autophagic and apoptotic pathways as targets for chemotherapy in glioblastoma. *International journal of molecular sciences*, *19*(12), 3773.

Valdés-Rives, S. A., Casique-Aguirre, D., Germán-Castelán, L., Velasco-Velázquez, M. A., & González-Arenas, A. (2017). Apoptotic signaling pathways in glioblastoma and therapeutic implications. *BioMed research international*, *2017*, 1-12.

Wang, Q., Wang, F., Xu, Z., & Ding, Z. (2017). Bioactive mushroom polysaccharides: a review on monosaccharide composition, biosynthesis and regulation. *Molecules*, *22*(6), 955.

Wilkinson, I. V., Terstappen, G. C., & Russell, A. J. (2020). Combining experimental strategies for successful target deconvolution. *Drug discovery today*, *25*(11), 1998-2005.

Xia, Q., Zhang, H., Sun, X., Zhao, H., Wu, L., Zhu, D., & Zhang, L. (2014). A comprehensive review of the structure elucidation and biological activity of triterpenoids from *Ganoderma* spp. *Molecules*, *19*(11), 17478-17535.

Xiong, Z. Q., Yang, Y. Y., Zhao, N., & Wang, Y. (2013). Diversity of endophytic fungi and screening of fungal paclitaxel producer from Anglojap yew, Taxus x media. *BMC microbiology*, *13*(1), 1-10.

Yang, X., Guo, S., Zhang, L., & Shao, H. (2003). Select of producing podophyllotoxin endophytic fungi from podophyllin plant. *Natural product research and development*, *15*(5), 419-422.

Ye, Y., Josten, I., Arnold, N., Steffan, B., and Steglich, W. (1996) Isolation ofa fluorone pigment from the Indian paint fungus *Echinodontium tinctorium* and *Pyrofomes albomarginatus. Tetrahedron* 52, 5793-5798.

Ye, L., Liu, S., Xie, F., Zhao, L., & Wu, X. (2018). Enhanced production of polysaccharides and triterpenoids in *Ganoderma lucidum* fruit bodies on induction with signal transduction during the fruiting stage. *PLoS One*, *13*(4), e0196287.

Zhang, N., Tang, Z., Zhang, J., Li, X., Yang, Z., Yang, C., Zhang, Z., & Huang, Z. (2019). Comparative transcriptome analysis reveals the genetic basis underlying the biosynthesis of polysaccharides in *Hericium erinaceus*. *Botanical studies*, *60*(1), 1-14.

Zhang, L., Guo, B., Li, H., Zeng, S., Shao, H., Gu, S., & Wei, R. (2000). Preliminary study on the isolation of endophytic fungus of *Catharanthus roseus* and its fermentation to produce products of therapeutic value. *Chinese traditional and herbal drugs*, *31*(11), 805-807.

Zhao, J., Zhou, L., Wang, J., Shan, T., Zhong, L., Liu, X., & Gao, X. (2010). Endophytic fungi for producing bioactive compounds originally from their host plants. *Current research, technology and education topics in applied microbiology and microbial biotechnology*, 1, 567-576.